



The Ohio State University

LANGLEY GRANT
IN-32-CR
93199
P-319

ELECTROMAGNETIC SCATTERING FROM A CLASS OF OPEN-ENDED
WAVEGUIDE DISCONTINUITIES

By

A. Altintas
P.H. Pathak
W.D. Burnside

The Ohio State University

ElectroScience Laboratory

Department of Electrical Engineering
Columbus, Ohio 43212

Technical Report 716148-9
Grant No. NSG 1613
March 1986

National Aeronautics and Space Administration
Langley Research Center
Hampton, Virginia 23665

(NASA-CR-181271) ELECTROMAGNETIC SCATTERING
FROM A CLASS OF OPEN-ENDED WAVEGUIDE
DISCONTINUITIES (Ohio State Univ.) 319 p
Avail: NTIS HC A14/MF A01 CSCI 20N

N87-27874

Unclas
G3/32 C093199

NOTICES

When Government drawings, specifications, or other data are used for any purpose other than in connection with a definitely related Government procurement operation, the United States Government thereby incurs no responsibility nor any obligation whatsoever, and the fact that the Government may have formulated, furnished, or in any way supplied the said drawings, specifications, or other data, is not to be regarded by implication or otherwise as in any manner licensing the holder or any other person or corporation, or conveying any rights or permission to manufacture, use, or sell any patented invention that may in any way be related thereto.

REPORT DOCUMENTATION PAGE	1. REPORT NO.	2.	3. Recipient's Accession No.
4. Title and Subtitle ELECTROMAGNETIC SCATTERING FROM A CLASS OF OPEN-ENDED WAVEGUIDE DISCONTINUITIES			5. Report Date March 1986
7. Author(s) A. Altintas, P. Pathak, W. Burnside			6.
9. Performing Organization Name and Address The Ohio State University ElectroScience Laboratory 1320 Kinnear Road Columbus, Ohio 43212			8. Performing Organization Rept. No. 716148-9
12. Sponsoring Organization Name and Address National Aeronautics and Space Administration Langley Research Center Hampton, Virginia 23665			10. Project/Task/Work Unit No.
			11. Contract(C) or Grant(G) No. (C) (G) NSG-1613
			13. Type of Report & Period Covered Technical
15. Supplementary Notes			14.
16. Abstract (Limit: 200 words) <p>A relatively simple high frequency analysis of electromagnetic scattering from a class of open-ended waveguide discontinuities has been developed. The waveguides are composed of perfectly-conducting sections in which the electromagnetic field can be written as a sum of waveguide modes. Junctions are formed at the open-end and also within interior regions where different sections are joined. The interior modal field is expressed in terms of an equivalent set of "modal rays". The reflection and transmission properties of each junction are described in terms of a scattering matrix which is determined by combining the modal ray picture with high frequency techniques such as the geometrical theory of diffraction (GTD), the equivalent current method (ECM), and modifications of the physical theory of diffraction (PTD). A new set of equivalent currents are employed in this ECM analysis which leads to a simple treatment of many types of junction discontinuities. Also, a new procedure is presented to improve the efficiency of the aperture integration at the open end which is required in the PTD procedure for finding the fields radiated from (or coupled into) the open end. Once the scattering matrices are determined via the aforementioned high frequency techniques, they are then combined using a self-consistent multiple scattering method to obtain the total scattered fields. The accuracy of the present approach has been verified by comparison with other available solutions and measurements wherever possible.</p>			
17. Document Analysis a. Descriptors b. Identifiers/Open-Ended Terms c. COSATI Field/Group			
18. Availability Statement	19. Security Class (This Report) Unclassified	21. No. of Pages 301	
	20. Security Class (This Page) Unclassified	22. Price	

TABLE OF CONTENTS

	<u>PAGE</u>
LIST OF FIGURES	v
 <u>CHAPTER</u>	
I INTRODUCTION	1
II SELF CONSISTENT MULTIPLE SCATTERING MATRIX FORMULATION	13
III DEVELOPMENT OF THE ELEMENTS OF THE SCATTERING MATRICES IN THE MULTIPLE SCATTERING METHOD	27
3.1 <u>The Reflection Type Scattering Matrix</u>	27
3.1.1 <u>Reflection Back Into the Exterior Region</u>	28
a) Near field scattering by the open end of a semi-infinite circular waveguide:	34
b) Near field scattering by the open end of a semi-infinite rectangular waveguide:	46
3.1.2 <u>Modal Reflection from an Interior Discontinuity</u>	50
a) Modal reflection at the open-end of a parallel-plate waveguide:	61
i) TM_z case:	62
ii) TE_z^z case:	62

b)	Modal reflection from the open-end of a rectangular waveguide:	63
c)	Reflection of TE_{10} mode from an E-plane circular bend in a rectangular waveguide:	68
d)	Modal reflection from a junction between two linearly tapered waveguides:	73
i)	TE_x case:	73
ii)	TM_x case:	74
e)	Modal reflection from the junction of two sectoral waveguides:	75
i)	TE_x case:	76
ii)	TM_x case:	77
f)	Reflection from the open end of a circular waveguide:	79
i)	TE_z case:	79
ii)	TM_z case:	81
g)	Modal reflection in an annular waveguide terminated by a parallel-plate waveguide:	85
3.2.	<u>The Transmission Type Scattering Matrix</u>	90
3.2.1.	<u>Transmission Between Exterior and Interior Regions</u>	92
a)	Far zone radiation from an open-ended parallel-plate waveguide:	98
i)	Aperture integration analysis	99
ii)	GTD Analysis	106
b)	Radiation from an open-ended rectangular waveguide:	116
c)	Radiation from an open-ended circular waveguide:	126
3.2.2	<u>Transmission of Modal Energy Between Two Interior Regions</u>	128
	Transmission of a TEM wave in a parallel-plate waveguide into a whispering gallery mode in an annular waveguide:	131

IV	NUMERICAL AND MEASUREMENT RESULTS	132
	a) Reflection from a 2-D horn antenna:	132
	b) Reflection from sharp bends in a parallel-plate waveguide:	134
	c) Reflection from a circular bend in a parallel-plate waveguide:	137
	d) Electromagnetic backscattering from a waveguide cavity model:	139
	i) Results for the Scattering only from the Rim	143
	ii) Results for the Interior Cavity Effects	177
	e) Electromagnetic backscattering from a circular waveguide cavity:	225
V	CONCLUSIONS	231
<u>APPENDICES</u>		
A	MODAL FIELD EXPRESSIONS IN A RECTANGULAR WAVEGUIDE	235
B	MODAL FIELD EXPRESSIONS IN A PARALLEL PLATE WAVEGUIDE	240
C	MODAL FIELD EXPRESSIONS IN A SECTORAL WAVEGUIDE	243
D	MODAL FIELD EXPRESSIONS IN A 2-D LINEARLY TAPERED WAVEGUIDE	251
E	CIRCUMFERENTIALLY PROPAGATING MODES IN AN ANNULAR REGION	255
F	MODAL FIELD EXPRESSIONS IN A CIRCULAR WAVEGUIDE	265
G	WAVEGUIDE EXCITATION PROBLEM	270
H	EDGE CORRECTION FOR APERTURE INTEGRATION	275
I	APPLICATION OF THE RECIPROCITY THEOREM TO FIND THE RELATION BETWEEN THE SCATTERING MATRICES $[S_{12}]$ AND $[S_{21}^p]$	280
J	EQUIVALENT MAGNETIC LINE DIPOLE	286
K	DESCRIPTION OF THE EQUIVALENCE PRINCIPLE EMPLOYED IN THE CALCULATION OF SCATTERING MATRICES	290
L	ILLUSTRATION OF RECIPROCITY IN THE APERTURE INTEGRATION	293
	REFERENCES	297

LIST OF FIGURES

FIGURE	PAGE
1.1. Waveguide geometries considered.	2
1.2. A waveguide cavity with three junctions.	7
1.3. Isolation of scattering mechanisms and illustration of scattering matrices.	9
1.4. Effective scattering geometry for the problem in Figure 1.2.	10
2.1. An N-port junction.	14
2.2. An open-ended waveguide cavity problem.	16
2.3. Scattering by only the rim at the open end of the waveguide.	19
2.4. Radiation and reflection at the open end due to a waveguide mode incident at the open end.	20
2.5. Reflection of waveguide modes at junction ②.	20
3.1. The equivalent currents \bar{I}_{eq} and \bar{M}_{eq} at the rim of the open end.	31
3.2. Diffraction by a wedge. The angles $\tilde{\beta}_0$, $\tilde{\beta}$, ψ and ψ' which occur in the wedge diffraction coefficient.	33
3.3. Scattering from the open end of a semi-infinite circular waveguide.	35
3.4. Near field scattering from an open-ended circular waveguide using GTD and ECM. — GTD, --- ECM. $r=5\lambda$, $a=1\lambda$, $\theta^i=45^\circ$, $\phi^i=0$, $\phi^r=0$, $\bar{E}^i=\hat{\phi}^i$	36
3.5. Near field scattering from an open-ended circular waveguide using GTD and ECM. — GTD, --- ECM. $r=5\lambda$, $a=1\lambda$, $\theta^i=45^\circ$, $\phi^i=0$, $\phi^r=180^\circ$, $\bar{E}^i=\hat{\phi}^i$	37

FIGURE	PAGE
3.6. Near field scattering from an open-ended circular waveguide using GTD and ECM. — GTD, --- ECM. $r=5\lambda$, $a=2\lambda$, $\theta^i=45^\circ$, $\phi^i=0$, $\phi^r=0$, $\bar{E}^i=\hat{\phi}^i$	38
3.7. Near field scattering from an open-ended circular waveguide using GTD and ECM. — GTD, --- ECM. $r=5\lambda$, $a=2\lambda$, $\theta^i=45^\circ$, $\phi^i=0$, $\phi^r=180^\circ$, $\bar{E}^i=\hat{\phi}^i$	39
3.8. Near field scattering from an open-ended circular waveguide using GTD and ECM. — GTD, xxx ECM. $r=10\lambda$, $a=5\lambda$, $\theta^i=45^\circ$, $\phi^i=0$, $\phi^r=0$, $\bar{E}^i=\hat{\phi}^i$	40
3.9. Near field scattering from an open-ended circular waveguide using GTD and ECM. — GTD, --- ECM. $r=10\lambda$, $a=5\lambda$, $\theta^i=45^\circ$, $\phi^i=0$, $\phi^r=180^\circ$, $\bar{E}^i=\hat{\phi}^i$	41
3.10. Near field scattering from an open-ended circular waveguide using GTD and ECM. — GTD, --- ECM. $r=10\lambda$, $a=5\lambda$, $\theta^i=45^\circ$, $\phi^i=0$, $\phi^r=90^\circ$, $\bar{E}^i=\hat{\phi}^i$	42
3.11. Near field scattering from an open-ended circular waveguide using GTD and ECM. — GTD, --- ECM. $r=10\lambda$, $a=5\lambda$, $\theta^i=45^\circ$, $\phi^i=0$, $\phi^r=0$, $\bar{E}^i=\hat{\theta}^i$	43
3.12. Near field scattering from an open-ended circular waveguide using GTD and ECM. — GTD, --- ECM. $r=10\lambda$, $a=5\lambda$, $\theta^i=45^\circ$, $\phi^i=0$, $\phi^r=180^\circ$, $\bar{E}^i=\hat{\theta}^i$	44
3.13. Near field scattering from an open-ended circular waveguide using GTD and ECM. — GTD, --- ECM. $r=10\lambda$, $a=5\lambda$, $\theta^i=45^\circ$, $\phi^i=0$, $\phi^r=90^\circ$, $\bar{E}^i=\hat{\theta}^i$	45
3.14. Scattering from the open end of a semi-infinite rectangular waveguide.	46
3.15. Modal rays in a parallel-plate waveguide.	51
3.16. Modal rays in a rectangular waveguide.	51
3.17. Modal rays in a circular waveguide.	52

FIGURE	PAGE
3.18. Modal rays in a 2-D linearly tapered waveguide.	52
3.19. Modal rays in a 2-D annular waveguide.	53
3.20. A waveguide junction J between two sections.	54
3.21. Diffraction of modal rays at the junction discontinuity.	57
3.22. Excitation of modes by equivalent sources \bar{M}_e and \bar{M}_d .	59
3.23. Open-ended parallel-plate waveguide.	61
3.24. Modal reflection coefficients due to an incident TE_{10} mode in an open-ended rectangular waveguide ($a=2b$).	66
3.25. Comparisons of the calculated and measured reflection coefficients in an X-band and KU-band open-ended rectangular waveguide.	67
3.26. Junction between a rectangular waveguide and a circular bend of rectangular cross section.	68
3.27. A discontinuity in the radius of curvature.	69
3.28. Reflection coefficient for the TE_{10} mode in a rectangular waveguide due to an \bar{E} -plane circular bend.	71
3.29. Reflection coefficient for the TE_{10} mode in a rectangular waveguide due to an \bar{E} -plane circular bend.	72
3.30. Junction between two linearly tapered waveguides.	73
3.31. Junction between two sectoral waveguides.	75
3.32. Open-ended semi-infinite circular waveguide.	79
3.33. Modal reflection coefficients due to an incident TE_{01} mode in an open-ended circular waveguide.	82
3.34. Modal reflection coefficients due to an incident TM_{01} mode in an open-ended circular waveguide.	83
3.35. Modal reflection coefficients due to an incident TM_{11} mode in an open-ended circular waveguide.	84
3.36. Junction between parallel-plate and annular waveguide sections.	85

FIGURE	PAGE
3.37. Reflection of the whispering gallery mode.	89
3.38. Geometry associated with $[S_{21}]$ calculation.	93
3.39. Open-ended parallel plate waveguide geometry.	98
3.40. Variation of modal ray angle with frequency.	102
3.41. Geometry for the edge diffraction analysis.	106
3.42. Comparison of far zone modal radiation patterns from an open-ended parallel-plate waveguide. Mode index = $m=5$, modal ray angle = 10° , — GTD, — AI, xxx modified PTD.	109
3.43. Comparison of far zone modal radiation patterns from an open-ended parallel-plate waveguide. Mode index = $m=5$, modal ray angle = 50° , — GTD, — AI, xxx modified PTD.	110
3.44. Comparison of far zone modal radiation patterns from an open-ended parallel-plate waveguide. Mode index = $m=5$, modal ray angle = 80° , — GTD, — AI, xxx modified PTD.	111
3.45. Comparison of far zone modal radiation patterns from an open-ended parallel-plate waveguide. Mode index = $m=6$, modal ray angle = 80° , — GTD, — AI, xxx modified PTD.	112
3.46. Comparison of far zone modal radiation patterns from an open-ended parallel-plate waveguide. Mode index = $m=6$, modal ray angle = 85° , — GTD, — AI, xxx modified PTD.	113
3.47. Open-ended staggered parallel plate waveguide.	114
3.48. Comparison of far zone modal radiation patterns from an open-ended staggered, parallel-plate waveguide. Modal index = $m=3$, modal ray angle = 50° , staggering angle = $t_0 = 60^\circ$, — GTD, — AI, xxx modified PTD.	117
3.49. Comparison of far zone modal radiation patterns from an open-ended staggered, parallel-plate waveguide. Modal index = $m=3$, modal ray angle = 30° , staggering angle = $t_0 = 60^\circ$, — GTD, — AI, xxx modified PTD.	118
3.50. Comparison of far zone modal radiation patterns from an open-ended staggered, parallel-plate waveguide. Modal index = $m=4$, modal ray angle = 30° , staggering angle = $t_0 = 60^\circ$, — GTD, — AI, xxx modified PTD.	119

FIGURE	PAGE
3.51. Comparison of far zone modal radiation patterns from an open-ended staggered, parallel-plate waveguide. Modal index = $m=3$, modal ray angle = 30° , staggering angle = $t_0=45^\circ$, — GTD, — — AI, xxx modified PTD.	120
3.52. Comparison of far zone modal radiation patterns from an open-ended staggered, parallel-plate waveguide. Modal index = $m=4$, modal ray angle = 30° , staggering angle = $t_0=45^\circ$, — GTD, — — AI, xxx modified PTD.	121
3.53. A waveguide junction joining two sections.	129
3.54. Equivalent sources at the aperture radiate in a uniform waveguide.	130
3.55. Termination of a parallel-plate waveguide with an annular waveguide.	131
4.1. The geometry and VSWR of horn antenna.	133
4.2. A planar 90° bend in a parallel-plate waveguide.	134
4.3. The magnitude of the reflection from the sharp bend of Figure 4.2 as a function of bend angle.	135
4.4. The magnitude of the reflection from the sharp bend of Figure 4.2 as a function of section length L .	136
4.5. A uniform 90° bend in a parallel-plate waveguide.	137
4.6. Magnitude of the reflection from a circular bend in a parallel-plate waveguide as a function of radius b .	138
4.7. The geometry of the cavity model.	139
4.8. Side and top view of the cavity model.	140
4.9. Geometry of an open-ended rectangular waveguide cavity.	141
4.10. Radar cross section pattern at $f=8.02$ GHz, $\vec{E}^i = \hat{\phi}$, $\phi=0$ plane.	145
4.11. Radar cross section pattern at $f=9.98$ GHz, $\vec{E}^i = \hat{\phi}$, $\phi=0$ plane.	146

FIGURE	PAGE
4.12. Radar cross section pattern at $f=11.95$ GHz, $\bar{E}^i = \hat{\phi}$, $\phi=0$ plane.	147
4.13. Radar cross section pattern at $f=8.02$ GHz, $\bar{E}^i = \hat{\theta}$, $\phi=0$ plane.	148
4.14. Radar cross section pattern at $f=9.98$ GHz, $\bar{E}^i = \hat{\theta}$, $\phi=0$ plane.	149
4.15. Radar cross section pattern at $f=11.95$ GHz, $\bar{E}^i = \hat{\theta}$, $\phi=0$ plane.	150
4.16. Radar cross section pattern at $f=8.02$ GHz, $\bar{E}^i = \hat{\phi}$, $\phi=90^\circ$ plane.	151
4.17. Radar cross section pattern at $f=9.98$ GHz, $\bar{E}^i = \hat{\phi}$, $\phi=90^\circ$ plane.	152
4.18. Radar cross section pattern at $f=11.95$ GHz, $\bar{E}^i = \hat{\phi}$, $\phi=90^\circ$ plane.	153
4.19. Radar cross section pattern at $f=8.02$ GHz, $\bar{E}^i = \hat{\theta}$, $\phi=90^\circ$ plane.	154
4.20. Radar cross section pattern at $f=9.98$ GHz, $\bar{E}^i = \hat{\theta}$, $\phi=90^\circ$ plane.	155
4.21. Radar cross section pattern at $f=11.95$ GHz, $\bar{E}^i = \hat{\theta}$, $\phi=90^\circ$ plane.	156
4.22. Variation of radar cross section with frequency. $\bar{E}^i = \hat{\phi}$, $\phi=0$, $\theta=0$.	159
4.23. Inverse Fourier transforms (i.e., time domain plots) of the results in Figure 4.22.	160

FIGURE	PAGE
4.24. Variation of radar cross section with frequency. $\bar{E}^i = \hat{\phi}, \phi=0, \theta=15^\circ$	161
4.25. Inverse Fourier transforms (i.e., time domain plots) of the results in Figure 4.24.	162
4.26. Variation of radar cross section with frequency. $\bar{E}^i = \hat{\phi}, \phi=0, \theta=30^\circ$	163
4.27. Inverse Fourier transforms (i.e., time domain plots) of the results in Figure 4.26.	164
4.28. Variation of radar cross section with frequency. $\bar{E}^i = \hat{\phi}, \phi=0, \theta=45^\circ$	165
4.29. Inverse Fourier transforms (i.e., time domain plots) of the results in Figure 4.28.	166
4.30. Variation of radar cross section with frequency. $\bar{E}^i = \hat{\theta}, \phi=0, \theta=0^\circ$	167
4.31. Inverse Fourier transforms (i.e., time domain plots) of the results in Figure 4.30.	168
4.32. Variation of radar cross section with frequency. $\bar{E}^i = \hat{\theta}, \phi=0, \theta=15^\circ$	169
4.33. Inverse Fourier transforms (i.e., time domain plots) of the results in Figure 4.32.	170
4.34. Variation of radar cross section with frequency. $\bar{E}^i = \hat{\theta}, \phi=0, \theta=30^\circ$	171
4.35. Inverse Fourier transforms (i.e., time domain plots) of the results in Figure 4.34.	172
4.36. Variation of radar cross section with frequency. $\bar{E}^i = \hat{\theta}, \phi=0, \theta=45^\circ$	173

FIGURE	PAGE
4.37. Inverse Fourier transforms (i.e., time domain plots) of the results in Figure 4.36.	174
4.38. Variation of radar cross section with frequency. $\vec{E}^i = \hat{\phi}, \phi=0, \theta=45^\circ$	175
4.39. Inverse Fourier transforms (i.e., time domain plots) of the results in Figure 4.38.	176
4.40. Importance of modes whose modal ray angles are near the angle of incidence. $f=10 \text{ GHz}, \vec{E}^i = \hat{\phi}, \phi=0 \text{ plane.}$	179
4.41. Radar cross section pattern at $f=8.00 \text{ GHz},$ $\vec{E}^i = \hat{\phi}, \phi=0 \text{ plane.}$	181
4.42. Calculated RCS pattern corresponding to Figure 4.41.	182
4.43. Radar cross section pattern at $f=10.00 \text{ GHz},$ $\vec{E}^i = \hat{\phi}, \phi=0 \text{ plane.}$	183
4.44. Calculated RCS pattern corresponding to Figure 4.43.	184
4.45. Radar cross section pattern at $f=12.00 \text{ GHz},$ $\vec{E}^i = \hat{\phi}, \phi=0 \text{ plane.}$	185
4.46. Calculated RCS pattern corresponding to Figure 4.45.	186
4.47. Radar cross section pattern at $f=8.02 \text{ GHz},$ $\vec{E}^i = \hat{\theta}, \phi=0 \text{ plane.}$	187
4.48. Calculated RCS pattern corresponding to Figure 4.47.	188
4.49. Radar cross section pattern at $f=9.98 \text{ GHz},$ $\vec{E}^i = \hat{\theta}, \phi=0 \text{ plane.}$	189
4.50. Calculated RCS pattern corresponding to Figure 4.49.	190

FIGURE	PAGE
4.51. Radar cross section pattern at $f=11.95$ GHz, $\bar{E}^i=\hat{\theta}$, $\phi=0$ plane.	191
4.52. Calculated RCS pattern corresponding to Figure 4.51.	192
4.53. Radar cross section pattern at $f=8.02$ GHz, $\bar{E}^i=\hat{\theta}$, $\phi=90^\circ$ plane.	193
4.54. Calculated RCS pattern corresponding to Figure 4.53.	194
4.55. Radar cross section pattern at $f=10.01$ GHz, $\bar{E}^i=\hat{\theta}$, $\phi=90^\circ$ plane.	195
4.56. Calculated RCS pattern corresponding to Figure 4.55.	196
4.57. Radar cross section pattern at $f=11.96$ GHz, $\bar{E}^i=\hat{\theta}$, $\phi=90^\circ$ plane.	197
4.58. Calculated RCS pattern corresponding to Figure 4.57.	198
4.59. Radar cross section pattern at $f=8.02$ GHz, $\bar{E}^i=\hat{\phi}$, $\phi=90^\circ$ plane.	199
4.60. Calculated RCS pattern corresponding to Figure 4.59.	200
4.61. Radar cross section pattern at $f=10.01$ GHz, $\bar{E}^i=\hat{\phi}$, $\phi=90^\circ$ plane.	201
4.62. Calculated RCS pattern corresponding to Figure 4.61.	202
4.63. Radar cross section pattern at $f=11.96$ GHz, $\bar{E}^i=\hat{\phi}$, $\phi=90^\circ$ plane.	203
4.64. Calculated RCS pattern corresponding to Figure 4.63.	204
4.65. Radar cross section pattern at $f=10.00$ GHz, $\bar{E}^i=\hat{\phi}$, $\phi=45^\circ$ plane.	205

FIGURE	PAGE
4.66. Radar cross section pattern at $f=10.00$ GHz, $\bar{E}^i=\hat{\theta}$, $\phi=45^\circ$ plane.	206
4.67. Radar cross section pattern at $f=10.00$ GHz, $\bar{E}^i=\hat{\theta}$, $\phi=45^\circ$ plane.	207
4.68. Variation of RCS with frequency $\bar{E}^i=\hat{\phi}$, $\phi=0$, $\theta=0$.	208
4.69. Inverse Fourier transforms (i.e., time domain plots) of the results in Figure 4.68.	209
4.70. Variation of RCS with frequency $\bar{E}^i=\hat{\phi}$, $\phi=0$, $\theta=15^\circ$.	210
4.71. Inverse Fourier transforms (i.e., time domain plots) of the results in Figure 4.70.	211
4.72. Variation of RCS with frequency $\bar{E}^i=\hat{\phi}$, $\phi=0$, $\theta=30^\circ$.	212
4.73. Inverse Fourier transforms (i.e., time domain plots) of the results in Figure 4.72.	213
4.74. Variation of RCS with frequency $\bar{E}^i=\hat{\phi}$, $\phi=0$, $\theta=45^\circ$.	214
4.75. Inverse Fourier transforms (i.e., time domain plots) of the results in Figure 4.74.	215
4.76. Variation of RCS with frequency $\bar{E}^i=\hat{\theta}$, $\phi=0$, $\theta=0$.	216
4.77. Inverse Fourier transforms (i.e., time domain plots) of the results in Figure 4.76.	217
4.78. Variation of RCS with frequency $\bar{E}^i=\hat{\theta}$, $\phi=0$, $\theta=15^\circ$.	218
4.79. Inverse Fourier transforms (i.e., time domain plots) of the results in Figure 4.78.	219
4.80. Variation of RCS with frequency $\bar{E}^i=\hat{\theta}$, $\phi=0$, $\theta=30^\circ$.	220
4.81. Inverse Fourier transforms (i.e., time domain plots) of the results in Figure 4.80.	221
4.82. Variation of RCS with frequency $\bar{E}^i=\hat{\theta}$, $\phi=0$, $\theta=45^\circ$.	222
4.83. Inverse Fourier transforms (i.e., time domain plots) of the results in Figure 4.82.	223

FIGURE	PAGE
4.84. The separate returns of modes for the case in Figure 4.75.	224
4.85. Circular waveguide cavity terminated by a short circuit.	225
4.86. Backscattered field from a circular waveguide cavity, as a function of the angle from the axis. All propagating modes are included. $E^i = \hat{\phi}$.	227
4.87. Backscattered field from a circular waveguide cavity, as a function of the angle from the axis. Only modes with modal ray angles closer than 10 degrees are included. $E^i = \hat{\phi}$.	228
4.88. Backscattered field from a circular waveguide cavity, as a function of the angle from the axis. All propagating modes are included. $E^i = \hat{\theta}$.	229
4.89. Backscattered field from a circular waveguide cavity, as a function of the angle from the axis. Only modes with modal ray angles closer than 10 degrees are included. $E^i = \hat{\theta}$.	230
A.1. Rectangular waveguide geometry.	235
B.1. Parallel-plate waveguide geometry.	240
B.2. Ray picture of n^{th} mode.	242
C.1. Geometry of a sectoral waveguide.	243
C.2. Projection of ray picture into y-z plane.	250
C.3. Projection of ray picture into x-z plane.	250
D.1. Geometry of a linearly tapered waveguide.	252
D.2. Ray picture of n^{th} mode.	253

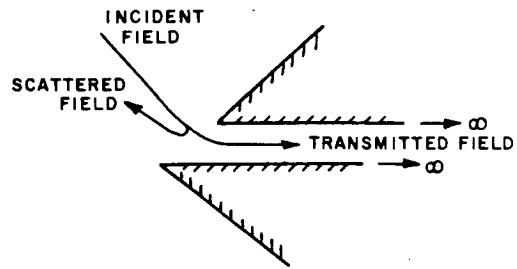
FIGURE	PAGE
E.1. Geometry of the annular region.	255
E.2. Contours used in the Watson transformation.	259
E.3. Location of eigenvalues in the complex v -plane.	262
E.4. Ray picture of regular modes.	263
E.5. Ray picture of whispering gallery modes.	264
F.1. The circular waveguide geometry.	266
F.2. Conversion of waveguide modal field into the conical ray field.	269
G.1. Waveguide Geometry	270
G.2. Waveguide geometry with fields radiated to the left ($n > n_+$) of \bar{S} being of concern.	273
H.1. Scattering from a perfectly-conducting half-plane.	275
H.2. The integration path C_α .	278
I.1 The geometry of the problem.	280
J.1. A wedge illuminated by a $\hat{\beta}_0$ -polarized plane wave.	286
J.2. Magnetic line dipoles along z -axis.	288
K.1. Radiation of a dipole $d\bar{p}_e$ in the presence of the semi-infinite waveguide.	290
K.2. The equivalent problem of Figure K.1.	291
K.3. The dipole $d\bar{p}_e$ radiating in the infinite waveguide.	292
L.1. Modal radiation from the open end.	293
L.2. Coupling of incident dipole field.	295

CHAPTER I

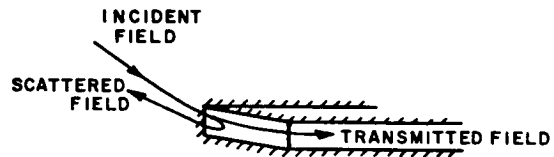
INTRODUCTION

In this report a combination of high frequency and modal ray techniques is employed to develop a relatively simple analysis of electromagnetic (EM) scattering by electrically large, open-ended waveguide cavities with discontinuities. It is assumed that the medium exterior and interior to these waveguide cavities is homogeneous, isotropic and lossless. The waveguides possess perfectly-conducting walls. Therefore, they do not radiate energy transversally, so they are in the class of closed waveguides as opposed to open waveguides whose cross-section does not confine the field by impenetrable walls. Specifically, the two dimensional (2-D) and three dimensional (3-D) waveguide cavities which are considered here are formed by joining different uniformly tapered or curved sections as shown in Figure 1.1. Junctions are formed at the open-end and within interior regions where different sections are joined. Although the semi-infinite waveguide geometries in Figure 1.1 do not indicate any interior termination, the present analysis can also account for some simple terminations for which the modal reflection matrix is known, such as a planar short circuit, an impedance surface termination, or even a homogeneous dielectric loading.

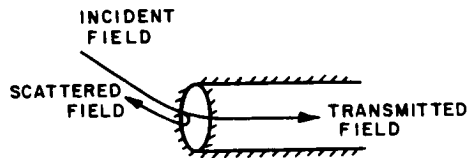
- a) 2-D Open-ended, flanged, staggered parallel plate waveguide.



- b) 3-D Open-ended rectangular waveguide



- c) 3-D Open-ended circular waveguide.



- d) Discontinuities formed by 2-D linearly tapered waveguide sections.

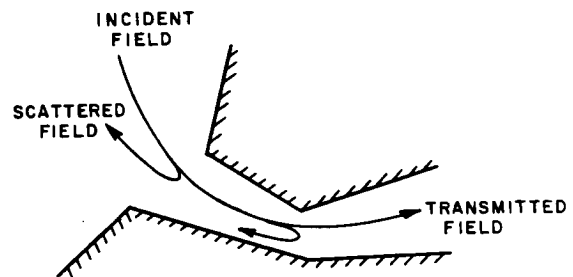
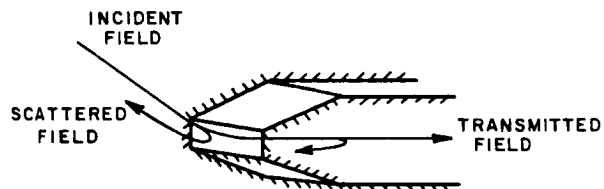


Figure 1.1. Waveguide geometries considered.

- e) 3-D Open-ended waveguide with two different sectoral parts.



- f) A 2-D uniform circular bend in a parallel-plate waveguide.

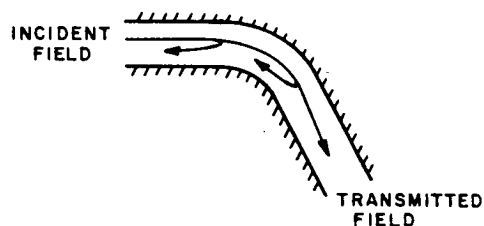


Figure 1.1. (continued)

It is well known that the EM field in a waveguide can be expressed in terms of a characteristic set of functions called waveguide modes. If the waveguide geometry conforms to constant coordinate surfaces of a coordinate system in which the Helmholtz equation is separable, then the modes can be determined analytically. These analytical modal expressions inherently include the variation of the field along a non-uniform (or tapered) waveguide as long as modes do not experience cut-off as they propagate within the guide. In the waveguide geometries considered, the above conditions are assumed to prevail. Therefore, under the above conditions, any scattering which occurs within the waveguide arises from the abrupt junction discontinuities between

different sections. Such a scattering can be expressed in terms of modal reflection and transmission coefficients.

In closed waveguide structures, the modal set is discrete, and the classical approach for the analysis of a waveguide discontinuity is to expand the fields in terms of the modal sets on each side of the discontinuity and then match these fields at the discontinuity by enforcing the appropriate boundary conditions. The presence of a discontinuity gives rise to a storage of reactive energy in the vicinity of the discontinuity in terms of evanescent modes; i.e., the modes which decay exponentially with distance away from the junction. Therefore, the mode matching approach results in an infinite set of equations to be solved. In some cases, exact solutions can be obtained by direct matrix inversion techniques, by transform techniques (Wiener-Hopf) or, by the residue calculus technique. In the latter residue calculus technique, it is necessary to construct a complex valued function which, when integrated along a specified contour gives the infinite set of mode matching equations. Also, variational and perturbational techniques are used very extensively for waveguides with a single propagating mode. The above methods are described in [1,2,3]. These techniques are limited to certain geometries and they are difficult, if not impossible, to generalize to other structures; however, they are usually easier to apply to waveguides of smaller cross-sections which allow only a few, and in most cases only the dominant, mode or modes to propagate. Similar techniques can be applied to open waveguide structures where the problem is more complicated by the fact that the modal spectrum has a

continuous part. The discussion of continuous transitions in open waveguide structures is presented in [4], which also includes a very complete list of references on the subject.

A powerful method to analyze wave propagation through waveguide transitions, couplers and tapers is based on the concept of generalized transmission line or coupled wave equations. This concept was first proposed and studied in detail by Schellkunoff [5]. An extensive bibliography and study of different applications of this method are in [6]. However, the coupled wave equations are mostly applied to the problems of smooth transitions where one converts the Maxwell's equations into telegrapher's equations and obtains a matrix differential equation for the unknown voltages. A limiting approach can be employed for abrupt discontinuities, and in this case, it reduces to the mode matching procedure [6]. Adiabatic or slowly varying coupling constitutes an extension of coupled wave theory [7], and reduces to the WKB approximation. Curved waveguides were studied in detail by Lewin [8] and asymptotic approximations with respect to the radius of curvature of the waveguide are used for the fields. These approximate fields are then matched at the junction to get an integral equation for the junction fields. However, coupled wave equations and integral equation formulations are related to mode matching procedures; consequently, they are cumbersome to employ in practice.

Application of ray optics to waveguide discontinuity problems is relatively new; yet it has received substantial attention in the literature because of its usefulness and conceptual simplicity. Both Rudduck [9] and Yee, Felsen and Keller [10] applied the geometrical

theory of diffraction (GTD) [11] to determine the modal reflection coefficients of an open-ended parallel plate waveguide. In [10], the effect of multiple interactions between the edges is taken into account in a simple, elegant but approximate manner. More rigorous approaches to determine the effect of multiple ray interactions at the aperture of an open-ended semi-infinite parallel plate geometry were described later by Boersma and Lee [12-16]. Their results [12-16] agree with the asymptotic expansion of the exact solution. An application of the GTD to calculate the reflection from the aperture of an E-plane sectoral horn was described by Jull [17]. The ray-optical techniques require that at each uniform waveguide section, the fields incident at the junction be expressed in terms of a set of rays associated with each of the characteristic waveguide modes. The latter set is referred to as modal rays. For parallel plate, circular and tapered waveguide sections, the modal ray representations have been discussed by Felsen and Maurer [18,19].

Yee and Felsen also described the ray-optical procedure for the reflection of acoustic waves from an open-ended circular pipe [20]. A ray picture for the EM waves in a circular waveguide is described by Ivanyan [21]; however, his rays do not appear to exhibit the usual plane wave propagation constant. In [22], a different ray picture which consists of a set of conical wavefronts that converge and diverge with respect to the waveguide axis is used for the circular waveguide. The results based on this modal ray description which are presented in [22] are excellent.

The basic approach employed in this work combines the use of modal rays discussed above, with the high frequency techniques, to calculate the relevant reflection and transmission properties associated with waveguide discontinuities using the multiple scattering matrix (MSM) formulation. The general idea behind this approach is briefly illustrated as follows. Figure 1.2 shows a waveguide cavity with three sections. The scattered field in the exterior region is composed of two main contributions; one of these is due to the field scattered from the open end alone, and the other is due to the field which is coupled into the interior and then re-radiated from the open end. The latter undergoes multiple reflections between the open end and the discontinuities inside the cavity, after it is initially coupled into

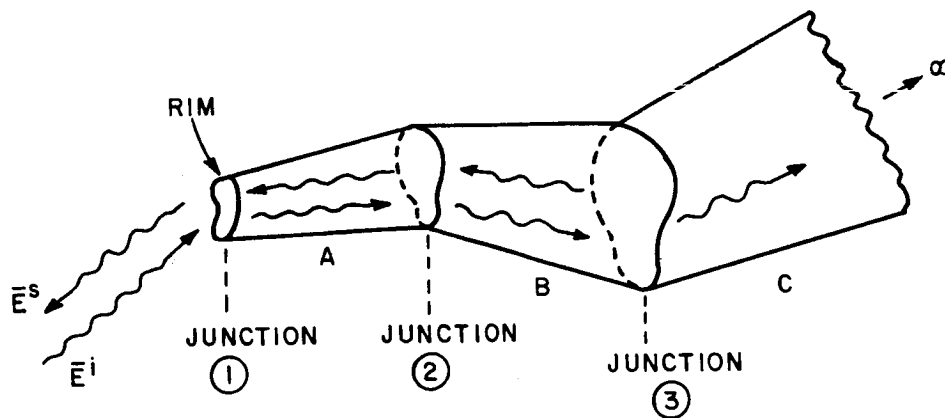


Figure 1.2. A waveguide cavity with three junctions.

the waveguide from the incident field. The fields resulting from these multiple interactions may be expressed as a convergent Neumann series as done by Pace and Mittra [23]. The same result is directly obtained by an alternative procedure based on a self-consistent multiple scattering matrix (MSM) method [22]. Therefore, it is possible to identify and isolate the wave scattering mechanisms in terms of the scattering matrices $[S]$ of the junction which describe the reflection and transmission properties of the discontinuity at the junction. In Figure 1.3 the junction discontinuities are isolated and the wave interaction described by the various scattering matrices are illustrated. Once the elements of these scattering matrices are determined, then they can be combined using the self-consistent MSM procedure indicated above. Therefore, the effects of all multiple interactions can be viewed as being associated with a single effective discontinuity with its corresponding scattering matrix. In particular, the effects of scattering from the discontinuities beyond Junction ② for the problem in Figure 1.2, can be represented by an effective reflection matrix $[S_r]$, as shown in Figure 1.4.

A dielectric loading inside the waveguide cavity will cause modal reflections determined by the geometry and the electrical properties of the dielectric material. These reflections can similarly be represented by the scattering matrix $[S_r]$, whose entries relate the incident and reflected modal field amplitudes. Therefore, Figure 1.4 may also simulate the scattering by a dielectric loading located at the position ② in waveguide A, as shown in the figure.

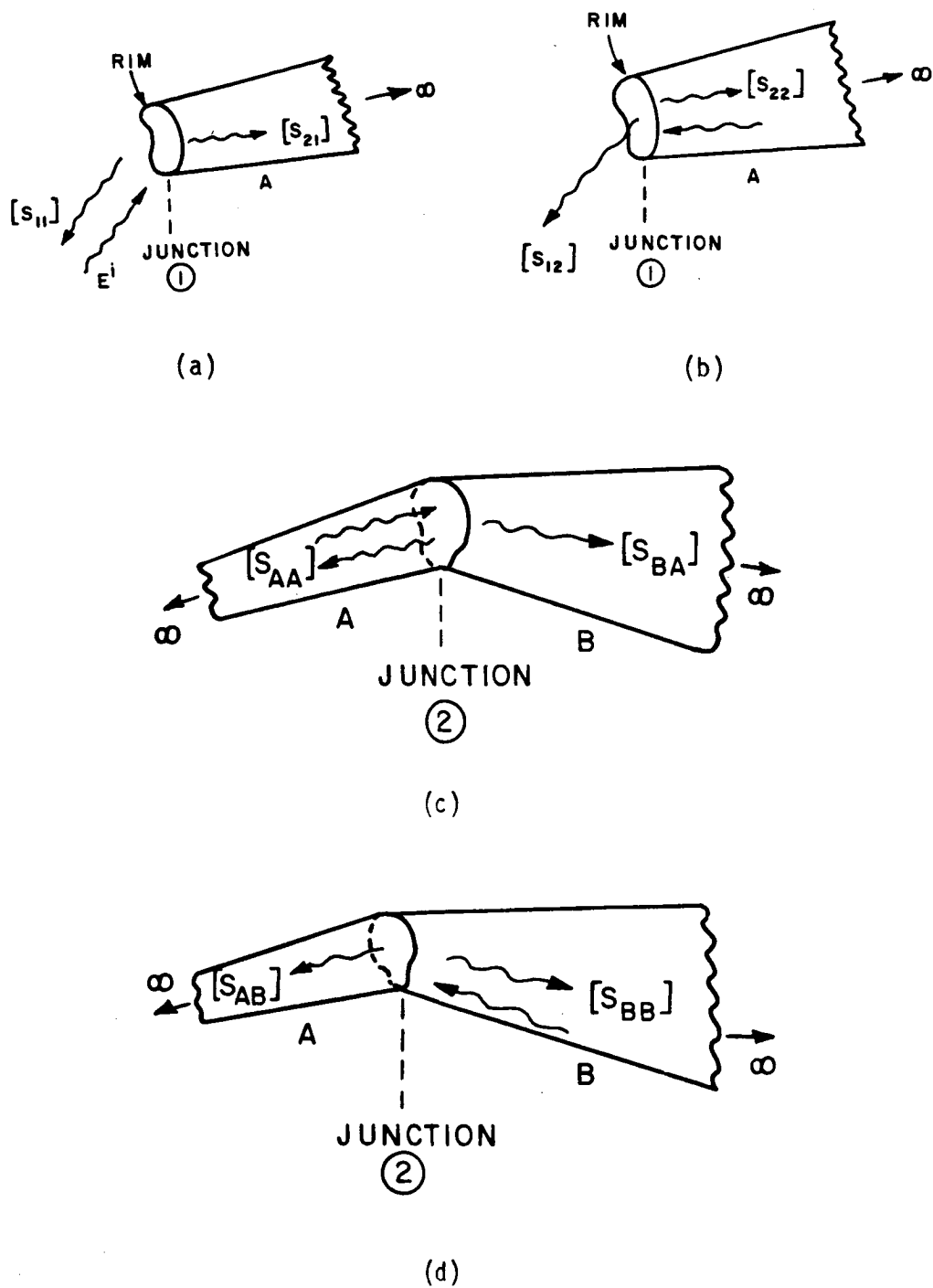


Figure 1.3. Isolation of scattering mechanisms and illustration of scattering matrices.

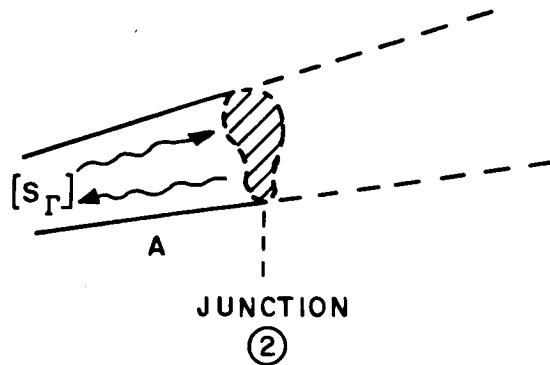


Figure 1.4. Effective scattering geometry for the problem in Figure 1.2.

As indicated earlier, relatively simple expressions have been developed in this work for the elements of the scattering matrices via the use of high frequency techniques combined with the modal ray description for the fields inside the waveguide. In particular, the high-frequency techniques which are employed here include the GTD, the equivalent current method (ECM) [24,25,26], and a modification of the physical theory of diffraction (PTD) [26,27], depending on the scattering matrix being calculated. The previous ray optical approaches [9,10] seem to be applicable to certain geometries with some symmetry properties. In contrast, the present approach besides being relatively simple is more general than the previous ray optical treatments and also

allows one to treat many junction types which would otherwise be intractable or cumbersome to analyze via the classical mode matching approach. Furthermore, since the present approach deals with the interactions in a sequential manner, by isolating the effects of the different junctions, it is therefore also physically appealing. Some of the special junctions treated here have rigorous Wiener-Hopf solutions, e.g., open-ended circular pipe and parallel plate geometries [28]. These Wiener-Hopf solutions are relatively more difficult to obtain and are limited to very special geometries such as those mentioned above. However, they provide a good check for the present high frequency based solutions. As it is common to all ray methods, the procedure described here is valid for waveguides which are sufficiently far from cut-off. Furthermore, the approximation in the high frequency approaches improves as the number of propagating modes inside the waveguide increases. This latter property is actually a merit, rather than a drawback of the high frequency based procedures since for small waveguides the other approximate methods can safely be used.

The format of the report is as follows. Definition of the relevant scattering matrices and a description of the multiple scattering matrix approach which employs these scattering matrices are included in Chapter II. Chapter III is devoted to the development of scattering matrices for several specific waveguide geometries. They are presented under two categories; namely, reflection type scattering matrices and transmission type scattering matrices. For a junction between two interior waveguide sections, the elements of the scattering

matrices are the modal reflection and transmission coefficients. In the case of a waveguide discontinuity formed by the open-end; the elements of the scattering matrices describe the interior modal reflection as well as the exterior rim scattering associated with the open-end; likewise, they also describe the exterior radiation and interior coupling phenomena. The radiation from the open-ended waveguide into the exterior region and the coupling into the interior region due to excitation from the exterior may be viewed as being described by transmission coefficients. All of these mechanisms are described separately, and in some case illustrative examples and comparisons are provided. In Chapter IV, the scattering matrices of Chapter III are used to solve some two and three dimensional problems. Whenever possible, the results are compared with other methods of solution or measurements. Finally, some conclusions based on this work are given in Chapter V. An $e^{j\omega t}$ time convention for the fields has been assumed and suppressed throughout the analysis.

CHAPTER II

SELF CONSISTENT MULTIPLE SCATTERING MATRIX FORMULATION

As mentioned in the previous chapter, the solution to the problem of the scattering from a waveguide cavity can be constructed by first calculating the isolated scattering matrices associated with the pertinent discontinuities and then combining these matrices using a self consistent MSM formulation. Essentially, MSM is the same as the generalized scattering matrix technique (GSMT) introduced previously to generalize the Wiener-Hopf solutions [2,23].

The concept of the scattering matrix is widely used in microwave circuit theory and relates the scattered wave amplitudes to the incident wave amplitudes. Therefore, it characterizes circuit properties of a microwave network.

An N-port junction is shown in Figure 2.1. The incident wave amplitudes propagating toward the junction are represented by V^+ , $n=1, \dots, N$, and scattered wave amplitudes are shown by V^- , $n=1, \dots, N$. The scattering matrix $[S]$ of the junction relate these quantities. Thus, in general, one can write

$$\begin{bmatrix} V_1^- \\ V_2^- \\ \vdots \\ V_N^- \end{bmatrix} = [S] \begin{bmatrix} V_1^+ \\ V_2^+ \\ \vdots \\ V_N^+ \end{bmatrix} \quad (2.1)$$

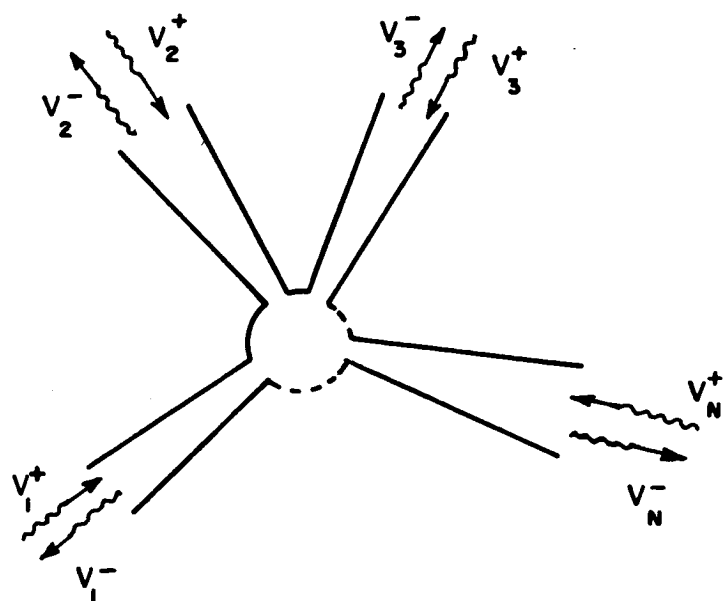


Figure 2.1. An N-port junction.

A waveguide containing N "propagating" modes can be represented by an N-port junction. The incident and reflected wave (or mode) amplitudes are denoted by $[V^+]$ and $[V^-]$. In addition, one can extend the scattering matrix definition to include the scattering of "evanescent" modes; however in this case, the modes are not normalized to carry unit power. A waveguide cavity with junctions ① and ② is shown in Figure 2.2. It is assumed that the Helmholtz equation is separable in the orthogonal curvilinear coordinate system (η, γ, ξ) shown in the figure, in which the η -coordinate coincides with the propagation axis of the waveguide. Therefore, the η -coordinate corresponds to the direction of propagation of the modal field sets inside the cavity. Junction ① is the open end of the cavity and junction ② is the termination inside the

cavity which is separated from junction ¹ by the distance (L), along the η coordinate. Therefore, the phase delay of the modal field sets that propagate from junction ¹ to junction ² is given by the propagation constant of the modes multiplied the distance (L). For convenience, only the fields exterior to the waveguide are expressed in spherical coordinates.

Let a plane wave \vec{E}^i be incident at the open end of the cavity. One may express incident field as follows:

$$\vec{E}^i = \hat{\theta}^i E_{\theta}^i + \hat{\phi}^i E_{\phi}^i \quad (2.2a)$$

with

$$E_{\theta}^i = A_{\theta}^i e^{-jk^i \cdot \vec{r}} \quad (2.2b)$$

$$E_{\phi}^i = A_{\phi}^i e^{-jk^i \cdot \vec{r}} \quad (2.2c)$$

where

$$\vec{k}^i = -k(\sin\theta^i \cos\phi^i \hat{x} + \sin\theta^i \sin\phi^i \hat{y} + \cos\theta^i \hat{z}) \quad (2.3)$$

and

$$\vec{r} = x\hat{x} + y\hat{y} + z\hat{z} \quad (2.4)$$

It is noted that $k=2\pi/\lambda$ refers to the free space wavenumber, (λ =wavelength in free space) and \vec{r} refers to the position vector of an observation point. The angles θ^i and ϕ^i are the elevation and azimuth angles of the direction of incoming field in the spherical coordinates.

The corresponding magnetic field \vec{H}^i is obtained from

$$\vec{H}^i = Y_0 \hat{k}^i \times \vec{E}^i \quad (2.5)$$

where $Y_0 = Z_0^{-1}$ is the admittance of free-space.

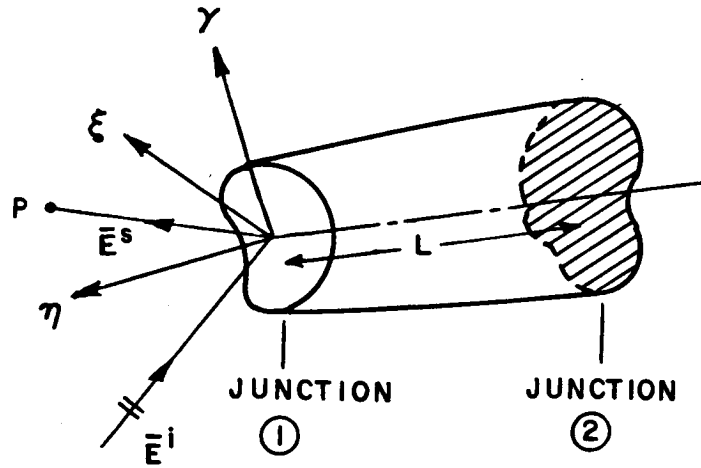


Figure 2.2. An open-ended waveguide cavity problem.

The scattering matrix $[S_{11}]$ (see Figure 2.3), defines a scattering mechanism which converts the incident exterior region field into a field scattered back into the exterior region without including any interior region effects. In other words, it relates the electric field (\bar{E}^{s0}) scattered from only the open end, to the field \bar{E}^i which is incident at the open end as follows:

$$\begin{bmatrix} E_x^{s0} \\ E_y^{s0} \\ E_z^{s0} \end{bmatrix} = [S_{11}] \begin{bmatrix} A_\theta^i \\ A_\phi^i \end{bmatrix} \quad (2.6)$$

where

$$\bar{E}^{s0}(P) = E_x^{s0} \hat{x} + E_y^{s0} \hat{y} + E_z^{s0} \hat{z} \quad (2.7)$$

and

$$[S_{11}] = \begin{bmatrix} S_{x\theta} & S_{x\phi} \\ S_{y\theta} & S_{y\phi} \\ S_{z\theta} & S_{z\phi} \end{bmatrix} \quad (2.8)$$

When the observation point recedes to infinity, i.e., the far zone case, then the range dependent part of the scattered field can be brought out of the scattering matrix, so $[S_{11}^f]$ for the latter case is defined as follows:

$$\begin{bmatrix} E_{\theta}^{so} \\ E_{\phi}^{so} \end{bmatrix} = [S_{11}^f] \begin{bmatrix} A_{\theta}^i \\ A_{\phi}^i \end{bmatrix} \frac{e^{-jkr}}{r} \quad (2.9)$$

with

$$[S_{11}^f] = \begin{bmatrix} S_{\theta\theta} & S_{\theta\phi} \\ S_{\phi\theta} & S_{\phi\phi} \end{bmatrix} \quad (2.10)$$

The scattering matrix $[S_{12}]$ converts the waveguide modal fields incident at the open end (from the interior region) to the exterior region fields radiated by these modes as shown in Figure 2.4. The modal electric field \bar{E}_w^{\pm} within the uniform waveguide region may be represented by

$$\bar{E}_w^{\pm} = \sum_n C_n^{\pm} (\bar{e}_{nt} \pm \bar{e}_{n\eta}) e^{\mp j\beta_n \eta} \quad (2.11)$$

Here, \bar{e}_{nt} denotes the transverse (to $\hat{\eta}$) modal electric field of a waveguide uniform in the $\hat{\eta}$ -direction, and β_n is the propagation constant of the corresponding mode. The axial (or $\hat{\eta}$) component of the modal

field is denoted by \bar{e}_{nn} . It is noted that the index n denotes a compact mode index, which corresponds to the double index nm in 3-D waveguides. The superscripts $+$ and $-$ in (2.11) refer to modes propagating in $+\hat{n}$ and $-\hat{n}$ directions, respectively. It is convenient to define the magnetic field \bar{H}_w^\pm in the waveguide region following the representation for the electric field \bar{E}_w^\pm in (2.11); thus, the magnetic field is given by [1]

$$\bar{H}_w^\pm = \sum_n C_n^\pm (\pm \bar{h}_{nt} + \bar{h}_{nn}) e^{\mp j\beta_n n} \quad (2.12)$$

The C_n^\pm in (2.11) and (2.12) are the modal coefficients. If $\bar{E}^{ro}(P)$ denotes the electric field at P exterior to the waveguide region, which is radiated by the modes that impinge on the open end, then the scattering matrix $[S_{12}]$ relates \bar{E}^{ro} to \bar{E}_w^+ as follows:

$$\begin{bmatrix} E_x^{ro} \\ E_y^{ro} \\ E_z^{ro} \end{bmatrix} = \begin{bmatrix} [S_x^{ro}] \\ [S_y^{ro}] \\ [S_z^{ro}] \end{bmatrix} [C_n^+] \quad (2.13)$$

where the rim is located at $n=0$,

$$\bar{E}^{ro}(P) = E_x^{ro} \hat{x} + E_y^{ro} \hat{y} + E_z^{ro} \hat{z} \quad (2.14)$$

and

$$[S_{12}] = \begin{bmatrix} [S_x^{ro}] \\ [S_y^{ro}] \\ [S_z^{ro}] \end{bmatrix} \quad (2.15)$$

with

$$[S_u^{ro}] = [S_{u1} \ S_{u2} \ S_{u3} \ \dots] \quad (2.16)$$

where u corresponds to any one of the cartesian coordinates x , y or z .

As explained before, for observation points in the far field, the scattering matrix $[S_{12}^f]$ can be written as follows:

$$\begin{bmatrix} E_\theta^{ro} \\ E_\phi^{ro} \end{bmatrix} = [S_{12}^f] [C_n^+] \frac{e^{-jkr}}{r} \quad (2.17)$$

where

$$[S_{12}^f] = \begin{bmatrix} [S_\theta^{ro}] \\ [S_\phi^{ro}] \end{bmatrix} \quad (2.18)$$

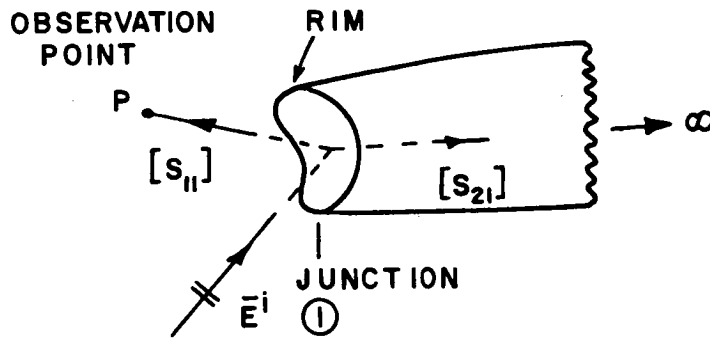


Figure 2.3. Scattering by only the rim at the open end of the waveguide.

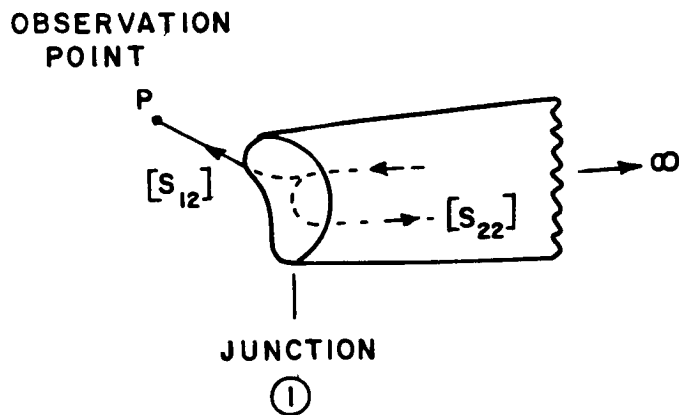


Figure 2.4. Radiation and reflection at the open end due to a waveguide mode incident at the open end.

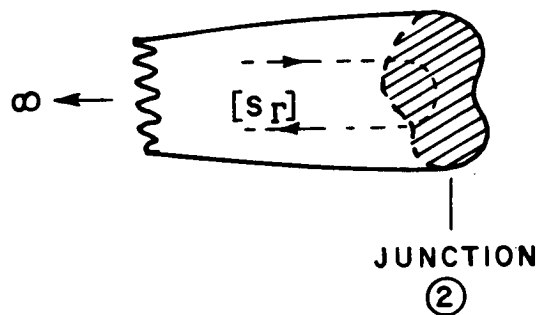


Figure 2.5. Reflection of waveguide modes at junction ②.

The scattering matrix $[S_{21}]$ describes the transformation or the coupling of the incident plane wave field into the waveguide modes as illustrated in Figure 2.3. It is clear that $[S_{21}]$ can therefore relate \bar{E}_w^- to \bar{E}^i by

$$[C_n^-] = [S_{21}] \begin{bmatrix} A_\theta^i \\ A_\phi^i \end{bmatrix} \quad (2.19)$$

with

$$[S_{21}] = \begin{bmatrix} [S_\theta] \\ [S_\phi] \end{bmatrix} \quad (2.20)$$

The present development can also deal with a near zone source \bar{P}_e type illumination, in which case the scattering matrix is defined via the following relationship:

$$[C_n^-] = [S_{21}^P] \begin{bmatrix} \hat{x} \cdot \bar{P}_e \\ \hat{y} \cdot \bar{P}_e \\ \hat{z} \cdot \bar{P}_e \end{bmatrix} \quad (2.21)$$

where

$$[S_{21}^P] = [[S_x] [S_y] [S_z]] \quad (2.22)$$

and

$$[S_u] = \begin{bmatrix} S_{u1} \\ S_{u2} \\ \vdots \\ \vdots \end{bmatrix} \quad (2.23)$$

Here, u corresponds to any one of the cartesian coordinates.

It is noted that the problem of determining $[S_{21}^P]$ is related to the problem of determining $[S_{12}]$ via reciprocity. The precise relationship between $[S_{21}^P]$ and $[S_{12}]$ is discussed in Appendix I.

The scattering matrix $[S_{22}]$ is a modal reflection coefficient matrix which is associated with the interaction in Figure 2.4. In particular, the elements of $[S_{22}]$ describe the reflection coefficients associated with the modes reflected back from the open end into the waveguide region when a mode is incident on that open end from within the waveguide. Thus, the matrix $[S_{22}]$ relates \bar{E}_w^- to \bar{E}_w^+ as follows:

$$[C_n^-] = [S_{22}] [C_n^+] \quad . \quad (2.24)$$

The scattering matrix $[S_r]$, like $[S_{22}]$, is also a reflection coefficient type matrix which is associated with the discontinuity at junction ②. Thus, one can write

$$[C_n^+] = [S_r] [C_n^-] \quad . \quad (2.25)$$

As mentioned before, $[S_r]$ may also represent a reflection due to a dielectric loading, or an effective modal reflection at junction ② which includes the totality of any other reflection effects arising from the presence of all of the discontinuities (or junctions) to the right of junction ② in Figure 2.2.

At any given operating frequency, the waveguide region can support a finite number of propagating modes and an infinite number of evanescent (non-propagating) modes. Therefore, the matrices $[S_{12}]$, $[S_{21}]$, $[S_{22}]$ and $[S_T]$ are of infinite order in a formal sense; however one needs to retain only a finite number of elements of these scattering matrices in practice, because the distance L shown in Figure 2.2 is generally large enough so that the infinite number of evanescent modes generated at junction ① do not contribute significantly at junction ②, and vice versa. The finite number of elements of the scattering matrix which are retained in practice thus correspond to only the finite number of all the propagating (or non-evanescent) modes which can exist within the waveguide region. If the distance L in Figure 2.2 is small enough so that the "lower order" evanescent modes become important, then one must include these "lower order" modes. In either case, in practice, one always retains a finite number of elements in the scattering matrices which formally may be of infinite order.

The scattering matrices defined above are combined in a self-consistent procedure to obtain the field \bar{E}^S scattered from the open-ended waveguide cavity of Figure 2.2 as follows. For an incident plane wave \bar{E}^i as defined in (2.2), \bar{E}^S can be written as

$$\begin{bmatrix} E_x^S \\ E_y^S \\ E_z^S \end{bmatrix} = [R_{11}] \begin{bmatrix} A_\theta^i \\ A_\phi^i \end{bmatrix} \quad (2.26)$$

where

$$\vec{E}^S = E_x^S \hat{x} + E_y^S \hat{y} + E_z^S \hat{z} \quad (2.27)$$

and $[R_{11}]$ is the effective scattering matrix of the cavity. The scattered field \vec{E}^S consists of the field reflected from the rim of the open end, and the field transmitted into the waveguide through the open end from the incident field at the open end. This transmitted field undergoes multiple interactions between the junctions ① and ② before being radiated from the open end. Let us represent the modal field in the waveguide region after taking all these multiple interactions into account as follows:

$$\vec{E}_g^\pm = \sum_m A_m^\pm (\vec{e}_{mt} \pm \vec{e}_{m\eta}) e^{\mp j\beta_m \eta} \quad (2.28)$$

Here, the modal sets are compactly represented by a single index "m" as before, and $[A^+]$ and $[A^-]$ denote the amplitudes of the modes propagating in $+\hat{\eta}$ and $-\hat{\eta}$ directions, respectively.

As described earlier, one can decompose the scattered field \vec{E}^S of (2.27) as:

$$\begin{bmatrix} E_x^S \\ E_y^S \\ E_z^S \end{bmatrix} = [S_{11}] \begin{bmatrix} A_\theta^i \\ A_\phi^i \end{bmatrix} + [S_{12}] [A^+] \quad (2.29)$$

The vector $[A^+]$ represents the amplitudes of the modal field set \vec{E}_g^+ propagating in $+\hat{\eta}$ direction due to the reflection of the modal field set \vec{E}_g^- with amplitudes $[A^-]$ at junction ②. Therefore, one can write:

$$[A^+] = [P] [S_r] [P] [A^-] \quad (2.30)$$

where $[P]$ is the diagonal matrix accounting for the propagation phase delay of the modes over the path length (L) .

At junction ①, the modal field represented by the vector $[A^-]$ is excited by the incident field and the reflection of the modes propagating in the $+\hat{n}$ direction from the interior of the open end. This effect can be represented by the equation:

$$[A^-] = [S_{22}] [A^+] + [S_{21}] \begin{bmatrix} A_\theta^i \\ A_\phi^i \end{bmatrix} \quad (2.31)$$

Combining (2.30) and (2.31), one obtains

$$[I - S_{22} P S_r P] [A^-] = [S_{21}] \begin{bmatrix} A_\theta^i \\ A_\phi^i \end{bmatrix} \quad (2.32)$$

Using (2.32) in (2.30) gives:

$$[A^+] = [P] [S_r] [P] [I - S_{22} P S_r P]^{-1} [S_{21}] \begin{bmatrix} A_\theta^i \\ A_\phi^i \end{bmatrix} \quad (2.33)$$

Substituting (2.33) into (2.29) yields:

$$\begin{bmatrix} E_x^s \\ E_y^s \\ E_z^s \end{bmatrix} = \{ S_{11} + S_{12} P S_r P [I - S_{22} P S_r P]^{-1} S_{21} \} \begin{bmatrix} A_\theta^i \\ A_\phi^i \end{bmatrix} \quad (2.34)$$

The matrix in curly brackets is the effective scattering matrix $[R_{11}]$ as defined in (2.26), so

$$[R_{11}] = [S_{11}] + [S_{12} \text{ } P S_T P [I - S_{22} \text{ } P S_T P]^{-1} S_{21}] \quad . \quad (2.35)$$

As can be observed from the analysis, $[R_{11}]$ includes the effects of the presence of the second junction. By this procedure, the self consistent method can be directly extended to the analysis of waveguide cavities having more than two junctions.

CHAPTER III

DEVELOPMENT OF THE ELEMENTS OF THE SCATTERING MATRICES IN THE MULTIPLE SCATTERING METHOD

In this chapter, expressions for the elements of the scattering matrices associated with the discontinuities of waveguide cavities shown in Figure 1.1 are developed using a combination of high frequency and modal ray techniques. It is noted that there are basically two mechanisms described by the scattering matrices:

- 1) The reflection mechanism which describes the field reflected back into a region due to a field incident on a discontinuity from within the same region, and
- 2) the transmission mechanism which specifies the field coupled into a region through a discontinuity when a field is incident on that discontinuity from the adjacent region; i.e., from the other side of that discontinuity. The reflection and transmission type scattering matrices will be treated separately.

3.1 The Reflection Type Scattering Matrix

The scattering matrices defining a reflection phenomenon is described by either $[S_{11}]$, $[S_{22}]$ or $[S_r]$ type scattering matrices. The

first one describes the field scattered back into the exterior region due to a field incident from the exterior region. The last two describe the modal reflection back into the interior region when a waveguide field is incident from the same interior region onto a waveguide discontinuity. The exterior region scattering (reflection) described by the scattering matrix $[S_{11}]$ is going to be discussed separately from the case involving interior or modal reflection even though the approach employed for both cases are very similar.

3.1.1 Reflection Back Into the Exterior Region

In this section, the direct scattering from the rim edge at the open end expressed by the scattering matrix $[S_{11}]$ is calculated using techniques based on the GTD. According to the GTD, the scattered field is initiated from some distinct points (diffraction points) on the rim edge as well as from the corners of the rim (if they exist) as a result of Keller's generalization of Fermat's principle [11]. In addition to the single edge and corner diffracted fields, there exist multiply diffracted fields which are produced by rays that undergo multiple diffractions across the aperture. These multiple interactions may become important if the aperture dimensions are not sufficiently large in terms of the wavelength.

In 2-D problems the open end is formed by the edges at which the semi-infinite waveguide walls are terminated. Therefore, the scattering matrix $[S_{11}]$ describes the diffraction of the incident field by these edges. The treatment of multiple diffractions is complicated in the

situations where one of the edges is in the transition region of the shadow boundary of the other edge. In the unstaggered parallel-plate waveguide, the edges are exactly on the reflection shadow boundaries of multiply diffracted fields. In this special case, the diffracted field can be simply decomposed into its ray optical components so that further diffractions can be calculated using the GTD [10]. The results of this procedure agree with the asymptotic expansion of the exact result up to the second order interaction contributions; for the higher order interactions, this ray-optical procedure underestimates the asymptotic result [29]. However, for numerical calculations the discrepancy is negligible. A formally asymptotic ray-optical analysis is proposed in [14] based on the uniform asymptotic theory of diffraction (UAT) [30]. This lengthy analysis consists of decomposing the interaction field into a Taylor series and applying uniform asymptotic theory to each term in the series and summing up the results. Another attempt to get an accurate multiple diffraction field contribution is described in [12,13]. In this approach, the canonical problem of the diffraction by two staggered parallel half-planes is solved and the asymptotic approximation to that solution is identified as the modified diffraction coefficient (MDC), which includes the presence of the other edge. Later on, this solution is extended to non-staggered parallel-plates [15].

In 3-D problems, the diffraction points migrate around the rim edge as the observation point changes position. In some cases, there may be a continuum of diffraction points contributing to the scattered field which produces a caustic of diffracted rays. The GTD predicts singular

fields at a caustic; therefore in order to get a bounded result, one can use the so-called equivalent current method (ECM) based on the GTD. The ECM is valid provided the diffracted fields are to be found away from the shadow boundaries. Away from the caustic regions where GTD is valid, the ECM generally blends into the GTD solution as long as the waveguide opening is sufficiently large in terms of the wavelength. The use of ECM also, automatically, but in an approximate sense, takes into account the presence of the corners at the waveguide opening.

In the ECM, the equivalent currents (\bar{I}_{eq} and \bar{M}_{eq}) of the electric and magnetic type, respectively, are located at the rim, and they radiate in free space to give the diffracted field as shown in Figure 3.1. The strengths of the equivalent currents are calculated indirectly from the GTD, but since they are incorporated in an integral, they give bounded results in the caustic regions of the GTD. This definition of the equivalent currents makes them correct for the observation points lying on the Keller edge diffracted ray cone [11]. In order to extend the definition for observation points which are not restricted on the Keller cone of edge diffracted rays, it has been proposed to modify the expressions heuristically in a manner consistent with reciprocity [31]. In the following expressions this modification is included.

The strengths of equivalent electric and magnetic currents are given by [26]

$$\bar{I}_{eq} = \frac{-\hat{x}' \cdot \bar{E}^i(rim)}{Z_0 \sqrt{\sin \tilde{\beta}_0 \sin \tilde{\beta}}} D_s(\psi, \psi'; \tilde{\beta}_0, \tilde{\beta}, \alpha) \sqrt{\frac{8\pi}{jk}} \hat{x}' \quad (3.1)$$

and

$$\bar{M}_{eq} = - \frac{\hat{\ell}' \cdot \bar{H}^i(rim)}{Y_0 \sqrt{\sin \tilde{\beta}_0 \sin \tilde{\beta}}} D_h(\psi, \psi'; \tilde{\beta}_0, \tilde{\beta}, \alpha) \sqrt{\frac{8\pi}{jk}} \hat{\ell}' \quad (3.2)$$

where $\hat{\ell}'$ is the unit vector along the edge direction, and Y_0 , k , \bar{E}^i and \bar{H}^i are as defined earlier in (2.2) through (2.5).

The angles $(\psi, \psi', \tilde{\beta}_0$ and $\tilde{\beta})$ are associated with the soft and hard diffraction coefficients (D_s and D_h) which are present in (3.1) and (3.2). In particular, these edge diffraction coefficients

$D_h(\psi, \psi', \tilde{\beta}_0, \tilde{\beta}, \alpha)$ in (3.1) and (3.2) are defined for each point on the rim, and they are associated with a wedge which locally represents the

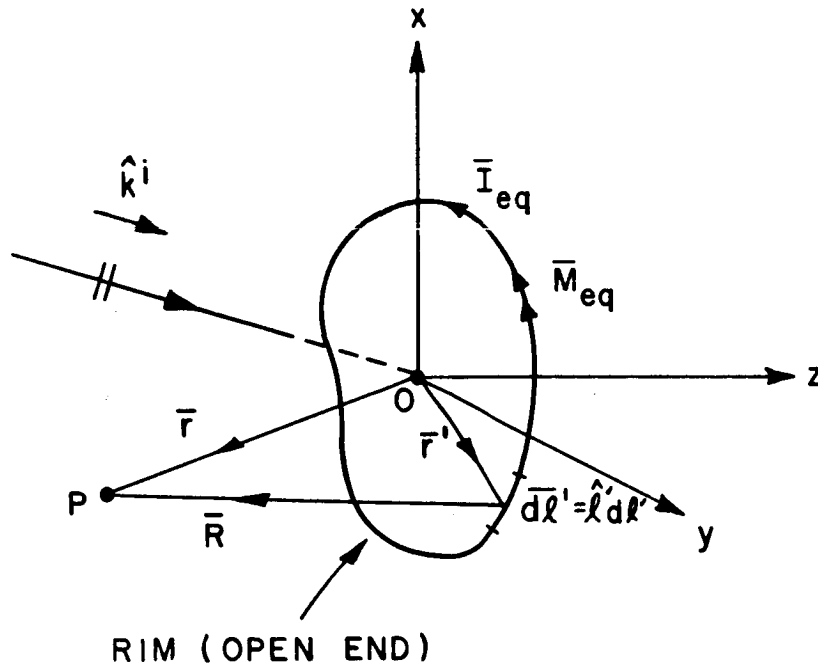


Figure 3.1. The equivalent currents \bar{I}_{eq} and \bar{M}_{eq} at the rim of the open end.

rim geometry. Assuming that Q is any such point of diffraction on an edge in an arbitrary curved wedge, the meaning of $\psi, \psi', \tilde{\beta}_0$ and $\tilde{\beta}$ with respect to the point of diffraction Q becomes clear from Figures 3.2(a) and (b) for this wedge configuration.

The soft and the hard diffraction coefficients are given by [11]

$$D_{\tilde{h}}(\psi, \psi', \tilde{\beta}_0, \tilde{\beta}, \alpha) = \frac{e^{-j\pi/4} \sin \frac{\pi}{\alpha}}{\alpha \sqrt{2\pi k} \sqrt{\sin \tilde{\beta}_0 \sin \tilde{\beta}}} \left[\frac{1}{\cos \frac{\pi}{\alpha} - \cos \frac{\psi - \psi'}{\alpha}} \mp \frac{1}{\cos \frac{\pi}{\alpha} - \cos \frac{\psi + \psi'}{\alpha}} \right] \quad (3.3)$$

where the parameter α is related to the exterior wedge angle as shown in Figure 3.2(b).

Finally, the equivalent currents (\bar{I}_{eq} and \bar{M}_{eq}) are valid provided one is observing these sources in directions away from the geometrical optics incident and reflection shadow boundaries as mentioned earlier. These conditions are certainly met when one is interested in the scattering from the waveguide cavity at and near the axial direction. The radiated electric field is then given by

$$\bar{E}^{so} = \frac{jkZ_0}{4\pi} \int_{rim} [\hat{R} \times \hat{R} \times \bar{I}_{eq}(\ell') + Y_0 \hat{R} \times \bar{M}_{eq}(\ell')] \frac{e^{-jkR}}{R} d\ell' \quad (3.4)$$

where $\bar{R} = R\hat{R}$ is the vector pointing toward the observation point from a source point on the rim.

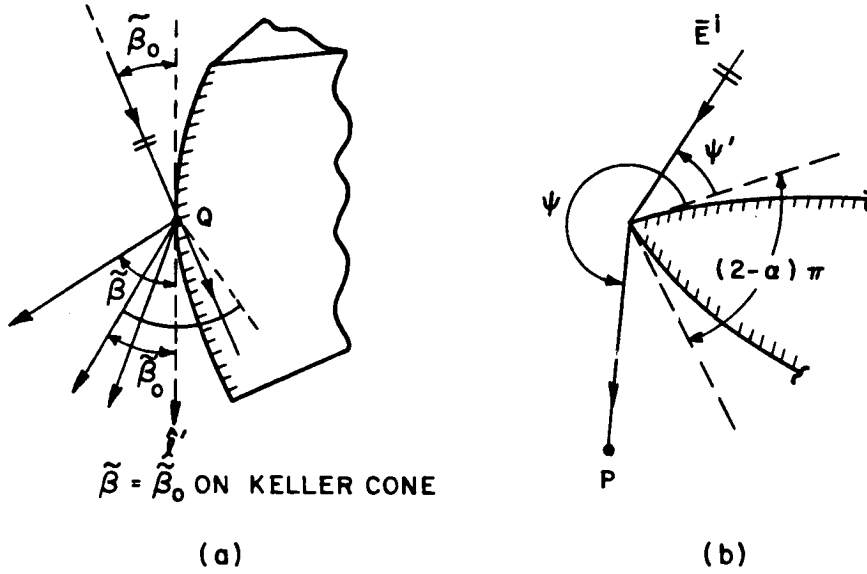


Figure 3.2. Diffraction by a wedge. The angles $\tilde{\beta}_0$, $\tilde{\beta}$, ψ and ψ' which occur in the wedge diffraction coefficient.

The use of Equations (3.1) and (3.2) in (3.4) allows one to easily identify $[S_{11}]$. Thus, one obtains

$$S_{u\theta} = \frac{jkZ_0}{4\pi} \int_{\text{rim}} d\ell' \hat{u} \cdot \left\{ \hat{R}x\hat{R}x\hat{\ell}' \left[-Y_0 \sqrt{\frac{8\pi}{jk}} \frac{D_s(\psi, \psi'; \tilde{\beta}_0, \tilde{\beta}, \alpha)}{\sqrt{\sin\tilde{\beta}_0 \sin\tilde{\beta}}} \hat{\ell}' \cdot \hat{\theta}^i \right] \right. \\ \left. - Y_0 \hat{R}x\hat{\ell}' \left[-\sqrt{\frac{8\pi}{jk}} \frac{D_h(\psi, \psi'; \tilde{\beta}_0, \tilde{\beta}, \alpha)}{\sqrt{\sin\tilde{\beta}_0 \sin\tilde{\beta}}} \hat{\ell}' \cdot \hat{\phi}^i \right] \right\} \frac{e^{-jk\hat{k}^i \cdot \vec{r}' - jkR}}{R} \quad (3.5)$$

and

$$S_{u\phi} = \frac{jkZ_0}{4\pi} \int_{\text{rim}} d\ell' \hat{u} \cdot \left\{ \hat{R}x\hat{R}x\hat{\ell}' \left[-Y_0 \sqrt{\frac{8\pi}{jk}} \frac{D_s(\psi, \psi'; \tilde{\beta}_0, \tilde{\beta}, \alpha)}{\sqrt{\sin\tilde{\beta}_0 \sin\tilde{\beta}}} \hat{\ell}' \cdot \hat{\phi}^i \right] \right. \\ \left. + Y_0 \hat{R}x\hat{\ell}' \left[-\sqrt{\frac{8\pi}{jk}} \frac{D_h(\psi, \psi'; \tilde{\beta}_0, \tilde{\beta}, \alpha)}{\sqrt{\sin\tilde{\beta}_0 \sin\tilde{\beta}}} \hat{\ell}' \cdot \hat{\theta}^i \right] \right\} \frac{e^{-jk\bar{k}^i \cdot \bar{r}' - jkR}}{R} \quad (3.6)$$

with

$$\hat{u} = \begin{bmatrix} \hat{x} \\ \hat{y} \\ \hat{z} \end{bmatrix} \quad \text{and} \quad u = \begin{bmatrix} x \\ y \\ z \end{bmatrix} \quad (3.7a;b)$$

Examples:

- a) Near field scattering by the open end of a semi-infinite circular waveguide:

The geometry is shown in Figure 3.3. An incident plane wave is propagating parallel to the x-z plane ($\phi^i=0$) and makes an angle (θ^i) with the \hat{z} -axis. The electric field is evaluated at the observation point (P), which is radially separated from the origin by the distance (r) and has azimuth and elevation angles ϕ^r and θ , respectively. The results are plotted as a function of θ in different azimuth planes (indicated by ϕ^r) for different values of r and the radius (a). In the near field of the rim of the circular waveguide, there can be four points of diffraction for a certain set of observation points (P) as a consequence of Keller's generalization of Fermat's principle in the GTD;

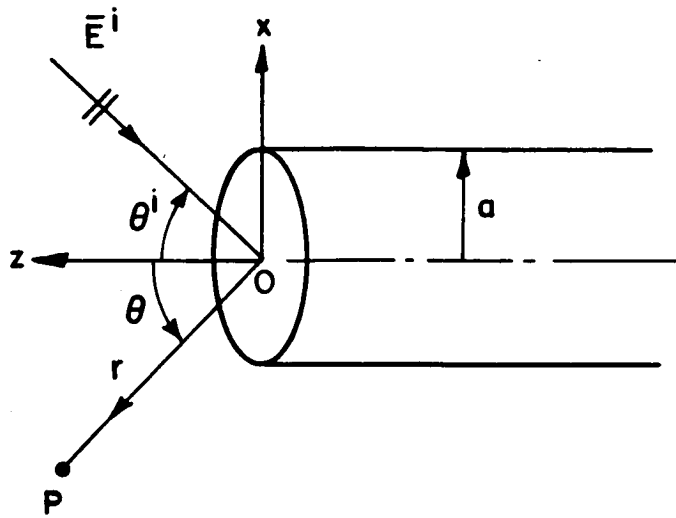


Figure 3.3. Scattering from the open end of a semi-infinite circular waveguide.

whereas, at other observation points (P) only two points of edge diffraction on the circular rim contribute to the scattered field. A direct application of the GTD fails in the range of observation points, within which such a coalescence of the four points into two points of diffraction occurs on the rim edge, since the stationary phase condition is violated as these points coalesce. Typically, such a disappearance of rays results when three of the four points merge together. Conversely, one can also experience a transition from two to four rays diffracted to P. A detailed analysis of the migration of diffraction points along the rim is given in [32]. In such cases where the GTD fails, the ECM still gives bounded and reasonably accurate results. In the Figures 3.4 through 3.13, calculations based on the GTD and the ECM are compared with each other. The comparison gets better in the regions where the GTD is valid for large cylinder sizes; elsewhere, the ECM is far more accurate.

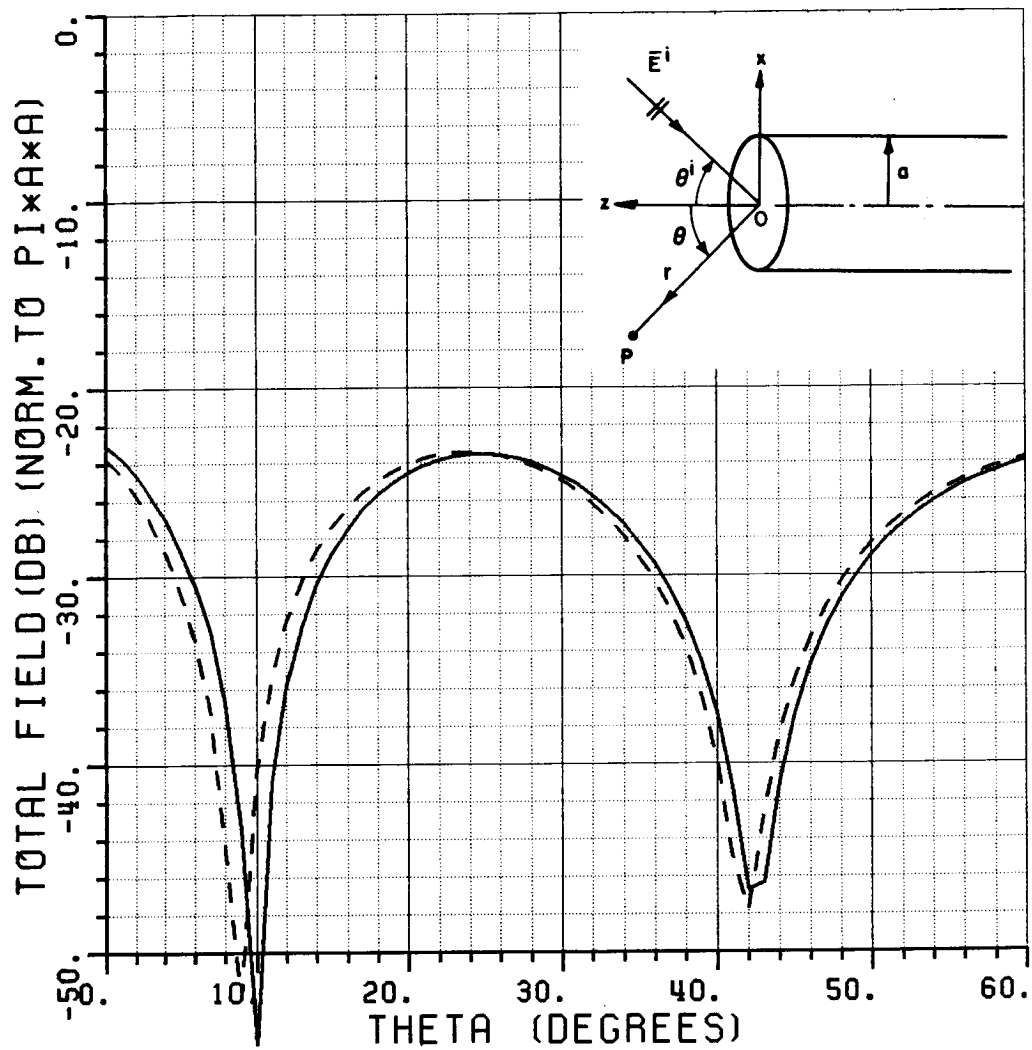


Figure 3.4. Near field scattering from an open-ended circular waveguide using GTD and ECM. — GTD, --- ECM.
 $r=5\lambda$, $a=1\lambda$, $\theta^i=45^\circ$, $\phi^i=0$, $\phi^r=0$, $\vec{E}^i=\hat{\phi}^i$

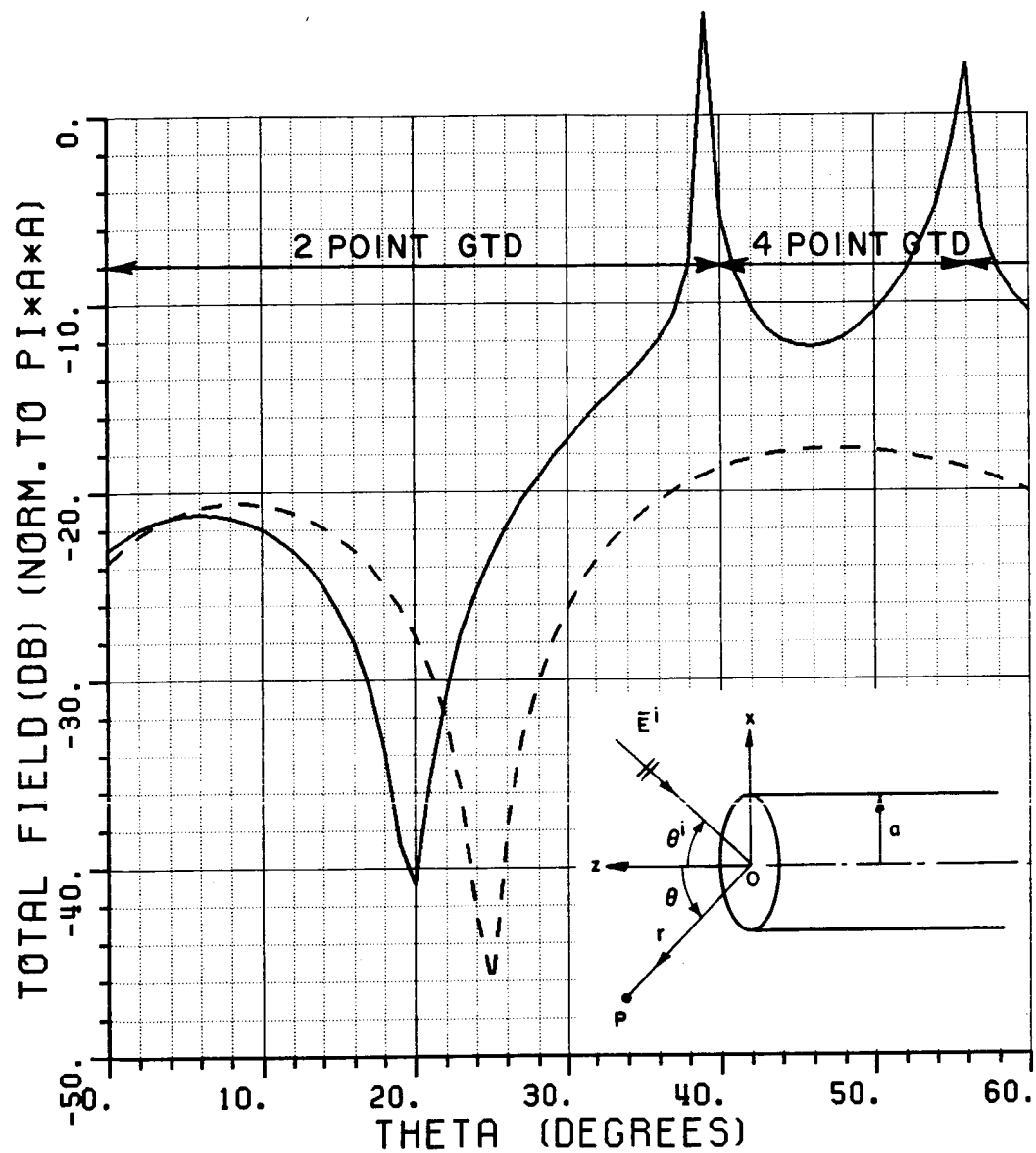


Figure 3.5. Near field scattering from an open-ended circular waveguide using GTD and ECM. — GTD, --- ECM.
 $r=5\lambda$, $a=1\lambda$, $\theta^i=45^\circ$, $\phi^i=0$, $\phi^r=180^\circ$, $\vec{E}^i=\hat{\phi}$

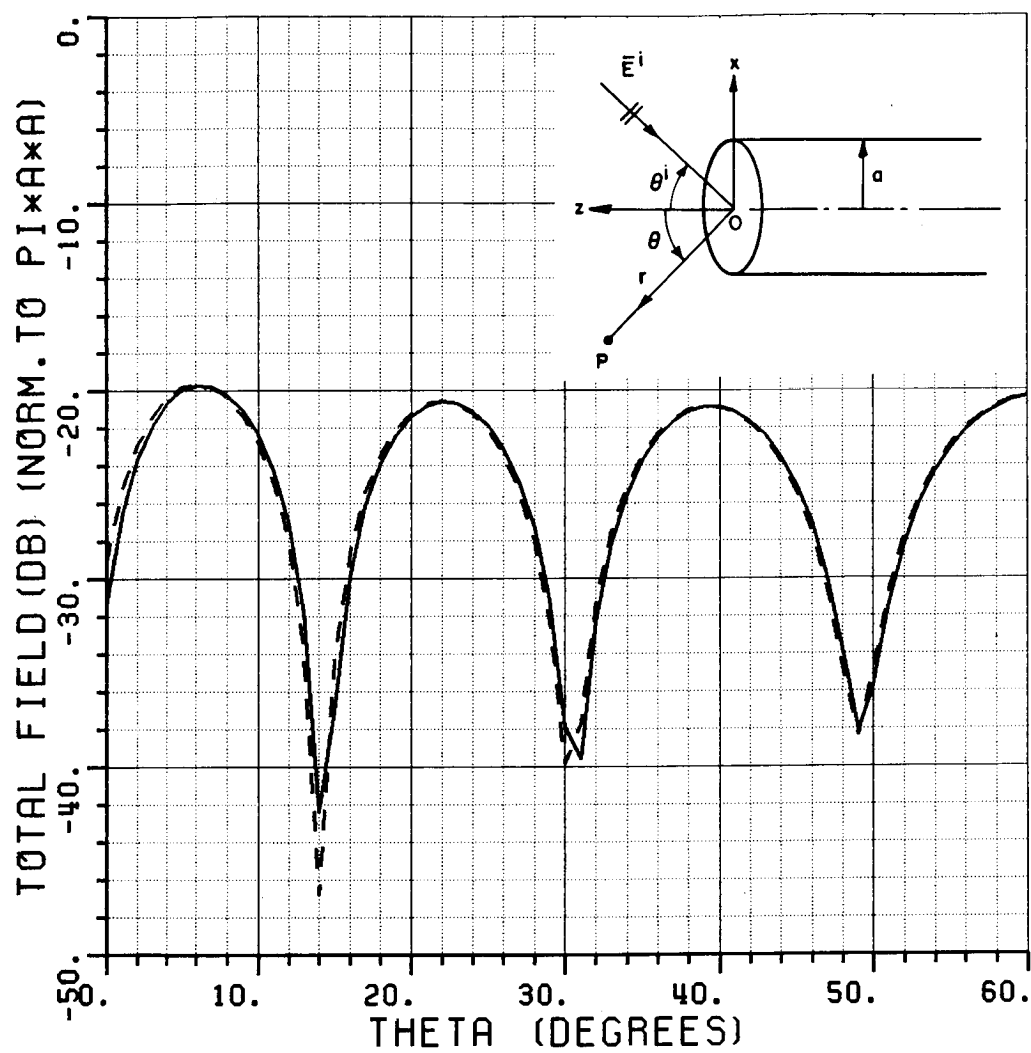


Figure 3.6. Near field scattering from an open-ended circular waveguide using GTD and ECM. — GTD, --- ECM.
 $r=5\lambda$, $a=2\lambda$, $\theta^i=45^\circ$, $\phi^i=0$, $\phi^r=0$, $\vec{E}^i=\hat{\phi}^i$

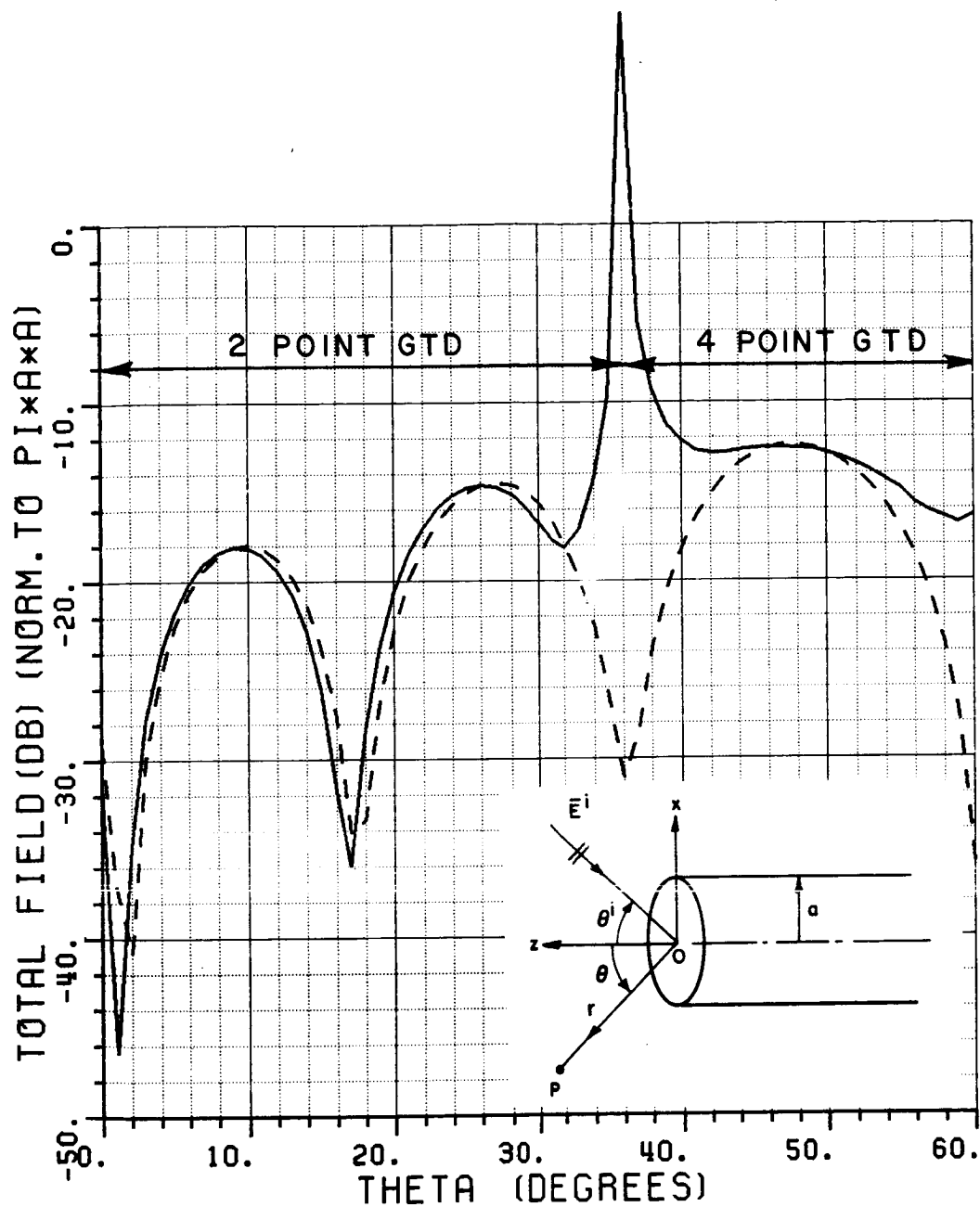


Figure 3.7. Near field scattering from an open-ended circular waveguide using GTD and ECM. — GTD, --- ECM.
 $r=5\lambda$, $a=2\lambda$, $\theta^i=45^\circ$, $\phi^i=0$, $\phi^r=180^\circ$, $\vec{E}^i=\hat{\phi}^i$

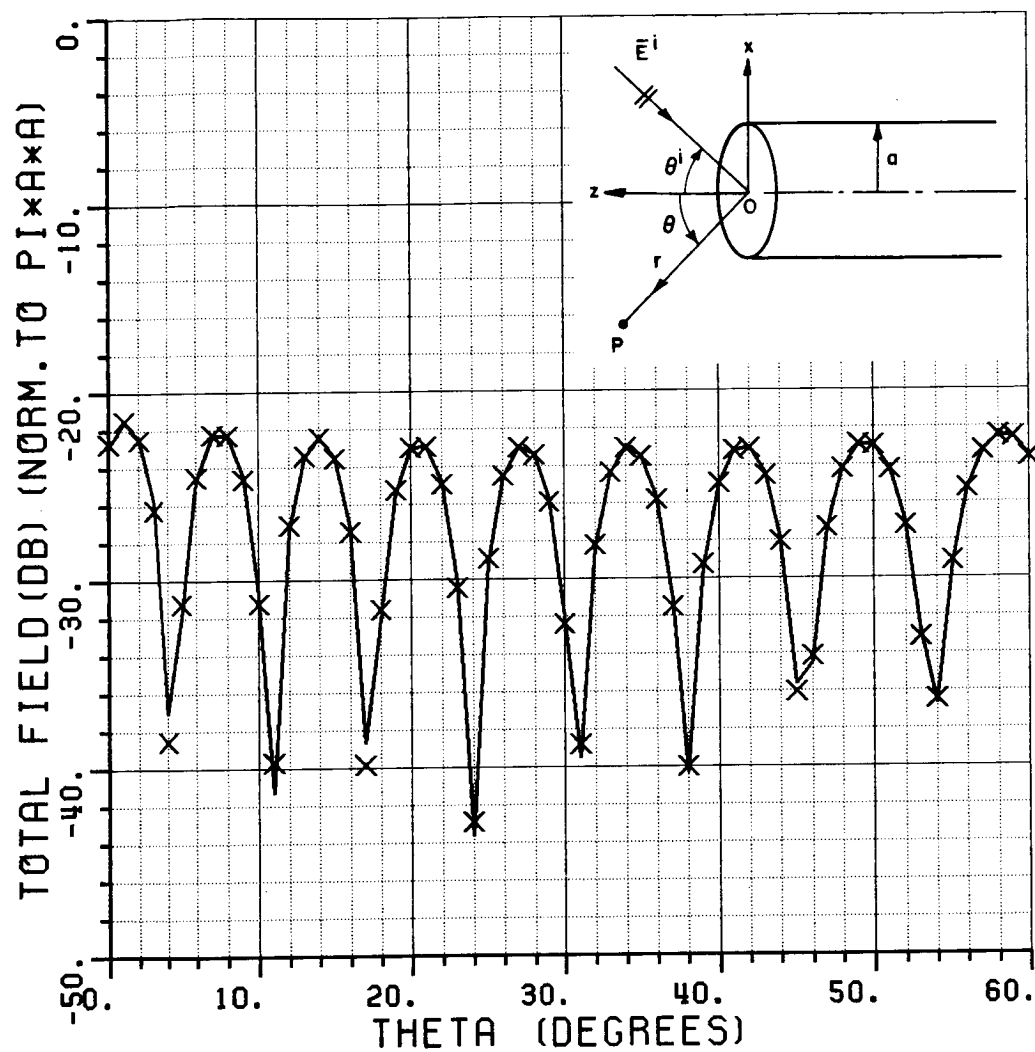


Figure 3.8. Near field scattering from an open-ended circular waveguide using GTD and ECM. — GTD, xxx ECM.
 $r=10\lambda$, $a=5\lambda$, $\theta^i=45^\circ$, $\phi^i=0$, $\phi^r=0$, $\vec{E}^i=\hat{\phi}$

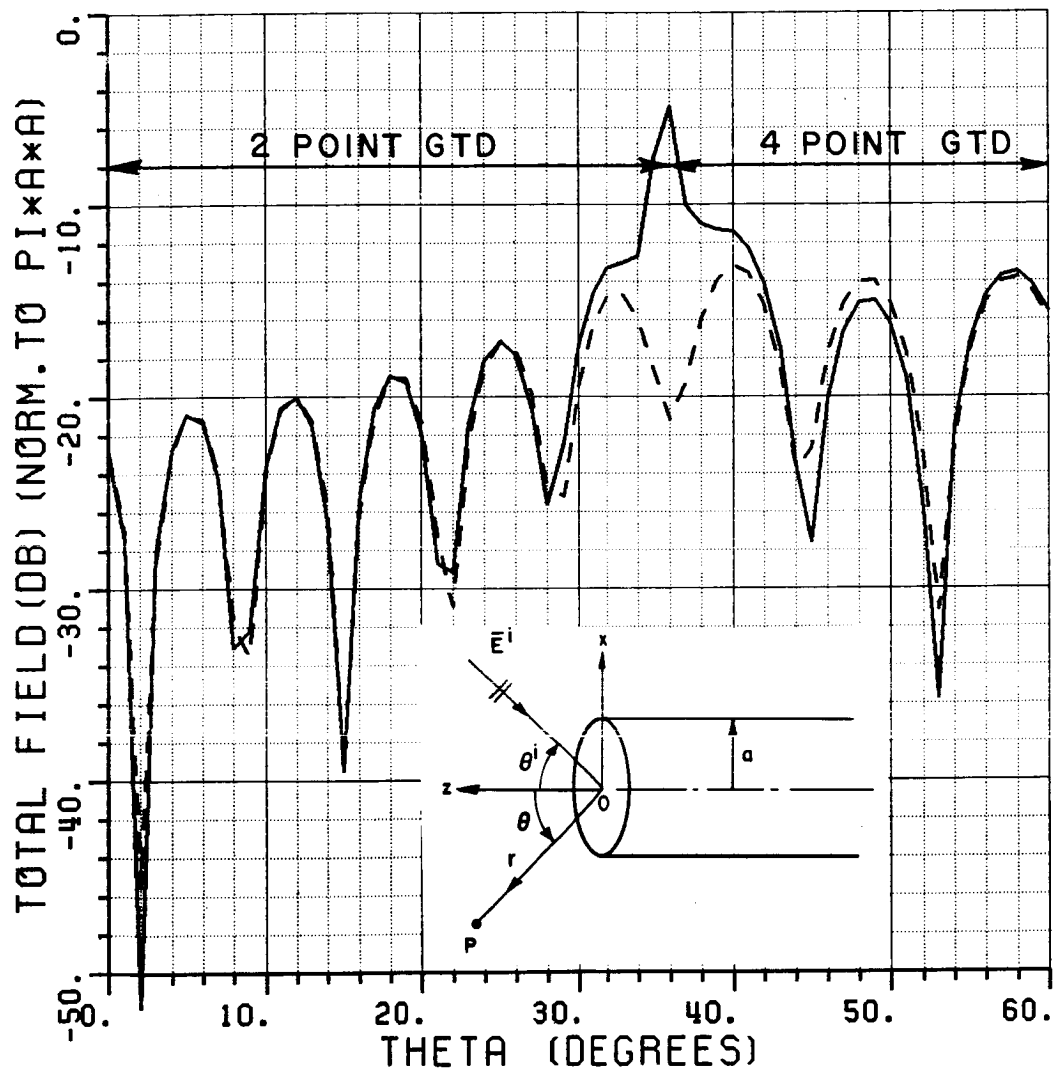


Figure 3.9. Near field scattering from an open-ended circular waveguide using GTD and ECM. — GTD, --- ECM.
 $r=10\lambda$, $a=5\lambda$, $\theta^i=45^\circ$, $\phi^i=0$, $\phi^r=180^\circ$, $\hat{E}^i=\hat{\phi}^i$

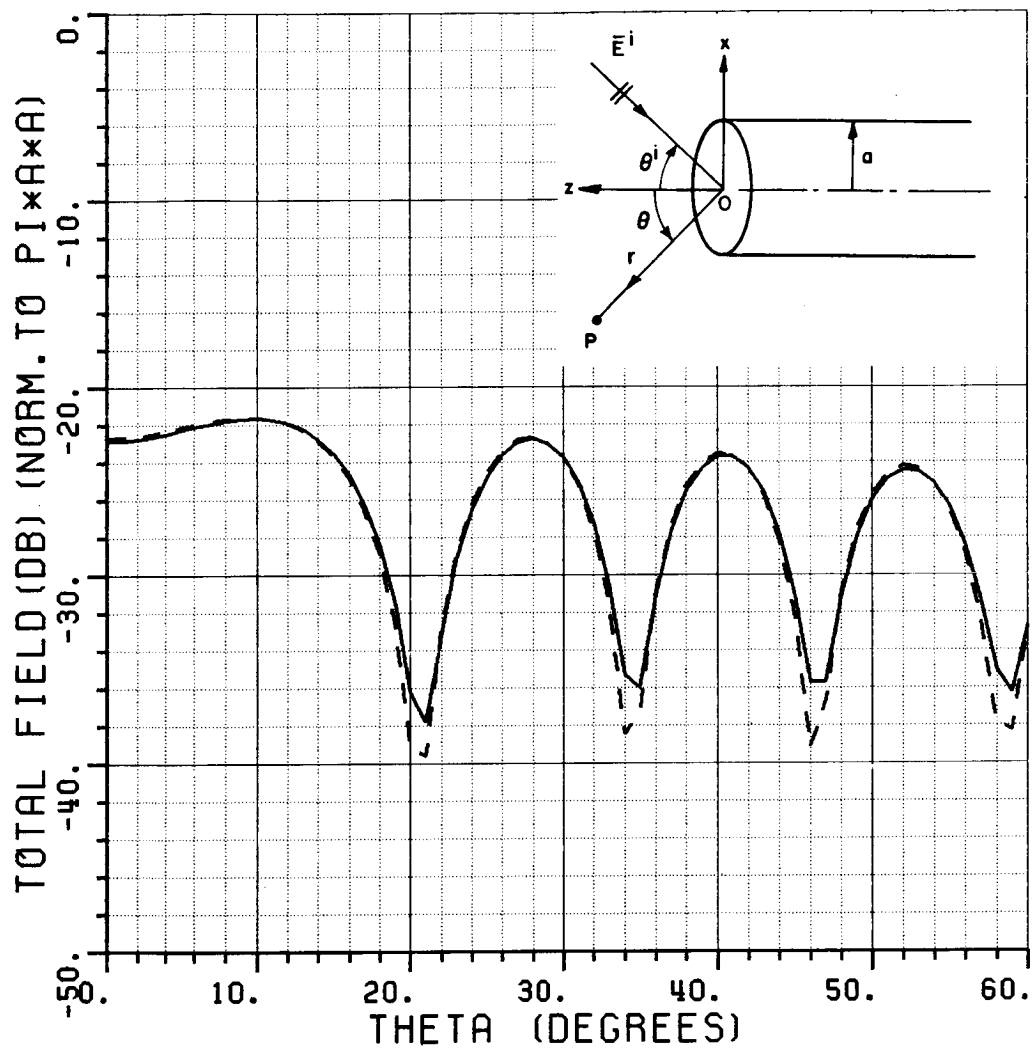


Figure 3.10. Near field scattering from an open-ended circular waveguide using GTD and ECM. — GTD, --- ECM. $r=10\lambda$, $a=5\lambda$, $\theta^i=45^\circ$, $\phi^i=0$, $\phi^r=90^\circ$, $\vec{E}^i=\hat{\phi}^i$

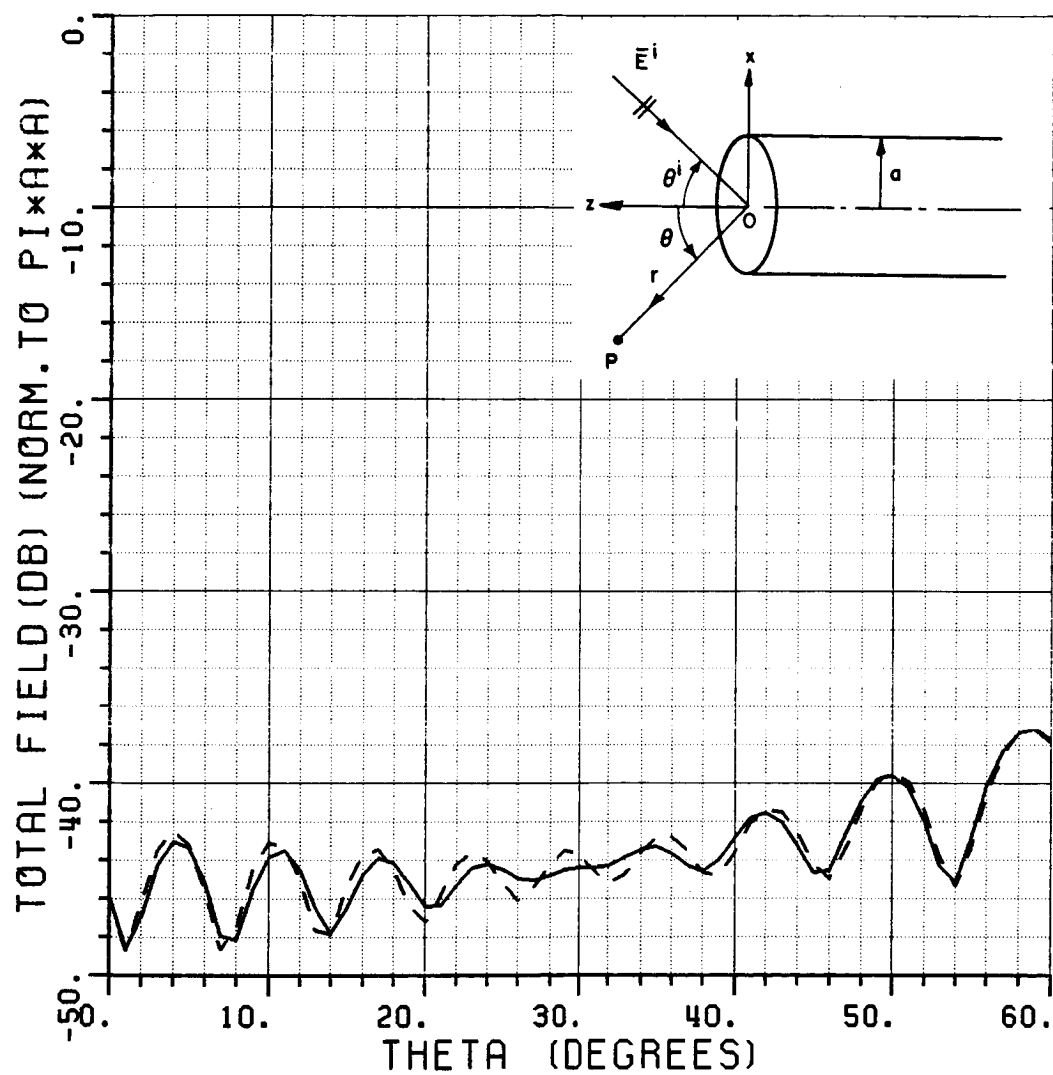


Figure 3.11. Near field scattering from an open-ended circular waveguide using GTD and ECM. — GTD, --- ECM.
 $r=10\lambda$, $a=5\lambda$, $\theta^i=45^\circ$, $\phi^i=0$, $\phi^r=0$, $\vec{E}^i=\hat{\theta}^i$

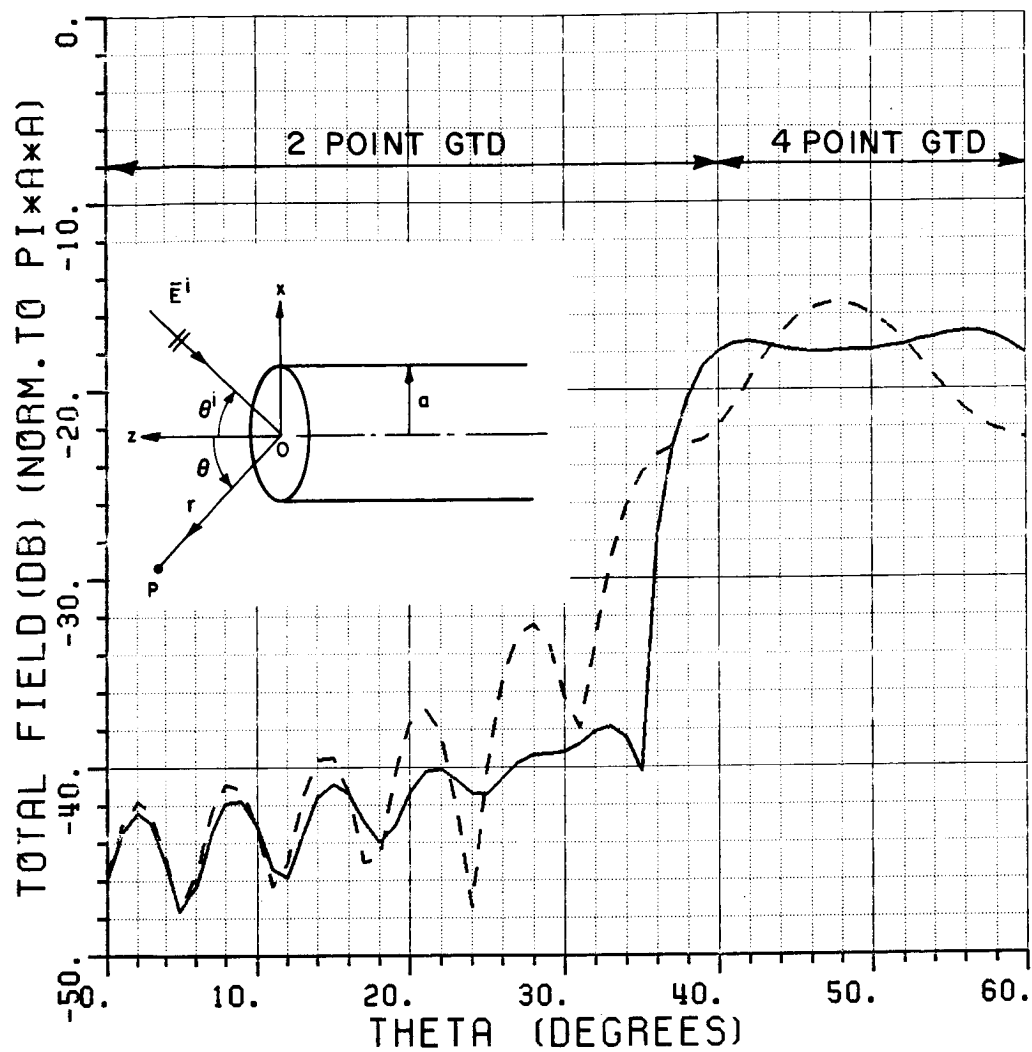


Figure 3.12. Near field scattering from an open-ended circular waveguide using GTD and ECM. — GTD, --- ECM.
 $r=10\lambda$, $a=5\lambda$, $\theta^i=45^\circ$, $\phi^i=0$, $\phi^r=180^\circ$, $\vec{E}^i=\hat{\theta}^i$

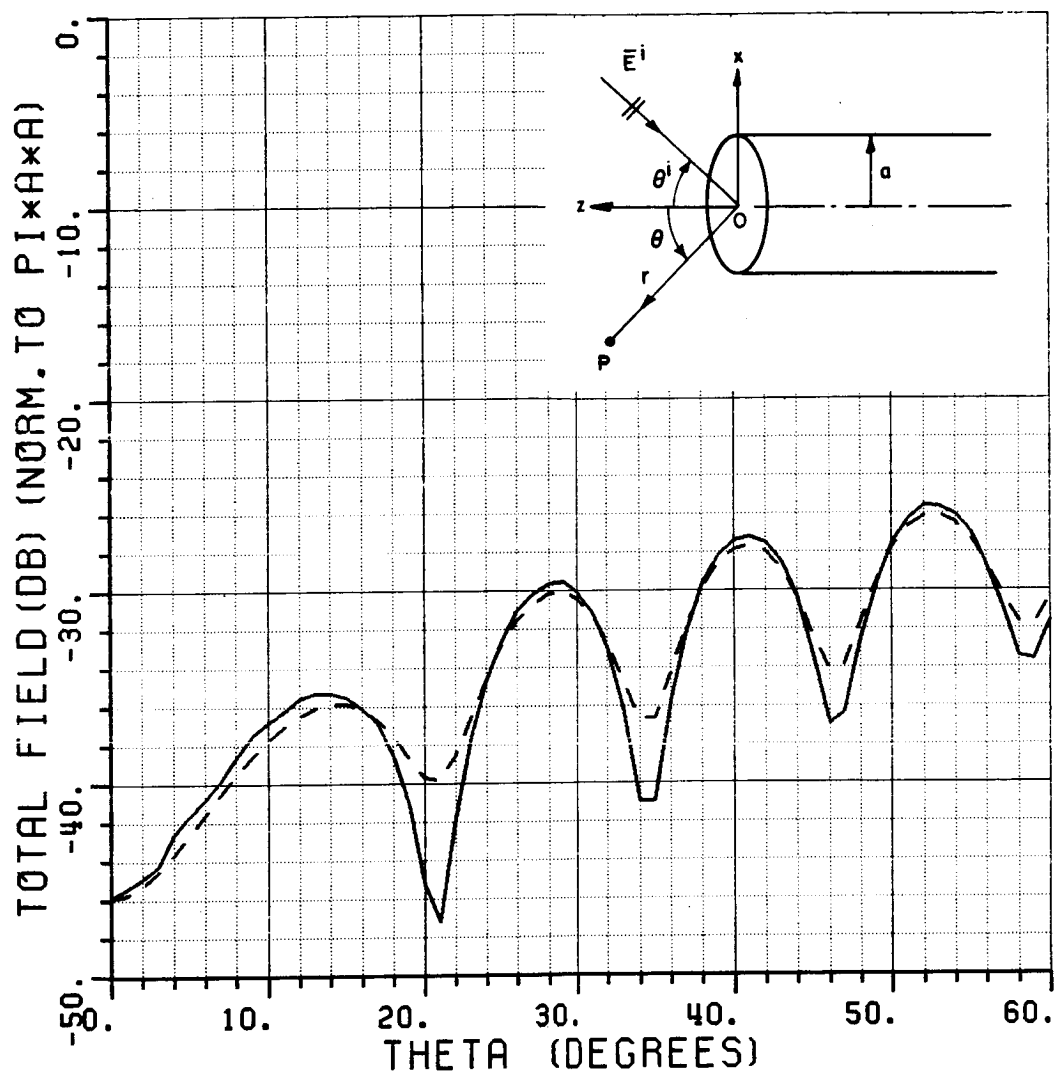


Figure 3.13. Near field scattering from an open-ended circular waveguide using GTD and ECM. — GTD, --- ECM. $r=10\lambda$, $a=5\lambda$, $\theta^i=45^\circ$, $\phi^i=0$, $\phi^r=90^\circ$, $\vec{E}^i=\hat{\theta}^i$

- b) Near field scattering by the open end of a semi-infinite rectangular waveguide:

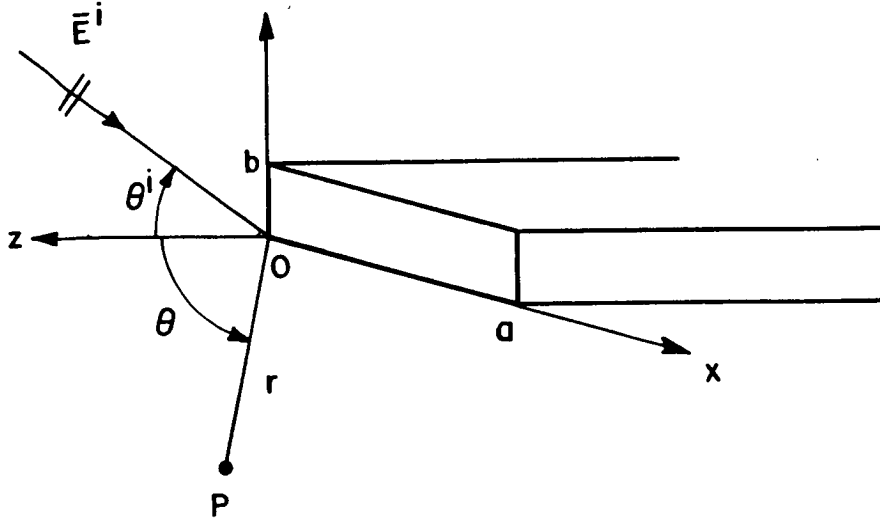


Figure 3.14. Scattering from the open end of a semi-infinite rectangular waveguide.

The rectangular waveguide has perfectly conducting infinitely thin walls, therefore the diffraction coefficients of Equation (3.3) can be written as follows ($\alpha=2$)

$$D_{sh}(\psi, \psi', \tilde{\beta}_0, \tilde{\beta}) = \frac{2 e^{-j\pi/4}}{\sqrt{2\pi k}} \frac{\begin{Bmatrix} \sin(\psi/2)\sin(\psi'/2) \\ -\cos(\psi/2)\cos(\psi'/2) \end{Bmatrix}}{\cos\psi + \cos\psi'} \frac{1}{\sqrt{\sin\tilde{\beta}_0\sin\tilde{\beta}}} \quad (3.8)$$

For the incident plane wave fields of (2.2) and (2.5) the equivalent currents can be written explicitly as

$$\bar{I}_{eq} = \frac{4j}{kZ_0 \sin \tilde{\beta}_0 \sin \tilde{\beta}} \frac{\sin(\psi/2)\sin(\psi'/2)}{\cos \psi + \cos \psi'} e^{jk \sin \theta^i (x' \cos \phi^i + y' \sin \phi^i)}$$

$$\cdot \begin{cases} (A_\theta^i \cos \theta^i \cos \phi^i - A_\phi^i \sin \phi^i) \hat{x} & \text{for horizontal edges} \\ (A_\theta^i \cos \theta^i \sin \phi^i + A_\phi^i \cos \phi^i) \hat{y} & \text{for vertical edges} \end{cases} \quad (3.9)$$

and

$$\bar{M}_{eq} = \frac{4j}{k \sin \tilde{\beta}_0 \sin \tilde{\beta}} \frac{\cos(\psi/2)\cos(\psi'/2)}{\cos \psi + \cos \psi'} e^{jk \sin \theta^i (x' \cos \phi^i + y' \sin \phi^i)}$$

$$\cdot \begin{cases} -(A_\theta^i \sin \phi^i + A_\phi^i \cos \theta^i \cos \phi^i) \hat{x} & \text{for horizontal edges} \\ (A_\theta^i \cos \phi^i - A_\phi^i \cos \theta^i \sin \phi^i) \hat{y} & \text{for vertical edges} \end{cases} \quad (3.10)$$

The equivalent currents, \bar{I}_{eq} and \bar{M}_{eq} are located on the rectangular rim with the dimensions "a" and "b" as shown in Figure 3.14.

The angles $\tilde{\beta}_0$, $\tilde{\beta}$, ψ' and ψ in (3.9) and (3.10) are determined as follows;

$$\sin \tilde{\beta}_0 = \begin{cases} (1 - \sin^2 \theta^i \cos^2 \phi^i)^{1/2} & ; \text{ for horizontal edges} \\ (1 - \sin^2 \theta^i \sin^2 \phi^i)^{1/2} & ; \text{ for vertical edges} \end{cases} \quad (3.11)$$

$$\sin \tilde{\beta} \approx \begin{cases} (1 - \sin^2 \theta \cos^2 \phi)^{1/2} & ; \text{ for horizontal edges} \\ (1 - \sin^2 \theta \sin^2 \phi)^{1/2} & ; \text{ for vertical edges} \end{cases} \quad (3.12)$$

The angles ψ' and ψ are measured from the inner faces of the waveguide.

$$\cos \psi' = - \frac{\cos \theta^i}{\sin \tilde{\beta}_0} \quad (3.13)$$

$$\cos \psi \approx - \frac{\cos \theta}{\sin \tilde{\beta}} \quad (3.14)$$

The scattered field at point P with spherical coordinates (r, θ, ϕ) due to these equivalent currents is given by

$$\begin{aligned} \bar{E}^S \approx (\pi \sin \tilde{\beta}_0 \sin \tilde{\beta} (\cos \psi + \cos \psi') r)^{-1} & \left[\hat{\theta} [E_{\theta}^h(\gamma_1 + \gamma_2) + E_{\theta}^v(\delta_1 + \delta_2)] \right. \\ & \left. + \hat{\phi} [E_{\phi}^h(\gamma_1 + \gamma_2) + E_{\phi}^v(\delta_1 + \delta_2)] \right] \end{aligned} \quad (3.15)$$

where

$$\begin{aligned} \gamma_1 = e^{jk b \sin \theta^i \sin \phi^i} \int_0^a e^{-jk \sqrt{r^2 + b^2 - 2rx' \sin \theta \cos \phi - 2rb \sin \theta \sin \phi + x'^2}} \\ \cdot e^{jk x' \sin \theta^i \cos \phi} dx' \end{aligned} \quad (3.16)$$

$$\gamma_2 = \int_0^a e^{-jk \sqrt{r^2 - 2rx' \sin \theta \cos \phi + x'^2}} + jk x' \sin \theta^i \cos \phi^i dx' \quad (3.17)$$

$$\begin{aligned} \delta_1 = e^{jk a \sin \theta^i \cos \phi^i} \int_0^b e^{-jk \sqrt{r^2 + a^2 - 2ry' \sin \theta \sin \phi - 2ra \sin \theta \cos \phi + y'^2}} \\ \cdot e^{jk y' \sin \theta^i \sin \phi^i} dy' \end{aligned} \quad (3.18)$$

$$\delta_2 = \int_0^b e^{-jk \sqrt{r^2 - 2ry' \sin \theta \sin \phi + y'^2}} + jk y' \sin \theta^i \sin \phi^i dy' \quad (3.19)$$

and

$$E_{\theta}^h = S \cdot A \cos \theta \cos \phi + C \cdot B \sin \phi \quad (3.20)$$

$$E_{\theta}^v = S \cdot D \cos \theta \sin \phi + C \cdot E \cos \phi \quad (3.21)$$

$$E_{\phi}^h = -S \cdot A \sin \phi + C \cdot B \cos \phi \quad (3.22)$$

$$E_{\phi}^v = S \cdot D \cos \phi - C \cdot E \sin \phi \quad (3.23)$$

in which

$$S = \sin(\psi/2) \sin(\psi'/2) \quad (3.24)$$

$$C = \cos(\psi/2) \cos(\psi'/2) \quad (3.25)$$

$$A = A_{\theta}^i \cos \theta^i \cos \phi^i - A_{\phi}^i \sin \phi^i \quad (3.26)$$

$$B = A_{\theta}^i \sin \phi^i + A_{\phi}^i \cos \theta^i \cos \phi^i \quad (3.27)$$

$$D = A_{\theta}^i \cos \theta^i \sin \phi^i + A_{\phi}^i \cos \phi^i \quad (3.28)$$

$$E = A_{\phi}^i \cos \phi^i - A_{\theta}^i \cos \theta^i \sin \phi^i \quad (3.29)$$

The result in (3.15) can be simplified if $r \gg a, b$, in which case the integrals can be approximated by Fresnel integrals. The numerical results for the scattering from the open end of a rectangular waveguide are presented in [33] and compared with the Fresnel approximations.

3.1.2 Modal Reflection from an Interior Discontinuity

The scattering matrix which describes the modal reflections due to a junction inside the waveguide is examined here using ray optical techniques.

In the ray optical procedure, the incident mode is decomposed into ray-optical components, and the GTD is used to determine the field diffracted by the junction. These diffracted fields then excite the reflected modes. The computation of reflected mode amplitudes has been discussed in [10] for the parallel-plate waveguide geometry using image theory. However, this procedure is difficult to apply to other geometries which lack analogous symmetry properties. In order to overcome this difficulty, it is proposed here to make use of an equivalent current approach to get the coefficients of reflected modes, which, in the case of parallel-plate waveguide gives the same result as in [10]. The proposed procedure can be easily generalized to other interior waveguide discontinuities as long as the diffraction coefficients for the discontinuities are known.

Basically, the procedure requires that the modal field expressions inside the waveguide sections can be given a ray interpretation. Such a ray interpretation of the modal fields for some waveguide geometries in terms of the so called "modal rays" is shown in the Appendices. Some of these modal rays are illustrated here in Figures 3.15 through 3.19. For example, each mode in a parallel-plate waveguide corresponds to two plane waves which propagate in the modal ray directions as shown in Figure 3.15. Likewise in the case of the rectangular waveguide, each

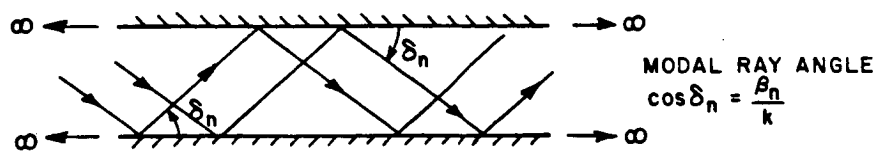


Figure 3.15. Modal rays in a parallel-plate waveguide.

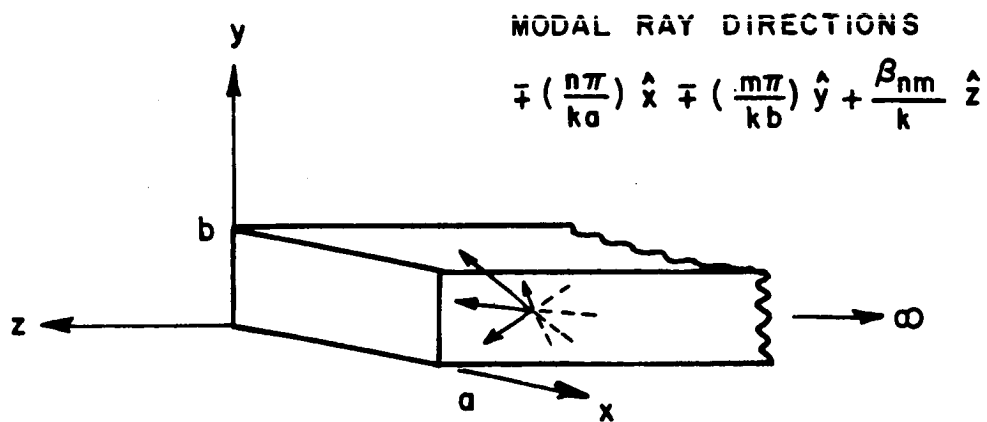


Figure 3.16. Modal rays in a rectangular waveguide.

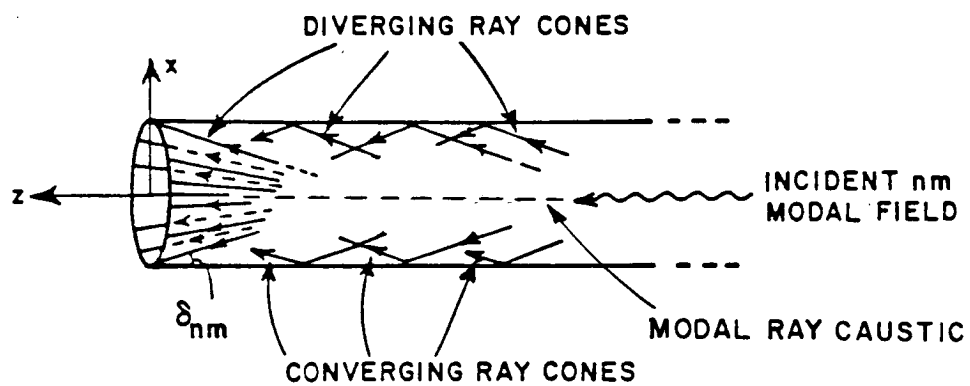


Figure 3.17. Modal rays in a circular waveguide.

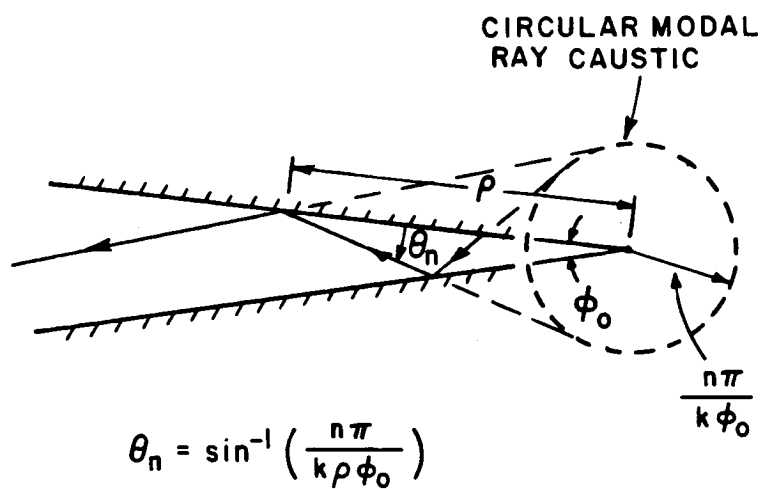


Figure 3.18. Modal rays in a 2-D linearly tapered waveguide.

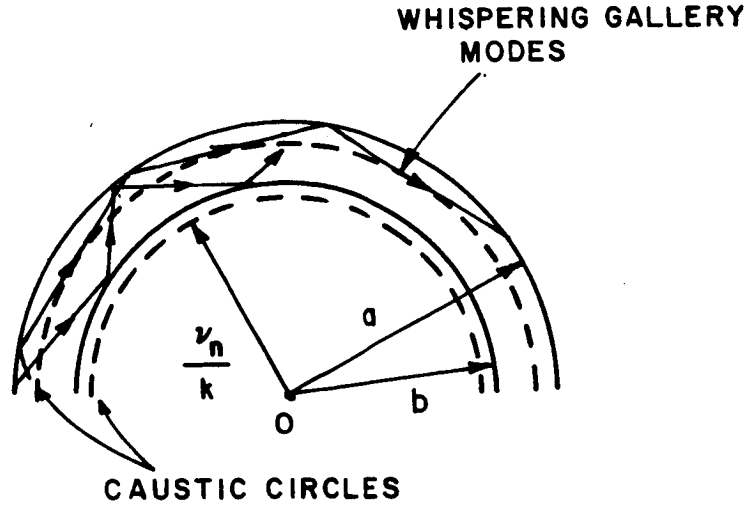


Figure 3.19. Modal rays in a 2-D annular waveguide.

mode is decomposed into four plane waves (or modal rays) propagating in the directions:

$$\hat{r}_{nm} = \pm \left(\frac{n\pi}{ka} \right) \hat{x} \pm \left(\frac{m\pi}{kb} \right) \hat{y} + \frac{\beta_{nm}}{k} \hat{z} \quad . \quad (3.30)$$

In a circular waveguide the modal ray picture that is employed in this work is shown in Figure 3.17. Each mode consists of two conical modal rays which are converging and diverging at the axis of the waveguide. Linearly tapered waveguide modes in the 2-D case can be interpreted in terms of modal rays bouncing from the two walls. The ray trajectories are tangent to the circular modal ray caustic whose radius is determined by the mode index as shown in Figure 3.18. It is noted that modal ray

representation is valid only in the region outside the circular modal ray caustic. The 3-D sectoral waveguide modal rays are similar to the 2-D linearly tapered modal rays, but due to the existence of the third dimension the ray trajectories are also oblique to the parallel walls (see Figures C.2 and C.3 in Appendix C). Lastly, the ray interpretation of 2-D annular waveguide modes is described in Appendix E, and they include trajectories bouncing from both walls, as well as from only the outer wall associated with the whispering gallery modes, as depicted in Figure 3.19.

In order to describe the ray optical procedure which makes use of the above modal rays, let us assume that a waveguide section represented by A is connected to another section called B, through a junction J, as illustrated in Figure 3.20. For convenience, an orthogonal curvilinear coordinate system (η, γ, ξ) is assumed in which the Helmholtz equation is separable. Furthermore, let the coordinate η coincide with the

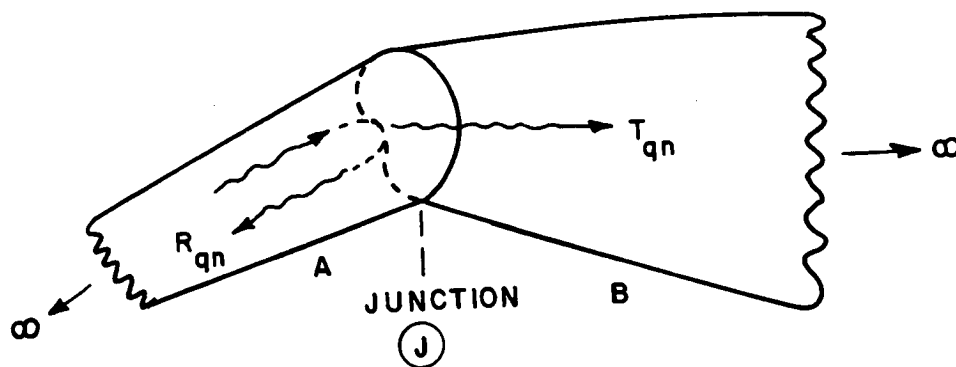


Figure 3.20. A waveguide junction J between two sections.

propagation axis of the waveguide section A; it is also assumed that the modal field expressions are orthogonal over the waveguide cross-section described by the coordinates transverse to n .

The modal fields in region A propagating through the junction will undergo diffraction at the junction and give rise to a set of reflected modes in region A which then propagate away from the junction. The relationship between the reflected and incident mode amplitudes is expressed by the reflection matrix $[S_{AA}]$. The fields entering back into the section A as reflected modes are produced entirely via edge diffraction of the incident modal rays. Let the n^{th} modal field incident at J be represented by

$$\bar{E}_n^+ = (\bar{E}_{nt} + \bar{E}_{nn}) e^{-j\beta_n n} \quad (3.31)$$

where, as before, a compact index "n" is used for double modal indices and \bar{E}_{nt} is the transverse component of the incident electric modal field vector; whereas, \bar{E}_{nn} is the axial component. Also, $e^{-j\beta_n n}$ denotes the propagation phase factor. The superscript (\pm) denotes a mode propagating in the $(\pm n)$ direction.

Let the ray-optical part of the incident modal field undergoing diffraction at the junction be represented by $\bar{E}_{op,ni}^+$. (Note that $\bar{E}_{op,ni}^+$ is the part of the incident field which is polarized perpendicular to the ray trajectory). As explained before, there might be more than one modal ray "incident" at a point of discontinuity on the junction for a given mode; therefore, the index "i" refers to any one of the "incident" modal rays associated with the n^{th} mode. For example, in the

parallel-plate waveguide only one of the two modal ray plane waves is "incident" at the upper or lower edges, therefore, $i=1$ in that case. On the other hand, the four plane wave ray fields in the rectangular waveguide are also made up of a pair of rays that propagate toward each of the four edges as well as a pair of rays that propagate away from those edges. Thus, out of the four modal rays, there exists only one pair of modal rays which become "incident" at a given edge; therefore, the index "i" goes from $i=1$ to $i=2$. In the case of a circular waveguide, only the axially divergent modal rays are incident at the rim edge, so the index "i" takes the value 1. The modal rays in the 2-D linearly tapered, and in the 3-D sectoral waveguide are similar to parallel-plate and rectangular waveguide modal rays, respectively; therefore, $i=1$ for the linearly tapered waveguides, and "i" goes from $i=1$ to $i=2$ for sectoral waveguides. Finally, the situation in an annular waveguide is clear from Figure 3.19, where the index $i=1$ is used in the case of modal rays that bounce from both walls because there is only one modal ray that is incident on the discontinuities at inner and outer shells, respectively; however, for the whispering gallery modes, there is no modal ray incident at a discontinuity on the inner shell (and $i=0$ in the inner shell) and there is only one "incident" modal ray for a discontinuity on the outer shell (and thus $i=1$ for the outer shell). The corresponding "incident" ray optical magnetic field is calculated from:

$$\vec{H}_{op,ni}^+ = Y_0 \hat{r}_{ni} \times \vec{E}_{op,ni}^+ \quad (3.32)$$

where \hat{r}_{ni} is the unit vector in the direction of propagation of the i^{th} "incident" modal ray associated with the n^{th} modal field.

As in the calculation of $[S_{11}]$, the ECM will be used to determine the entries (or elements) of the reflection matrix $[S_{AA}]$. According to the GTD, the diffracted field at a point P, which as shown in Figure 3.21 is produced by the diffraction at a point Q located at the discontinuity is given by

$$\begin{aligned} \bar{E}^d(P) = & \sum_{i=1}^N \bar{E}_{op,ni}^+(Q) \cdot [\hat{\beta}_{oni} \hat{\beta} D_s(\psi_{ni}', \psi; \tilde{\beta}_{oni}, \tilde{\beta}, \alpha(Q)) \\ & + \hat{\psi}_{ni}' \hat{\psi} D_h(\psi_{ni}', \psi; \tilde{\beta}_{oni}, \tilde{\beta}, \alpha(Q))] \sqrt{\frac{\rho}{s(s+\rho)}} e^{-jks} \end{aligned} \quad (3.33)$$

where a total of N "incident" modal rays are assumed to exist for the n^{th} mode. The diffraction coefficients D_h and the angles of incidence and diffraction are defined as before. The unit vectors $\hat{\beta}_{oni}$, $\hat{\beta}$, $\hat{\psi}_{ni}'$

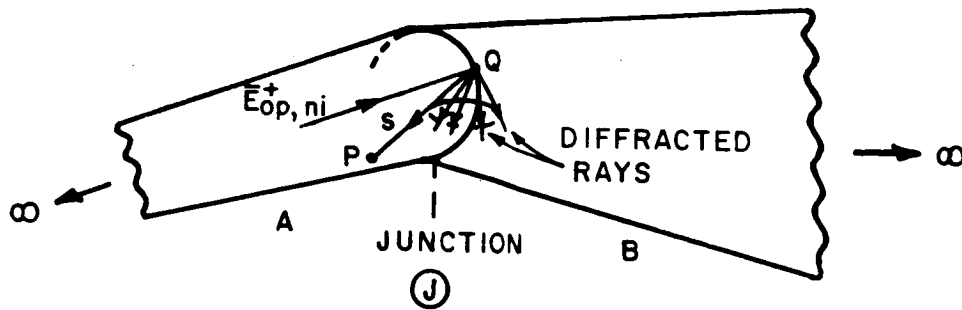


Figure 3.21. Diffraction of modal rays at the junction discontinuity.

and $\hat{\psi}$ are in their respective increasing angle directions. The distance from Q to P is shown by s, and ρ is the caustic distance for the diffracted rays as described in [26].

The diffracted field of (3.33) may be viewed as being generated by equivalent currents located along the rim of the discontinuity if $\rho \gg s$. However, the equivalent currents in this case will be assumed to radiate in the presence of a waveguide obtained by the geometric extension of the walls of section A, as shown in Figure 3.22. It is noted that the equivalent electric edge currents would be shorted out if they were to radiate in the presence of the waveguide walls. Therefore, in the present work the equivalent edge sources are only of the magnetic type, and they radiate within the waveguide. This is different from the previous works which employ equivalent electric and magnetic line sources in free space [10,14].

The equivalent currents are equivalent magnetic line sources and magnetic line dipoles given by [34]

$$\bar{M}_\ell(Q) = \sum_{i=1}^N \bar{M}_\ell^i(Q) = -\hat{\ell}' \sum_{i=1}^N \frac{1}{Y_0} \sqrt{\frac{8\pi}{jk}} (\bar{H}_{op,ni}^+ \cdot \hat{\ell}') \frac{D_h(\psi_{ni}', \psi; \tilde{\beta}_{oni}, \tilde{\beta}, \alpha(Q))}{2 \sqrt{\sin \tilde{\beta}_{oni} \sin \tilde{\beta}}} \quad (3.34)$$

and

$$\begin{aligned} \bar{M}_d(Q) = \sum_{i=1}^N \bar{M}_d^i(Q) = \sum_{i=1}^N -\sqrt{\frac{8\pi}{jk}} (\bar{E}_{op,ni}^+ \cdot \hat{\ell}') \frac{D_s(\psi_{ni}', \psi; \tilde{\beta}_{oni}, \tilde{\beta}, \alpha(Q))}{2 |\sin \psi| \sqrt{\sin \tilde{\beta}_{oni} \sin \tilde{\beta}}} \\ \cdot [\hat{n} \sqrt{1 - (\hat{\ell}' \cdot \hat{r}_{ni})^2} + \hat{n} \times \hat{n} (\hat{\ell}' \cdot \hat{r}_{ni}) \cos \psi] \end{aligned} \quad (3.35)$$

where \hat{x}' is the unit vector along the rim of the junction and \hat{n} is the unit vector normal to the walls of the uniform waveguide of Figure 3.22 at the junction ① and pointing into the waveguide region. The derivation of the expression for equivalent magnetic line dipole is included in Appendix J. The factor 1/2 is included in the expressions since the equivalent sources are radiating in the presence of waveguide walls.

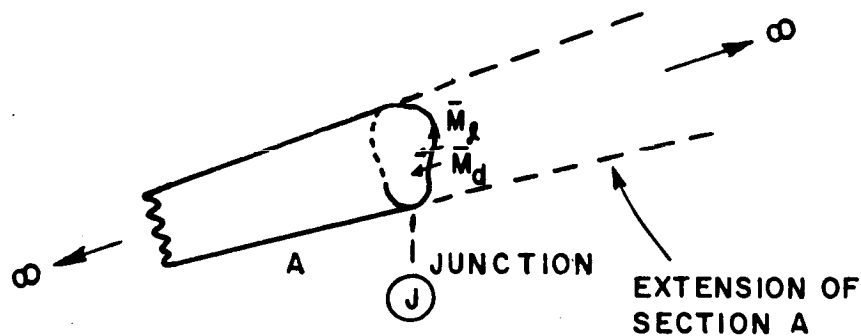


Figure 3.22. Excitation of modes by equivalent sources \vec{M}_l and \vec{M}_d .

The excitation of the modal fields due to these sources can be obtained by employing the usual reciprocity theorem as described in Appendix G. However, this method must be employed here with a slight modification because of the use of "equivalent" currents \bar{M}_ℓ and \bar{M}_d which excite the modes; that modification is consistent with reciprocity and so requires that the excitation of the q^{th} mode with modal ray angles $\psi_{qi} (i=1, \dots, N)$ is due only to the rays diffracted in those directions. Therefore, in the expressions for the equivalent sources of (3.34) and (3.35) appropriate angles are used to obtain:

$$\bar{M}_\ell(Q) = \hat{\ell}' \sum_{i=1}^N \frac{1}{Y_0} \sqrt{\frac{8\pi}{jk}} (\bar{H}_{op,ni}^+ \cdot \hat{\ell}') \frac{D_h(\psi_{ni}', \psi_{qi}; \tilde{\beta}_{oni}, \tilde{\beta}_{qi}, \alpha(Q))}{2 \sqrt{\sin \tilde{\beta}_{oni} \sin \tilde{\beta}_{qi}}} \quad (3.36)$$

and

$$\begin{aligned} \bar{M}_d(Q) = & \sum_{i=1}^N -\sqrt{\frac{8\pi}{jk}} (\bar{E}_{op,ni}^+ \cdot \hat{\ell}') \frac{D_s(\psi_{ni}', \psi_{qi}; \tilde{\beta}_{oni}, \tilde{\beta}_{qi}, \alpha(Q))}{2 |\sin \psi_{qi}| \sqrt{\sin \tilde{\beta}_{oni} \sin \tilde{\beta}_{qi}}} \\ & \cdot [\hat{n} \sqrt{1 - (\hat{\ell}' \cdot \hat{r}_{ni})^2} + \hat{n} \times \hat{n} (\hat{\ell}' \cdot \hat{r}_{ni}) \cos \psi_{qi}] \end{aligned} \quad (3.37)$$

Applying the result in Appendix G, one then obtains the expression for the reflection coefficients as follows:

$$R_{qn} = \frac{1}{2 \iint_S \bar{E}_{qt} \times \bar{H}_{qt}^* \cdot \hat{n} h_Y h_\xi \, dy d\xi} \int_{\text{rim}} \bar{H}_q^+ \cdot (\bar{M}_\ell + \bar{M}_d) \, d\ell' \quad (3.38)$$

where h_γ and h_ξ are the metric coefficients (scale factors) for the γ and ξ coordinates, respectively, and S is the cross sectional area of section A.

The reflection coefficients above give the qn^{th} element of the scattering matrix $[S_{AA}]$.

The result in (3.37) can be improved for small guide widths by including the effects of multiply diffracted rays at the aperture of the junction; that effect can be incorporated as an additional term in the above expression [10].

Examples;

- a) Modal reflection at the open-end of a parallel-plate waveguide:

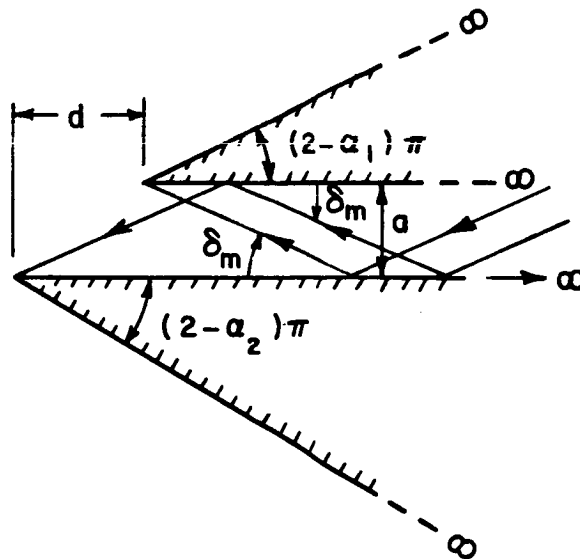


Figure 3.23. Open-ended parallel-plate waveguide.

Following the analysis presented in this section and the modal field expressions given in Appendix B, one finds that the reflection coefficients relating the amplitude of the q^{th} reflected mode to the amplitude of the m^{th} incident mode are explicitly given by

i) TM_z case:

$$R_{qm} = \frac{\sqrt{2\pi k}}{2\sqrt{\beta_m\beta_q}} \frac{e^{-j\pi/4}}{a\sqrt{\epsilon_{om}\epsilon_{oq}}} \left\{ (-1)^{m+q} D_h(\delta_m, \delta_q, \tilde{\beta}_0 = \frac{\pi}{2}, \tilde{\beta} = \frac{\pi}{2}, \alpha_1) + e^{-j(\beta_m + \beta_q)d} D_h(\delta_m, \delta_q, \tilde{\beta}_0 = \frac{\pi}{2}, \tilde{\beta} = \frac{\pi}{2}, \alpha_2) \right\} \quad (3.39)$$

where ϵ_{om} , β_m and δ_n for the n^{th} mode are as defined in Appendix A and the angles α_1 , and α_2 are shown in Figure 3.23. Also shown in the figure are the waveguide width (a) and the staggering distance (d).

ii) TE_z case:

$$R_{qm} = - \frac{\sqrt{2\pi k}}{2\sqrt{\beta_m\beta_q}} \frac{e^{-j\pi/4}}{a} \left[(-1)^{m+q} D_s(\delta_m, \delta_q, \tilde{\beta}_0 = \frac{\pi}{2}, \tilde{\beta} = \frac{\pi}{2}, \alpha_1) + e^{-j(\beta_m + \beta_q)d} D_s(\delta_m, \delta_q, \tilde{\beta}_0 = \frac{\pi}{2}, \tilde{\beta} = \frac{\pi}{2}, \alpha_2) \right] \quad (3.40)$$

The results in (3.39) and (3.40) agree with that obtained in [10] via a different procedure.

b) Modal reflection from the open-end of a rectangular waveguide:

The geometry and the modal field expressions are presented in Appendix A. The elements of the reflection coefficients which relate the pq^{th} reflected mode amplitude to nm^{th} incident mode amplitude are calculated via (3.38) and given explicitly as follows:

$$\begin{aligned}
 R_{pq;nm} = & \frac{1}{4} \sqrt{\frac{\pi}{2jk}} \frac{[1+(-1)^{n+p}][1+(-1)^{m+q}]}{4} \frac{N_{nm} N_{pq} Y_{nm} Y_{pq}}{Y_o} \\
 & \left\{ \frac{a \delta_{np}}{\sqrt{\sin \beta_{oh} \sin \beta_h}} \left[D_h(\psi_h, \psi'_h) V_{nm} V_{pq} (1 - \delta_{no}) \right. \right. \\
 & + D_s(\psi_h, \psi'_h) \frac{Y_o U_{nm}}{Y_{nm} \sin \psi_h} \left(\epsilon_{on} W_{pq} \frac{p_a^2 + q_b^2}{\beta_{pq}} \sin \beta_h - \frac{V_{pq} p_a}{k} \cos \psi_h \right) \left. \right] \\
 & + \frac{b \delta_{mq}}{\sqrt{\sin \beta_{ov} \sin \beta_v}} [D_h(\psi_v, \psi'_v) U_{nm} U_{pq} (1 - \delta_{mo}) \\
 & + D_s(\psi_v, \psi'_v) \frac{Y_o V_{nm}}{Y_{nm} \sin \psi_v} \left(\epsilon_{om} W_{pq} \frac{p_a^2 + q_b^2}{\beta_{pq}} \sin \beta_v - \frac{U_{pq} q_b}{k} \cos \psi_v \right) \left. \right] \left. \right\} \quad (3.41)
 \end{aligned}$$

where

$$D_{S,h}(\psi, \psi') = \frac{-e^{-j\pi/4}}{2\sqrt{2\pi k}} \left[\sec\left(\frac{\psi - \psi'}{2}\right) \mp \sec\left(\frac{\psi + \psi'}{2}\right) \right] \quad (3.42)$$

$$\delta_{pq} = \begin{cases} 0 & p \neq q \\ 1 & p = q \end{cases} \quad (3.43)$$

$$\epsilon_{on} = \begin{cases} 2 & n=0 \\ 1 & n \neq 0 \end{cases} \quad (3.44)$$

$$\sin \beta_{oh} = [1 - (n_a/k)^2]^{1/2} \quad (3.45)$$

$$\sin \beta_h = [1 - (p_a/k)^2]^{1/2} \quad (3.46)$$

$$\sin \beta_{ov} = [1 - (m_b/k)^2]^{1/2} \quad (3.47)$$

$$\sin \beta_v = [1 - (q_b/k)^2]^{1/2} \quad (3.48)$$

$$\cos(\psi_h) = \frac{\beta_{nm}/k}{\sin \beta_{oh}} \quad (3.49)$$

$$\cos(\psi_h) = \frac{\beta_{pq}/k}{\sin \beta_h} \quad (3.50)$$

$$\cos(\psi_v) = \frac{\beta_{nm}/k}{\sin \beta_{ov}} \quad (3.51)$$

$$\cos(\psi_v) = \frac{\beta_{pq}/k}{\sin \beta_v} \quad (3.52)$$

$$V_{nm} = \begin{cases} n_a & \text{for TE}_{nm} \text{ mode} \\ -m_b & \text{for TM}_{nm} \text{ mode} \end{cases} \quad (3.53)$$

$$U_{nm} = \begin{cases} m_b & \text{for TE}_{nm} \text{ mode} \\ n_a & \text{for TM}_{nm} \text{ mode} \end{cases} \quad (3.54)$$

$$W_{nm} = \begin{cases} 1 & \text{for TE}_{nm} \text{ mode} \\ 0 & \text{for TM}_{nm} \text{ mode} \end{cases} \quad (3.55)$$

$$p_a = \frac{p\pi}{a} \quad (3.56)$$

$$q_b = \frac{q\pi}{b} \quad (3.57)$$

N_{nm} , Y_{nm} , n_a , and m_b are as defined in Appendix A.

The result in (3.41) is plotted for different incident and reflected mode values by Dr. C.D. Chuang of the Ohio State University, ElectroScience Laboratory and presented in [35]. Some of those results are shown in Figures 3.24 and 3.25. In Figure 3.25, the calculation is compared with measurements [36]. In this case, the waveguide dimensions allow only the dominant TE_{10} mode to propagate. It is noted that, even though at such low frequencies the neglected multiple order diffractions at the open end become important, the comparison between the measurement and calculation is quite reasonable. One would expect the comparison to get better as the frequency increases.

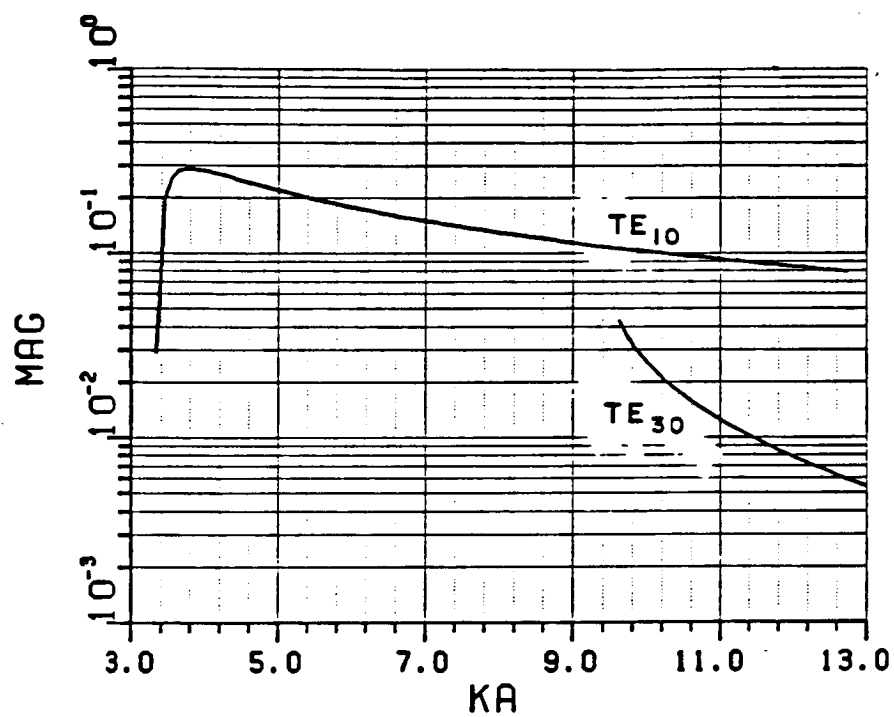


Figure 3.24. Modal reflection coefficients due to an incident TE_{10} mode in an open-ended rectangular waveguide ($a=2b$).

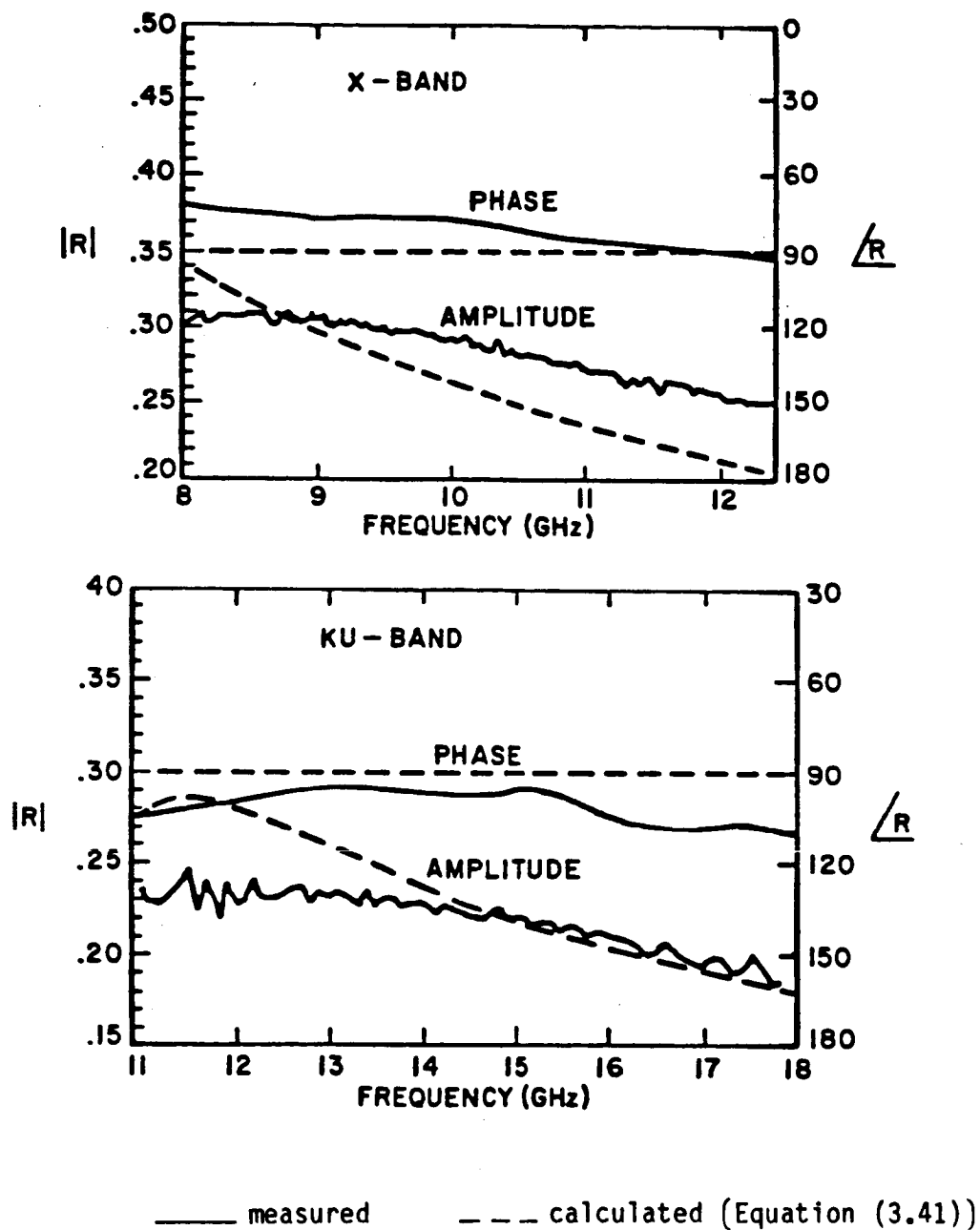


Figure 3.25. Comparisons of the calculated and measured reflection coefficients in an X-band and KU-band open-ended rectangular waveguide.

c) Reflection of TE_{10} mode from an \bar{E} -plane circular bend in a rectangular waveguide:

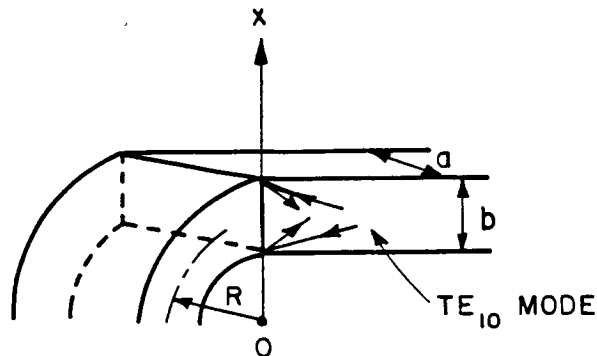


Figure 3.26. Junction between a rectangular waveguide and a circular bend of rectangular cross section.

The dimensions of the rectangular waveguide shown by "a" and "b" allow only TE_{10} mode to propagate. This rectangular waveguide is joined to a uniform circular bend of rectangular cross section, as shown in Figure 3.26. The mean radius of the circular bend is shown by R. In this case the edge diffraction coefficients in the expressions for equivalent sources given by (3.36) and (3.37) will have to be modified, because the diffraction is now due to a discontinuity in the radius of curvature as shown in Figure 3.26. One can employ the diffraction coefficients presented in [37] for this case; they are expressed as follows:

$$D_{sh}^c(v_1, v_2) = e^{+j\pi/4} \sqrt{\frac{2}{\pi k}} \quad (F \neq G) \quad (3.58)$$

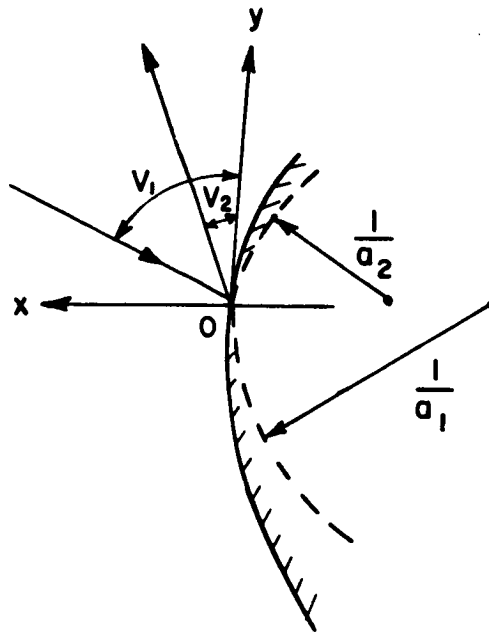


Figure 3.27. A discontinuity in the radius of curvature.

where

$$F = -\frac{a_2 - a_1}{2k} \frac{1 + \cos(v_1 + v_2)}{(\cos v_1 + \cos v_2)^3} \quad (3.59)$$

and

$$G = -\frac{a_2 - a_1}{2k} \frac{1 + \cos(v_1 - v_2)}{(\cos v_1 + \cos v_2)^3} \quad (3.60)$$

In (3.59) and (3.60), a_1 and a_2 refer to the curvature of the surfaces which make up the discontinuity, v_1 is the angle of the incidence and v_2 is the angle of diffraction, measured from the tangent direction (\hat{y} -direction) as shown in Figure 3.27.

The expression in (3.41) for the reflection coefficient can be applied here together with the diffraction coefficients of (3.58) to calculate the reflection of the TE_{10} mode. This calculation is done and plotted in Figures 3.28 and 3.29 (denoted by GTD) as a function of radius R for two different values of the waveguide height " b ". This ray optical result is found to be independent of the waveguide width " a " and is not varying appreciably with the value of " b " for comparably large values of R . A result based on the variational approach for the equivalent circuit parameters is presented in [38]. The approximate reflection coefficient based on that approach in [38] is also presented in Figures 3.28 and 3.29. That reflection coefficient is likewise very insensitive to the dimension " a " for the selected range of parameters. However, its magnitude increases rapidly with the dimension " b " which is unexpected based on the physics of the problem.

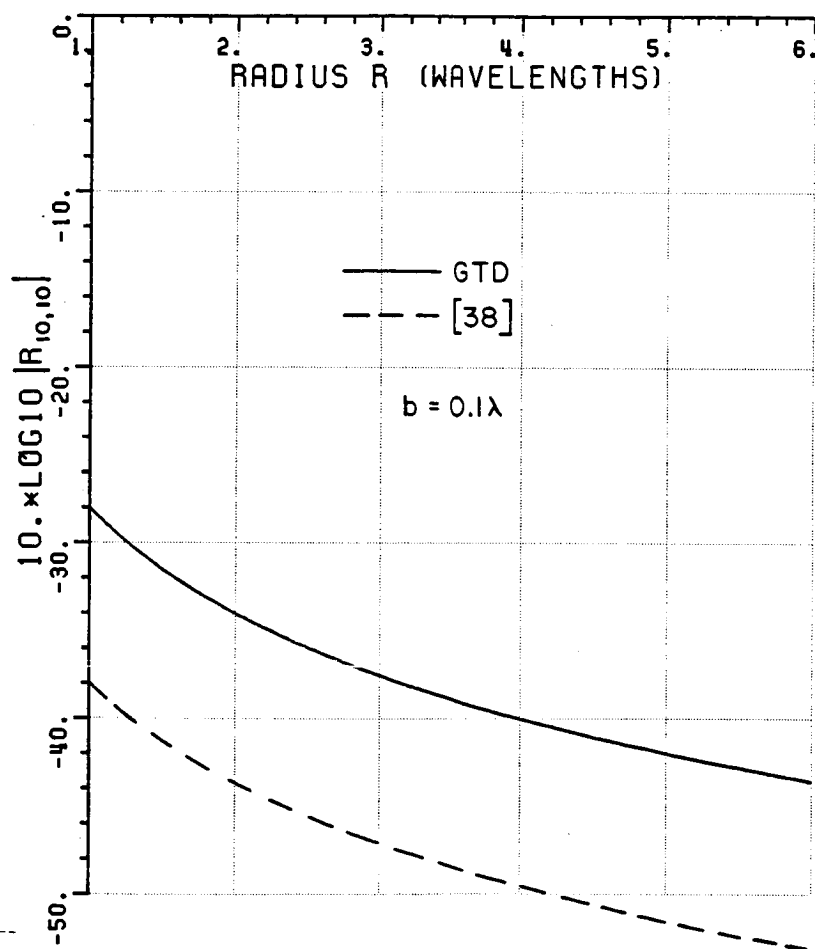


Figure 3.28. Reflection coefficient for the TE_{10} mode in a rectangular waveguide due to an \bar{E} -plane circular bend.

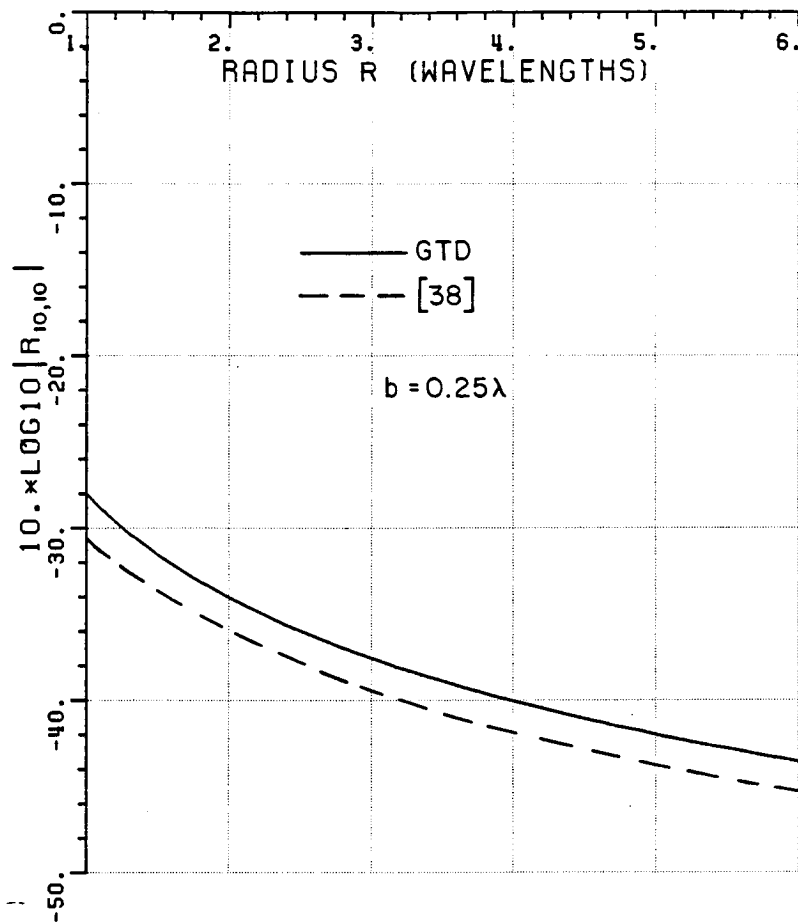


Figure 3.29. Reflection coefficient for the TE_{10} mode in a rectangular waveguide due to an \bar{E} -plane circular bend.

- d) Modal reflection from a junction between two linearly tapered waveguides:

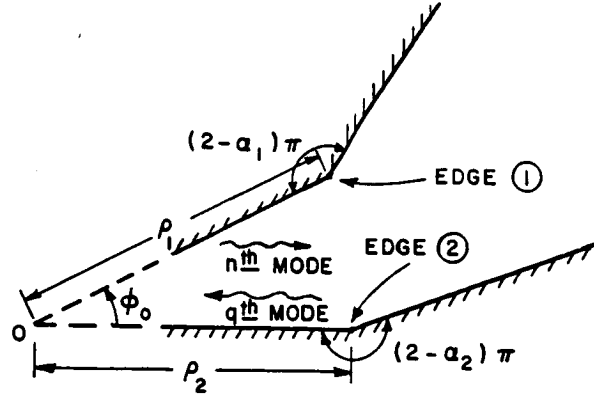


Figure 3.30. Junction between two linearly tapered waveguides.

The reflection coefficients for this 2-D configuration can be determined employing the modal field expressions of Appendix D in (3.38). The amplitude of the q^{th} reflected mode due to an n^{th} incident mode is given by

- i) TE_x case:

$$R_{qn} = \frac{\sqrt{2\pi k} e^{-j\pi/4}}{\sqrt{\epsilon_{on}} \epsilon_{oq} 2\phi_0} \left[(-1)^{q+n} \frac{D_h(\theta_{1n}, \theta_{1q}; \tilde{\beta}_0 = \frac{\pi}{2}, \tilde{\beta} = \frac{\pi}{2}, \alpha_1)}{\sqrt{\beta_n(\rho_1)\beta_q(\rho_1)} \rho_1} \right. \\ \left. + \frac{e^{-j(\beta_n(\rho_2)+\beta_q(\rho_2))\rho_2 + j(\beta_n(\rho_1)+\beta_q(\rho_1))\rho_1}}{\sqrt{\beta_n(\rho_2)\beta_q(\rho_2)} \rho_2} D_h(\theta_{2n}, \theta_{2q}; \tilde{\beta}_0 = \frac{\pi}{2}, \tilde{\beta} = \frac{\pi}{2}, \alpha_2) \right] \quad (3.61)$$

ii) TM_x case:

$$R_{qn} = \frac{\sqrt{2\pi k} e^{-j\pi/4}}{2\phi_0} \left[\frac{(-1)^{q+n} D_s(\theta_{1n}, \theta_{1q}; \tilde{\beta}_0 = \frac{\pi}{2}, \tilde{\beta} = \frac{\pi}{2}, \alpha_1)}{\sqrt{\beta_n(\rho_1)\beta_q(\rho_1)} \rho_1} \right. \\ \left. + \frac{e^{-j(\beta_n(\rho_2)+\beta_q(\rho_2))\rho_2 + j(\beta_n(\rho_1)+\beta_q(\rho_1))\rho_1}}{\sqrt{\beta_n(\rho_2)\beta_q(\rho_2)} \rho_2} D_s(\theta_{2n}, \theta_{2q}; \tilde{\beta}_0 = \frac{\pi}{2}, \tilde{\beta} = \frac{\pi}{2}, \alpha_2) \right] \quad (3.62)$$

In (3.61) and (3.62), the parameters ϵ_{on} , β_n , ϕ_0 and ρ_1, ρ_2 are defined in Appendix D. The angles α_1 , and α_2 are determined from the wedge angles as shown in Figure 3.30, and the modal ray angles θ_{1n} and θ_{2n} for the n^{th} mode is calculated via the expression given in Figure D.2, for edges ① and ②, respectively.

e) Modal reflection from the junction of two sectoral waveguides:

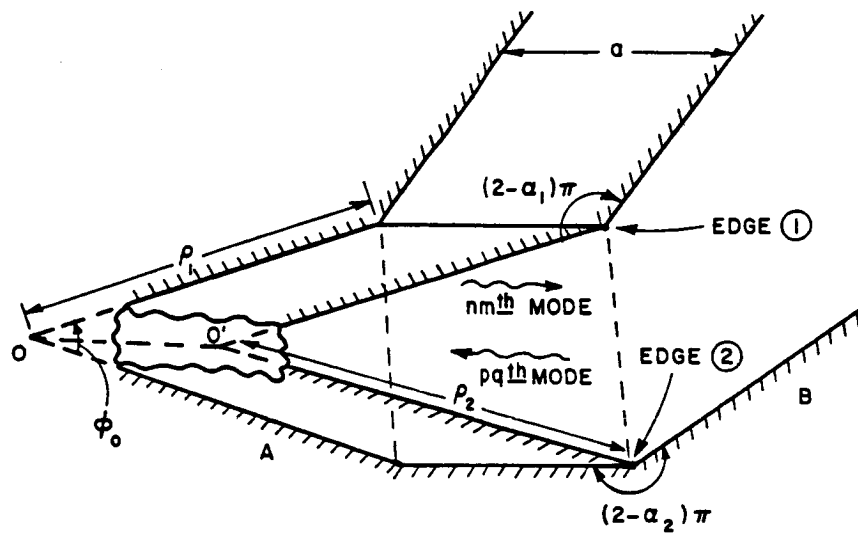


Figure 3.31. Junction between two sectoral waveguides.

The modal field expressions have been given in Appendix C for TE_x and TM_x type of modes. The ray interpretation of these modes is also discussed in the same appendix. The reflection coefficients are presented below for TE_x and TM_x incident modes.

i) TE_x case:

In order to excite the pq^{th} reflected mode, equivalent magnetic line sources due to an incident nm^{th} mode are located at edges ① and ② and they are given by

$$\bar{M}_{\ell 1} = \hat{x} \sum_{i=1}^2 Y_0 \sqrt{\frac{8\pi}{jk}} \left[\frac{L_{nm} Y_0 (k^2 - (\frac{n\pi}{a})^2)}{jk \sqrt{\rho_1} \beta_{nm}(\rho_1)} \right] \left\{ \frac{(-1)^m}{(1)} \right\} \frac{1}{2} (-1)^i e^{j(\frac{n\pi}{a})x(i-1)}$$

$$\left[e^{-j\beta_{nm}(\rho_1)\rho_1} \right] \frac{D_h(\theta_{1nm}^x, \theta_{1pq}^x; \tilde{\beta}_n, \tilde{\beta}_p, \alpha_1)}{4 \cdot j} \quad (3.63)$$

The upper characters correspond to edge ① and the lower ones give the value of the equivalent source at edge ②, as illustrated in Figure 3.31. The modal ray angles (corresponding to nm^{th} mode) θ_{1nm}^x and θ_{2nm}^x present in the diffraction coefficients are determined via the expression given in Figure C.2 for edges ① and ②, respectively. Finally, the acute angle β_n is determined using $\cos \beta_n = \frac{n\pi}{ka}$.

The amplitude of the reflected pq^{th} mode due to an nm^{th} incident mode is obtained as follows:

$$R_{pq,nm} = \sqrt{\frac{\pi}{2jk}} \frac{\sqrt{k^2 - (\frac{n\pi}{a})^2} \sqrt{k^2 - (\frac{p\pi}{a})^2}}{k \sqrt{\epsilon_{on} \epsilon_{om} \epsilon_{op} \epsilon_{oq}}} \phi_0 \delta_{np} (1 - \delta_{no})$$

$$\left[\frac{(-1)^{q+m} D_h(\theta_{1nm}^x, \theta_{1pq}^x; \tilde{\beta}_n, \tilde{\beta}_p, \alpha_1)}{\sqrt{\beta_{nm}(\rho_1) \beta_{pq}(\rho_1)} \rho_1} \right. \\ \left. + \frac{e^{-j(\beta_{nm}(\rho_2) + \beta_{pq}(\rho_2))\rho_2 + j(\beta_{nm}(\rho_1) + \beta_{pq}(\rho_1))\rho_1}}{\sqrt{\beta_{nm}(\rho_2) \beta_{pq}(\rho_2)} \rho_2} D_h(\theta_{2nm}^x, \theta_{2pq}^x; \tilde{\beta}_n, \tilde{\beta}_p, \alpha_2) \right] \quad (3.64)$$

ii) TM_x case:

In this case, the equivalent magnetic line dipoles are located at edges ① and ② and are given by:

$$\bar{M}_{d1} = - \sum_{i=1}^2 \frac{2 \sqrt{8\pi}}{jk} \frac{L_{nm}}{jk} \frac{(k^2 - (\frac{n\pi}{a})^2)}{\sqrt{\beta_{nm}(\rho_1)} \rho_1} \frac{\begin{Bmatrix} (-1)^m \\ (-1) \end{Bmatrix}}{2} e^{-j\beta_{nm}(\rho_1)\rho_1 + j(\frac{n\pi}{a})x(i-1)}$$

$$\frac{D_s(\theta_{1nm}^x, \theta_{1pq}^x; \tilde{\beta}_n, \tilde{\beta}_p, \alpha_1)}{4 \sin \theta_{1pq}^x} \left[\hat{\rho} \sqrt{1 - (\frac{n\pi}{ka})^2} \mp \hat{x} \left(\frac{n\pi}{ka} \right) \cos \theta_{1,pq}^x \right] \quad (3.65)$$

For the modes away from cut-off, the \hat{x} component of the magnetic dipoles are small compared to the radial ($\hat{\rho}$) component. Therefore, in the calculations it is assumed that the equivalent line dipoles have a radial orientation and excite a pq^{th} reflected mode due to an incident

nm^{th} mode. It is noted that the equivalent currents of (3.65) can excite a TM_x mode as well as a TE_x mode. Therefore, the reflection coefficient corresponding to a pq^{th} type TM_x mode will be represented by $R_{pq,nm}^{ee}$; whereas the reflection coefficient corresponding to a pq^{th} type TE_x mode will be represented by $R_{pq,nm}^{he}$. The explicit expressions for $R_{pq,nm}^{ee}$ and $R_{pq,nm}^{he}$ are presented below:

$$R_{pq,nm}^{ee} = -\sqrt{\frac{8\pi}{jk}} \frac{q\pi}{\phi_0} \frac{\sqrt{k^2 - (\frac{n\pi}{a})^2}}{\sqrt{k^2 - (\frac{p\pi}{a})^2}} \frac{\delta_{np} \epsilon_{on}}{\sqrt{\epsilon_{on} \epsilon_{om} \epsilon_{op} \epsilon_{oq}} \phi_0}$$

$$\left[\begin{aligned} & D_s(\theta_{1nm}^x, \theta_{1pq}^x; \tilde{\beta}_n, \tilde{\beta}_p, \alpha_1) \\ & (-1)^{q+m} \frac{D_s(\theta_{1nm}^x, \theta_{1pq}^x; \tilde{\beta}_n, \tilde{\beta}_p, \alpha_1)}{\sqrt{\beta_{nm}(\rho_1) \beta_{pq}(\rho_1)} \rho_1^2 \sin \theta_{1pq}^x} \\ & + \frac{e^{-j(\beta_{nm}(\rho_2) + \beta_{pq}(\rho_2))\rho_2 + j(\beta_{nm}(\rho_1) + \beta_{pq}(\rho_1))\rho_1}}{\sqrt{\beta_{nm}(\rho_2) \beta_{pq}(\rho_2)} \rho_2^2 \sin \theta_{2pq}^x} D_s(\theta_{2nm}^x, \theta_{2pq}^x; \tilde{\beta}_n, \tilde{\beta}_p, \alpha_2) \end{aligned} \right] \quad (3.66)$$

$$R_{pq}^{he} = -\frac{p\pi}{a} \sqrt{\frac{2\pi}{jk}} \frac{\sqrt{k^2 - (\frac{n\pi}{a})^2}}{k \phi_0 \sqrt{\epsilon_{on} \epsilon_{om} \epsilon_{op} \epsilon_{oq}} \sqrt{k^2 - (\frac{p\pi}{a})^2}} \delta_{np} \epsilon_{on}$$

$$\left[\begin{aligned} & \beta_{pq}(\rho_1) D_s(\theta_{1nm}^x, \theta_{1pq}^x; \tilde{\beta}_n, \tilde{\beta}_p, \alpha_1) \\ & (-1)^{m+q} \frac{\beta_{pq}(\rho_1) D_s(\theta_{1nm}^x, \theta_{1pq}^x; \tilde{\beta}_n, \tilde{\beta}_p, \alpha_1)}{2 \sin \theta_{1pq}^x \sqrt{\beta_{nm}(\rho_1) \beta_{pq}(\rho_1)} \rho_1} \\ & + e^{-j(\beta_{nm}(\rho_2) + \beta_{pq}(\rho_2))\rho_2 + j(\beta_{nm}(\rho_1) + \beta_{pq}(\rho_1))\rho_1} \\ & \frac{\beta_{pq}(\rho_2) D_s(\theta_{2nm}^x, \theta_{2pq}^x; \tilde{\beta}_n, \tilde{\beta}_p, \alpha_2)}{2 \sin \theta_{2pq}^x \sqrt{\beta_{nm}(\rho_2) \beta_{pq}(\rho_2)} \rho_2} \end{aligned} \right] \quad (3.67)$$

f) Reflection from the open end of a circular waveguide:

The geometry of the circular waveguide is shown in Figure 3.32. The modal expressions and their modal ray interpretation are left to Appendix F.

i) TE_z case:

The equivalent currents \bar{M}_ℓ and \bar{M}_d at the rim of the open end excite TE_z and TM_z modes. The reflection coefficient corresponding to a reflected TE_z (TM_z) mode will be represented by $R_{pq,nm}^{ee}$ ($R_{pq,nm}^{he}$). They are given by

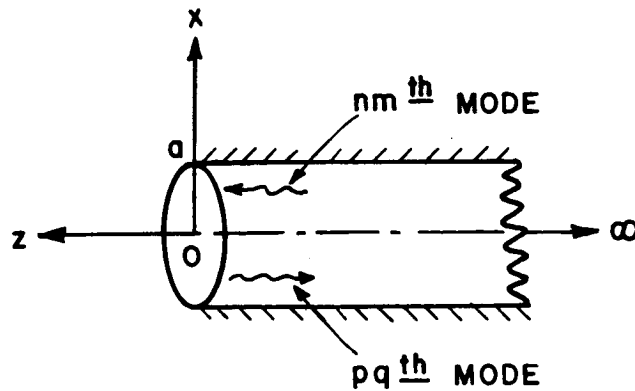


Figure 3.32. Open-ended semi-infinite circular waveguide.

$$R_{pq;nm}^{ee} = \frac{\pi k Z_o}{j4a} \frac{N_{pq} N_{nm} J_n(P'_{pq}) J_n(P'_{nm})}{\cos \delta_{pq} + \cos \delta_{nm}} [n_p \cos \delta_{pq} \cos \delta_{nm} \cdot f - k^2 a^2 \epsilon_{on} \sin \delta_{pq} \sin \delta_{nm} \cdot g] \delta_{np} \quad (3.68)$$

$$R_{pq,nm}^{he} = \frac{\pi k^2}{j4} \frac{N_{pq} N_{nm} J_n(P'_{pq}) J'_n(P_{nm})}{\cos \delta_{pq} + \cos \delta_{nm}} [\cos \delta_{pq} \sin \delta_{nm} \cdot f + \sin \delta_{pq} \cos \delta_{nm} \cdot g] \delta_{np} \quad (3.69)$$

where

$$f = \cos \frac{\delta_{pq}}{2} \cos \frac{\delta_{nm}}{2} [1 + 2 (\sec \delta_{pq} + \sec \delta_{nm}) \frac{AD}{1-AD}] \quad (3.70)$$

$$g = \sin \frac{\delta_{pq}}{2} \sin \frac{\delta_{nm}}{2} [1 - 2 (\sec \delta_{pq} + \sec \delta_{nm}) \frac{AC}{1-AC}] \quad (3.71)$$

$$A = (-1)^n \frac{e^{-j(2ka - \pi/4)}}{4\sqrt{\pi ka}} \quad (3.72)$$

$$C = 1 + \sum_{\ell=1}^{\infty} (jB)^{\ell} / \sqrt{\ell+1} \quad (3.73)$$

$$D = 1 + \sum_{\ell=1}^{\infty} (-jB)^{\ell} / \sqrt{\ell+1} \quad (3.74)$$

$$B = (-1)^n \frac{1}{2} e^{-j2ka} \quad (3.75)$$

It is noted that the effect of all the multiply interacting rays across the aperture are included in the above expressions for the circular waveguide opening; in particular, that information is contained in the "f" and "g" terms given above.

ii) TM_z case:

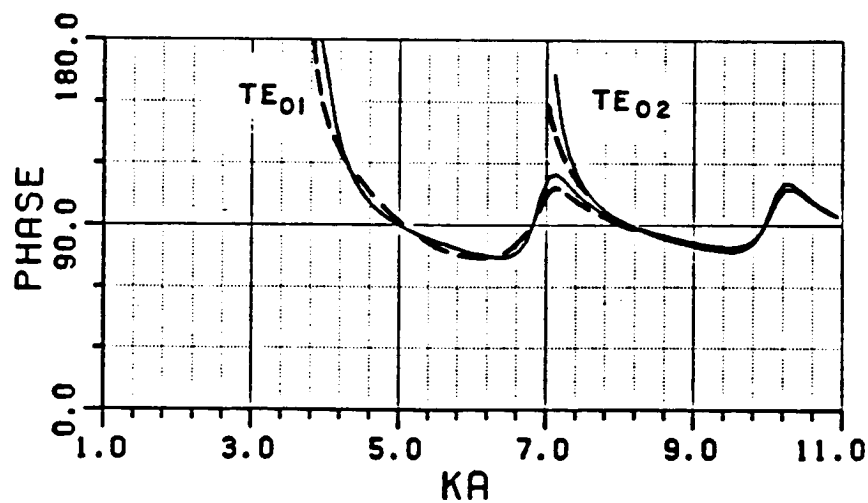
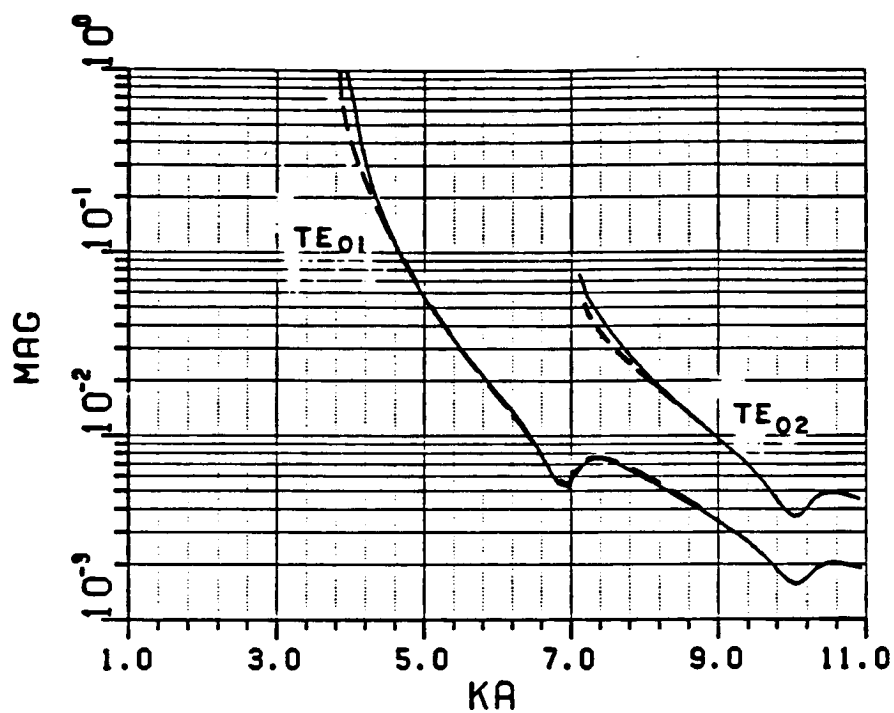
Similar to the TE_z case, the reflected modes may be TM_z or TE_z type. The reflection coefficient corresponding to a reflected TM_z (TE_z) mode will be represented by $R_{pq,nm}^{hh}$ ($R_{pq,nm}^{eh}$). The expression for $R_{pq,nm}^{eh}$ is the same as (3.69), namely;

$$R_{pq,nm}^{eh} = R_{pq,nm}^{he} \quad (3.76)$$

and

$$R_{pq,nm}^{hh} = \frac{\pi k Y_0 N_{pq} N_{nm} J'_n(P_{pq}) J'_n(P_{nm})}{j 4 a \cos \delta_{pq} + \cos \delta_{nm}} \left[k^2 a^2 \epsilon_{on} \sin \delta_{pq} \sin \delta_{nm} \cdot f - n^2 \cos \delta_{pq} \cos \delta_{nm} \cdot g \right] \delta_{np} \quad (3.77)$$

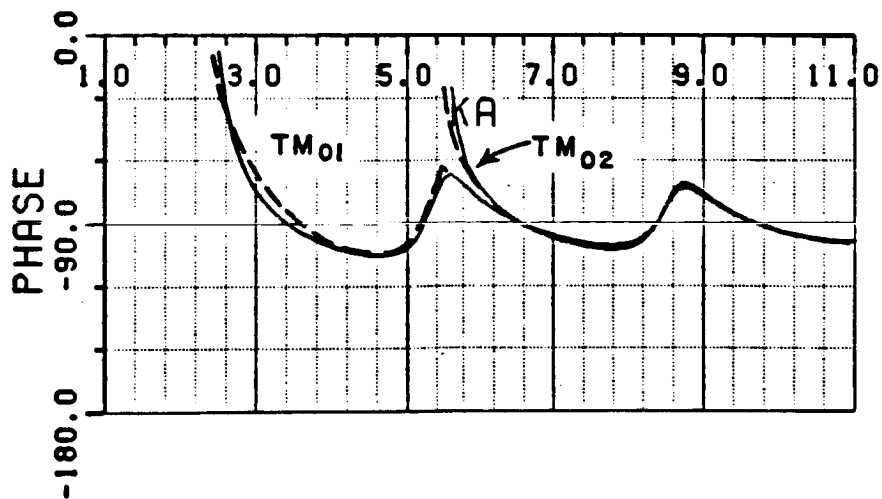
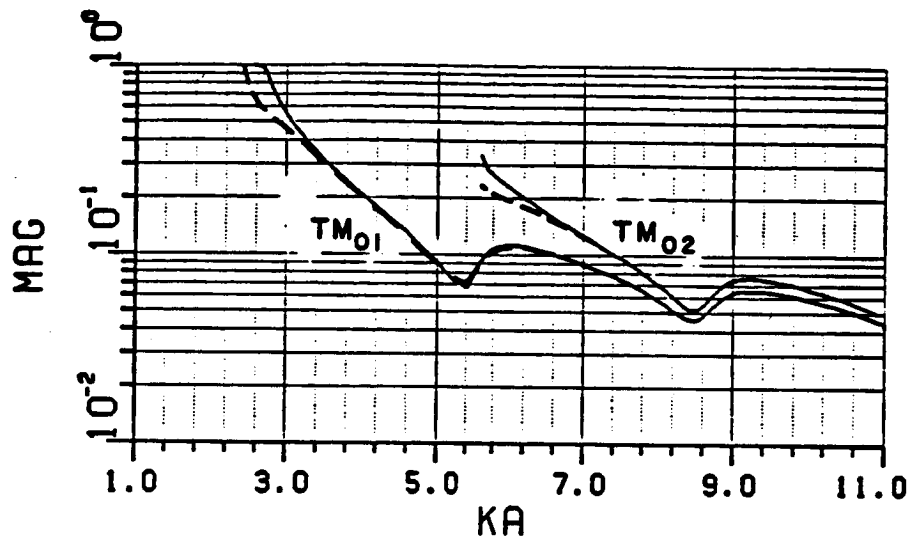
The results in (3.68) through (3.77) are compared with the exact Wiener-Hopf solutions for various modal reflections at the open-end of a circular waveguide. The comparisons are shown in Figures 3.33 through 3.35. The ray-optical solution closely approximates the exact solution especially at higher frequencies.



—— present solution

---- Wiener-Hopf [28]

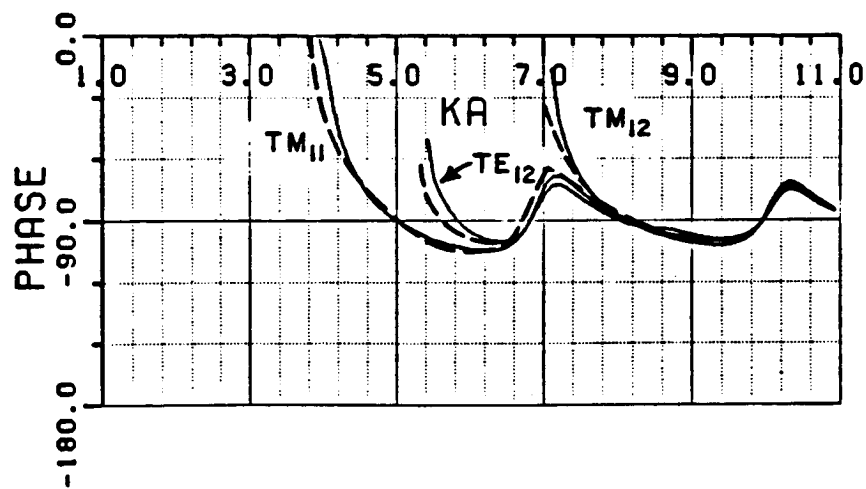
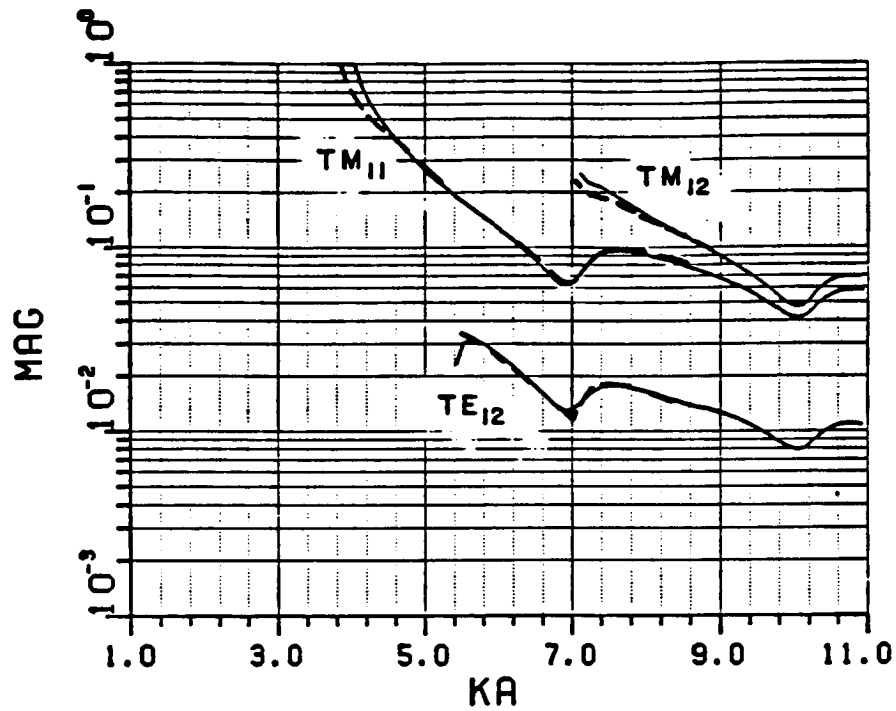
Figure 3.33. Modal reflection coefficients due to an incident TE_{01} mode in an open-ended circular waveguide.



—— present solution

--- Wiener-Hopf [28]

Figure 3.34. Modal reflection coefficients due to an incident TM_{01} mode in an open-ended circular waveguide.



— present solution - - - - Wiener-Hopf [28]

Figure 3.35. Modal reflection coefficients due to an incident TM_{11} mode in an open-ended circular waveguide.

- g) Modal reflection in an annular waveguide terminated by a parallel-plate waveguide:

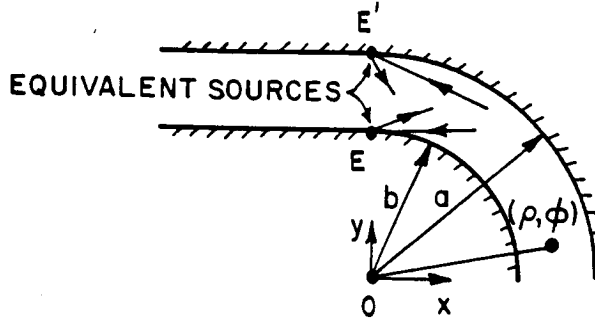


Figure 3.36. Junction between parallel-plate and annular waveguide sections.

In this example, the reflection coefficients corresponding to annular waveguide modes are derived by considering the discontinuity at the junction between an annular and a parallel-plate waveguide as shown in Figure 3.36. The annular waveguide has outer and inner shell radii shown by "a" and "b", respectively. The polar coordinates ρ and ϕ are used to define a point with respect to the center of the annular section. The geometry is assumed to be infinite in \hat{z} -direction, and in this example only the reflection of TE_z modes will be considered. The treatment of TM_z modes follows similar lines. The modal field expressions in the TE_z case are obtained from a magnetic field given by

$$\bar{H}_n^{\pm} = \mp \hat{z} A_n^h(k_a, k_b) f_n^h(k\rho) e^{-j\nu_n|\phi|} \quad (3.78)$$

so that

$$\bar{E}_n^{\pm} = \hat{\rho} \frac{1}{jk\rho Y_0} \frac{\partial}{\partial \phi} \bar{H}_n^{\pm} - \hat{\phi} \frac{1}{jkY_0} \frac{\partial}{\partial \rho} \bar{H}_n^{\pm} \quad (3.79)$$

In (3.78), the function $f_n^h(k\rho)$ is given by

$$f_n^h(k\rho) = H_{\nu_n}^{(2)'}(k\rho) \Big|_{\rho=b} H_{\nu_n}^{(1)}(k\rho) - H_{\nu_n}^{(1)'}(k\rho) \Big|_{\rho=b} H_{\nu_n}^{(2)}(k\rho) \quad (3.80)$$

where the primes denote differentiation with respect to the argument, and the ν_n 's are determined from

$$\frac{df_n^h}{d\rho} \Big|_{\rho=a} = 0 \quad . \quad (3.81)$$

The normalization factor $A_n^h(ka, kb)$ is used in (3.78) such that for a propagating mode one obtains

$$\frac{1}{2} \int_b^a \bar{E}_n^+ \times (\bar{H}_n^+)^* d\rho = 1 \quad . \quad (3.82)$$

To determine the normalization constants, one can generate the Green's function as done in Appendix E for TM_z polarization. Alternatively, one can also use the following identity [39]:

$$\int w_\nu(k\rho) W_\nu(k\rho) \frac{d\rho}{\rho} = -\frac{k\rho}{2\nu} \left[w_\nu' \frac{\partial W}{\partial \nu} - w_\nu \frac{\partial W'}{\partial \nu} \right] \quad (3.83)$$

where $w_\nu(k\rho)$ and $W_\nu(k\rho)$ are combinations of cylindrical functions (i.e., Bessel, Neumann, or Hankel functions) of order ν and primes denote differentiation with respect to the argument.

The equivalent magnetic line sources for the excitation of the q^{th} reflected mode are located at E and E' of Figure 3.36 and their values are given by

$$\bar{M}_{\pm 1} = \hat{z} \left[-\frac{1}{Y_0} \sqrt{\frac{8\pi}{jk}} \right] \frac{A_n^h(ka, kb)}{2} \begin{bmatrix} -H_{\nu_n}^{(1)'}(kb) & H_{\nu_n}^{(2)}(ka) \\ H_{\nu_n}^{(2)'}(kb) & H_{\nu_n}^{(1)}(kb) \end{bmatrix} D_h^C(\delta_{1n}, \delta_{1q}) \quad (3.84)$$

where D_h^C is the diffraction coefficient for the discontinuity in the radius of curvature (such as the one in (3.58)), and the incident and reflected modal ray angles are as determined in (E.31) and (E.34). The subscript 1 or 2 is relevant to the equivalent source at edge ① or ② of Figure 3.36, respectively.

The reflected q^{th} mode is obtained from (3.38) such that

$$R_{qn} = -\frac{1}{4Y_0} \sqrt{\frac{8\pi}{jk}} A_n^h A_q^h \left[f_q^h(ka) H_{\nu_n}^{(1)'}(kb) H_{\nu_n}^{(2)}(ka) D_h^C(\delta_{1n}, \delta_{1q}) - f_q^h(kb) H_{\nu_n}^{(2)'}(kb) H_{\nu_n}^{(1)}(kb) D_h^C(\delta_{2n}, \delta_{2q}) \right] \quad (3.85)$$

For whispering gallery modes, the line source $\bar{M}_{\ell 2}$ corresponding to the discontinuity at edge ② on the inner circle (of radius=b) has to be discarded since the whispering gallery modal rays do not illuminate this discontinuity. Therefore, the general expression for the reflection coefficient in (3.85) reduces to the following for whispering gallery (WG) modes:

$$R_{qn}^{WG} = -\frac{1}{4Y_0} \sqrt{\frac{8\pi}{jk}} A_n^h A_q^h f_q^h(ka) H_{\nu_n}^{(1)'}(kb) H_{\nu_n}^{(2)}(ka) D_h^C(\delta_{1n}, \delta_{1q}) . \quad (3.86)$$

The result in (3.86) for the magnitude of the reflection of a whispering gallery mode is plotted in Figure 3.37 as a function of the radius "b" while keeping $(a-b)=0.4\lambda$ (wavelengths). The diffraction coefficient of (3.58) is used in the calculation. For the range of radius "b" shown in Figure 3.37, it is found that the only propagating mode is the whispering gallery mode. The modal ray direction of the whispering gallery mode was sufficiently away from grazing (more than 20 degrees); therefore, the diffraction coefficients of (3.58) could safely be used. One observes that the amplitude of the reflection coefficient decreases as the radii of inner and outer circles are increased.

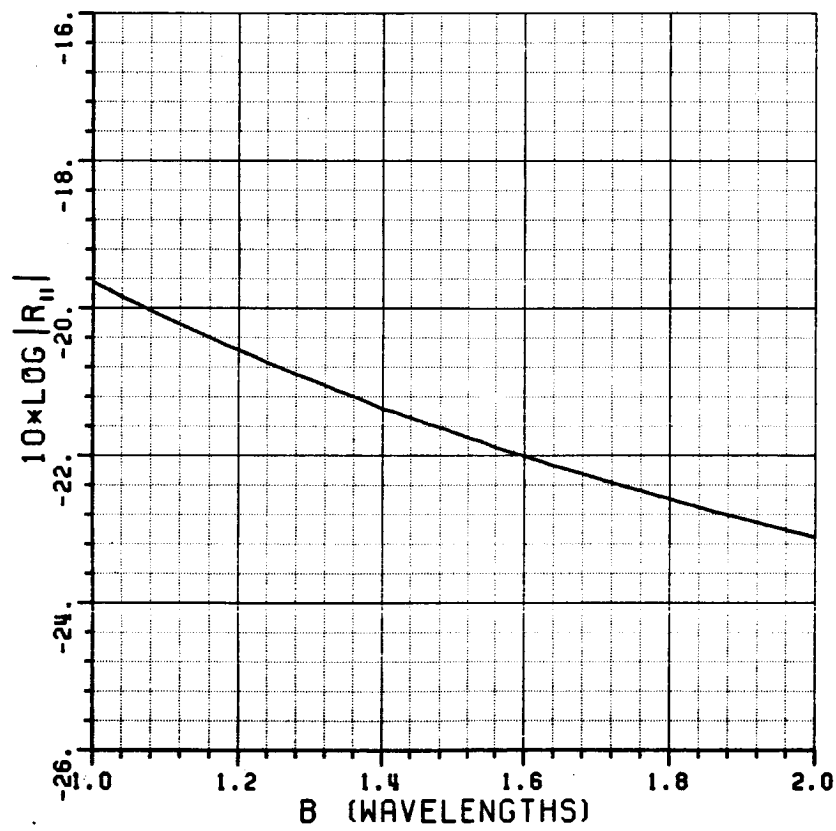


Figure 3.37. Reflection of the whispering gallery mode.

3.2. The Transmission Type Scattering Matrix

The scattering matrices $[S_{12}]$ and $[S_{21}]$ characterize the transmission of the field through the open end by relating the coefficients of modal field inside the cavity to the amplitude of the exterior field. One may also encounter the transmission of modal energy from an interior region to another adjacent interior region through the junction between them. These transmission mechanisms are discussed separately in this section.

In order to obtain expressions for the transmission coefficients one may be tempted to use the GTD equivalent currents employed in calculating the reflection coefficients. However, it is noted that the GTD equivalent current concept fails at and around the geometrical optics shadow boundaries where the diffracted field is not ray optical. This was not a problem in the calculation of reflection coefficients, because the incident and reflected modal ray angles were away from the shadow boundaries for the modes not close to cut-off. However, in the case of transmission through a junction, the modal rays corresponding to the transmitted modes may be close to the shadow boundaries of the incident modal rays, and their associated reflected modal rays, at the discontinuities. Therefore, to obtain the transmission coefficients, one can integrate the incident modal field across the aperture as in the Kirchhoff-Huygens' approximation for aperture integration (AI). Although the asymptotic evaluation of this integral gives some end point contributions to account for the edge effects, they are not as accurate as predicted by the GTD [40]. Therefore, in this section a modification of the PTD presented in [26] will be employed to get a proper correction

to the edge effects predicted by the Kirchhoff-Huygens' approximation. The PTD approach discussed in [26] modifies the original PTD developed by Ufimtsev [27] by employing equivalent currents to refine the approximate physical optics (PO) integral for the fields scattered by a conducting body. These equivalent currents are again placed at the edges of the scatterer, and their expressions are similar to the GTD equivalent currents as in (3.1) and (3.2); however, the GTD diffraction coefficients D_{sh} are now replaced by Ufimtsev diffraction coefficients D_{sh}^u which are given by;

$$D_{sh}^u = D_{sh} - D_{sh}^{PO} \quad (3.87)$$

In (3.87), D_{sh}^{PO} is the PO diffraction coefficient obtained from the asymptotic end-point contribution of the PO integral. Therefore, the PTD, in this format, requires an integration of the geometrical optics (GO) currents over the surface of the scatterer (which is the PO approximation) and another integration of the Ufimtsev type equivalent currents over the edges of the scatterer. The latter tends to correct for the incomplete edge effects contained in the PO approximation. The important property of the Ufimtsev type equivalent currents is that, unlike the GTD equivalent currents, they can be employed for observation points in the transition regions of the shadow boundaries. It is noted that when the result of PO integration is identically zero, then Ufimtsev diffraction coefficients have to be replaced by the GTD diffraction coefficients. One thing still remains to be shown; namely, the same Ufimtsev type equivalent currents employed to correct the PO approximation for the scattering by a perfectly-conducting surface with

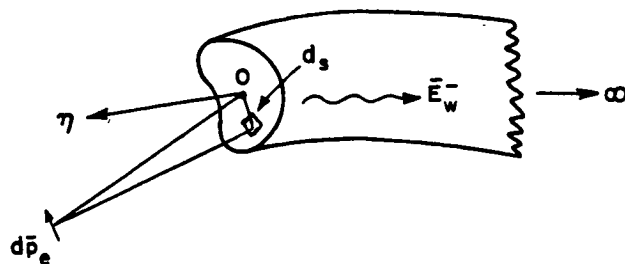
an edge also corrects the incomplete edge effects contained in the Kirchhoff-Huygens' approximation for the AI considered in this work. This is done in Appendix H where it is noted that the Kirchhoff-Huygens' integral basically plays the same role as the PO integral.

3.2.1. Transmission Between Exterior and Interior Regions

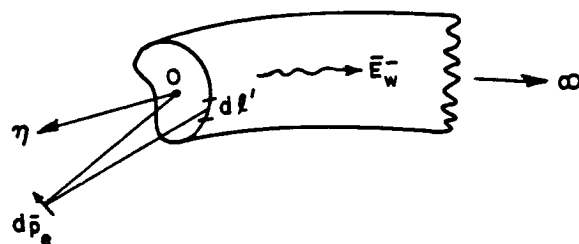
The interior to exterior coupling is the result of the radiation of modal energy from within the waveguide to the external free space region through the open end, and it is described by the scattering matrix $[S_{12}]$. The reciprocal problem of transmission into the waveguide region via a coupling of the exterior field incident at the open end is characterized by the scattering matrix $[S_{21}^P]$. As might be expected, $[S_{21}^P]$ can be directly related to $[S_{12}]$ via reciprocity; this relation is discussed in Appendix I, and $[S_{12}]$ will therefore be found here directly from $[S_{21}^P]$.

The scattering matrix $[S_{21}]$ describes the transmission or coupling of the incident plane wave field into the waveguide modes as illustrated in Figure 2.3. $[S_{21}]$ is defined in (2.19).

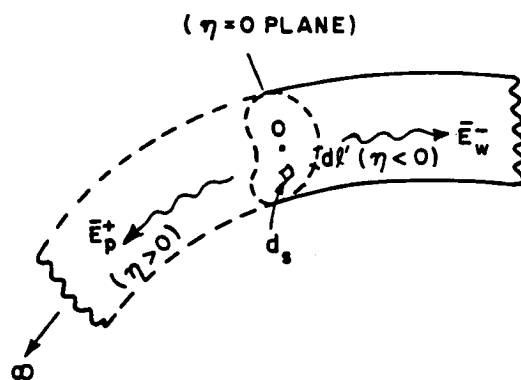
For later convenience, let the waveguide excitation be an electric current moment $d\vec{p}_e$ which lies at the point P in the region exterior to the waveguide as shown in Figure 3.38. $[S_{21}^P]$ will be developed here for estimating the coupling of the fields of the exterior source $d\vec{p}_e$ into the interior waveguide region, via the open end. This more general situation reduces to the special case of plane wave incidence on the waveguide opening as in Figure 2.3 if the source $d\vec{p}_e$ is allowed to recede to infinity.



- a) Part of $[S_{21}]$ due to coupling of the direct field of $d\vec{p}_e$ through the aperture.



- b) Part of $[S_{21}]$ due to diffraction correction from the rim.



- c) Equivalent problem.

Figure 3.38. Geometry associated with $[S_{21}]$ calculation.

The field \bar{E}_w^- which is coupled into the waveguide region by $d\bar{p}_e$ in Figure 3.38 may be expressed as in (2.11) by

$$\bar{E}_w^- = \sum_n C_n^- (\bar{E}_{nt} - \bar{E}_{nn}) e^{+j\beta_n n} = \sum_n C_n^- \bar{E}_n^- \quad (3.88)$$

The associated magnetic field \bar{H}_w^- is likewise given via (2.12) as

$$\bar{H}_w^- = \sum_n C_n^- (-\bar{H}_{nt} + \bar{H}_{nn}) e^{+j\beta_n n} = \sum_n C_n^- \bar{H}_n^- \quad (3.89)$$

The modal coupling or transmission coefficients (C_n^-) in (3.88) and (3.89) may be found from the equivalent problem in Figure 3.38(c) which illustrates an equivalent surface and line source distribution at $n=0$ within an infinite waveguide which is a geometric extension of the semi-infinite waveguide of Figure 3.38(a,b). The equivalent sources in Figure 3.38(c) generate the same fields in the waveguide region as those in Figures 3.38(a) and (b) if the equivalent sources are found exactly, as described in Appendix K. Here, the equivalent sources are determined from asymptotic high frequency techniques so that the field coupled into the waveguide are approximations to the true fields therein. These approximations are high frequency approximations which are expected to work well even down to the lowest propagating mode in the waveguide. According to the high frequency estimates based on the GTD, one obtains

$$\bar{J}_s \sim \bar{J}_s^{GO} + \bar{J}_s^d \quad (3.90)$$

and

$$\bar{M}_s \sim \bar{M}_s^{GO} + \bar{M}_s^d \quad (3.91)$$

where \bar{J}_s^{GO} and \bar{M}_s^{GO} represent the unperturbed or geometrical optics (GO) field produced by $d\bar{p}_e$ within the aperture region but in the absence of the waveguide structure. The additional contributions to \bar{J}_s and \bar{M}_s must arise from the diffraction by the edges of the aperture which are denoted by \bar{J}_s^d and \bar{M}_s^d in (3.90) and (3.91). It is easily seen that \bar{J}_s^{GO} and \bar{M}_s^{GO} may be expressed by

$$\bar{J}_s^{GO} = [\hat{n} \times \bar{H}_{dp_e}^i] \quad (3.92)$$

and

$$\bar{M}_s^{GO} = [\bar{E}_{dp_e}^i \times \hat{n}] \quad (3.93)$$

at the waveguide opening. The unit vector \hat{n} defines the unit normal at the aperture surface pointing into the waveguide. In (3.92) and (3.93) $\bar{E}_{dp_e}^i$ and $\bar{H}_{dp_e}^i$ are the electric and magnetic fields incident at the open end from the external source $d\bar{p}_e$ at P. The incident fields ($\bar{E}_{dp_e}^i$ and $\bar{H}_{dp_e}^i$) represent the unperturbed fields of $d\bar{p}_e$ which exists in the absence of the waveguide. Clearly, the incident fields are given by

$$\bar{E}_{dp_e}^i \approx \frac{jkZ_0}{4\pi} \hat{s}^i \times \hat{s}^i \times d\bar{p}_e \frac{e^{-jks^i}}{s^i} \quad (3.94)$$

$$\bar{H}_{dp_e}^i \approx \frac{-jk}{4\pi} \hat{s}^i \times d\bar{p}_e \frac{e^{-jks^i}}{s^i} \quad (3.95)$$

The expressions in (3.94) and (3.95) are valid for distances s^i which correspond to $d\bar{p}_e$ being in the near zone of the waveguide

aperture. However, s^i cannot be made extremely small to where the reactive field terms of the type $1/(s^i)^2$ and $1/(s^i)^3$ become significant; these higher order range dependent terms are ignored in (3.94) and (3.95) which pertain only to the radiation fields. Before proceeding to calculate the modal transmission coefficients (C_n^-) , it is convenient to decompose (C_n^-) as follows:

$$C_n^- = C_n^{GO} + C_n^d \quad (3.96)$$

where (C_n^{GO}) is the part of (C_n^-) due to \bar{J}_S^{GO} and \bar{M}_S^{GO} ; whereas (C_n^d) is the part of (C_n^-) which is produced by \bar{J}_S^d and \bar{M}_S^d . It is now an easy matter to find (C_n^{GO}) from \bar{J}_S^{GO} and \bar{M}_S^{GO} by employing the results of Appendix G which indicate the manner in which the electric and magnetic current sources excite modes inside a waveguide. Thus, from (G-8) of Appendix G, the GO part of the transmission coefficients are given by

$$C_n^{GO} = \frac{- \int \int_{\text{aperture}} [\bar{E}_n^+ \cdot \bar{J}_S^{GO} - \bar{H}_n^+ \cdot \bar{M}_S^{GO}] ds'}{2 \int \int_{\text{aperture}} \bar{E}_n^+ \times \bar{H}_n^{+*} \cdot d\bar{s}} \quad (3.97)$$

At this point it is also worth mentioning that the AI method, which is used to calculate the GO part of transmission into the waveguide and radiation from the waveguide to the exterior region, satisfies the reciprocity principle; this fact is shown in Appendix L. The edge contributions (C_n^d) may be calculated via the Ufimtsev equivalent edge sources given by (for N incident modal rays of each mode as in (3.33)):

$$M_\ell = \sum_{i=1}^N M_\ell^{-i} = \sum_{i=1}^N \left[\frac{1}{-Y_0} \sqrt{\frac{8\pi}{jk}} \right] \frac{D_h^u(\psi', \psi_{ni}; \beta_0, \beta_{ni})}{\sin \beta_0 \sin \beta_{ni}} \frac{(\bar{H}^{-i} \cdot \hat{\ell}')}{2} \quad (3.98)$$

and

$$\bar{M}_d = \sum_{i=1}^N \bar{M}_d^i \sim \hat{n} \sum_{i=1}^N \left[\sqrt{\frac{8\pi}{jk}} \right] \frac{D_s^u(\psi', \psi_{ni}; \tilde{\beta}_0, \tilde{\beta}_{ni})}{|\sin \psi_{ni}| \sqrt{\sin \beta_0 \sin \beta_{ni}}} \frac{(\bar{E}^i \cdot \hat{\ell}^i)}{2} \quad (3.99)$$

In (3.98) and (3.99), the incident ray from $d\bar{p}_e$ makes an azimuthal angle ψ' about the unit tangent $\hat{\ell}'$ at any point of diffraction on the rim.

(see Figures 3.2(a) and (b)). Likewise, ψ_{ni} in (3.98) and (3.99) corresponds to an azimuthal angle which the ray diffracted from the edge along the \hat{s}_n^i direction into the waveguide region makes about $\hat{\ell}'$ at the same point of diffraction [note; $\tilde{\beta}_{ni}$ and ψ_{ni} are like $\tilde{\beta}$ and ψ in Figures 3.2(a) and (b); likewise, $\tilde{\beta}_0$ and ψ' also have the same meaning as in those figures]. A more accurate analysis will include the obliquity of the equivalent magnetic dipole source of (3.99) with respect to the axial direction (\hat{n}). However, this effect is negligible for the modes sufficiently far from cut-off; hence, it is not shown in (3.99). The coefficients (C_n^d) excited by \bar{M}_ℓ and \bar{M}_d are explicitly given by

$$C_n^d = \frac{\sum_{j=1}^N \int_{\text{rim}} [\bar{H}_n^+ \cdot (\bar{M}_\ell^j + \bar{M}_d^j)] d\ell'}{2 \iint \bar{E}_n^+ \times \bar{H}_n^{+*} \cdot d\bar{S}'} \quad (3.100)$$

The scattering matrix $[S_{21}^p]$ can easily be identified via (3.96), (3.97) and (3.100). In the case of an infinitesimal electric current moment or $d\bar{p}_e$ type illumination as indicated in (3.94) and (3.95) the scattering matrix can be identified via the following relationship:

$$[C_n^-] = \begin{bmatrix} [S_{xn}] & [S_{yn}] & [S_{zn}] \end{bmatrix} \begin{bmatrix} dp_{ex} \\ dp_{ey} \\ dp_{ez} \end{bmatrix} \quad (3.101)$$

where

$$[S_{21}^p] = [[S_{xn}] [S_{yn}] [S_{zn}]] \quad (3.102)$$

and

$$\begin{bmatrix} dp_{ex} \\ dp_{ey} \\ dp_{ez} \end{bmatrix} = \begin{bmatrix} \hat{x}' \cdot d\bar{p}_e \\ \hat{y}' \cdot d\bar{p}_e \\ \hat{z}' \cdot d\bar{p}_e \end{bmatrix} \quad (3.103)$$

If the source recedes to infinity, then $\bar{E}_{pe}^i \rightarrow \bar{E}^i$, corresponding to a locally plane wave illumination. In this case $[S_{21}^p]$ takes the form of $[S_{21}]$ given in (2.19) and (2.20), by bringing out the range dependent part.

Example:

a) Far zone radiation from an open-ended parallel-plate waveguide:

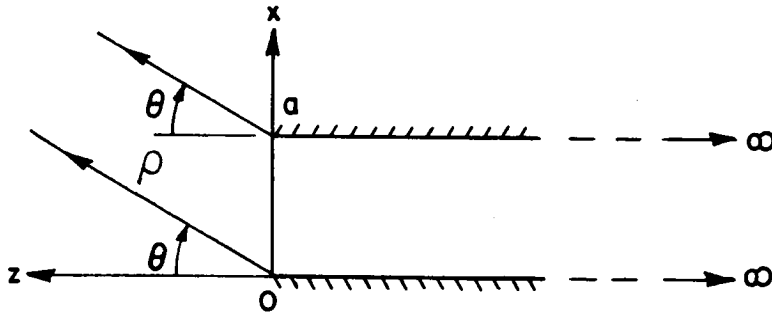


Figure 3.39. Open-ended parallel-plate waveguide geometry.

i) Aperture integration analysis

As shown in Figure 3.39, the geometry is independent of the \hat{y} -coordinate and the width of the waveguide is shown by "a". The AI analysis of the TM_y case will be considered first; the corresponding TE_y case will be discussed briefly later on in a similar fashion. The expressions for the surface equivalent currents at the aperture are as follows:

$$\bar{J}_{eq} = \hat{n} \times \bar{H}^i = \hat{y} H_x^i \quad (3.104)$$

and

$$\bar{M}_{eq} = \bar{E}^i \times \hat{n} = \hat{x} E_y^i \quad (3.105)$$

where $\hat{n}=\hat{z}$ is the unit normal vector pointing into the free space at the surface of the aperture.

The far field radiated by these equivalent currents is given by
(The distance from the origin to the far zone observation point is shown by ρ , in Figure 3.39.)

$$\bar{E}^{rad}(\rho, \theta) = \hat{y} \left[-Z_0 \sqrt{\frac{jk}{8\pi}} \int_0^a H_x^i \frac{e^{-jk\rho}}{\sqrt{\rho}} dx' - \sqrt{\frac{jk}{8\pi}} \int_0^a (-\cos\theta) E_x^i \frac{e^{-jk\rho}}{\sqrt{\rho}} dx' \right] \quad (3.106)$$

or

$$\bar{E}^{rad}(\rho, \theta) = \hat{y} C_m \sqrt{\frac{jk}{8\pi}} \left[\int_0^a \sin \frac{m\pi}{a} x \frac{e^{-jk\rho}}{\sqrt{\rho}} dx' \right] \left[\cos\theta + \sqrt{1 - \left(\frac{m\pi}{ka}\right)^2} \right] \quad (3.107)$$

The integral in (3.107) can be evaluated and the result is given by

$$\begin{aligned} \bar{E}^{\text{rad}}(\rho, \theta) = \hat{y} C_m \sqrt{\frac{jk}{8\pi}} \left[\cos \theta + \sqrt{1 - \left(\frac{m\pi}{ka}\right)^2} \right] \frac{e^{-jk[\rho - \frac{a}{2} \sin \theta]}}{\sqrt{\rho}} \frac{1}{2j} \\ \cdot \left[\frac{j^m \sin \left[\frac{ka}{2} \sin \theta + \frac{m\pi}{2} \right]}{\frac{k}{2} \sin \theta + \frac{m\pi}{2a}} - (-j)^m \frac{\sin \left[\frac{ka}{2} \sin \theta - \frac{m\pi}{2} \right]}{\frac{k}{2} \sin \theta - \frac{m\pi}{2a}} \right] \end{aligned} \quad (3.108)$$

As seen from (3.108), the far field pattern of each mode is composed of two $\frac{\sin x}{x}$ (sinc) functions with their peaks in the modal ray directions. Further simplification occurs in the expression if one separately examines the odd and even modes. For $m=2n+1$, where n is an integer one obtains

$$\begin{aligned} \bar{E}^{\text{rad}} = \hat{y} C_m \sqrt{\frac{jk}{8\pi}} \left[\cos \theta + \sqrt{1 - \left(\frac{m\pi}{ka}\right)^2} \right] \frac{e^{-jk[\rho - \frac{a}{2} \sin \theta]}}{\sqrt{\rho}} \\ \frac{2m\pi}{k^2 a} \frac{\cos \left(\frac{ka}{2} \sin \theta \right)}{\sin^2 \theta - \left(\frac{m\pi}{ka}\right)^2} \end{aligned} \quad (3.109)$$

and for $m=2n$, one finds that

$$\begin{aligned} \bar{E}^{\text{rad}} = -\hat{y} C_m \sqrt{\frac{jk}{8\pi}} \left[\cos \theta + \sqrt{1 - \left(\frac{m\pi}{ka}\right)^2} \right] \frac{e^{-jk[\rho - \frac{a}{2} \sin \theta]}}{\sqrt{\rho}} \\ \frac{2m\pi}{jk^2 a} \frac{\sin \left(\frac{ka}{2} \sin \theta \right)}{\sin^2 \theta - \left(\frac{m\pi}{ka}\right)^2} \end{aligned} \quad (3.110)$$

It is noted in the above equations that if one considers the radiation only from odd (or even) modes, their peaks occur at $\sin\theta = \frac{m\pi}{ka}$ for the m^{th} mode pattern. In this direction, the other odd (or even) modes have a null in their pattern due to the $\cos(\frac{ka}{2} \sin\theta)$ (or $\sin(\frac{ka}{2} \sin\theta)$) factor in the numerator. Therefore, around this m^{th} modal ray direction, the pattern is mainly governed by the m^{th} mode.

The aperture integration is reasonably accurate in the front half-space ($z > 0$) for frequencies exceeding the cut-off frequency by 5% [28]. It is also known that AI gives exact radiation in the modal ray angle directions [28]. In Figure 3.40, the variation of the modal ray angles with increasing frequency is plotted for several odd modes. Modal ray angles start at 90° from the waveguide axis at cut-off and sharply decrease with slight increase in frequency. In fact, the slope of the curves in Figure 3.40, are unbounded at the cut-off frequencies. As the frequency is increased above the cut-off, the modal ray angle decreases monotonically; however, the rate of decrease becomes slower. Therefore, at a fixed frequency (or ka), the angular separation between the different modal ray directions becomes smaller for points near the axis of the waveguide than farther away from the axis, as can be observed in Figure 3.40.

For all modes, at a frequency 5% above the cut-off the modal ray angles are about 71° from the axis. The accuracy of the aperture integration is limited to modes with modal ray angles less than 71° . For frequencies very close to cut-off, the AI result becomes unbounded which is not only inaccurate but also nonphysical. In [28], it is shown

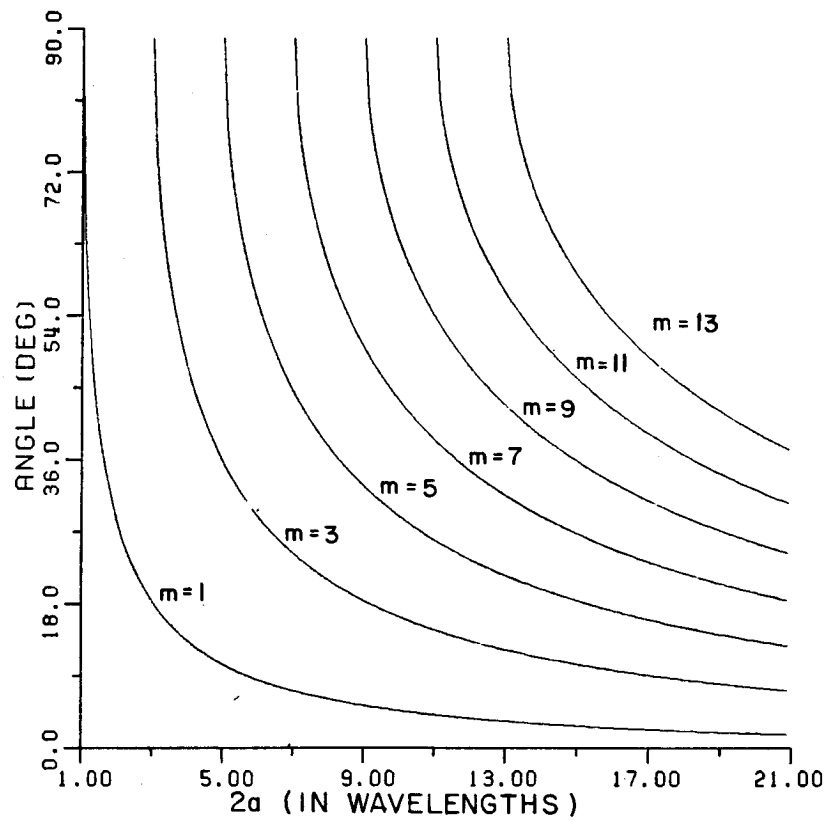


Figure 3.40. Variation of modal ray angle with frequency.

from the exact Wiener-Hopf solution for this problem that the radiation for frequencies very close to cut-off is very small.

As mentioned before, the form of (3.108) is such that the radiation in a fixed direction (θ) is mainly governed by the contributions of modes whose modal ray directions are closest to θ . Therefore, if the odd modes with modal ray directions in the θ_b neighborhood of θ are included, then the error resulting from neglecting the contribution of the other odd modes can be calculated as follows.

Let $\theta_1 = \theta - \theta_b$ and $\theta_2 = \theta + \theta_b$. Also one may define $N_1 \equiv \left\lceil \frac{ka}{\pi} \sin \theta_1 \right\rceil$ and $N_2 \equiv \left\lceil \frac{ka}{\pi} \sin \theta_2 \right\rceil$ where the symbol $\lceil \cdot \rceil$ denotes the odd integer part for the odd modes. From (3.109), the error resulting from the exclusion of odd modes with ray angles outside the θ_b neighborhood of θ is therefore given by

$$R^\circ = \sum_{n=1}^{N_1} E^{\text{rad}} + \sum_{n=N_2+1}^N E^{\text{rad}} \quad (3.111)$$

where $N \equiv \left\lceil \frac{ka}{\pi} \sin \theta_\ell \right\rceil$, in which $\theta_\ell < 90^\circ$ but θ_ℓ is close to 90° .

Therefore, in (3.111), it is assumed that the contribution of only a few (at most a couple of) modes with modal ray angles greater than θ_ℓ is neglected due to the fact that AI must be limited to modes not too close to cut-off for reasons indicated above.

From Equations (3.109) and (3.111), one finds

$$|R^\circ| < \frac{4}{\sqrt{8\pi k\rho}} \left[\sum_{\substack{n=1 \\ n=\text{odd}}}^{N_1} \frac{C_n A_n \sin \theta_1}{\sin^2 \theta - \sin^2 \theta_1} + \sum_{\substack{n=N_2+1 \\ n=\text{odd}}}^N \frac{C_n A_n \sin \theta_\ell}{\sin^2 \theta - \sin^2 \theta_2} \right] \quad (3.112)$$

where A_n is the amplitude of the n^{th} odd mode. For backscattering problems, these modes are excited by an incident plane wave with an incident angle. In Appendix I, it is shown that the amplitudes A_n of these excited modes can be determined from the radiation problem via reciprocity and they are given by

$$A_n = \frac{C_n}{jkZ_0} \left[\cos\theta + \sqrt{1 - \left(\frac{n\pi}{ka}\right)^2} \right] e^{j \frac{ka}{2} \sin\theta} \frac{n\pi}{ka} \frac{\cos\left(\frac{ka}{2} \sin\theta\right)}{\sin^2\theta - \left(\frac{n\pi}{ka}\right)^2} \quad (3.113)$$

Inserting these mode amplitudes into (3.112) one obtains

$$|R^o| < \frac{1}{\pi^2 \sqrt{k\rho}} \left[\frac{\sin^3\theta_1}{\cos\theta_1 [\sin^2\theta - \sin^2\theta_1]^2} + \frac{(\sin\theta_\ell - \sin\theta_2) \sin^2\theta_\ell}{\cos\theta_\ell [\sin^2\theta - \sin^2\theta_2]^2} \right] \cdot \quad (3.114)$$

A similar analysis can be performed for the even modes of (3.110). The important thing to be noticed from (3.114) is that, as the frequency increases, the number of propagating modes increases also; however, by retaining only the modes with modal ray angles in the θ_b neighborhood of θ , the error remains bounded. Also in the region close to the axis (i.e., $\theta \rightarrow 0$) one can reduce the value of θ_b and still expect to get the same error. This is due to the fact that modal ray directions are more densely clustered around the axis.

For the TE_y case, the equivalent currents are written as follows:

$$\bar{J}_{eq} = \hat{n} \times \bar{H}^i = -\hat{x} H_y^i \quad (3.115)$$

and

$$\bar{M}_{eq} = \bar{E}^i \times \hat{n} = \hat{y} E_x^i \quad (3.116)$$

The radiated field is given by

$$\bar{H}^{rad} = \hat{y} \left[-\gamma_0 \sqrt{\frac{jk}{8\pi}} \int_0^a E_x^i \frac{e^{-jk\rho}}{\sqrt{\rho}} dx' - \sqrt{\frac{jk}{8\pi}} \int_0^a (-\cos\theta) H_y^i \frac{e^{-jk\rho}}{\sqrt{\rho}} dx' \right] \quad (3.117)$$

or

$$\bar{H}^{rad} = \hat{y} C_m \gamma_m \sqrt{\frac{jk}{8\pi}} \left[\int_0^a \cos \frac{m\pi}{a} x' \frac{e^{-jk\rho}}{\sqrt{\rho}} dx' \right] \left[\cos\theta + \sqrt{1 - \left(\frac{m\pi}{ka}\right)^2} \right] \quad (3.118)$$

The integral in (3.118) can be performed in closed form and the result is given by

$$\bar{H}^{rad} = \hat{y} C_m \gamma_m \sqrt{\frac{jk}{8\pi}} \left[\cos\theta + \sqrt{1 - \left(\frac{m\pi}{ka}\right)^2} \right] \frac{e^{-jk\left[\rho - \frac{a}{2} \sin\theta\right]}}{\sqrt{\rho}} \left[j^m \frac{\sin\left[\frac{ka}{2} \sin\theta + \frac{m\pi}{2}\right]}{\frac{k}{2} \sin\theta + \frac{m\pi}{2a}} + (-j)^m \frac{\sin\left[\frac{ka}{2} \sin\theta - \frac{m\pi}{2}\right]}{\frac{k}{2} \sin\theta - \frac{m\pi}{2a}} \right] \quad (3.119)$$

Again, the pattern is composed of two $\frac{\sin x}{x}$ type functions. An error analysis similar to the TM_y case can be performed in this TE_y case to indicate the effect of excluding modes whose modal ray angles lie outside the θ_b neighborhood of θ .

ii) GTD Analysis

In the GTD approach, the far field radiation is due to the diffraction from the edges of the half planes making up the waveguide as shown in Figure 3.41. This analysis is described below for the TM_y case using only a first order GTD (which neglects rays multiply diffracted across the aperture). The analysis for the TE_y case is similar, hence, it will not be discussed here.

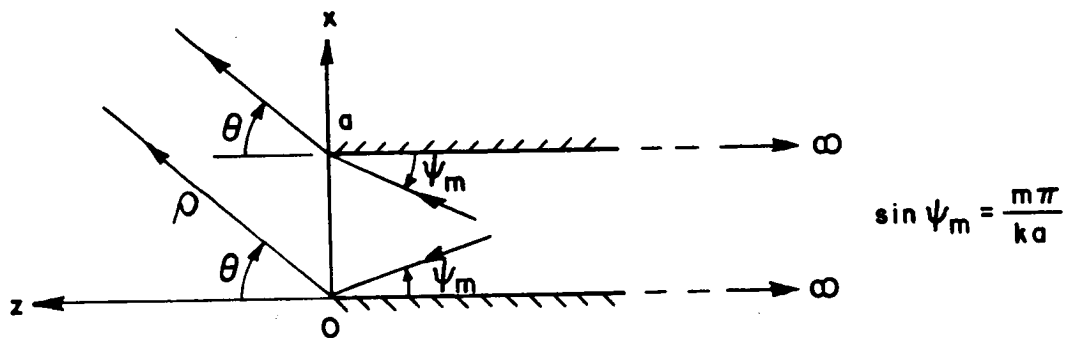


Figure 3.41. Geometry for the edge diffraction analysis.

For the TM_y case,

$$E_y^i = C_m \frac{e^{j\frac{m\pi}{a}x} - e^{-j\frac{m\pi}{a}x}}{2j} e^{-j\beta_m z} \quad (3.120)$$

as before. The modal plane wave corresponding to the first term on the right hand side of the previous equation is incident on the bottom edge at $(x=0, z=0)$ and the other one corresponding to the second term is incident on the top edge at $(x=a, z=0)$.

The electric field E_{y1}^d which is diffracted from the bottom edge at $x=0$ is given by

$$E_{y1}^d = E_y^i D_s \frac{e^{-jk\rho}}{\sqrt{\rho}} = \frac{e^{-jk\rho}}{\sqrt{\rho}} \frac{C_m}{2j} \frac{(-1)e^{-j\pi/4}}{2\sqrt{2\pi k}} \left[\frac{1}{\cos\left(\frac{\pi-\theta-\psi_m}{2}\right)} - \frac{1}{\cos\left(\frac{\pi-\theta+\psi_m}{2}\right)} \right] \quad (3.121)$$

using

$$E_y^i(x=0) = \frac{C_m}{2j} \quad \text{and} \quad \sin \psi_m = \frac{m\pi}{ka}, \quad (3.122a,b)$$

where ψ_m is the m^{th} modal ray direction (see Figure 3.41).

Similarly, the diffraction from the top edge at $x=a$, can be written as

$$E_{y2}^d = E_y^i D_s \frac{e^{-jk\rho}}{\sqrt{\rho}} = \frac{e^{-jk\rho}}{\sqrt{\rho}} C_m e^{jm\pi} e^{jk a \sin \theta} \frac{(-1)e^{-j\pi/4}}{2\sqrt{2\pi k}} \left[\frac{1}{\cos\left(\frac{\pi+\theta-\psi_m}{2}\right)} - \frac{1}{\cos\left(\frac{\pi+\theta+\psi_m}{2}\right)} \right] \quad (3.123)$$

The total diffracted field is obtained by superposing the diffractions from each edge; thus, one obtains

$$E_y^d = E_{y1}^d + E_{y2}^d = \frac{e^{-jk\rho}}{\sqrt{\rho}} C_m \sqrt{\frac{jk}{8\pi}} e^{j\frac{ka}{2}\sin\theta} \left[j^m \frac{\sin\left[\frac{ka}{2}\sin\theta + \frac{m\pi}{2}\right]}{\sin\left(\frac{\theta+\psi_m}{2}\right)} - (-j)^m \frac{\sin\left[\frac{ka}{2}\sin\theta - \frac{m\pi}{2}\right]}{\sin\left(\frac{\theta-\psi_m}{2}\right)} \right] \quad (3.124)$$

The result in (3.124) can be improved by including the contribution to the radiation resulting from the rays which undergo multiple diffraction across the aperture [10]. However, for wide apertures (approximately greater than one wavelength) these higher order effects are small enough to be neglected.

The Equations (3.108) and (3.124) based on AI and GTD, respectively, have the same limiting values at $\theta = \mp\psi_m$ [41]; however, away from the modal ray directions, the AI result differs from the GTD result, and as described in Appendix H, the AI result can be corrected using a modified PTD approach so that it agrees with the GTD.

In Figures 3.42 through 3.46 the pattern factors of certain modes obtained using AI, GTD and modified PTD are compared. As can be seen, the modified PTD approach gives results almost indistinguishable from the GTD result. Also, the agreement between the GTD and AI gets better for larger apertures.

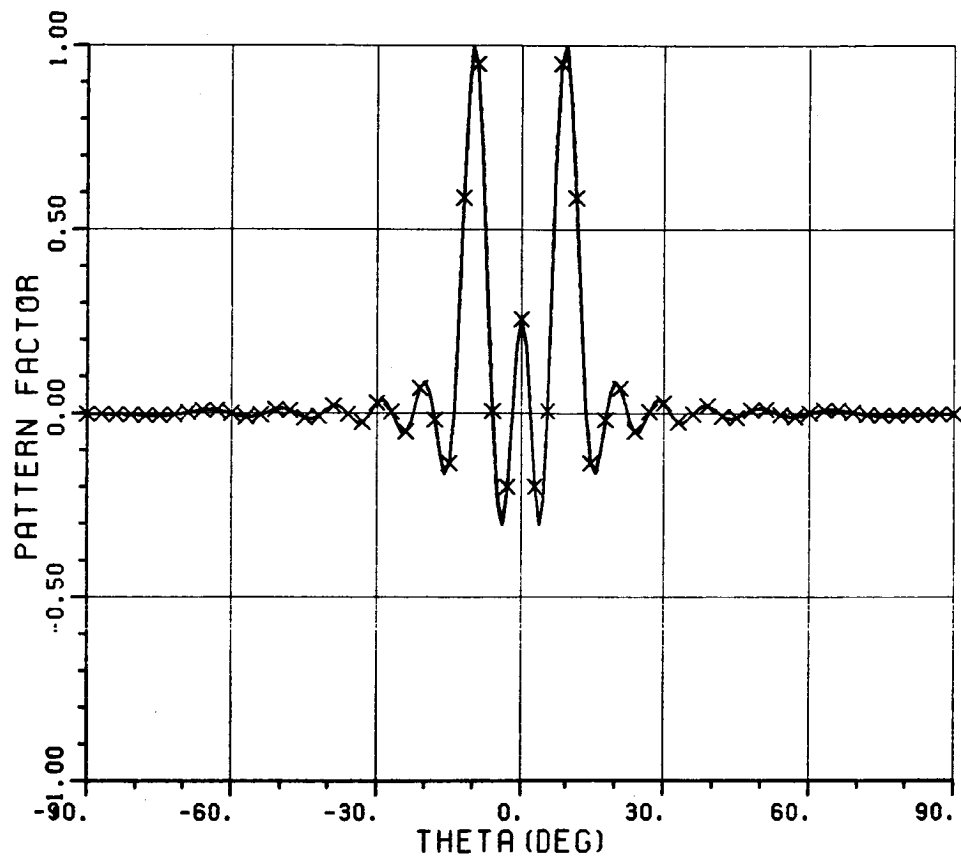


Figure 3.42. Comparison of far zone modal radiation patterns from an open-ended parallel-plate waveguide. Mode index = $m=5$, modal ray angle = 10° , — GTD, - - AI, xxx modified PTD.

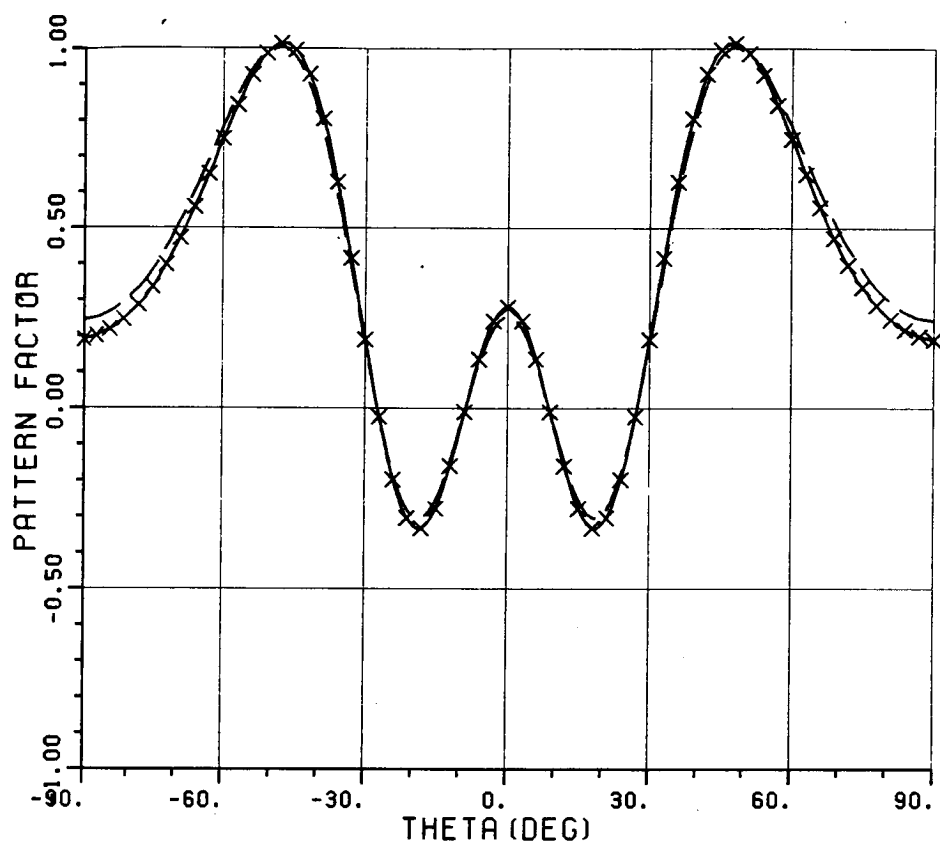


Figure 3.43. Comparison of far zone modal radiation patterns from an open-ended parallel-plate waveguide. Mode index = $m=5$, modal ray angle = 50° , — GTD, - - AI, xxx modified PTD.

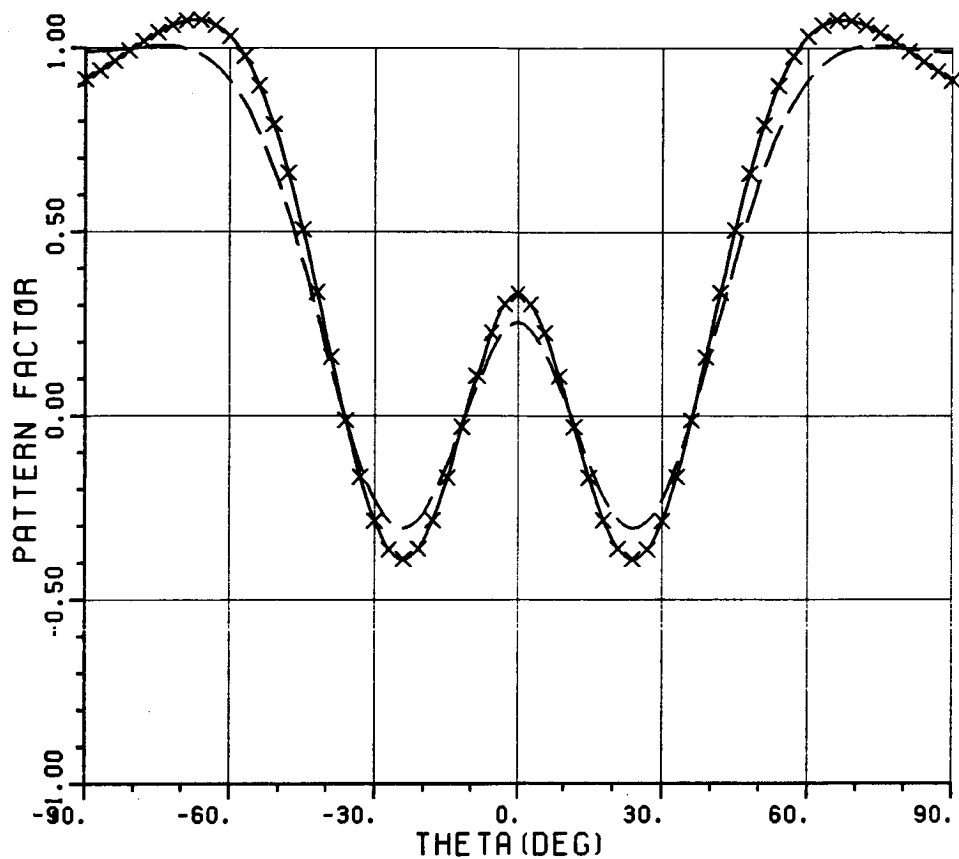


Figure 3.44. Comparison of far zone modal radiation patterns from an open-ended parallel-plate waveguide. Mode index = $m=5$, modal ray angle = 80° , — GTD, - - AI, xxx modified PTD.

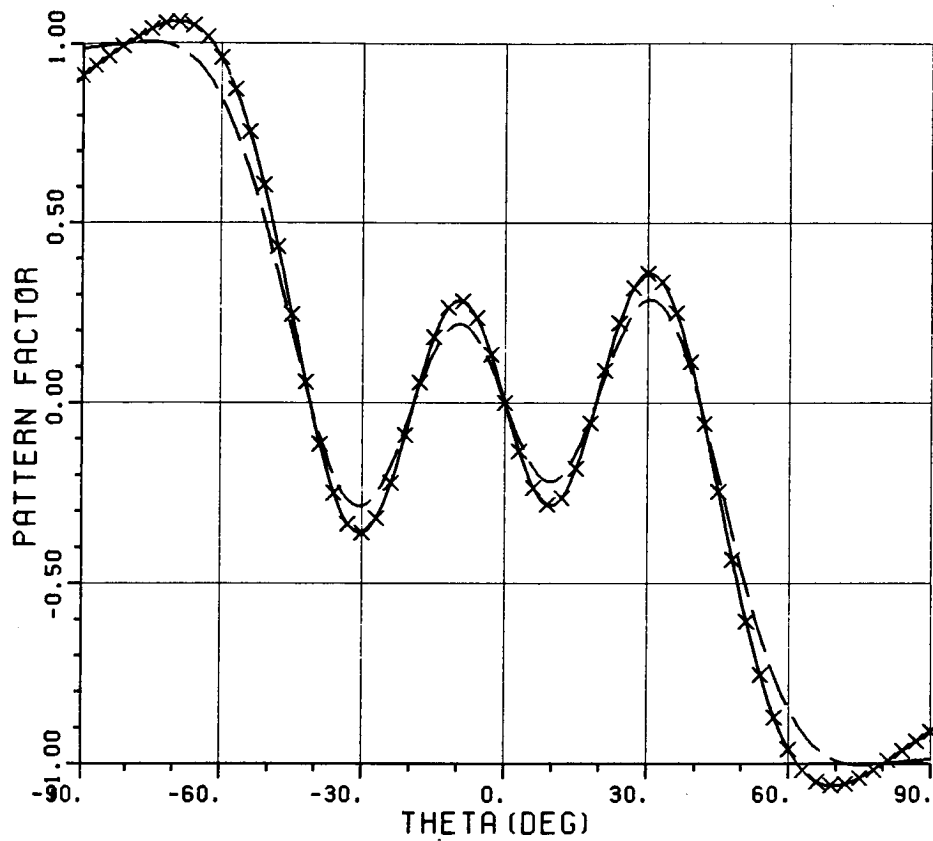


Figure 3.45. Comparison of far zone modal radiation patterns from an open-ended parallel-plate waveguide. Mode index = $m=6$, modal ray angle = 80° , — GTD, - - AI, xxx modified PTD.

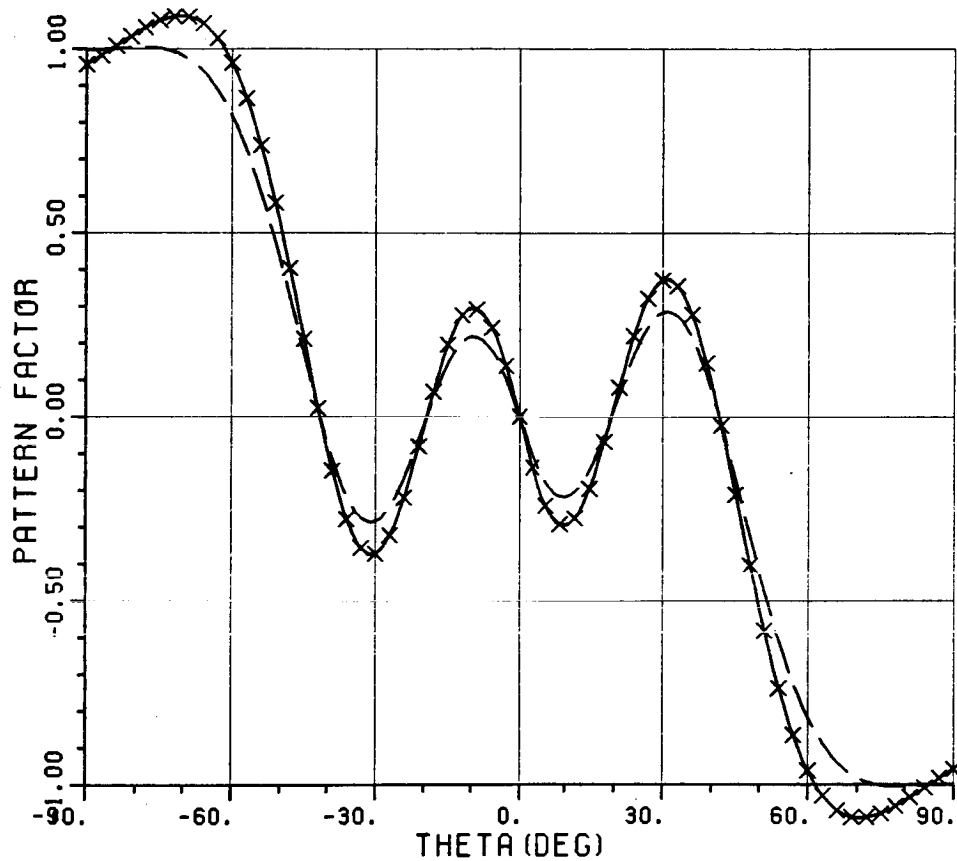


Figure 3.46. Comparison of far zone modal radiation patterns from an open-ended parallel-plate waveguide. Mode index = $m=6$, modal ray angle = 85° , — GTD, — — AI, xxx modified PTD.

The above results can be extended to the calculation of radiation from a pair of staggered, semi-infinite parallel plates as shown in Figure 3.47. The staggering is determined by the angle (t_0). The analysis is developed only for TM_y case here as an illustration. In this case, the equivalent currents of (3.104) and (3.105) take the following form

$$\bar{J}_{eq} = \hat{y} (-\cos t_0 H_z^i + \sin t_0 H_x^i) \quad (3.125)$$

and

$$\bar{M}_{eq} = (-\hat{z} \cos t_0 + \hat{x} \sin t_0) E_y^i \quad (3.126)$$

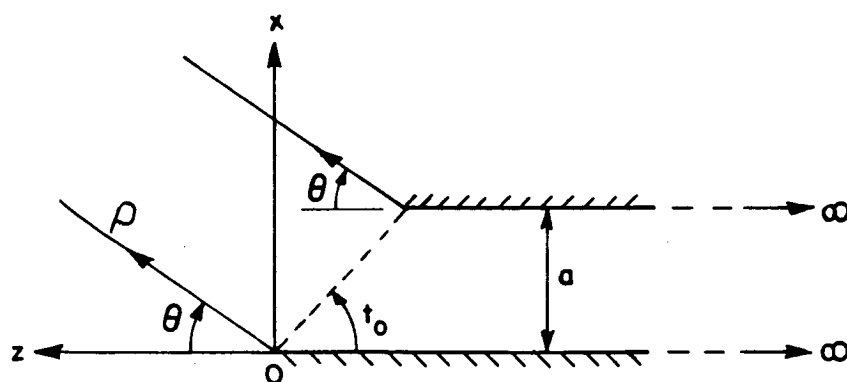


Figure 3.47. Open-ended staggered parallel plate waveguide.

The radiated field due to these equivalent sources is given by

$$\begin{aligned} \bar{E}_y^{\text{rad}}(\rho, \theta) = & \hat{y} C_m \sqrt{\frac{jk}{8\pi}} \frac{e^{-jk\rho} \left[-\frac{a}{2} (\cot(t_0)) \sqrt{1 - \left(\frac{m\pi}{ka}\right)^2} + \frac{\cos(t_0 + \theta)}{\sin t_0} \right]}{\sqrt{\rho} 2j} \\ & \left[-\left(\frac{m\pi}{a}\right) \frac{\cot(t_0)}{k} \left[(j)^m \frac{\sin(aA)}{A} + (-j)^m \frac{\sin(aB)}{B} \right] \right. \\ & \left. + \left[\sqrt{1 - \left(\frac{m\pi}{ka}\right)^2} + \frac{\sin(\theta + t_0)}{\sin t_0} \right] \left[(j)^m \frac{\sin(aA)}{A} - (-j)^m \frac{\sin(aB)}{B} \right] \right] \\ & \text{for } -t_0 < \theta < \pi - t_0 \end{aligned} \quad (3.127)$$

where

$$A = \frac{k}{2} \sqrt{1 - \left(\frac{m\pi}{ka}\right)^2} \cot(t_0) - \frac{k}{2\sin(t_0)} \cos(t_0 + \theta) + \frac{m\pi}{2a} \quad (3.128)$$

and

$$B = \frac{k}{2} \sqrt{1 - \left(\frac{m\pi}{ka}\right)^2} \cot(t_0) - \frac{k}{2\sin(t_0)} \cos(t_0 + \theta) - \frac{m\pi}{2a} \quad (3.129)$$

Equation (3.127) reduces to (3.108) for the non-staggered case when $t_0 = \frac{\pi}{2}$ as expected.

The first order GTD result of (3.124) becomes

$$\begin{aligned} E_y^d = & \frac{e^{-jk\rho}}{\sqrt{\rho}} C_m \sqrt{\frac{jk}{8\pi}} \frac{e^{jk \left[-\frac{a}{2} \cot(t_0) \sqrt{1 - \left(\frac{m\pi}{ka}\right)^2} - \frac{\cos(t_0 + \theta)}{\sin(t_0)} \right]}}{k} \\ & \left[(j)^m \frac{\sin(aA)}{\sin\left(\frac{\theta + \psi_m}{2}\right)} - (-j)^m \frac{\sin(aB)}{\sin\left(\frac{\theta - \psi_m}{2}\right)} \right] \quad (3.130) \end{aligned}$$

Figures 3.48 through 3.52 show the comparisons of the results obtained by AI, GTD and the modified PTD approaches. In all of the cases, the results based on the modified PTD agree with the corresponding GTD results.

The multiple diffractions between the edges can be treated as in [10] and can be added to the first order GTD result. This is done and compared with other methods for the transmission problem in [42]. Therefore, the higher order diffraction analysis is omitted here.

b) Radiation from an open-ended rectangular waveguide:

The far zone radiated field for the open-ended rectangular waveguide geometry of Figure A.1 can be obtained in closed form such that

$$\vec{E}^{\text{rad}} = \hat{\theta} E_{\theta} + \hat{\phi} E_{\phi} \quad (3.131)$$

where E_{θ} and E_{ϕ} can be further decomposed into contributions associated with the Kirchhoff-Huygens' (or aperture) integral and the equivalent Ufimtsev edge current integral. Thus, the electric field components are given by

$$E_{\theta} = E_{\theta k} + E_{\theta u} \quad (3.132)$$

and

$$E_{\phi} = E_{\phi k} + E_{\phi u} \quad (3.133)$$

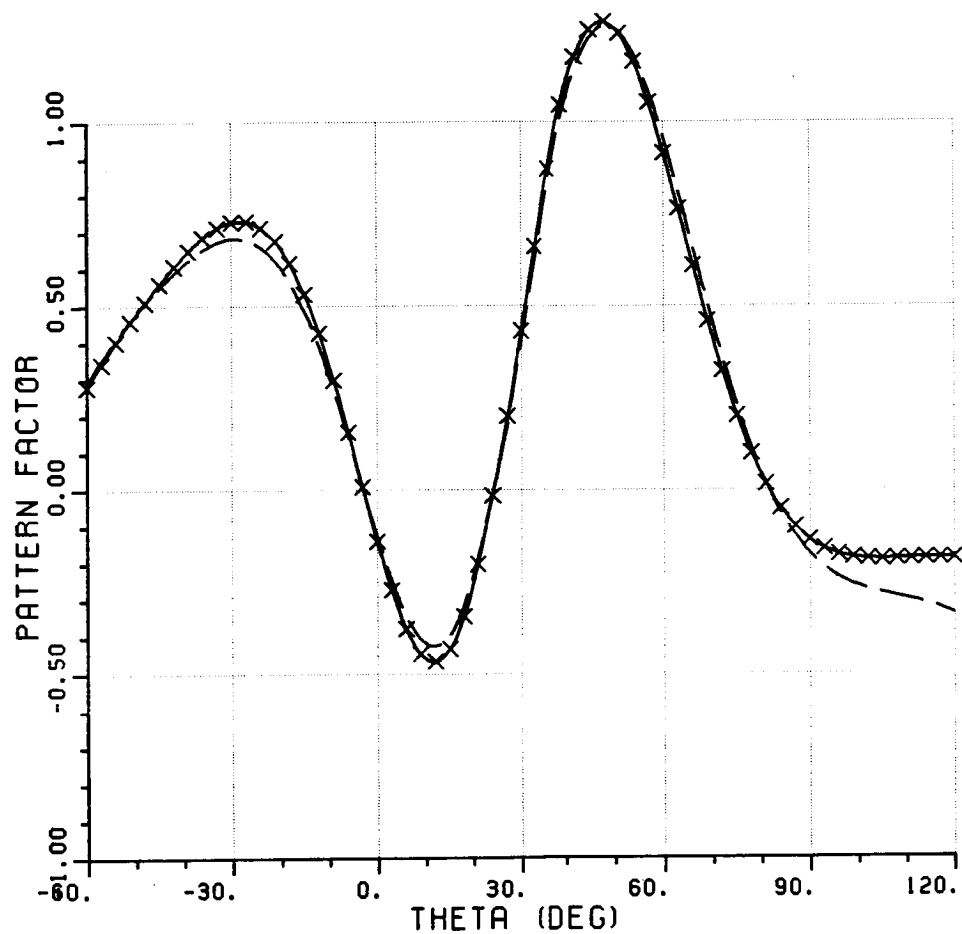


Figure 3.48. Comparison of far zone modal radiation patterns from an open-ended staggered, parallel-plate waveguide. Modal index = $m=3$, modal ray angle = 50° , staggering angle = $t_0=60^\circ$, — GTD, - - AI, xxx modified PTD.

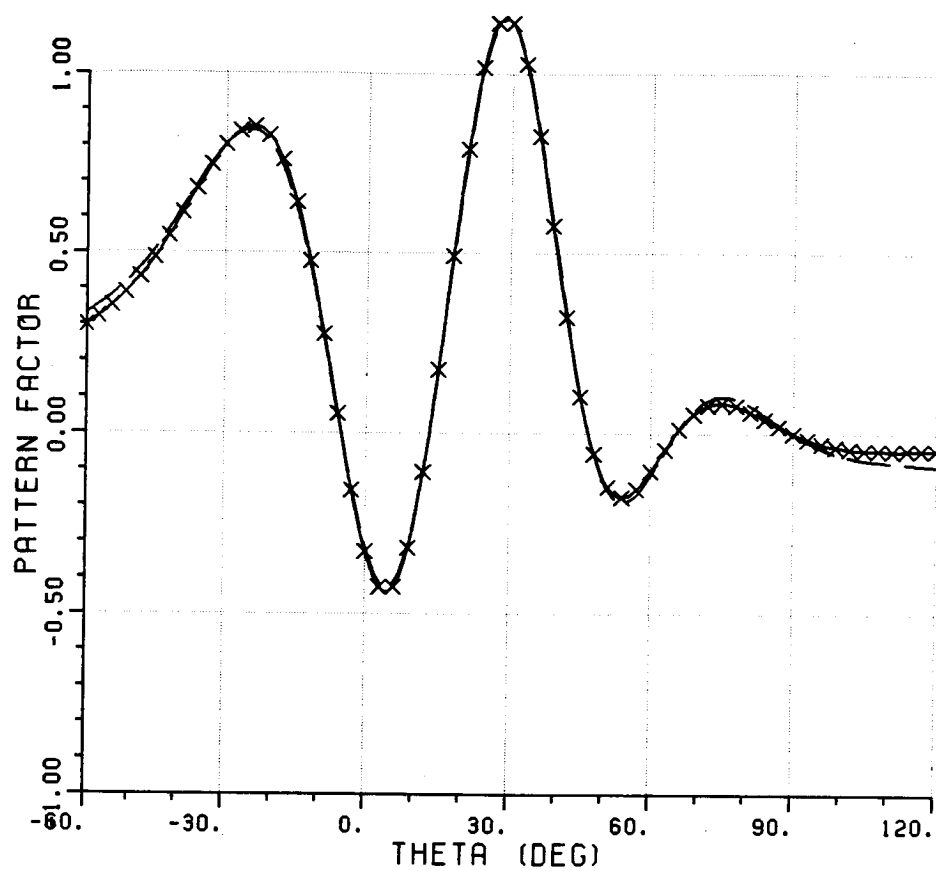


Figure 3.49. Comparison of far zone modal radiation patterns from an open-ended staggered, parallel-plate waveguide. Modal index = $m=3$, modal ray angle = 30° , staggering angle = $t_0=60^\circ$, — GTD, -- AI, xxx modified PTD.

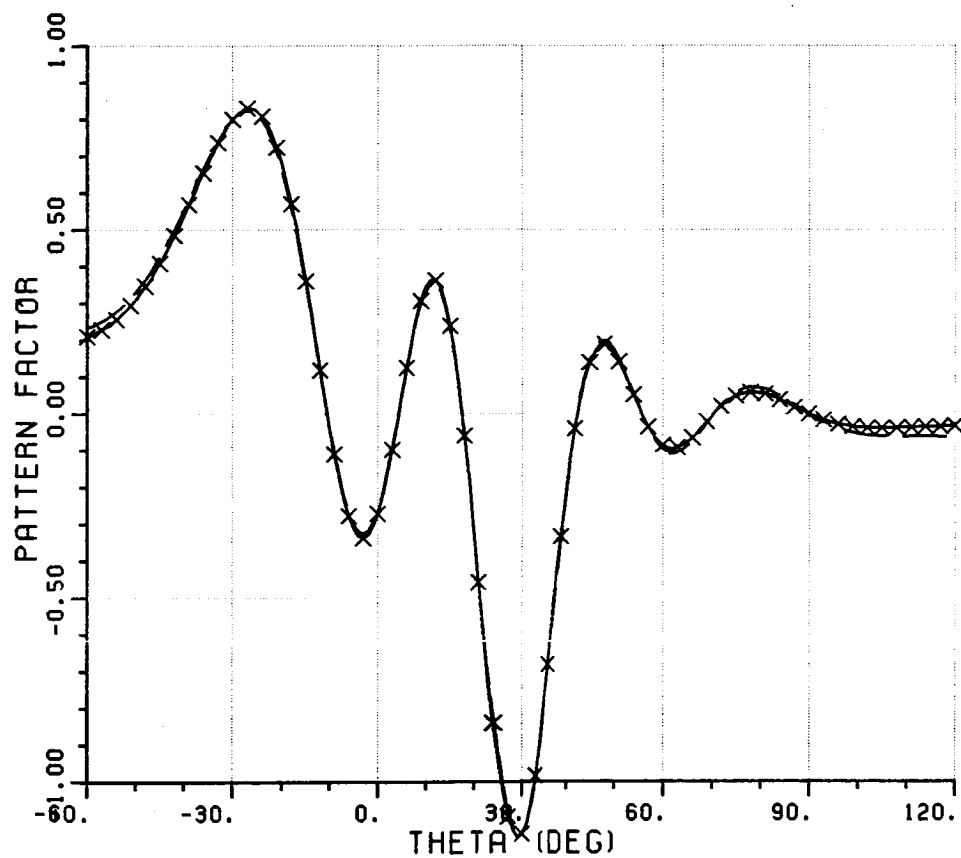


Figure 3.50. Comparison of far zone modal radiation patterns from an open-ended staggered, parallel-plate waveguide. Modal index = $m=4$, modal ray angle = 30° , staggering angle = $t_0=60^\circ$, — GTD, — — AI, xxx modified PTD.

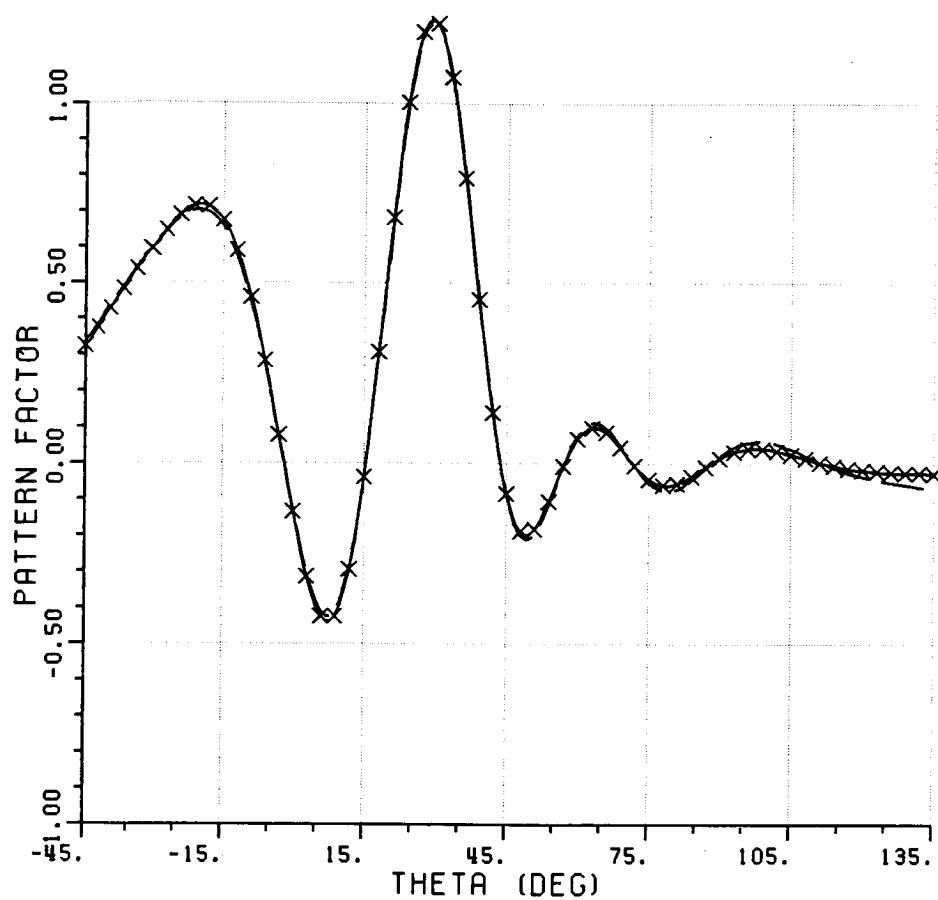


Figure 3.51. Comparison of far zone modal radiation patterns from an open-ended staggered, parallel-plate waveguide. Modal index = $m=3$, modal ray angle = 30° , staggering angle = $t_0=45^\circ$, — GTD, - - AI, xxx modified PTD.

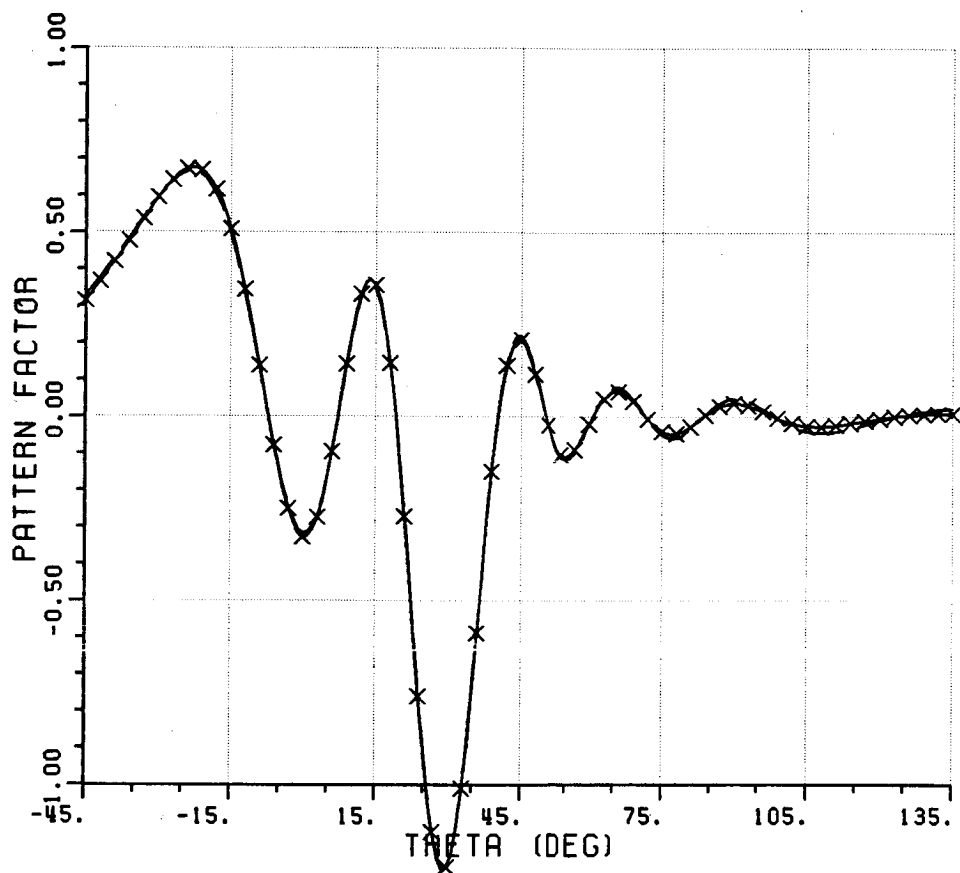


Figure 3.52. Comparison of far zone modal radiation patterns from an open-ended staggered, parallel-plate waveguide. Modal index = $m=4$, modal ray angle = 30° , staggering angle = $t_0=45^\circ$, — GTD, - - AI, xxx modified PTD.

The contribution from the Kirchhoff Huygens' approximation is given by

$$E_{\theta k} = \frac{j^{n+m} k N_{nm}}{4\pi} \frac{e^{-jkr}}{r} e^{\frac{jk}{2} (a \cos \phi + b \sin \phi) \sin \theta} \\ \left\{ u \cos \phi \left(1 + \frac{Y_{nm}}{Y_0} \cos \theta \right) [A_+ + (-1)^n A_-] [B_+ - (-1)^m B_-] \right. \\ \left. - v \sin \phi \left(1 + \frac{Y_{nm}}{Y_0} \cos \theta \right) [A_+ - (-1)^n A_-] [B_+ + (-1)^m B_-] \right\} \quad (3.134)$$

and

$$E_{\phi k} = \frac{j^{n+m} k N_{nm}}{4\pi} \frac{e^{-jkr}}{r} e^{\frac{jk}{2} (a \cos \phi + b \sin \phi) \sin \theta} \\ \left\{ -u \sin \phi \left(\cos \theta + \frac{Y_{nm}}{Y_0} \right) [A_+ + (-1)^n A_-] [B_+ - (-1)^m B_-] \right. \\ \left. - v \cos \phi \left(\cos \theta + \frac{Y_{nm}}{Y_0} \right) [A_+ - (-1)^n A_-] [B_+ + (-1)^m B_-] \right\} \quad (3.135)$$

where

$$A_{\pm} = \frac{\sin \left[\frac{1}{2} (k \sin \theta \cos \phi \pm n_a) a \right]}{k \sin \theta \cos \phi \pm n_a} \quad (3.136)$$

$$B_{\pm} = \frac{\sin \left[\frac{1}{2} (k \sin \theta \sin \phi \pm m_b) b \right]}{k \sin \theta \sin \phi \pm m_b} \quad (3.137)$$

and

$$u = \begin{cases} m_b & \text{for TE mode} \\ n_a & \text{for TM mode} \end{cases} \quad (3.138)$$

$$v = \begin{cases} n_a & \text{for TE mode} \\ -m_b & \text{for TM mode} \end{cases} \quad (3.139)$$

Likewise the contributions from the equivalent Ufimtsev edge currents are given by

$$\begin{aligned}
 E_{\theta u} = & \sqrt{\frac{k}{8\pi j}} N_{nm} \frac{e^{-jkr}}{r} e^{\frac{jk}{2} (a \cos \phi + b \sin \phi)} \sin \theta \\
 & \left[\frac{j^n}{\sqrt{\sin \beta_{oh} \sin \beta_h}} \left[e^{-\frac{jk}{2} b \sin \theta \sin \phi} - (-1)^m e^{\frac{jk}{2} b \sin \theta \sin \phi} \right] \right. \\
 & \cdot [D_S^u(\psi_h, \psi_h') u (A_+ + (-1)^n A_-) \cos \theta \cos \phi \\
 & - \frac{Y_{nm}}{Y_0} D_h^u(\psi_h, \psi_h') v (A_+ - (-1)^n A_-) \sin \phi] \\
 & + \frac{j^m}{\sqrt{\sin \beta_{ov} \sin \beta_v}} \left[e^{-\frac{jk}{2} a \sin \theta \cos \phi} - (-1)^n e^{\frac{jk}{2} a \sin \theta \cos \phi} \right] \\
 & \cdot [-D_S^u(\psi_v, \psi_v') v (B_+ + (-1)^m B_-) \cos \theta \sin \phi \\
 & + \frac{Y_{nm}}{Y_0} D_h^u(\psi_v, \psi_v') u (B_+ - (-1)^m B_-) \cos \phi] \quad (3.140)
 \end{aligned}$$

and

$$\begin{aligned}
E_{\phi u} = & \sqrt{\frac{k}{8\pi j}} N_{nm} \frac{e^{-jkr}}{r} e^{\frac{jk}{2} (a \cos \phi + b \sin \phi) \sin \theta} \\
& \left[\frac{-j^n}{\sqrt{\sin \beta_{oh} \sin \beta_h}} \left[e^{-\frac{jk}{2} b \sin \theta \sin \phi} - (-1)^m e^{\frac{jk}{2} b \sin \theta \sin \phi} \right] \right. \\
& \cdot [D_S^u(\psi_h, \psi_h') u (A_+ + (-1)^n A_-) \sin \phi \\
& + \frac{Y_{nm}}{Y_0} D_h^u(\psi_h, \psi_h') v (A_+ - (-1)^n A_-) \cos \theta \cos \phi] \\
& - \frac{j^m}{\sqrt{\sin \beta_{ov} \sin \beta_v}} \left[e^{-\frac{jk}{2} a \sin \theta \cos \phi} - (-1)^n e^{\frac{jk}{2} a \sin \theta \cos \phi} \right] \\
& \cdot [D_S^u(\psi_v, \psi_v') v (B_+ + (-1)^m B_-) \cos \phi \\
& + \frac{Y_{nm}}{Y_0} D_h^u(\psi_v, \psi_v') u (B_+ - (-1)^m B_-) \cos \theta \sin \phi] \left. \right] \quad (3.141)
\end{aligned}$$

where u, v, A_{\pm}, B_{\pm} are defined as before, and D_h is given in (3.42), and

$$\cos \psi_h = \frac{\beta_{nm}/k}{\sin \beta_{oh}} \quad (3.142)$$

$$\cos \psi_h = -\frac{\cos \theta}{\sin \beta_h} \quad (3.143)$$

$$\sin\beta_{oh} = [1 - (n_a/k)^2]^{1/2} \quad (3.144)$$

$$\sin\beta_h = (1 - \sin^2\theta\cos^2\phi)^{1/2} \quad (3.145)$$

$$\cos\psi_v = \frac{\beta_{nm}/k}{\sin\beta_{ov}} \quad (3.146)$$

$$\cos\psi_v = - \frac{\cos\theta}{\sin\beta_v} \quad (3.147)$$

$$\sin\beta_{ov} = [1 - (m_b/k)^2]^{1/2} \quad (3.148)$$

and

$$\sin\beta_v = [1 - \sin^2\theta\sin^2\phi]^{1/2} \quad (3.149)$$

As seen in (3.134), (3.135), (3.140) and (3.141) the pattern has a $\frac{\sin x}{x}$ type behavior in both the $\hat{\theta}$ and $\hat{\phi}$ directions. There are four different $\frac{\sin x}{x}$ forms, each of which is due to the integration of a plane wave component of the mode as described in (A.16). Therefore, each $\frac{\sin x}{x}$ exhibits a peak at the corresponding plane wave direction. Also, as the waveguide dimensions get larger electrically, the main beams get sharper. As a result, only a few modes contribute strongly to the radiation in a given direction of observation.

Numerical results for this case are left to Chapter IV, where the backscattering analysis of a waveguide cavity model is performed and numerical values are compared with experimental measurements.

c) Radiation from an open-ended circular waveguide:

For the open-ended circular waveguide geometry of Figure F.1, the far zone field can be written as

$$\vec{E}_r = [\hat{\theta} E_{\theta} \begin{pmatrix} -\sin n\theta \\ \cos n\theta \end{pmatrix} + \hat{\phi} E_{\phi} \begin{pmatrix} \cos n\phi \\ \sin n\phi \end{pmatrix}] \frac{e^{-jkr}}{r} \quad (3.150)$$

where E_{θ} and E_{ϕ} can be separated as contributions from the Kirchhoff-Huygens' approximation and the equivalent Ufimtsev edge currents such that

$$E_{\theta} = E_{\theta k} + E_{\theta u} \quad (3.151)$$

and

$$E_{\phi} = E_{\phi k} + E_{\phi u} \quad (3.152)$$

The contribution from the Kirchhoff-Huygens' approximation becomes

TE_{nm} modes incidence:

$$E_{\theta k} = j^n k Z_0 N_{nm} n \frac{1 + \cos \theta \cos \delta_{nm}}{2 \sin \theta} J_n(P'_{nm}) J_n(k \sin \theta) \quad (3.153)$$

$$E_{\phi k} = j^n k Z_0 N_{nm} P'_{nm} \frac{\sin \delta_{nm}}{2(\cos \delta_{nm} - \cos \theta)} J_n(P'_{nm}) J_n(k \sin \theta) \quad (3.154)$$

$$\delta_{nm} = \cos^{-1}(\beta_{nm}/k) \quad (3.155)$$

TM_{nm} modes incidence:

$$E_{\theta k} = j^n k N_{nm} P_{nm} \frac{\sin \theta}{2(\cos \delta_{nm} - \cos \theta)} J_n'(P_{nm}) J_n(k \sin \theta) \quad (3.156)$$

$$E_{\phi k} = 0 \quad (3.157)$$

Likewise, the contribution from the equivalent Ufimtsev edge currents is given by

TE_{nm} modes incidence:

$$E_{\theta u} = j^n Z_0 N_{nm} n f(\theta, \delta_{nm}) J_n'(P_{nm}) \left[\beta_{nm} \sin \frac{\theta}{2} J_n''(k \sin \theta) - k P_{nm}' \sin \frac{\delta_{nm}}{2} \frac{\cos \theta}{k \sin \theta} J_n(k \sin \theta) \right] \quad (3.158)$$

$$E_{\phi u} = j^n Z_0 N_{nm} f(\theta, \delta_{nm}) J_n'(P_{nm}) \left\{ k P_{nm}' \sin \frac{\delta_{nm}}{2} J_n'(k \sin \theta) - n^2 \beta_{nm} \sin \frac{\theta}{2} \frac{\cos \theta}{k \sin \theta} \left[J_n'(k \sin \theta) - \frac{J_n(k \sin \theta)}{k \sin \theta} \right] \right\} \quad (3.159)$$

TM_{nm} modes incidence:

$$E_{\theta u} = j^n N_{nm} f(\theta, \delta_{nm}) J_n'(P_{nm}) \left[n^2 \beta_{nm} \sin \frac{\delta_{nm}}{2} \frac{\cos \theta}{k \sin \theta} J_n(k \sin \theta) + k P_{nm}' \sin \frac{\theta}{2} J_n''(k \sin \theta) \right] \quad (3.160)$$

$$E_{\phi u} = - j^n N_{nm} n f(\theta, \delta_{nm}) J_n'(P_{nm}) \left\{ \beta_{nm} \sin \frac{\delta_{nm}}{2} J_n'(k \sin \theta) + k P_{nm}' \sin \frac{\theta}{2} \frac{\cos \theta}{k \sin \theta} \left[J_n'(k \sin \theta) - \frac{J_n(k \sin \theta)}{k \sin \theta} \right] \right\} \quad (3.161)$$

where

$$f(\theta, \delta_{nm}) = \frac{\cos \frac{\theta}{2} - \cos \frac{\delta_{nm}}{2}}{\cos \delta_{nm} - \cos \theta} \quad (3.162)$$

The validity and accuracy of these results are extensively discussed and numerical results are presented in [22].

3.2.2 Transmission of Modal Energy Between Two Interior Regions

A waveguide junction between two waveguide sections is shown in Figure 3.53. It is of interest to determine the transmission coefficient T_{qn} which gives the coefficient of the q^{th} mode transmitted into guide "B" when an n^{th} mode is incident on the junction from within the guide "A". These transmission coefficients T_{qn} then are the qn^{th} entry in the scattering matrix $[S_{BA}]$. The T_{qn} is found via the modified PTD approach involving an aperture integral and a Ufimtsev type equivalent current integration as discussed previously in 3.2.1. The equivalent currents at the aperture are calculated in terms of the incident field in the Kirchhoff-Huygens' approximation for the aperture integral. In addition, the Ufimtsev type equivalent currents which represent a correction to the above aperture integral approximation are located at the aperture edges; i.e., at the edges of the junction forming the aperture. Furthermore, the surface equivalent currents at the aperture are given by

$$\text{and } \bar{J}_{eq} = \hat{n} \times \bar{H}_n^+ \quad (3.163)$$

$$\bar{M}_{eq} = \bar{E}_n^+ \times \hat{n} \quad (3.164)$$

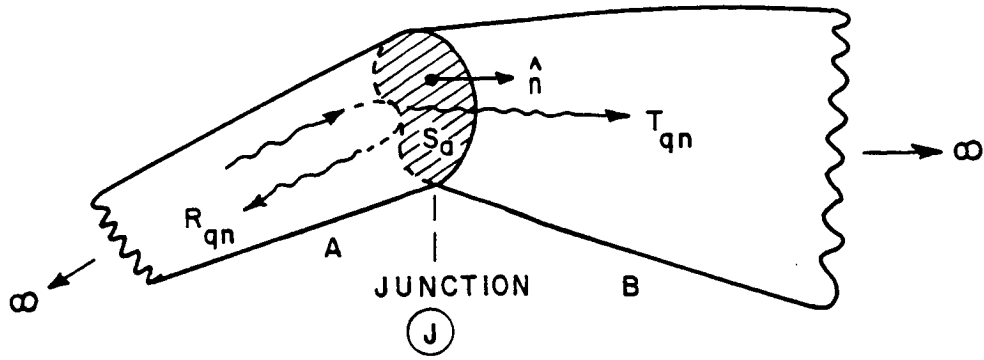


Figure 3.53. A waveguide junction joining two sections.

where \hat{n} is the unit vector at the aperture S_a pointing into region "B" as shown in Figure 3.53. These equivalent sources radiate into region "B".

An application of the reciprocity theorem to an appropriate set of fields in region "B" (as shown in Figure 3.54) will yield the strength of the modes transmitted into region "B". The Ufimtsev type equivalent currents are determined from the ray optical parts of incident electric and magnetic fields represented by $\bar{E}_{op,ni}^+$ and $\bar{H}_{op,ni}^+$ respectively, and they are given by

$$\bar{M}_\ell^u(Q) = \hat{\ell}' \sum_{i=1}^N \left[-\frac{1}{Y_0} \sqrt{\frac{8\pi}{jk}} \right] (\bar{H}_{op,ni}^+ \cdot \hat{\ell}') \frac{D_h^u(\psi_{ni}, \psi_{qi}; \tilde{\beta}_{oni}, \tilde{\beta}_{qi})}{2} \quad (3.165)$$

$$\bar{M}_d^u(Q) = \hat{n} \sum_{i=1}^N \left[-\sqrt{\frac{8\pi}{jk}} \right] (\bar{E}_{op,ni}^+ \cdot \hat{\ell}') \frac{D_s^u(\psi_{ni}, \psi_{qi}; \tilde{\beta}_{oni}, \tilde{\beta}_{qi})}{2 \cdot |\sin \psi_{qi}|} \quad (3.166)$$

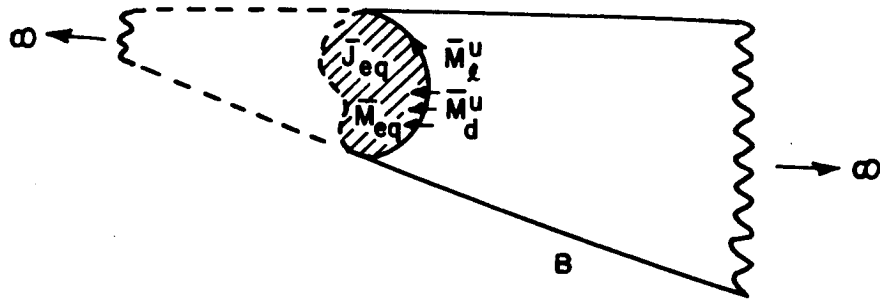


Figure 3.54. Equivalent sources at the aperture radiate in a uniform waveguide.

where the angles ψ_{qi} and β_{qi} are computed from the i^{th} ray trajectory of the q^{th} mode in region "B". Such an application of the reciprocity theorem was indicated earlier in Section 3.1, and hence it will not be described here. For the reasons presented earlier, only the η -directed component of the magnetic dipole source is included in (3.166).

The transmission coefficients are then given via reciprocity arguments by

$$T_{qn} = \frac{\int_{\text{rim}} \bar{H}_q^+ \cdot (\bar{M}_l^u + \bar{M}_d^u) d\ell' + \int_{S_a} (\bar{M}_{eq} \cdot \bar{H}_q^+) - \bar{J}_{eq} \cdot \bar{E}_q^+ ds'}{2 \iint_S \bar{E}_{qt} \times \bar{H}_{qt}^* h_\gamma h_\xi d\gamma d\xi} \quad (3.167)$$

Example:

Transmission of a TEM wave in a parallel-plate waveguide into a whispering gallery mode in an annular waveguide.

The geometry is shown in Figure 3.55. The dimensions and polarization allow only a TEM mode to propagate in the parallel-plate waveguide, and only one whispering gallery mode can likewise exist in the annular waveguide. The coupling from the incident TEM mode into the whispering gallery mode is found to be very close to unity for the values of radius "b" changing from 1λ (wavelength) to 2λ .

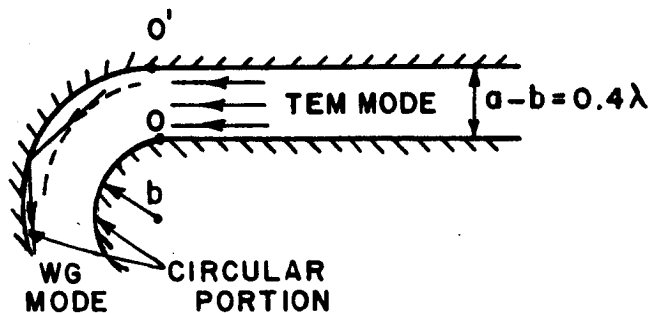


Figure 3.55 Termination of a parallel-plate waveguide with an annular waveguide.

CHAPTER IV

NUMERICAL AND MEASUREMENT RESULTS

In this chapter, the scattering matrices described above are combined to solve some two and three dimensional problems of interest. Whenever possible, the results are compared with other methods of solution or measurements.

a) Reflection from a 2-D horn antenna:

The voltage standing wave ratio (VSWR) of the two-dimensional horn antenna is calculated. The antenna is shown in Figure 4.1 and has a waveguide width of 0.375 wavelengths which is chosen so that only the dominant TEM mode will be excited far from the edges. As seen from the figure, the reflection is due to the discontinuities at the throat and the open end. The problem is solved using the procedure described in Chapter III, and the result is compared with the moment method calculation [43] in Figure 4.1. In the latter figure, the reflection due to the throat alone is shown separately, and as the horn angle (α) gets smaller, the reflection from the throat gets smaller also. However, for α small, there is strong reflection due to the discontinuity at the open end.

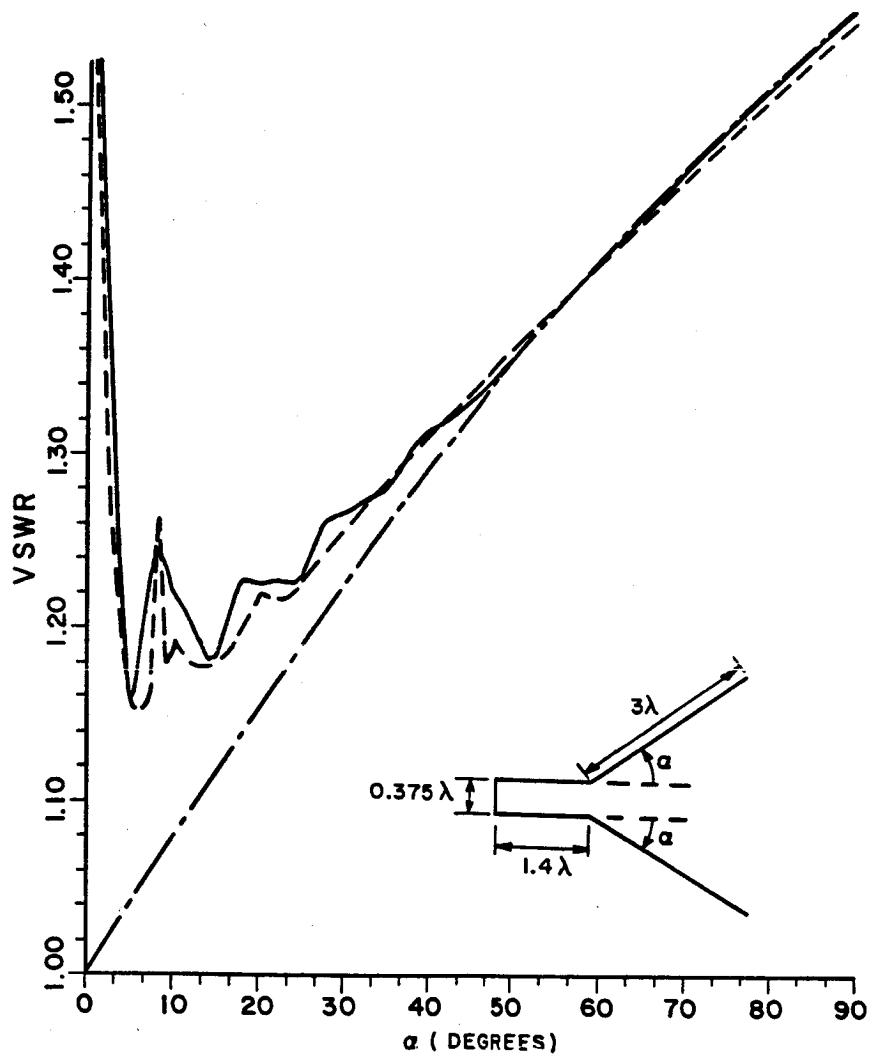


Figure 4.1. The geometry and VSWR of horn antenna.

- — — Only throat contribution
- Throat and rim contributions
- · - · - Moment method calculation

b) Reflection from sharp bends in a parallel-plate waveguide:

The reflection of the TEM mode due to sharp bends in the parallel plate waveguide of Figure 4.2 is calculated. The reflection and transmission coefficients are determined from the formulas developed in the previous chapter. The magnitude of the total reflection from both junctions is presented in Figures 4.3 and 4.4 for various bend angles (θ) and lengths (L) of the bent section, respectively.

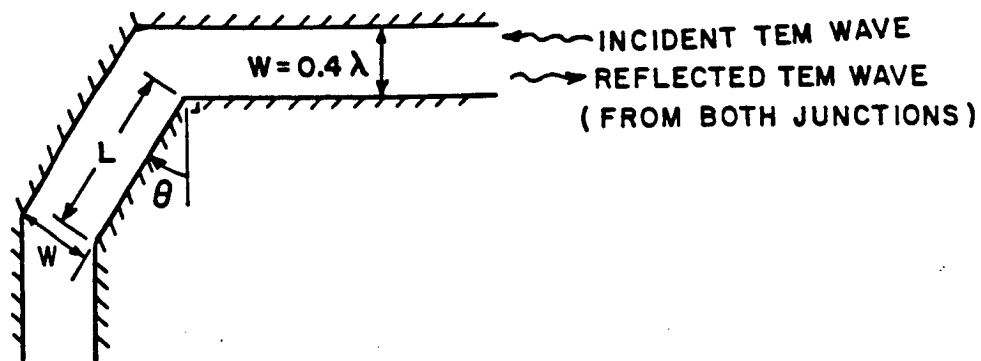


Figure 4.2. A planar 90° bend in a parallel-plate waveguide.

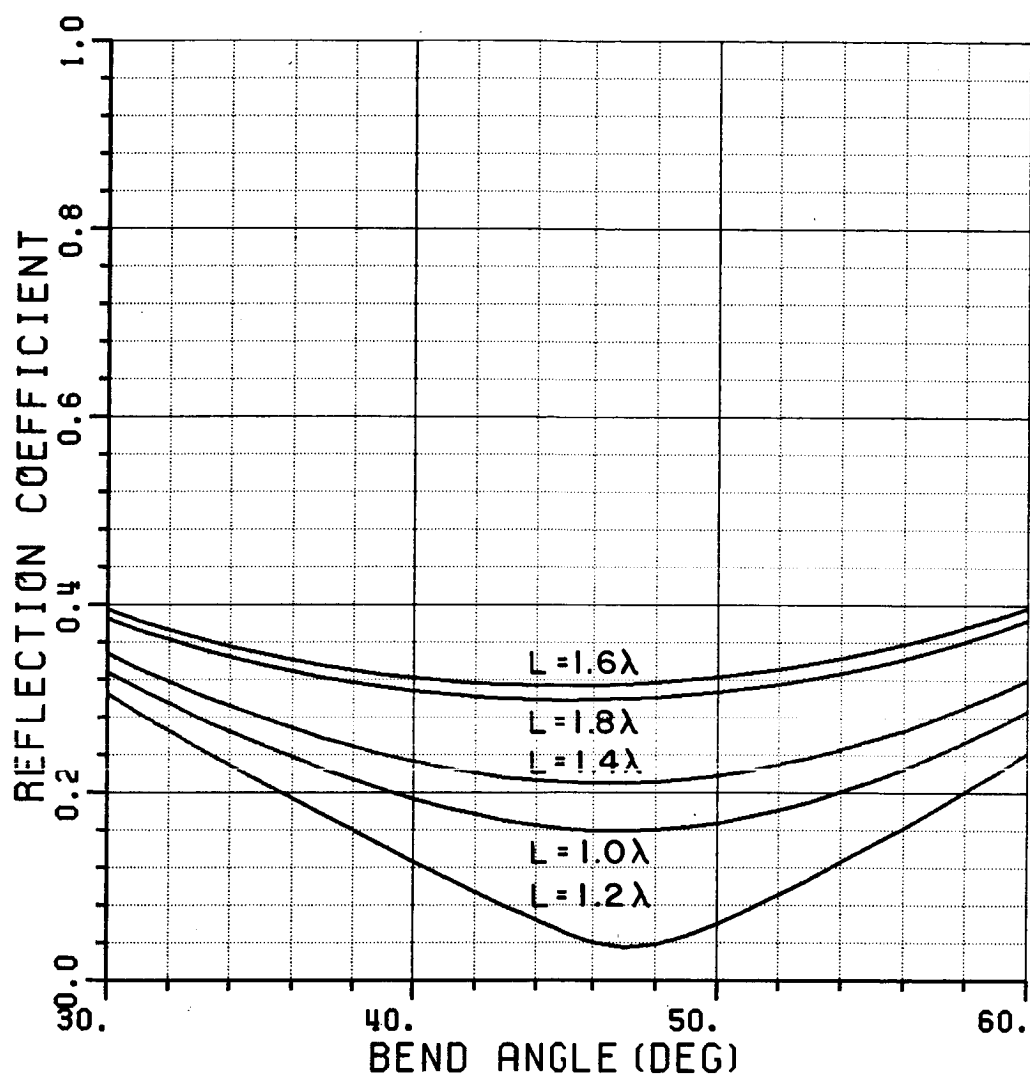


Figure 4.3. The magnitude of the reflection from the sharp bend of Figure 4.2 as a function of bend angle.

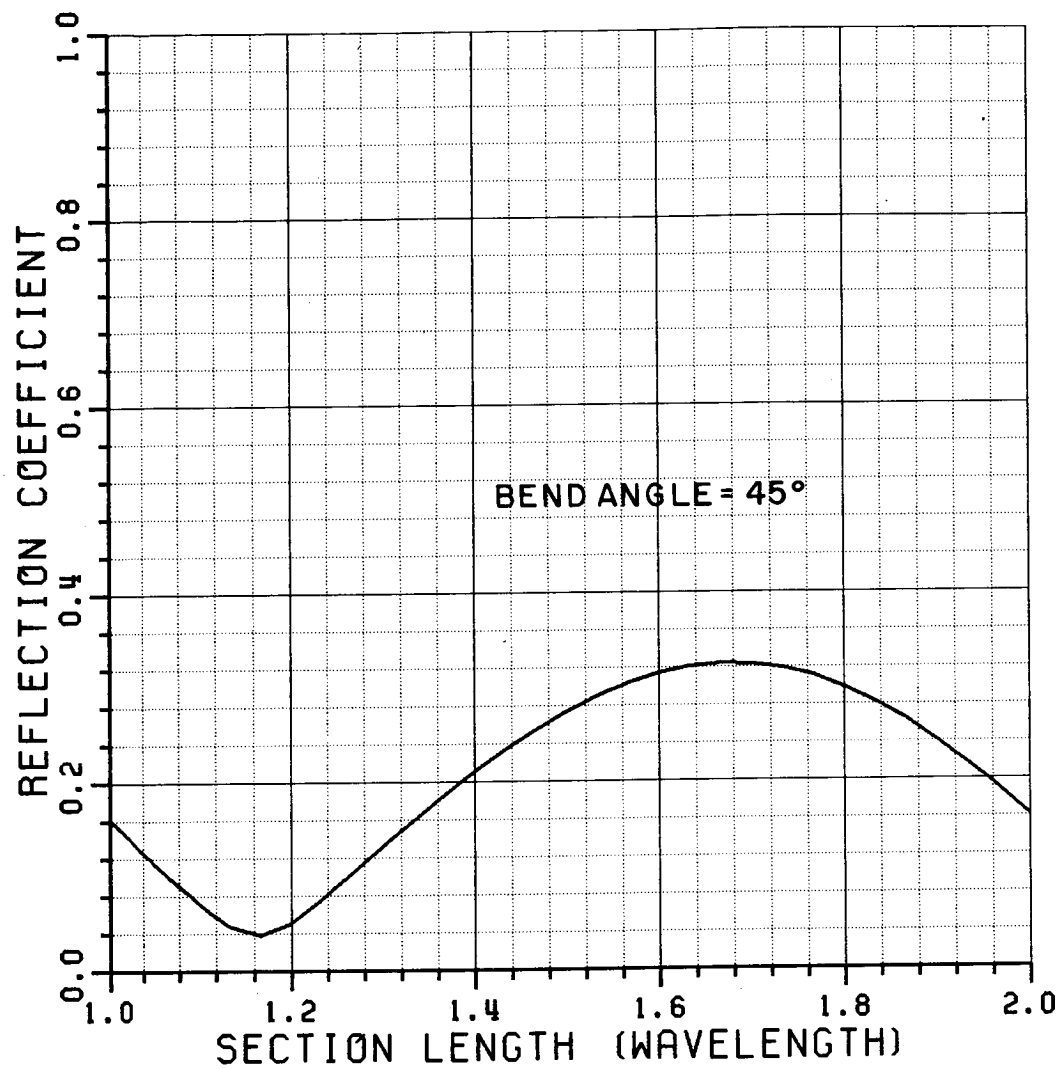


Figure 4.4. The magnitude of the reflection from the sharp bend of Figure 4.2 as a function of section length L .

c) Reflection from a circular bend in a parallel-plate waveguide:

The geometry of the circular (90°) bend in a parallel-plate waveguide is shown in Figure 4.5. The magnitude of the total reflection from both junctions is calculated as a function of the radius (b) as shown in Figure 4.6. Note that the reflection in the present case is very small compared to that which occurs in the case of a sharp bend as shown previously in example b).

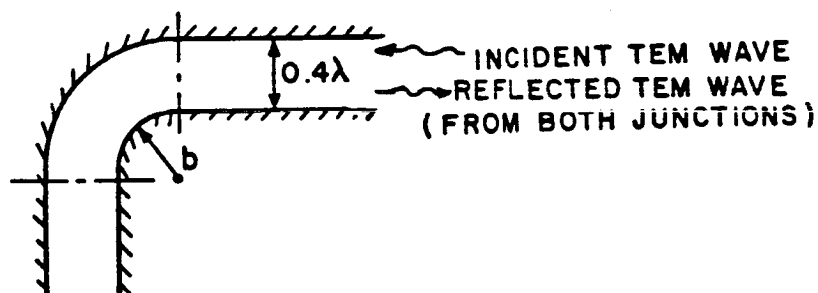


Figure 4.5. A uniform 90° bend in a parallel-plate waveguide.

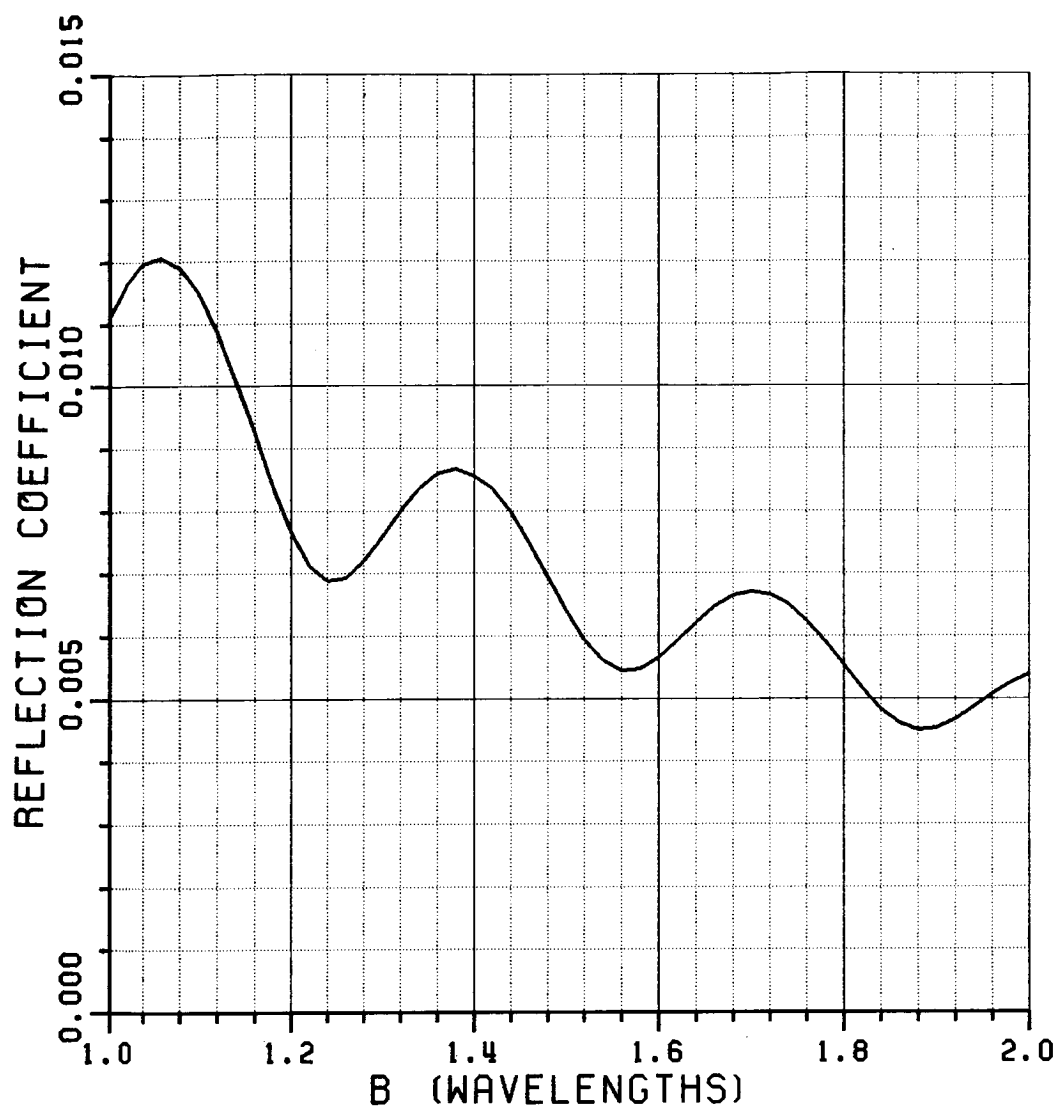


Figure 4.6. Magnitude of the reflection from a circular bend in a parallel-plate waveguide as a function of radius b .

d) Electromagnetic backscattering from a waveguide cavity model:

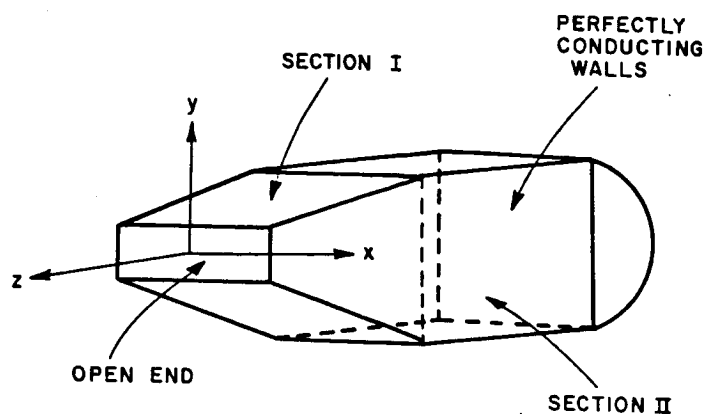
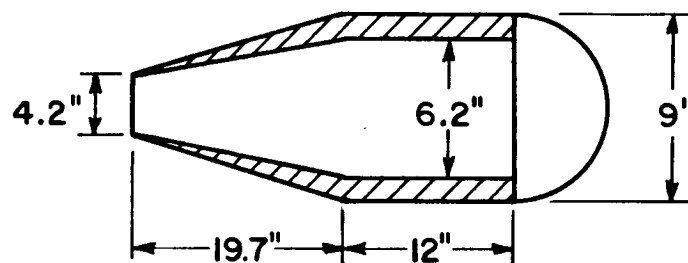


Figure 4.7. The geometry of the cavity model.

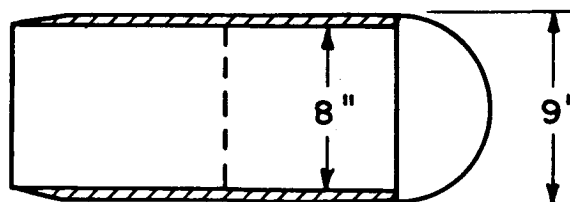
The waveguide model of interest in this work is shown in Figure 4.7. It is basically an open-ended cavity composed of two waveguide sections. The first section is part of a sectoral waveguide with one end open; whereas the other end of this section is connected to a second section which is a uniform waveguide with a planar termination at its far end. The exterior of the second section is curved at the back end to minimize the scattering coming from the exterior features of the structure. The axis of the waveguide coincides with the \hat{z} -axis of the

coordinate system, and the \hat{y} -axis is in the vertical direction. The model is made of wood and then coated with a conductive paint. The dimensions of the cavity are shown in Figure 4.8.

The side walls in each of the waveguide sections are parallel to the y - z plane; therefore, there is no tapering effect to be included for those walls. The first step in the analysis is finding the modal field expressions in the rectangular and sectoral waveguide sections. This is done in Appendices A and C where the expressions are given, and the relationship between the mode sets of sectoral and rectangular waveguides is shown. Therefore, the effect of tapering can be included



(a) SIDE VIEW



(b) TOP VIEW

Figure 4.8. Side and top view of the cavity model.

by modifying the propagation constant in the rectangular waveguide mode expressions which are transverse to the \hat{x} -direction. So, the analysis is first done on a rectangular cavity as shown in Figure 4.9, and the solution is modified subsequently to include the effect of tapering.

The geometry of the rectangular waveguide structure is shown in Figure 4.9. The cross-sectional dimensions of the waveguide are "a" and "b" in the x and y-coordinate directions, respectively. The length of the waveguide from the open end to the back wall is given by the dimension (L). All of the walls of the cavity are assumed to be perfectly conducting. The structure is illuminated by an incident plane wave which is given by

$$\vec{E}^i = (E_{\theta}^i \hat{\theta} + E_{\phi}^i \hat{\phi}) e^{jk(x \sin \theta^i \cos \phi^i + y \sin \theta^i \sin \phi^i + z \cos \theta^i)} \quad (4.1)$$

where $0 < \theta^i < \pi/2$, $0 < \phi^i < 2\pi$ are the elevation and aspect angles of the incident field direction, respectively.

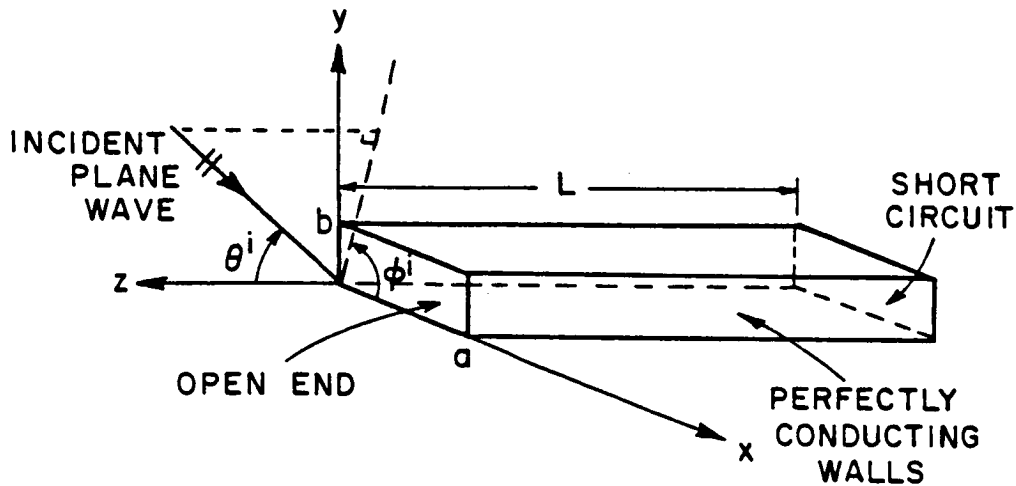


Figure 4.9. Geometry of an open-ended rectangular waveguide cavity.

The scattered field is composed of two main contributions: 1) the field scattered from the open end by itself, and 2) the field which is radiated from the open end. The latter undergoes multiple reflections between the open end and termination at the back wall after it is initially coupled into the waveguide from the incident field. However, from experimental measurements, these multiple interactions are determined to be negligibly small for the cavity model being considered here; therefore, their effect is ignored in this study. Only the first order interaction is discussed which includes the coupling of the incident energy into the interior waveguide modes through the open end, and subsequent reflection of these modes from the back wall and finally, the radiation of these reflected modes from the open end. In Appendix I, it is shown that the mechanisms of coupling into and radiation from the open-end are equivalent via the reciprocity principle.

For a finite cross-section, the field incident at the open-end excites a finite number of modes which propagate in the $-\hat{z}$ direction without attenuation, as well as an infinite number of evanescent modes which attenuate exponentially away from the open end in the $-\hat{z}$ direction. In this study, it will be assumed that the dimensions "a" and "b" are large enough to excite at least a few propagating modes and the length "L" is long enough for the effects of the evanescent modes to be negligible.

i) Results for the Scattering only from the Rim

To check the validity of the analysis, the scattering from the rim is calculated using (3.11), and results are compared with a set of measurements obtained using the Compact Range Facility at the ElectroScience Laboratory, The Ohio State University. The measurements were performed on a cavity model as shown in Figures 4.7 and 4.8. In order to remove the interior cavity effects, the inner surface of the back wall of the cavity was covered with absorbing material. Two sets of measurement results were obtained.

a) At a fixed frequency, the angle (θ) from the z-axis is varied in the horizontal ($\phi=0$) (or vertical ($\phi=90^\circ$)) plane from 0 to 90 degrees.

b) At a fixed angle (θ) in the horizontal ($\phi=0$) (or vertical ($\phi=90^\circ$)) plane the frequency is varied from 8 GHz to 12 GHz in 10 MHz steps. Therefore, a bandlimited frequency response is obtained. From this response, a time domain scattering response is generated to better illustrate the scattering mechanisms. This is accomplished by processing the frequency response through a Kaiser-Bessel window and inverse Fourier transforming the windowed result using an FFT algorithm. Since the measured spectrum is bandlimited, the time domain response represents the impulse response of the target which is convolved with

$$\frac{2}{\pi} \frac{\sin \omega_b t}{t} \cos \omega_0 t \quad (4.2)$$

where ω_b =half-bandwidth (2 GHz), and ω_0 is the center frequency which is 10 GHz in this case.

The measured and calculated radar cross section (RCS) patterns are shown in Figures 4.10 through 4.21 for different polarizations and frequencies. In each figure, measurements (solid line) and calculations (dashed line) are drawn on the same scale in terms of dB relative to square meter (dBSM). Figures 4.10 through 4.15 correspond to a horizontal (x-z) scan; whereas, Figures 4.16 through 4.21 correspond to a vertical (y-z) scan. In both the horizontal and vertical scans, the radar cross section is measured and analyzed for two polarizations ($\hat{\phi}$ and $\hat{\theta}$). Finally, each case is repeated at three different frequencies, namely around 8, 10 and 12 GHz. In both the horizontal and vertical scans, a $\hat{\phi}$ directed incident electric field will not diffract from two edges which are parallel to the scan plane. Therefore, the contribution to the radar cross section in these cases is dominated by the diffracted fields from the remaining two edges. As shown in Figures 4.10 through 4.12 and 4.16 through 4.18, the calculations agree reasonably well with the measurements. However, for the other polarization ($\hat{\theta}$), all four edges of the open end contribute to the radar cross section, and the contribution from two of these four edges reduces essentially to that from the end points (or corners). As shown in Figures 4.13 through 4.15 and 4.19 through 4.21, the agreement between the measured and calculated results is not as good as the $\hat{\phi}$ -polarization case, especially in the plane ($\phi=0$) pattern. The reason for this discrepancy will become clearer after discussing the frequency domain responses, suffice it to say for now that it is due to the imperfections of the model.

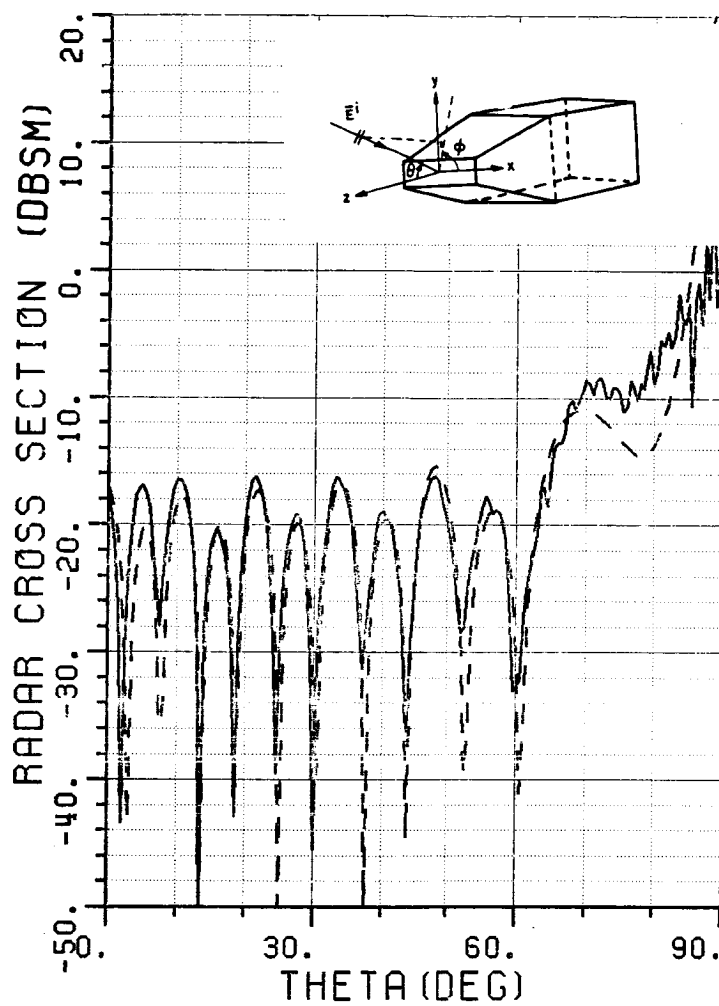


Figure 4.10. Radar cross section pattern at $f=8.02$ GHz,
 $\vec{E}^i = \hat{\phi}$, $\phi=0$ plane.
 — measured, --- calculated

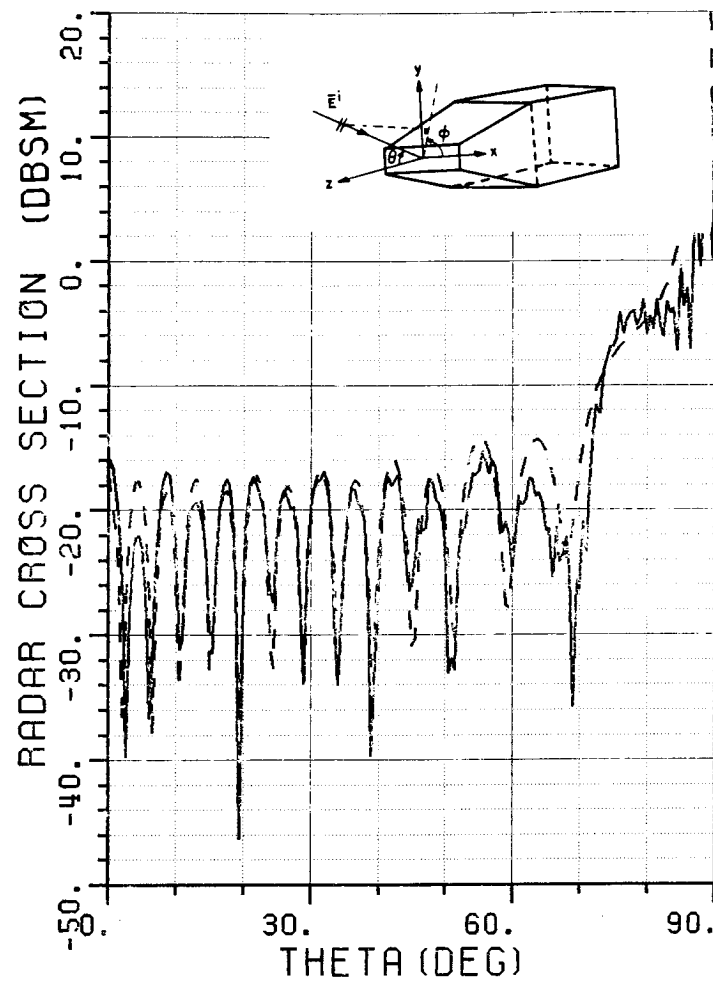


Figure 4.11. Radar cross section pattern at $f=9.98$ GHz,

$\vec{E}^i = \hat{\phi}$, $\phi=0$ plane.

— measured, --- calculated

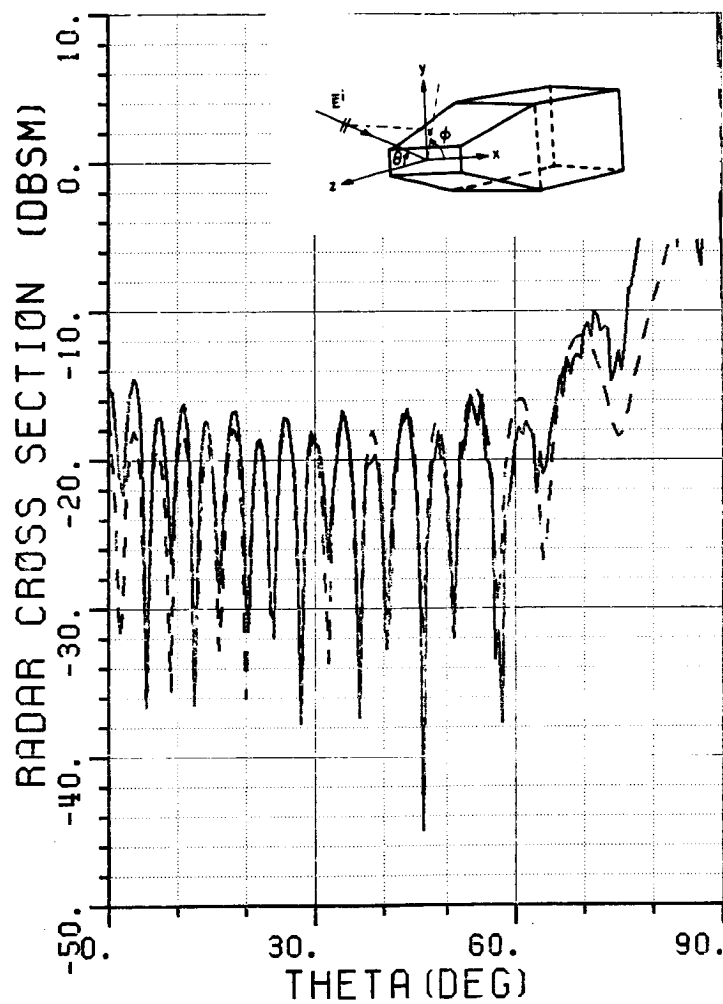


Figure 4.12. Radar cross section pattern at $f=11.95$ GHz,
 $\vec{E}^i = \hat{\phi}$, $\phi=0$ plane.
 — measured, --- calculated

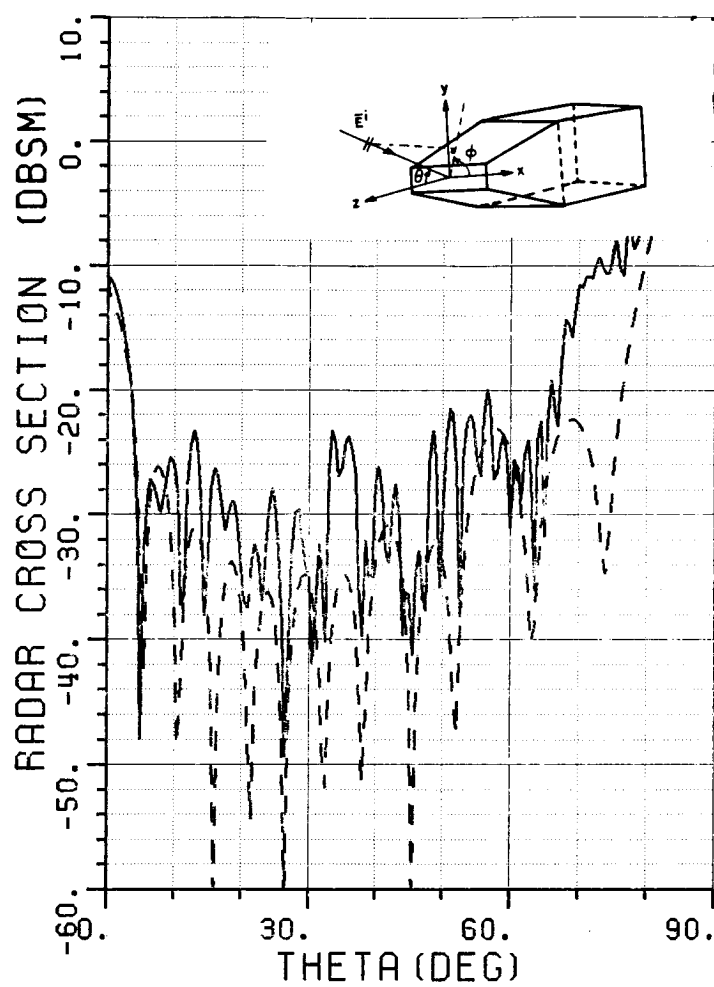


Figure 4.13. Radar cross section pattern at $f=8.02$ GHz,
 $\vec{E}^i = \hat{\theta}$, $\phi=0$ plane.
 — measured, --- calculated

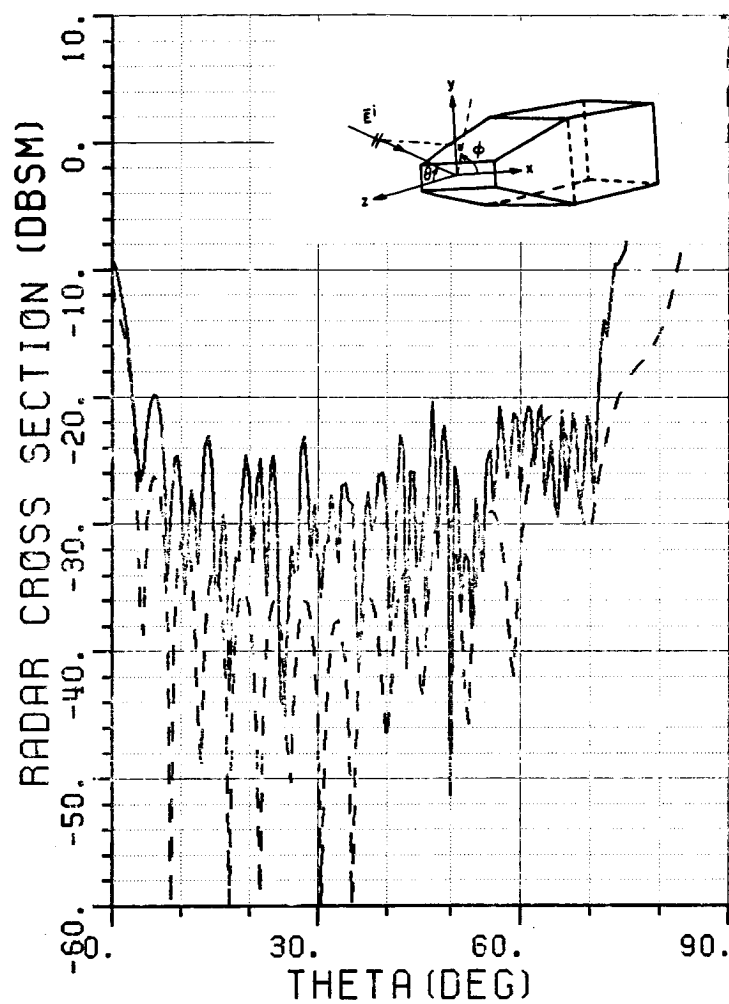


Figure 4.14. Radar cross section pattern at $f=9.98$ GHz,
 $\vec{E}^i = \hat{\theta}$, $\phi=0$ plane.
 — measured, --- calculated

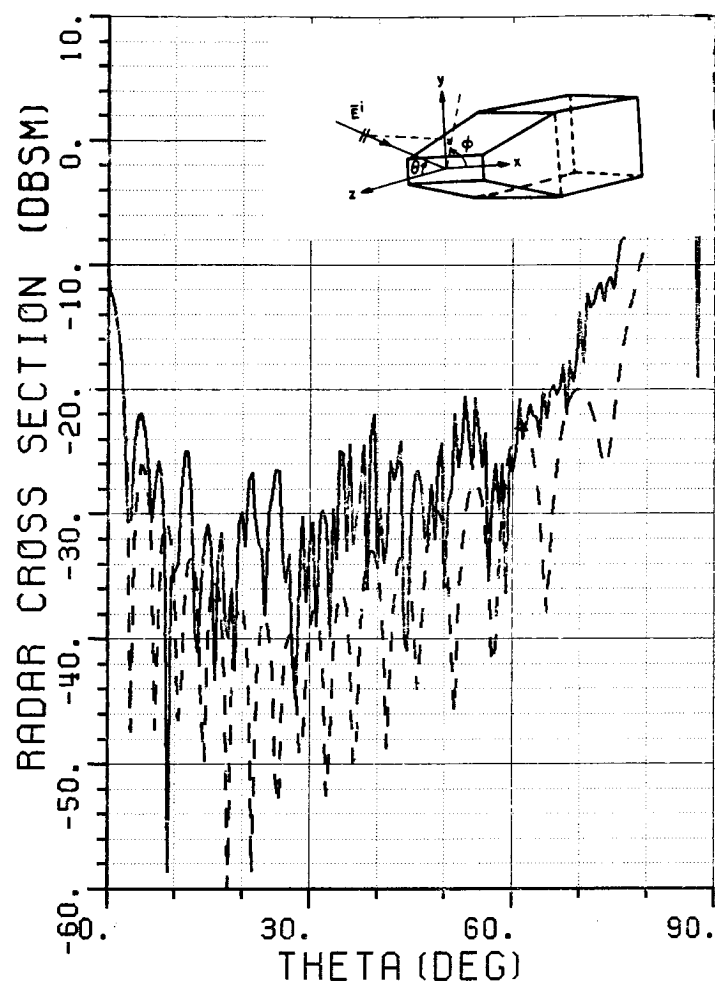


Figure 4.15. Radar cross section pattern at $f=11.95$ GHz,
 $\vec{E}^i = \hat{\theta}$, $\phi=0$ plane.
 — measured, --- calculated

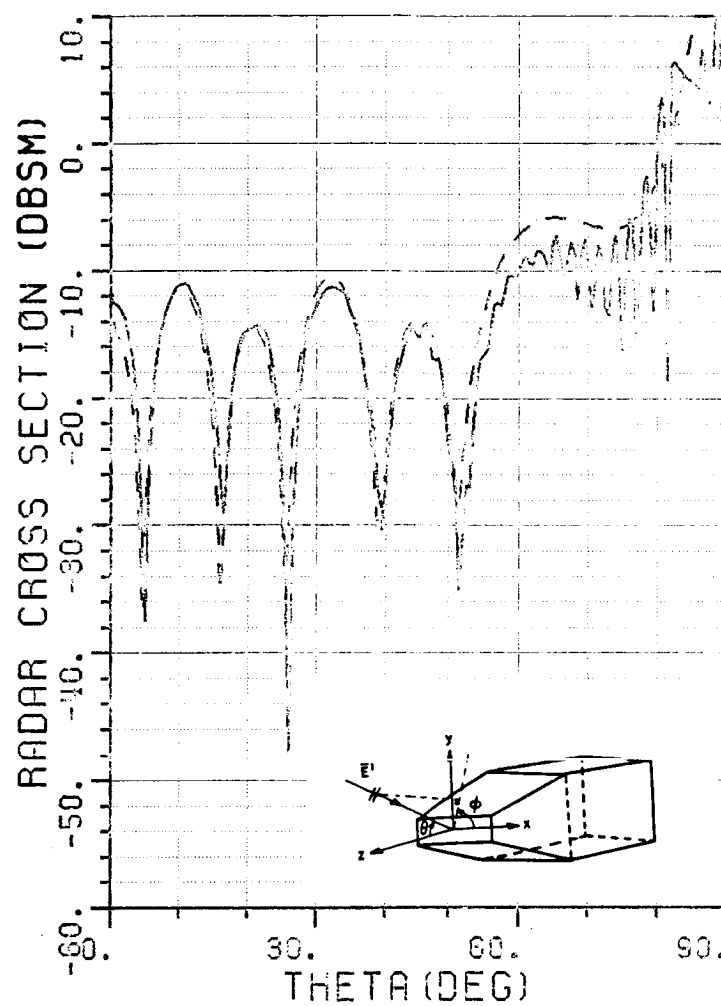


Figure 4.16. Radar cross section pattern at $f=8.02$ GHz,
 $\vec{E}^i = \hat{\phi}$, $\phi=90^\circ$ plane.
 — measured, --- calculated

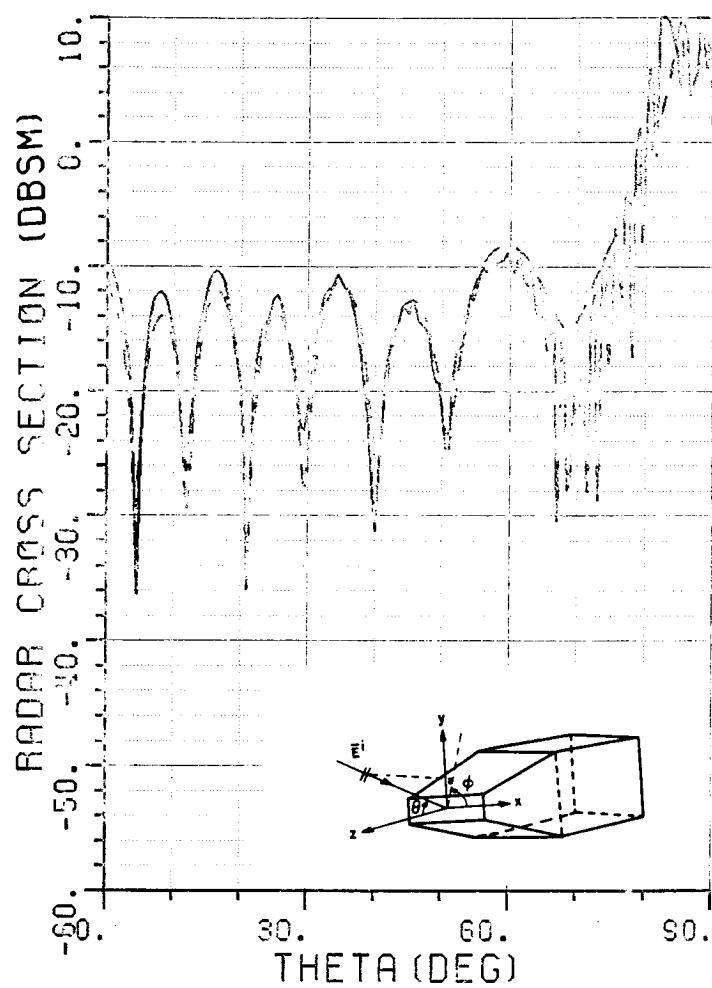


Figure 4.17. Radar cross section pattern at $f=9.98$ GHz,
 $\vec{E}_i = \hat{\phi}$, $\phi=90^\circ$ plane.
 — measured, --- calculated

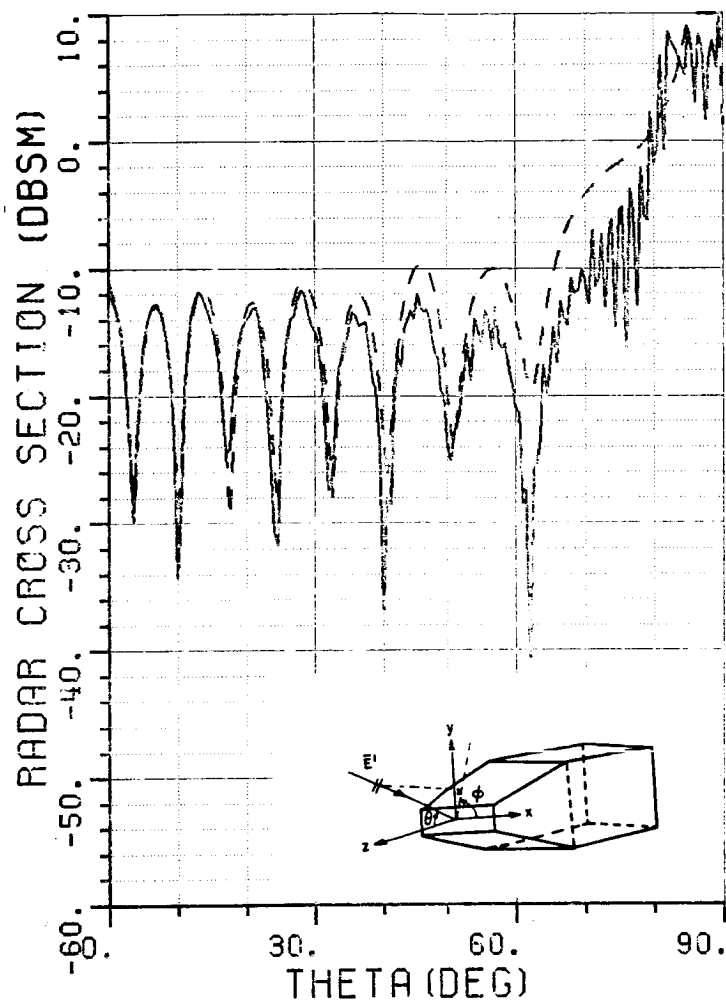


Figure 4.18. Radar cross section pattern at $f=11.95$ GHz,
 $\vec{E}^i = \hat{\phi}$, $\phi=90^\circ$ plane.
 — measured, --- calculated

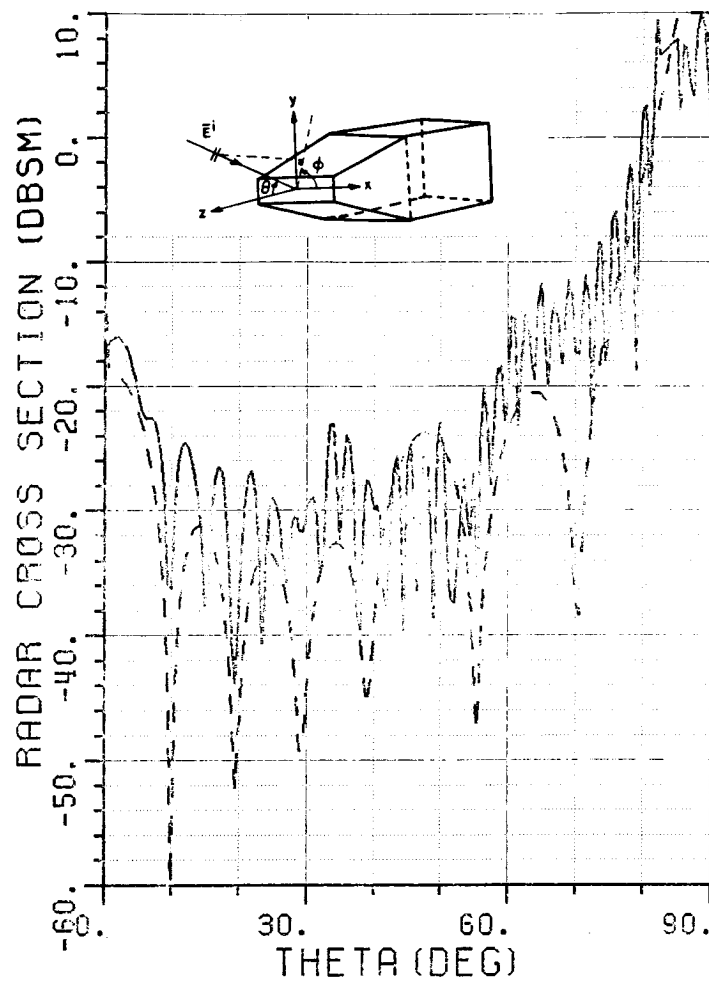


Figure 4.19. Radar cross section pattern at $f=8.02$ GHz,

$\vec{E}^i = \hat{\theta}$, $\phi=90^\circ$ plane.

— measured, --- calculated

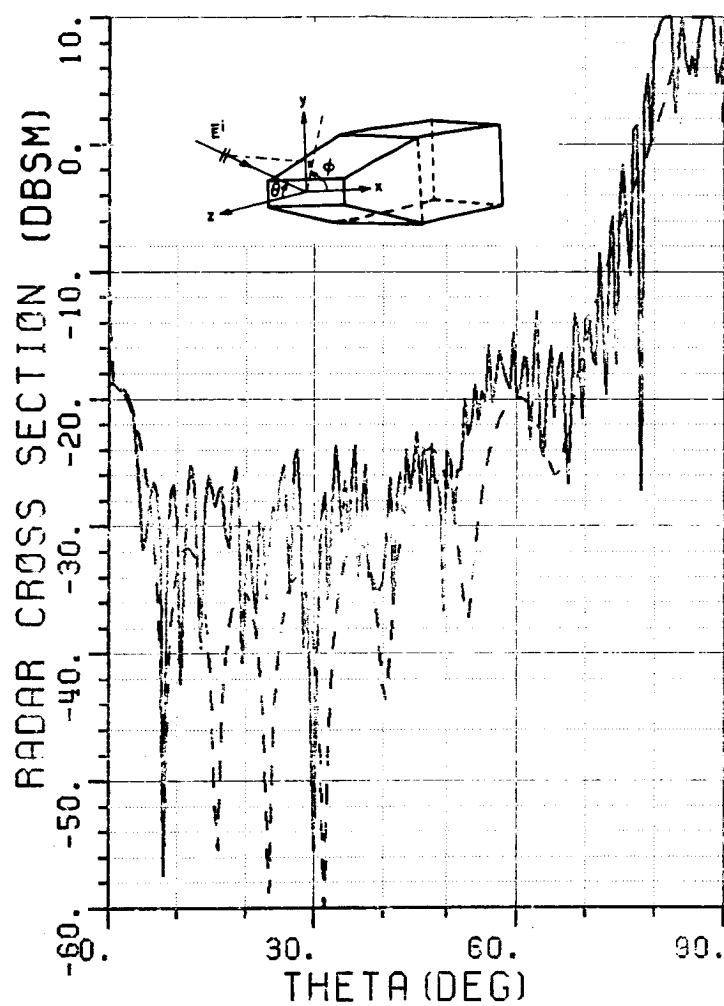


Figure 4.20. Radar cross section pattern at $f=9.98$ GHz,
 $\vec{E}^i = \hat{\theta}$, $\phi=90^\circ$ plane.
 — measured, --- calculated

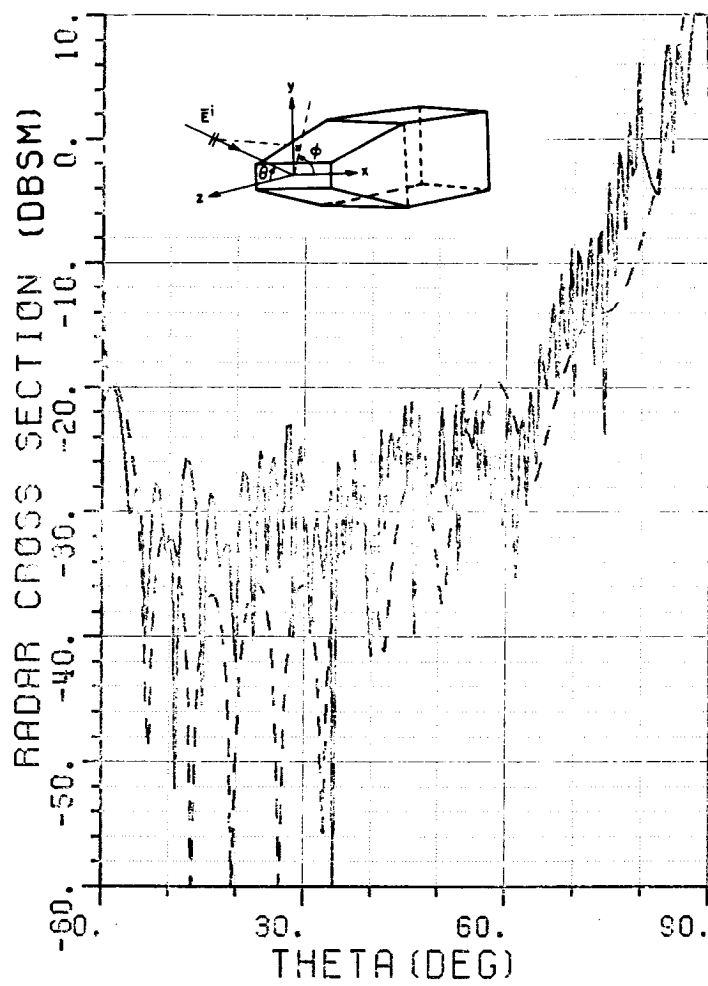


Figure 4.21. Radar cross section pattern at $f=11.95$ GHz,
 $\vec{E}^i = \hat{\theta}$, $\phi=90^\circ$ plane.
 — measured, --- calculated

Finally one notes that the rim scattering analysis performed here is valid for aspect angles away from the shadow boundaries of the diffracted field. For aspect angles close to the shadow boundaries of the edges (θ close to 90 degrees) the approach described here should be modified. This modification will not be given here.

Frequency scans are done in the horizontal ($\phi=0$) plane, for the two different polarizations and the angle (θ) fixed at four different values, namely, θ equals 0, 15, 30 and 45 degrees. The measured (solid line) and calculated (dashed line) radar cross section results are plotted on the same graph and given in dBSM. The phase variation of the radar cross section is also shown in the figures. In order to be able to make a phase comparison, the measured data has been processed so that the two results have the same phase center. The frequency spectra are then inverse Fourier transformed to obtain the time domain responses. As explained before the time domain response is not an impulse response although it has been denoted as such on the plot for descriptive purposes. Therefore, in order to make the comparison easier, the curves corresponding to measured and calculated time domain returns are shifted by an equal amount from the center line. The scale in the time domain is dimensionless and should be taken as a relative scale. Finally, due to the malfunctions of electronic instrument during measurements, there are some glitches in the measured data. They are kept as they appeared originally, since their presence does not affect the overall characteristics of the curves.

As in the case of angular patterns, the amplitude and phase of the measured and calculated RCS results as a function of the frequency are

in good agreement especially for a $\hat{\phi}$ polarized field (Figures 4.22 through 4.29). Also, it can be seen from the time domain plots that almost all of the measured return is from the rim at the open end. The absorber put at the back very effectively removed any internal cavity effects.

In the case of horizontal ($\hat{\theta}$) polarization, (Figures 4.30 through 4.37) the time domain plots show a relatively large return occurring later in time than the return from the open end. The variation of the position of this return with different values of (θ) implies that it is coming from the external surfaces of the cavity model. Therefore as shown in Figures 4.32 through 4.37, the comparison between calculated and measured radar cross section results is not good. This also explains the discrepancy in the angular patterns of Figures 4.13 through 4.15. In order to compare the returns coming from the open end only, the unwanted return was gated out from the measured time domain data as indicated in each figure. The actual measured and calculated returns are shown with constant shifts, as before. These time domain plots were then converted into the frequency domain and shown on the same graph. As can be seen in Figures 4.32, 4.34, and 4.36 the calculated (long-dashed line) and gated-out measured (short-dashed line) results agree fairly well since they both correspond to the returns pertaining to the rim of the cavity.

As explained before, the time domain responses shown are not the actual impulse responses because of the bandlimited nature of the data in frequency domain. If one had more frequency domain information then the time domain results would be closer to the true impulse responses.

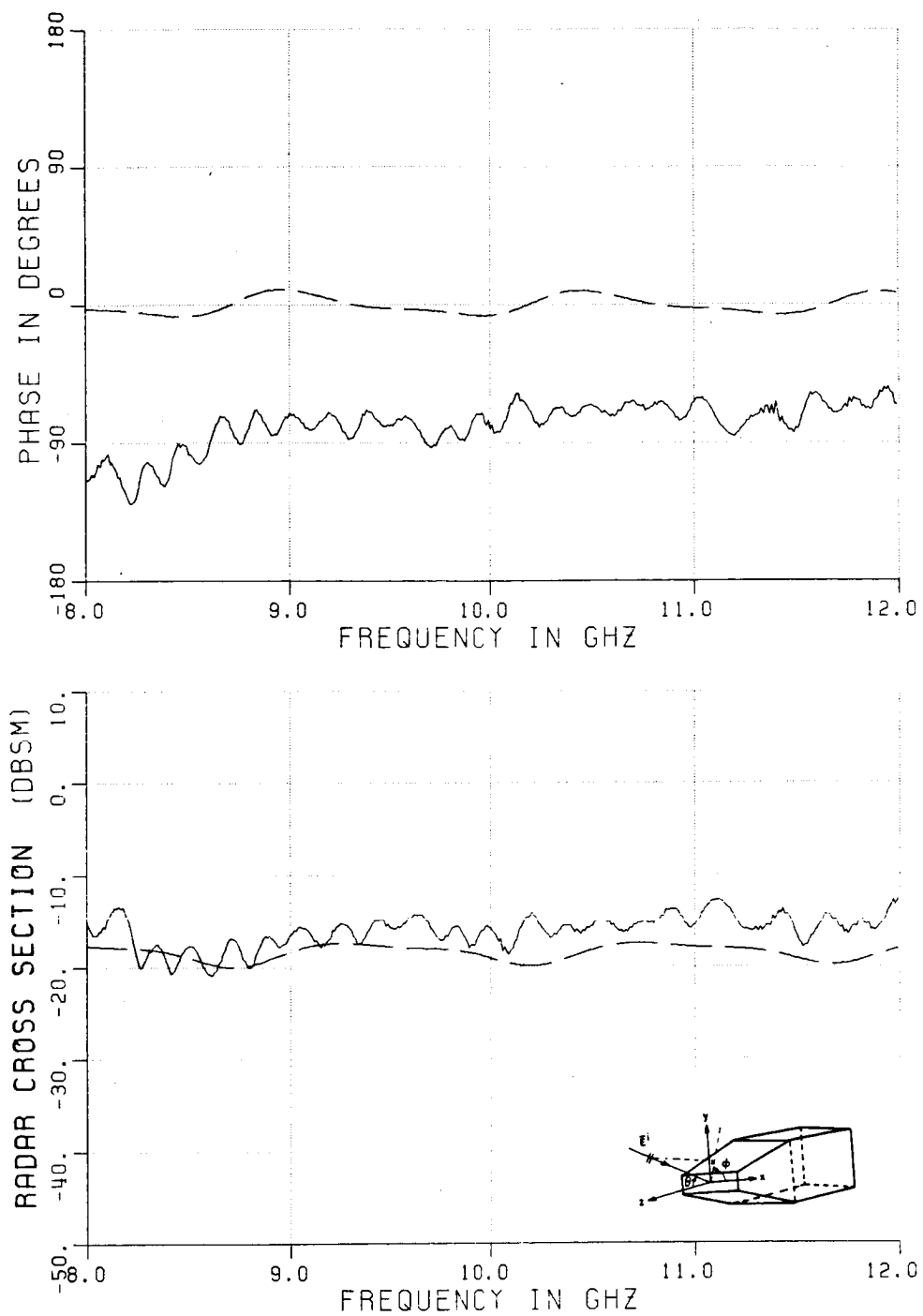


Figure 4.22. Variation of radar cross section with frequency.

$$\vec{E}^i = \hat{\phi}, \phi=0, \theta=0.$$

— measured, --- calculated

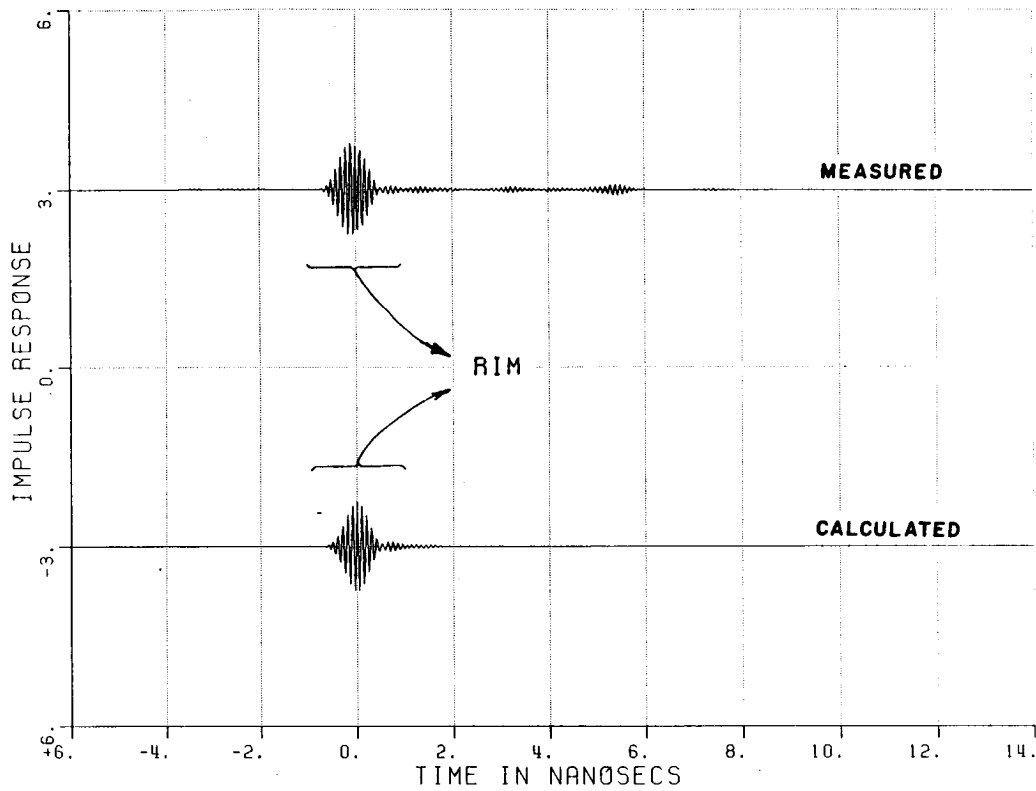


Figure 4.23. Inverse Fourier transforms (i.e., time domain plots) of the results in Figure 4.22.

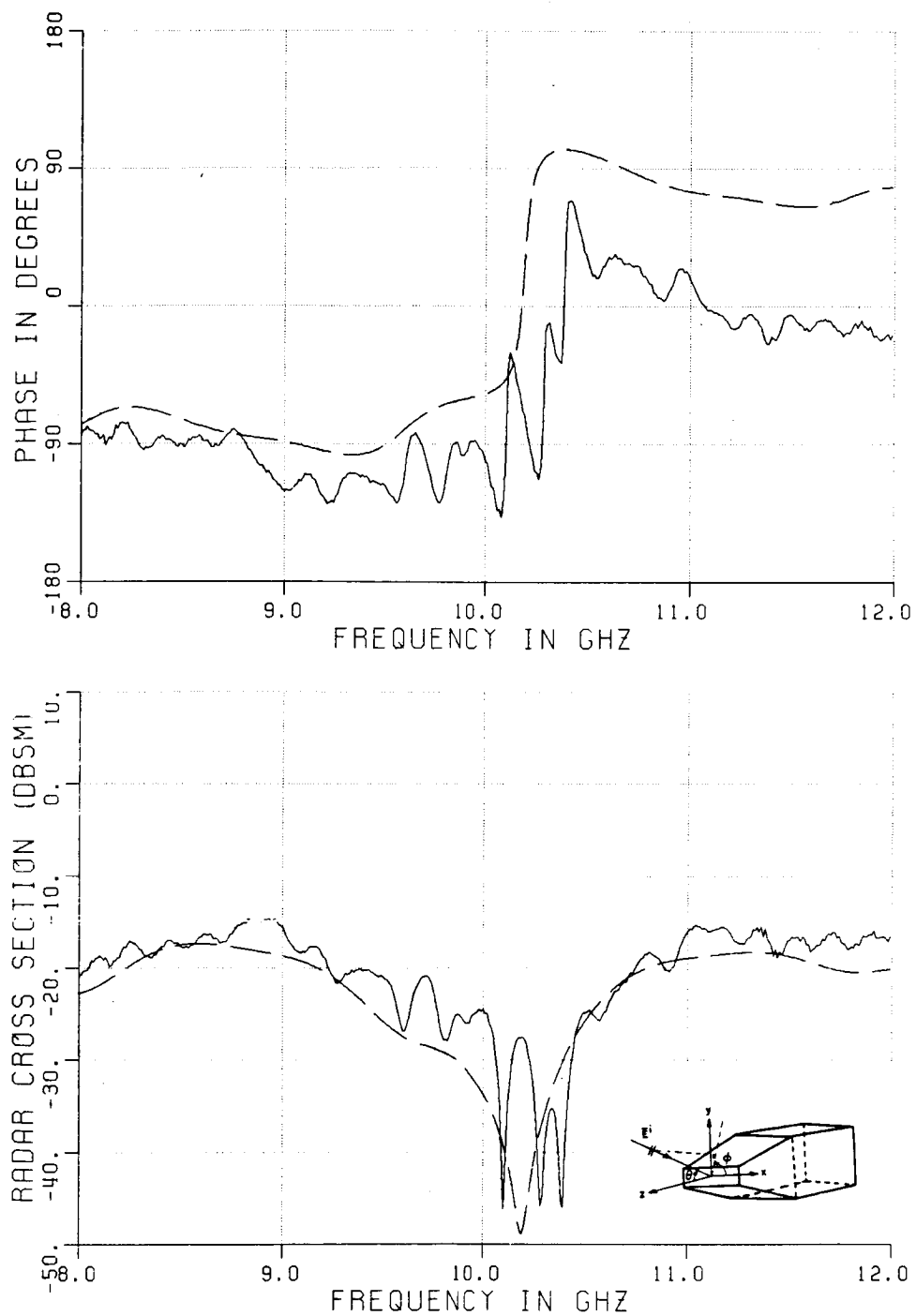


Figure 4.24. Variation of radar cross section with frequency.

$$\vec{E}^i = \hat{\phi}, \phi = 0, \theta = 15^\circ$$

— measured, --- calculated

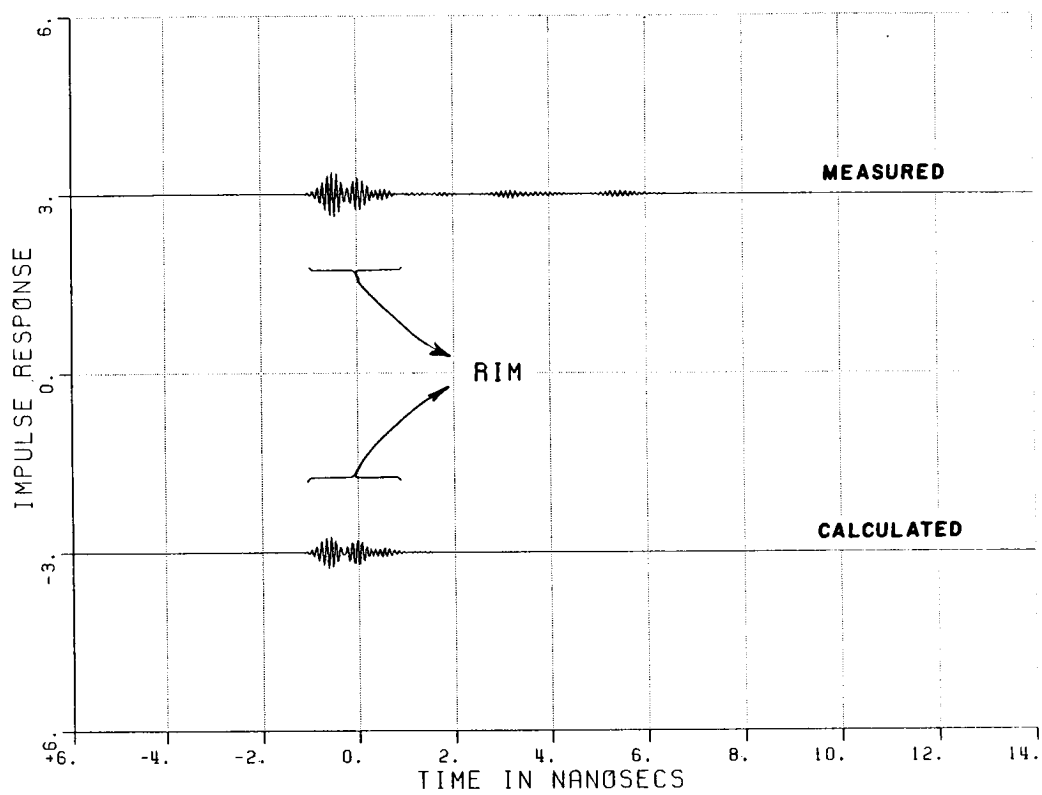


Figure 4.25. Inverse Fourier transforms (i.e., time domain plots) of the results in Figure 4.24.

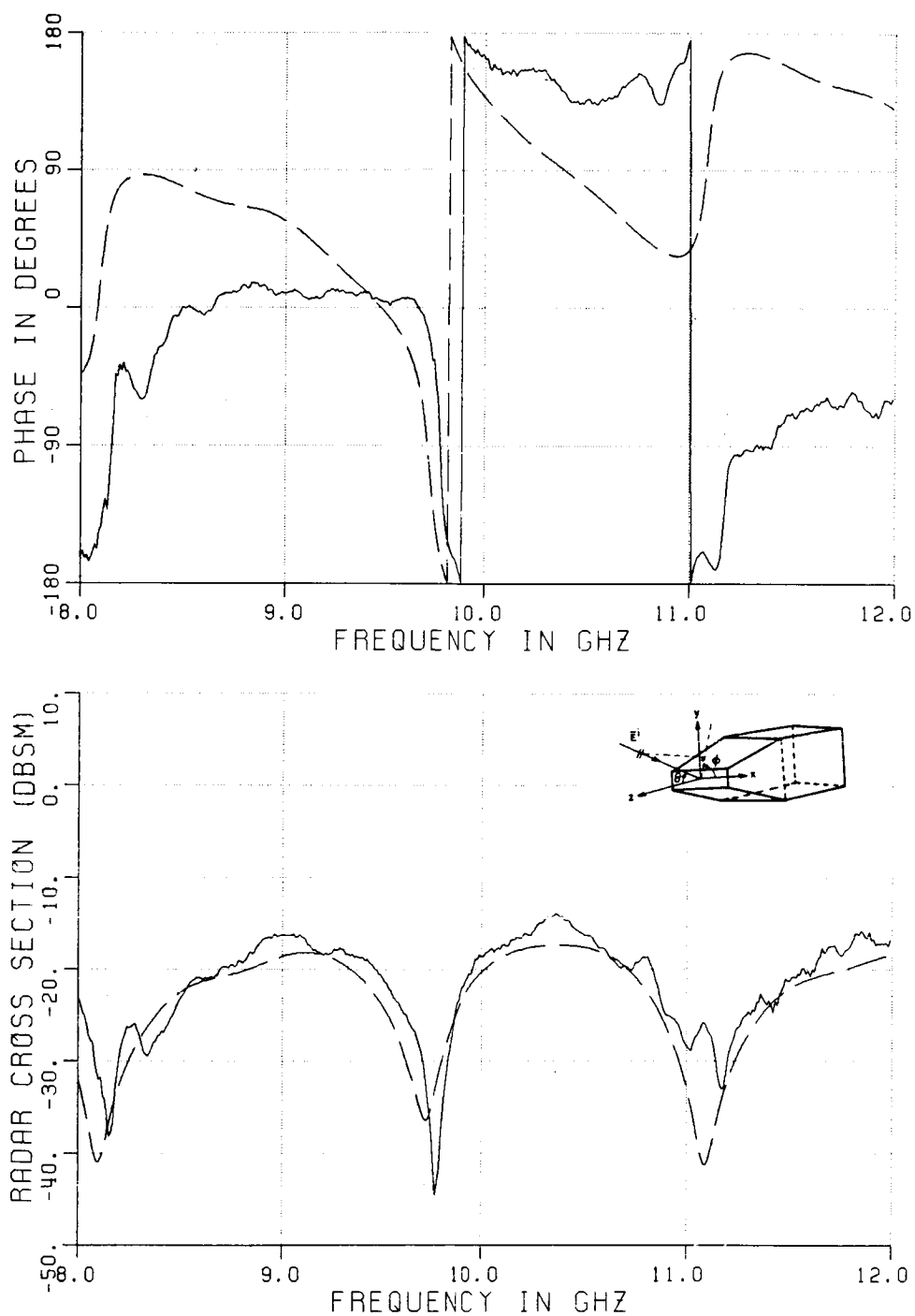


Figure 4.26. Variation of radar cross section with frequency.

$$\vec{E}^i = \hat{\phi}, \phi=0, \theta=30^\circ$$

— measured, --- calculated

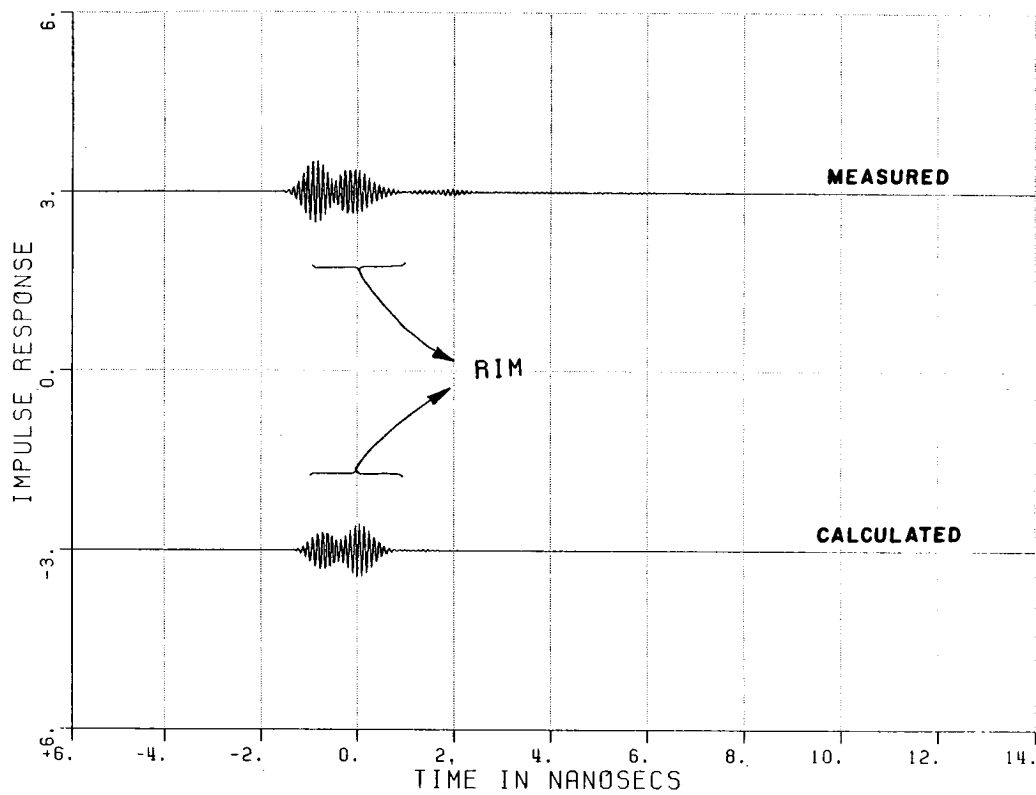


Figure 4.27. Inverse Fourier transforms (i.e., time domain plots) of the results in Figure 4.26.

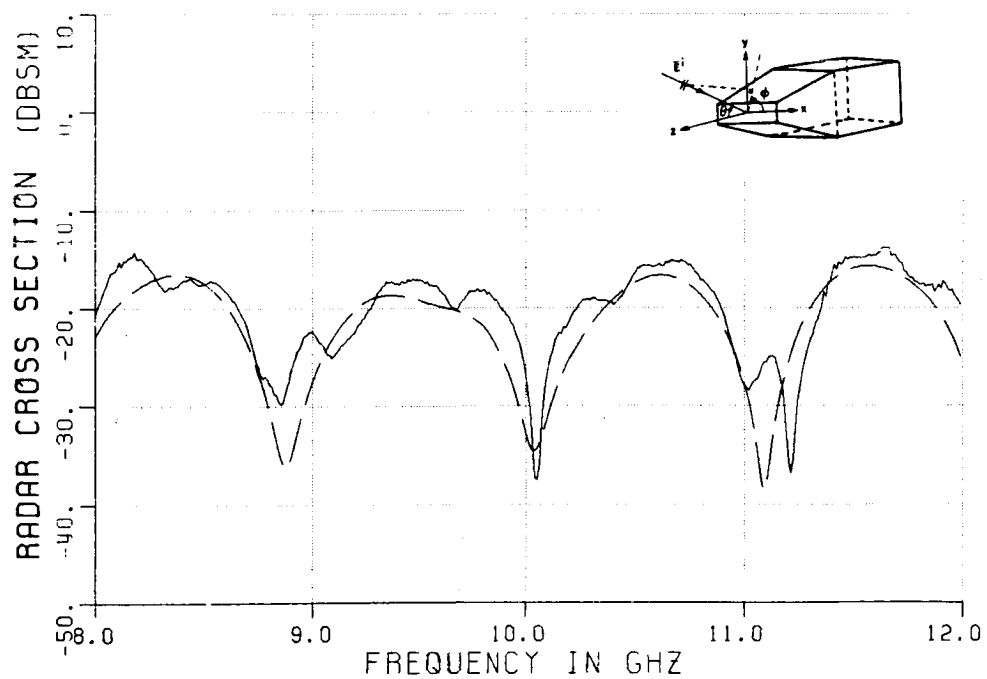
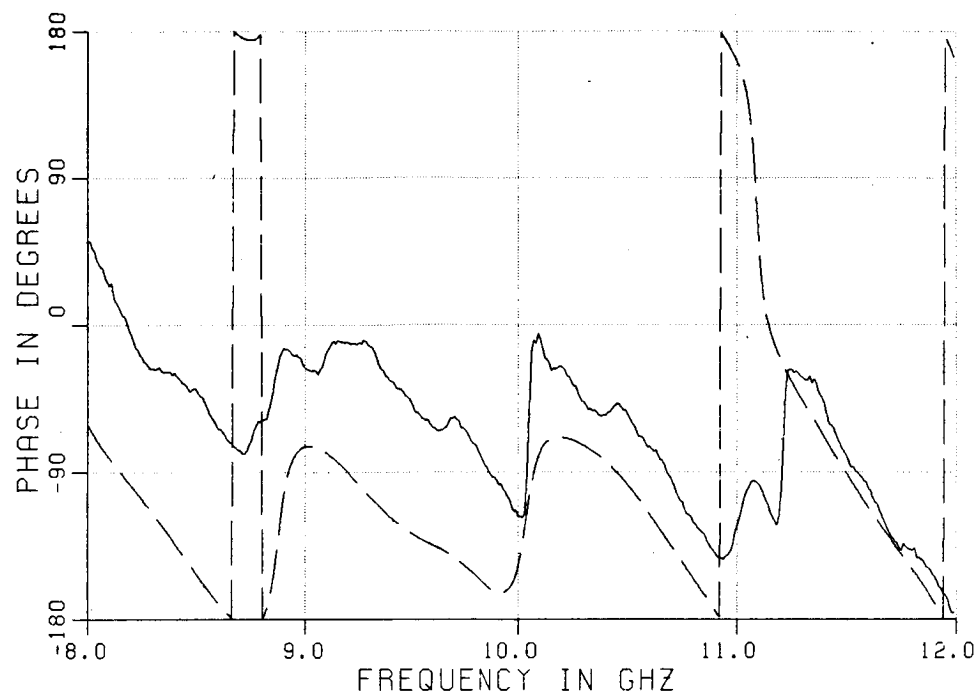


Figure 4.28. Variation of radar cross section with frequency.

$$\vec{E}^i = \hat{\phi}, \phi=0, \theta=45^\circ$$

— measured, --- calculated

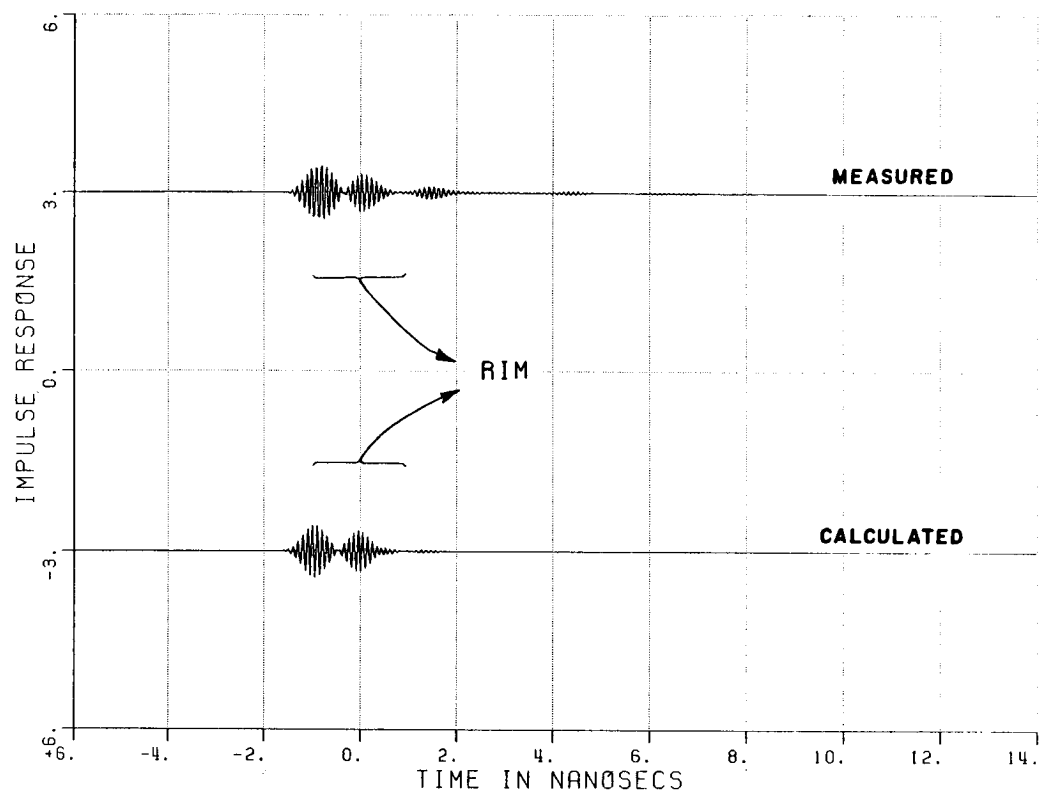


Figure 4.29. Inverse Fourier transforms (i.e., time domain plots) of the results in Figure 4.28.

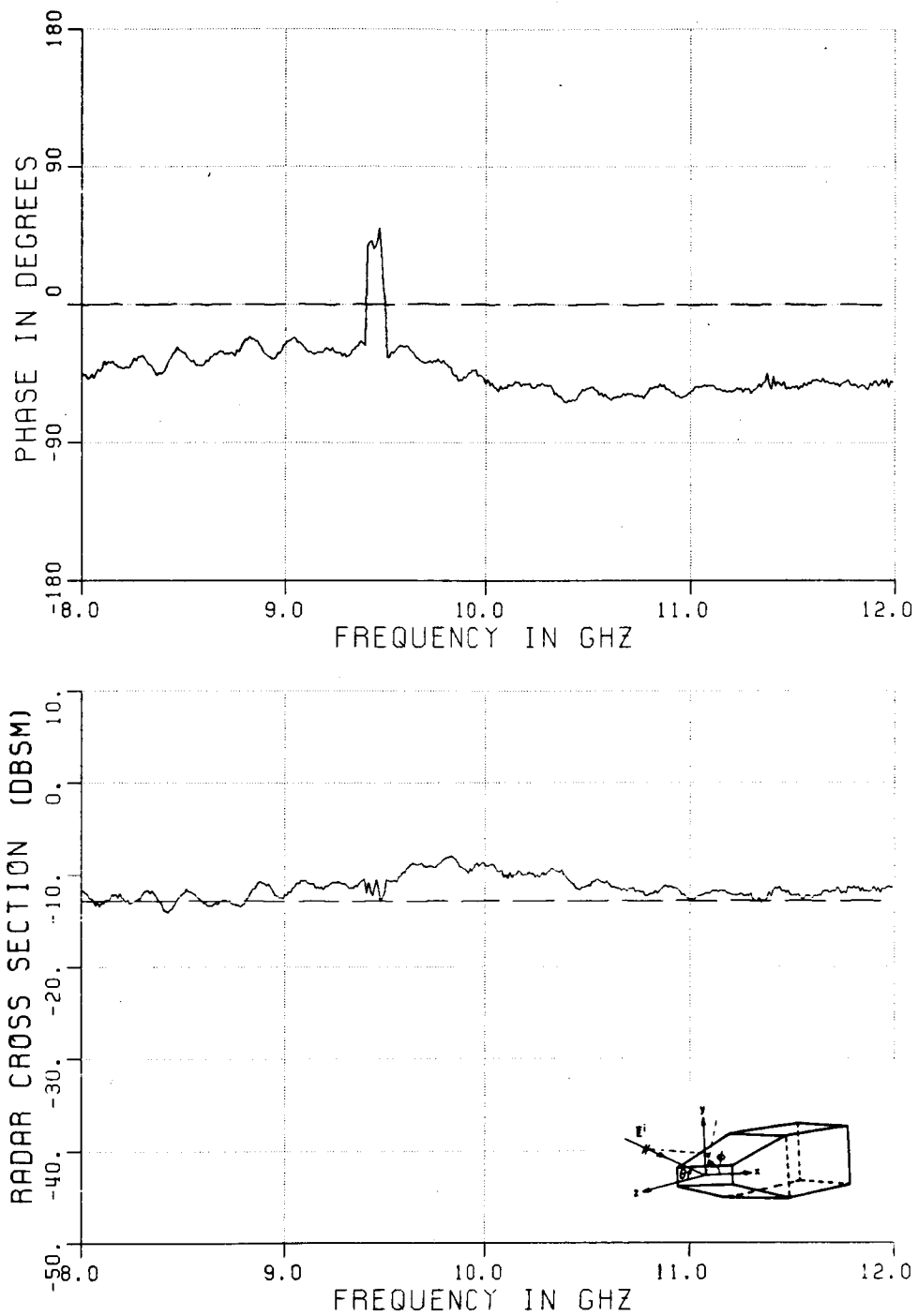


Figure 4.30. Variation of radar cross section with frequency.

$$\vec{E}^i = \hat{\theta}, \phi = 0, \theta = 0^\circ$$

— measured, --- calculated

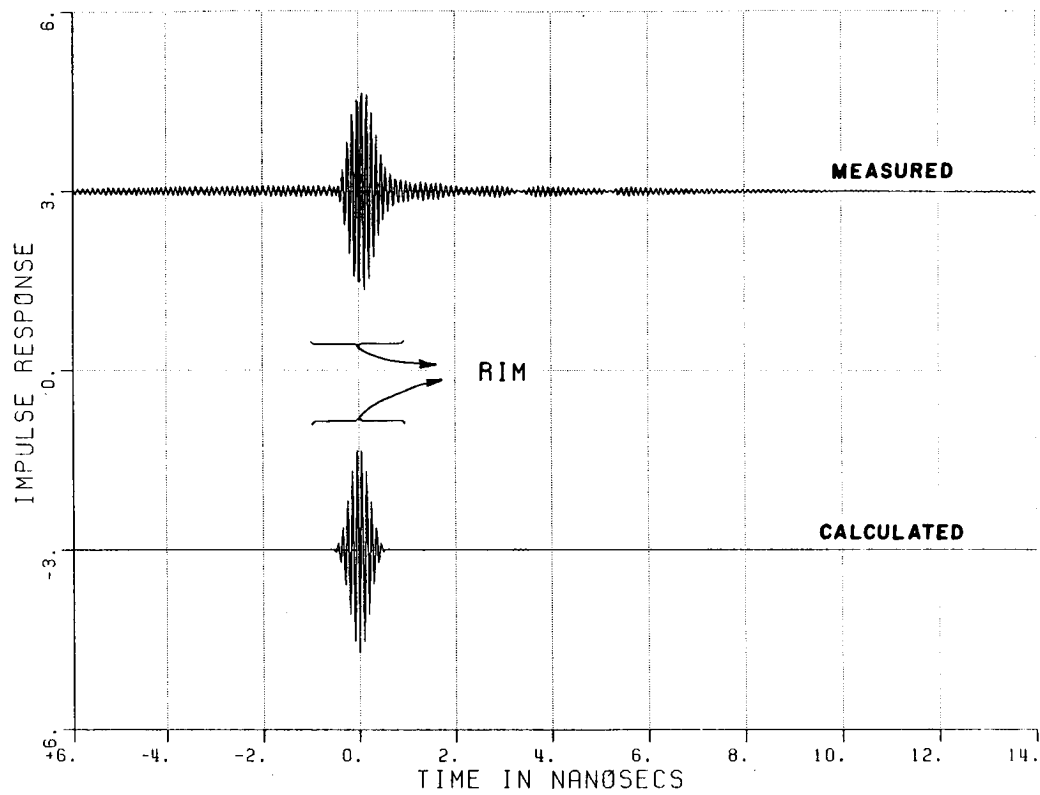


Figure 4.31. Inverse Fourier transforms (i.e., time domain plots) of the results in Figure 4.30.

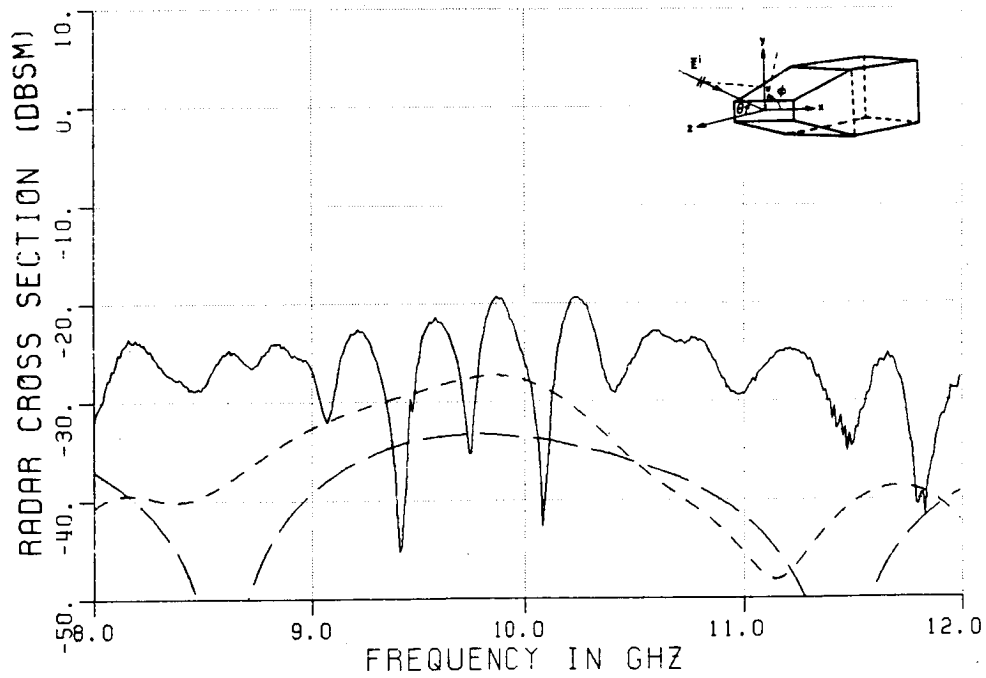
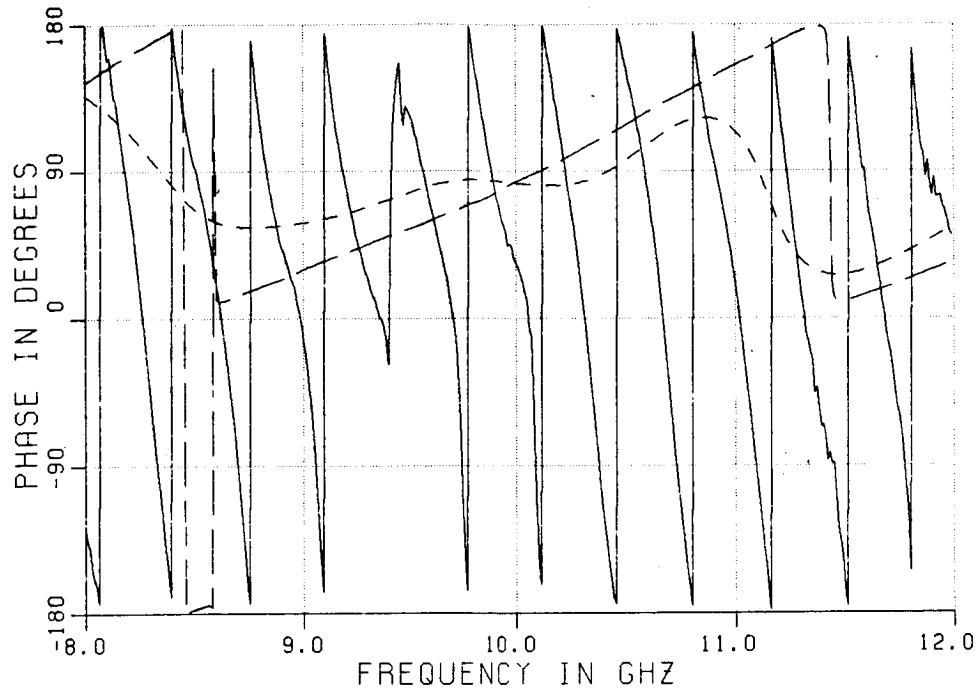


Figure 4.32. Variation of radar cross section with frequency.

$$\vec{E}^i = \hat{\theta}, \phi = 0, \theta = 15^\circ$$

— measured, --- calculated

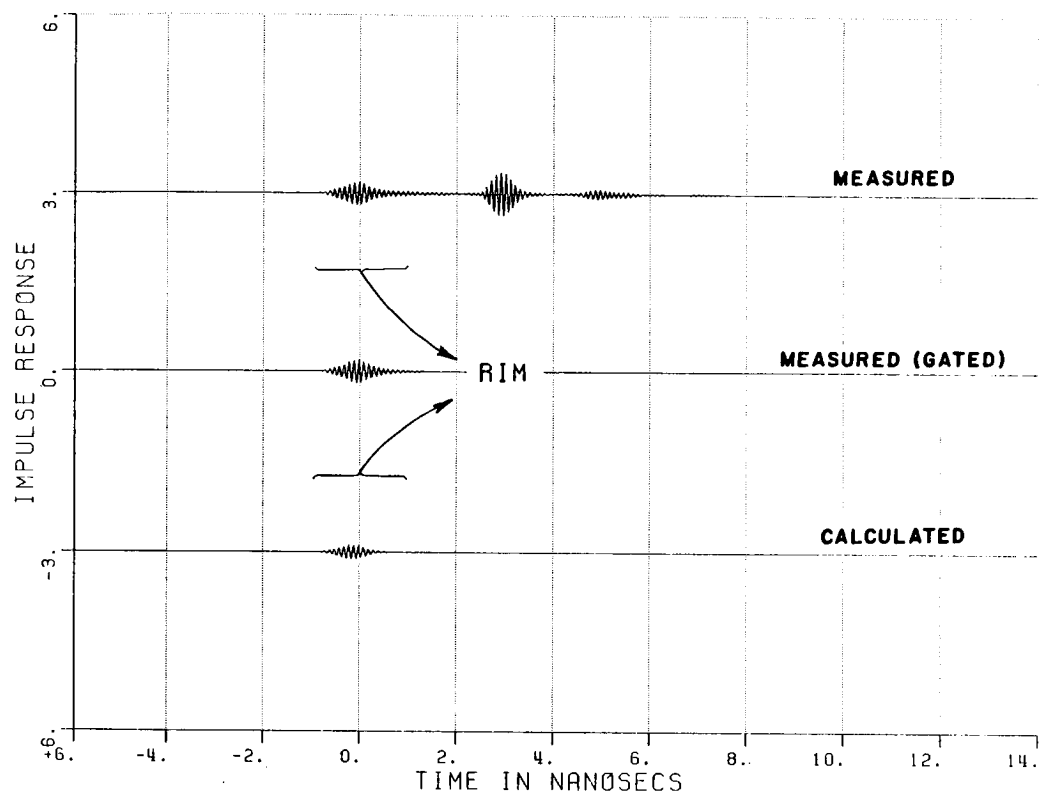


Figure 4.33. Inverse Fourier transforms (i.e., time domain plots) of the results in Figure 4.32.

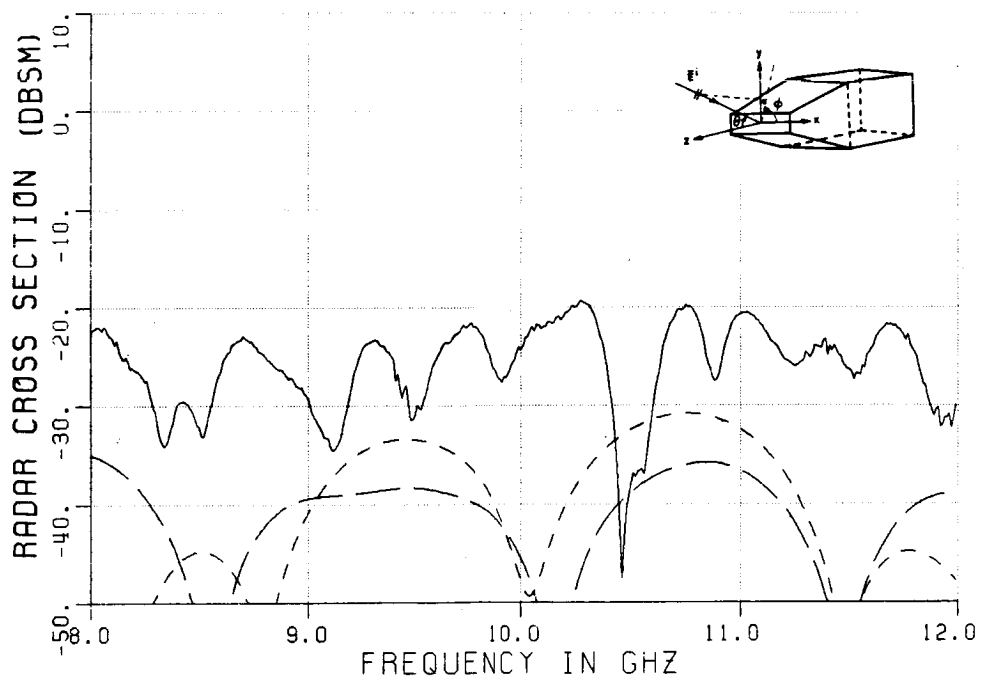
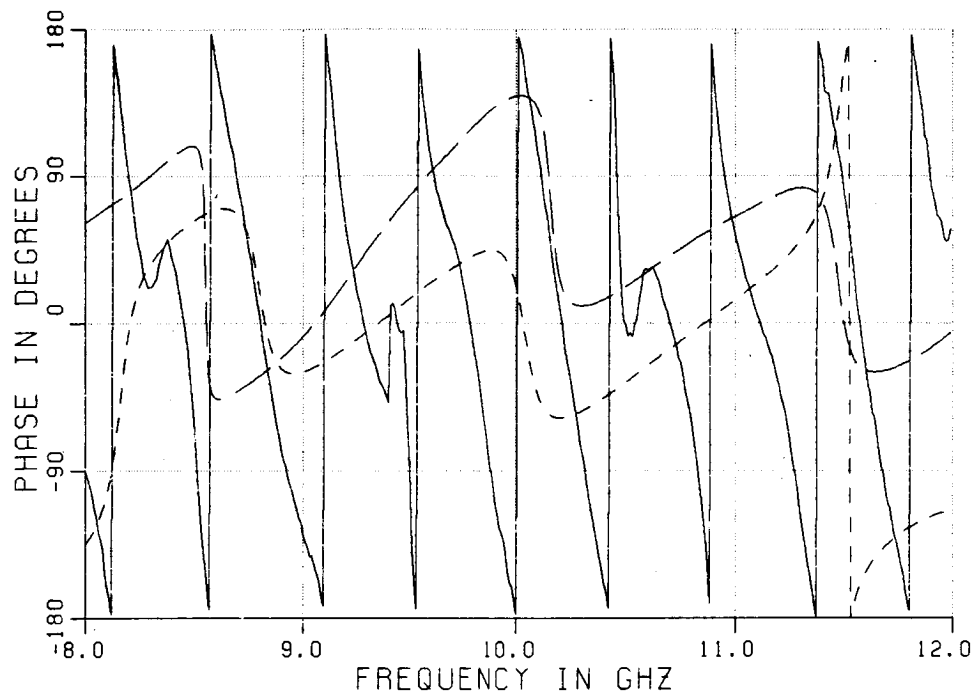


Figure 4.34. Variation of radar cross section with frequency.

$$\vec{E}^i = \hat{\theta}, \phi=0, \theta=30^\circ$$

— measured, --- calculated

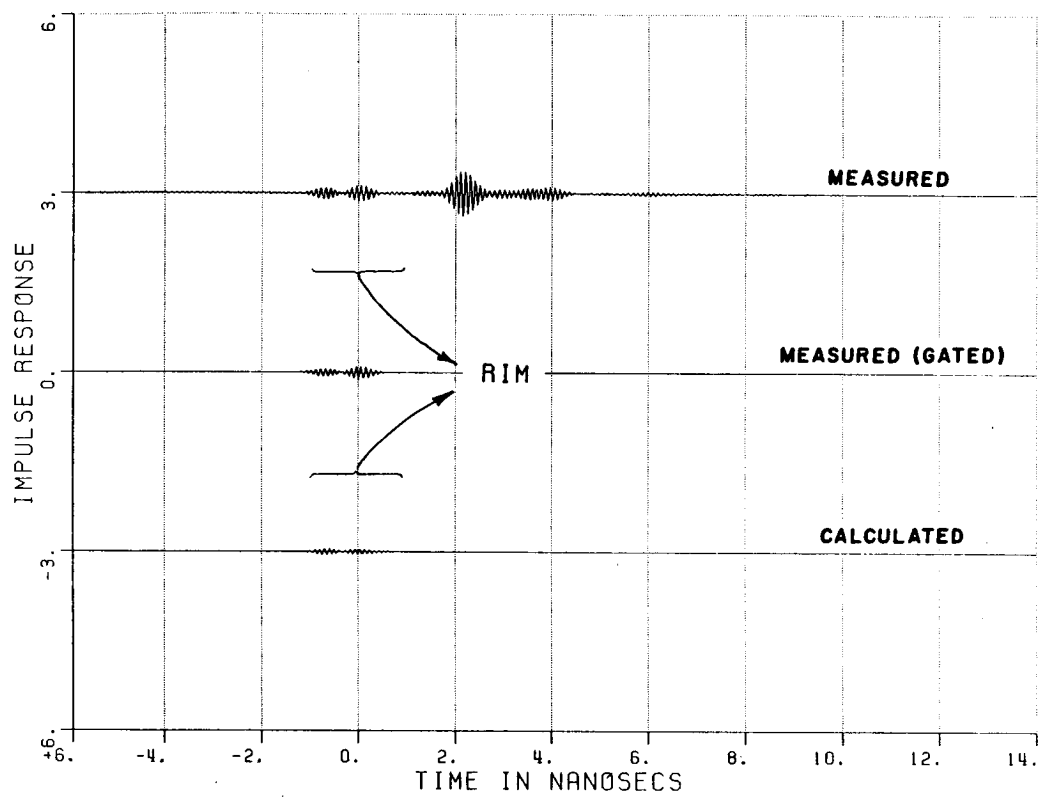


Figure 4.35. Inverse Fourier transforms (i.e., time domain plots) of the results in Figure 4.34.

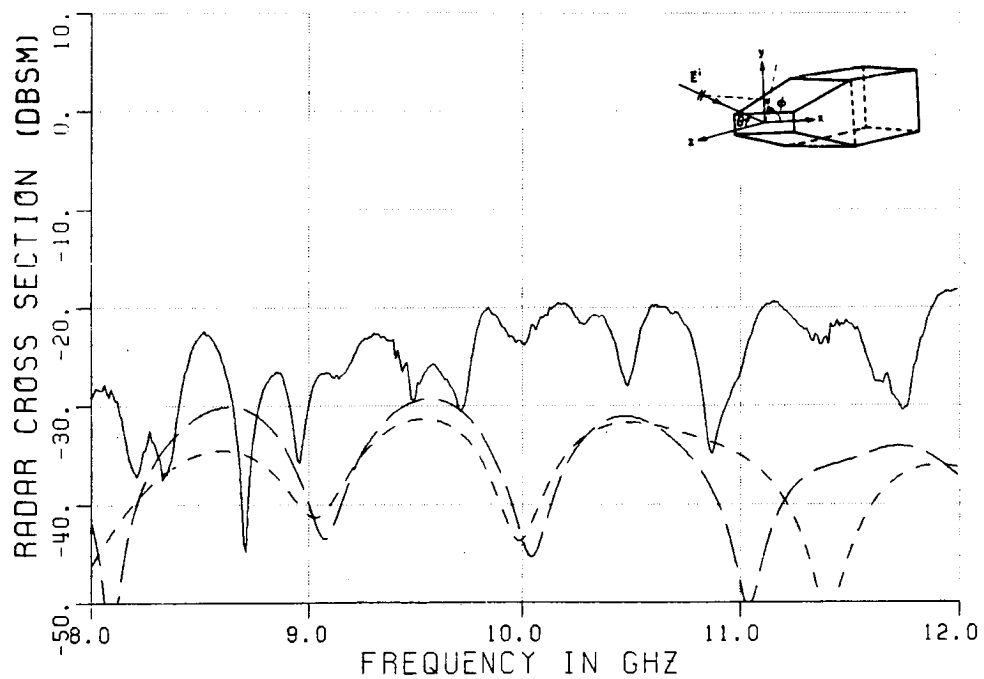
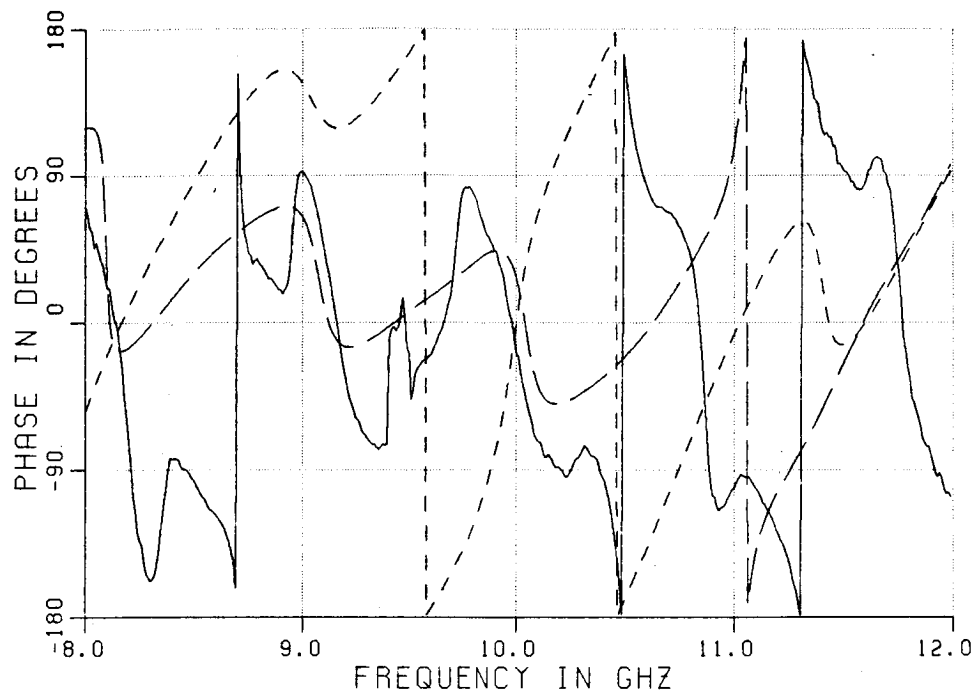


Figure 4.36. Variation of radar cross section with frequency.

$$\vec{E}^i = \hat{\theta}, \phi = 0, \theta = 45^\circ$$

— measured, --- calculated

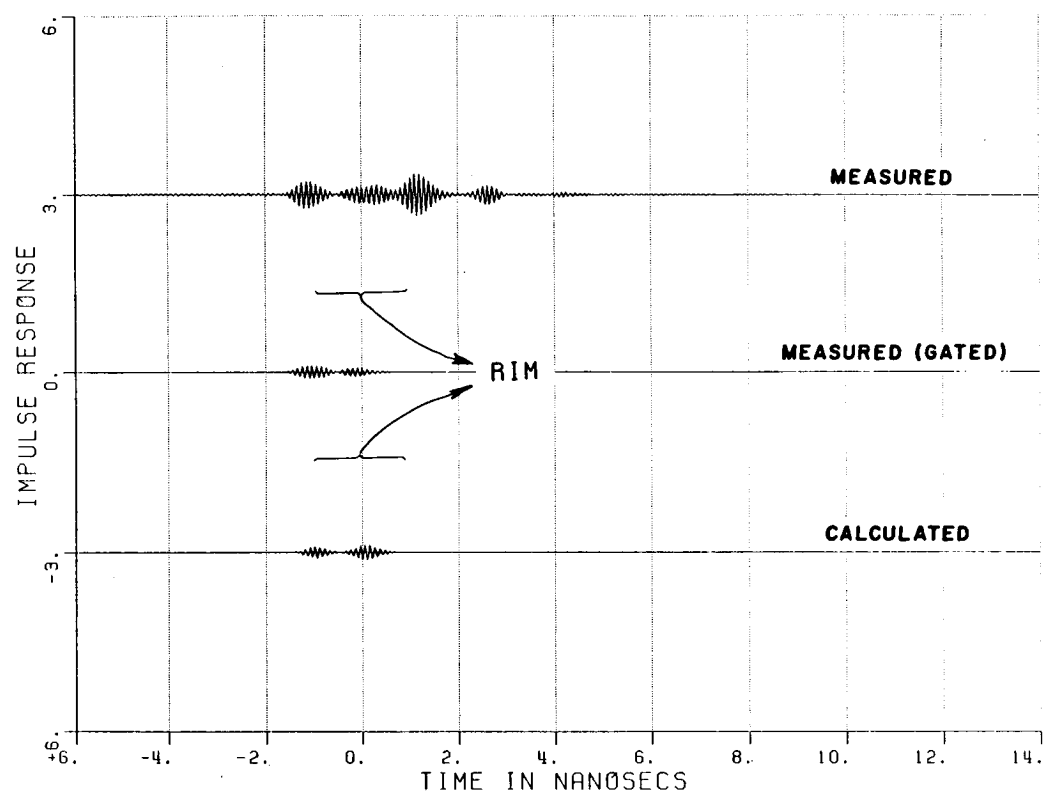


Figure 4.37. Inverse Fourier transforms (i.e., time domain plots) of the results in Figure 4.36.

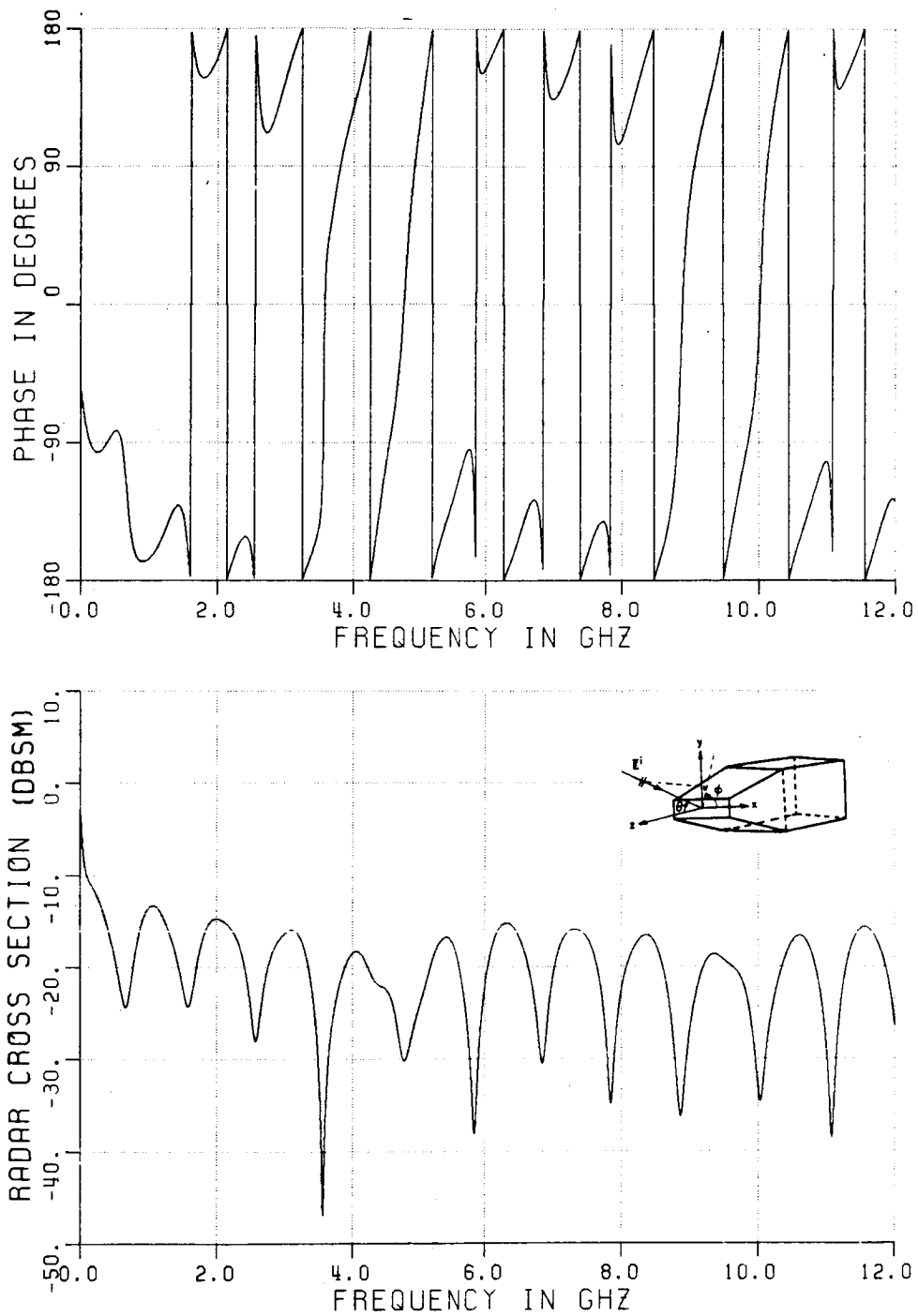


Figure 4.38. Variation of radar cross section with frequency.

$$\vec{E}^i = \hat{\phi}, \phi = 0, \theta = 45^\circ$$

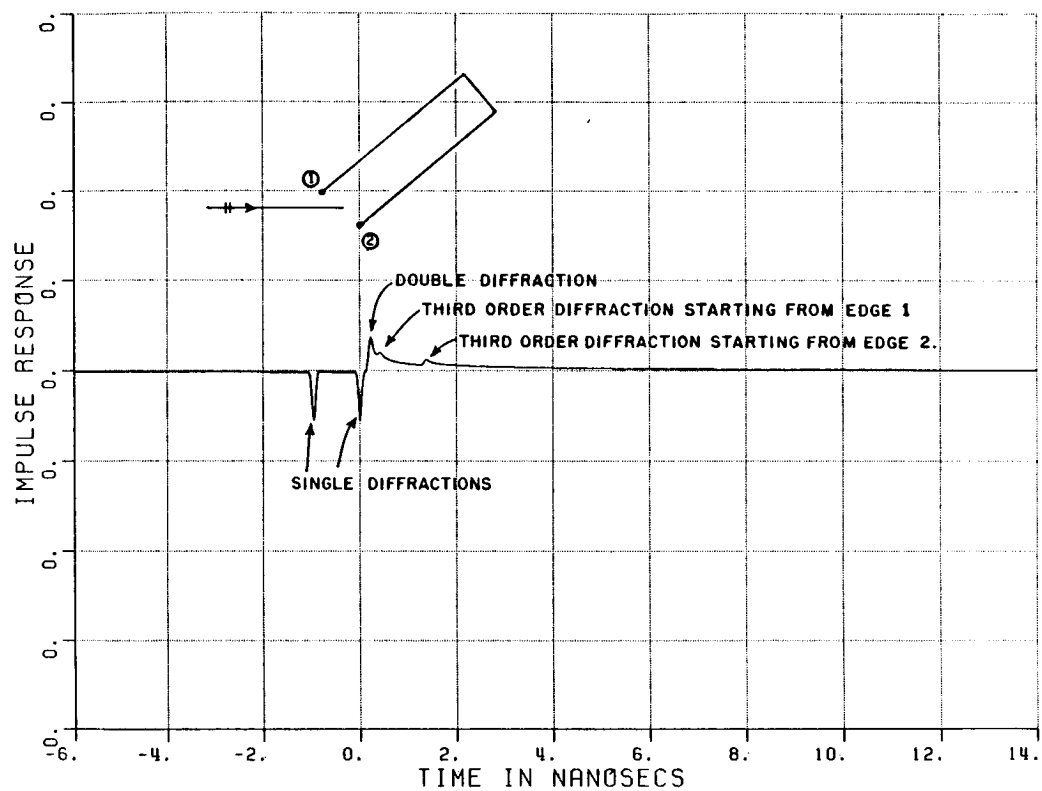


Figure 4.39. Inverse Fourier transforms (i.e., time domain plots) of the results in Figure 4.38.

In order to show this, calculations corresponding to Figure 4.28 were repeated and expressions of Equation (3.15) were extended down to 10 MHz. The resulting frequency domain plot is shown in Figure 4.38. Then, this data is inverse Fourier transformed, and the time domain result is shown in Figure 4.39. This result is closer to an actual impulse response and clearly shows the single, double and triple diffractions from the vertical edges of the open end. Note that the double order diffractions originating from both edges return to the receiver at the same time.

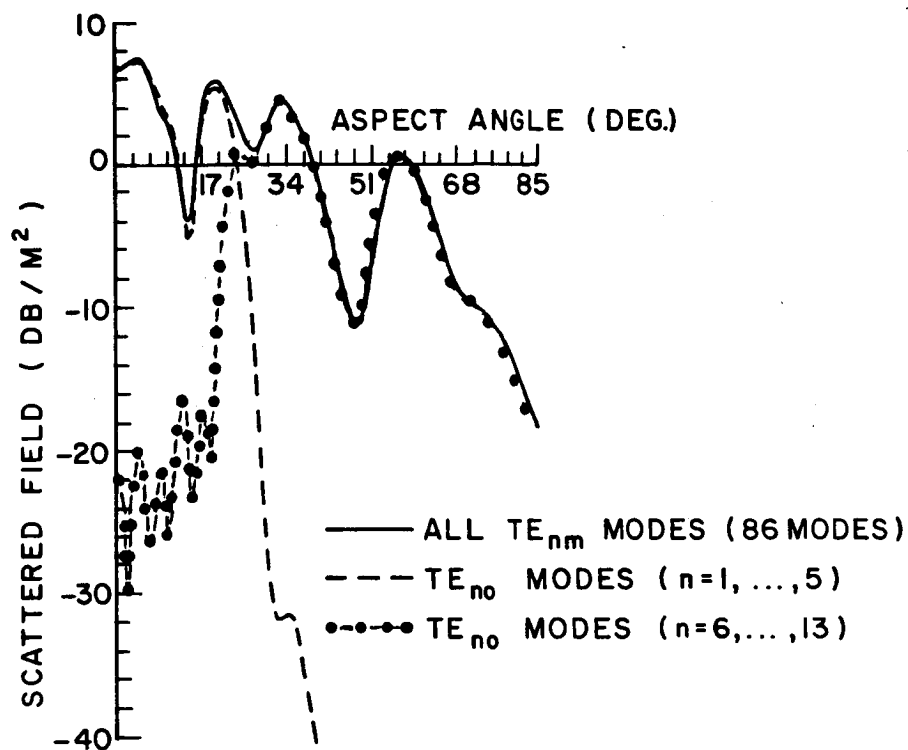
ii) Results for the Interior Cavity Effects

As described at the beginning, the coupling of incident energy into the interior waveguide modes and their subsequent radiation after undergoing multiple reflections between the back wall termination and the open end comprise the cavity effects.

Since it is difficult to experimentally isolate the open end rim scattering from the cavity effects, the calculations include both effects for comparison purposes; namely, the results of (3.15), (3.134), (3.135), (3.140) and (3.141). The measurements and calculations were performed in two categories as in Chapter III; namely, aspect angle and frequency scans with the results presented in dBSM.

The waveguide model is large in terms of the wavelength; therefore, a large number of propagating modes can exist inside the cavity. For example, at the frequency of 10 GHz, there are 152 propagating modes ($86 TE_{nm}$, $66 TM_{nm}$) as well as an infinite number of evanescent modes. Since

the waveguide axial length is very long with respect to the wavelength, the evanescent modes will decay very significantly such that they can be neglected. Then the next question is whether the propagating modes have a preferred direction of radiation in that one can choose a few special ones rather than all the propagating modes and include only those in the analysis. It has already been mentioned in the previous chapter that modal radiation is dominant along each of the discrete modal ray plane wave directions of that mode. Since each mode has discrete radiation directions, some will radiate strongly close to a desired direction, and others will not. This being the case, one can anticipate that only a few modes are significantly excited by the incident plane wave which radiate significantly in the backscatter direction. This claim has been checked numerically, and the results are shown in Figure 4.40. An open-ended rectangular waveguide with dimensions equal to the experimental model used in this study is analyzed at 10 GHz. The backscatter field is calculated in (x-z) plane by varying the aspect angle (θ). Note that only the modal effects are included and the incident field is assumed to be $\hat{\phi}$ -polarized. It is found that only the TE_{no} modes are excited in this plane for this polarization. Their plane wave directions or modal ray angles are tabulated in the figure. The scattered field is calculated by including all modal contributions as indicated by the solid line. For comparison purposes the contributions of TE_{no} ($n=1, \dots, 5$) modes and TE_{no} ($n=6 \dots 13$) modes are shown in the same figure. Note that the first five modes radiate strongly and almost replicate the solid curve in the region close to their modal ray angle directions. The remaining seven modes are major contributors for large



MODAL RAY ANGLES OF TE_{n0} MODES

TE ₁₀	4.23°	TE ₆₀	26.28°
TE ₂₀	9°	TE ₇₀	31.11°
TE ₃₀	12.8°	TE ₈₀	36.19°
TE ₄₀	17.17°	TE ₉₀	41.63°
TE ₅₀	21.65°	TE _{10,0}	47.57°
		TE _{11,0}	54.29°
		TE _{12,0}	62.34°
		TE _{13,0}	73.66°

Figure 4.40. Importance of modes whose modal ray angles are near the angle of incidence.

$f=10$ GHz, $\vec{E}^i = \hat{\phi}$, $\phi=0$ plane.

aspect angles. After observing this fact, the research focused on finding a rule of thumb procedure which could be used to select the minimum number of modes needed for a given direction of incident plane wave. From numerical results and comparisons with the experimental data, it was found that in the horizontal ($\phi=0$) and vertical ($\phi=90^\circ$) planes only three modes were sufficient for the cavity under test. These three modes are selected based on their modal radiation direction such that they are closest to the incident plane wave direction. The aspect angle scan results are shown in Figures 4.41 through 4.64. As done in the previous section, the experimental results are indicated by the solid line and calculations by the dashed one. In each case, a comparison is provided for the calculations which include all propagating modes versus three propagating modes. In all cases, a 1 dB/bounce energy loss is assumed to model the imperfection of the conductivity of the model used in the measurements.

Since this new concept proved to be so valuable in the principal planes; namely, $\phi=0$ and $\phi=90^\circ$ planes, it is next applied to $\phi=45^\circ$ plane to see if it fails when the incident plane wave direction is not aligned with the structural symmetry. The aspect angle scan is calculated in the $\phi=45^\circ$ plane for both the $\hat{\phi}$ and $\hat{\theta}$ polarized incident fields. The results are shown in Figures 4.65 and 4.66. In this case, the 18 preselected modes are compared with the complete 152 modes as shown in each figure. Note that more terms are necessary in this general case as indicated by the results shown in Figure 4.67 where the six mode result is compared with the 152 mode one. Even so it is clear that one can use far fewer modes than the complete propagating mode set.

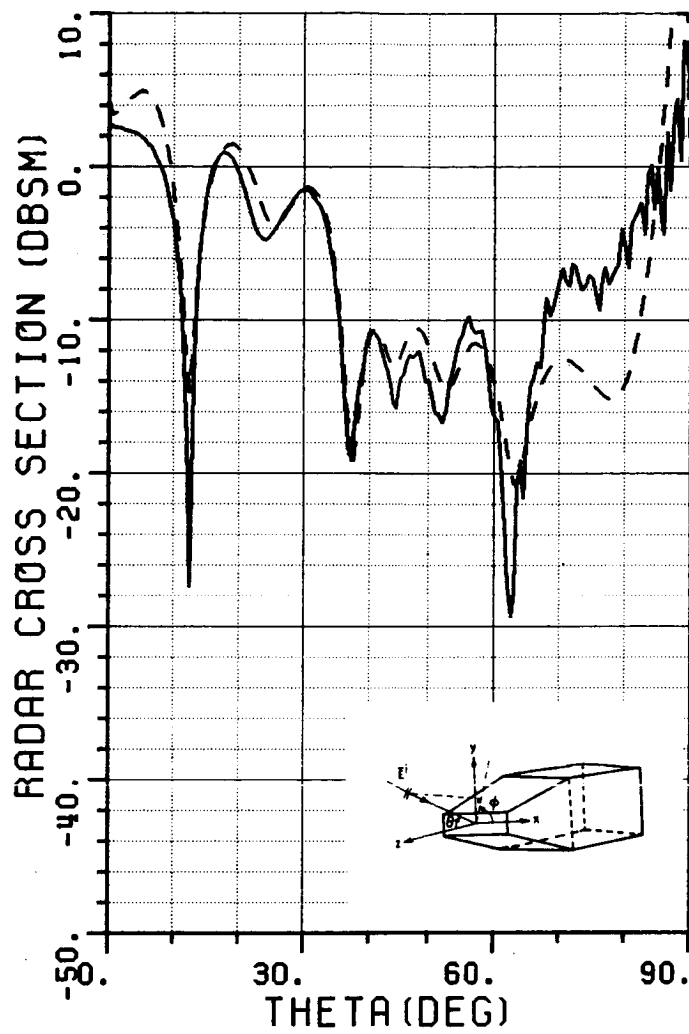


Figure 4.41. Radar cross section pattern at $f=8.00$ GHz,
 $\vec{E}^i = \hat{\phi}$, $\phi=0$ plane.
 — measured, --- calculated

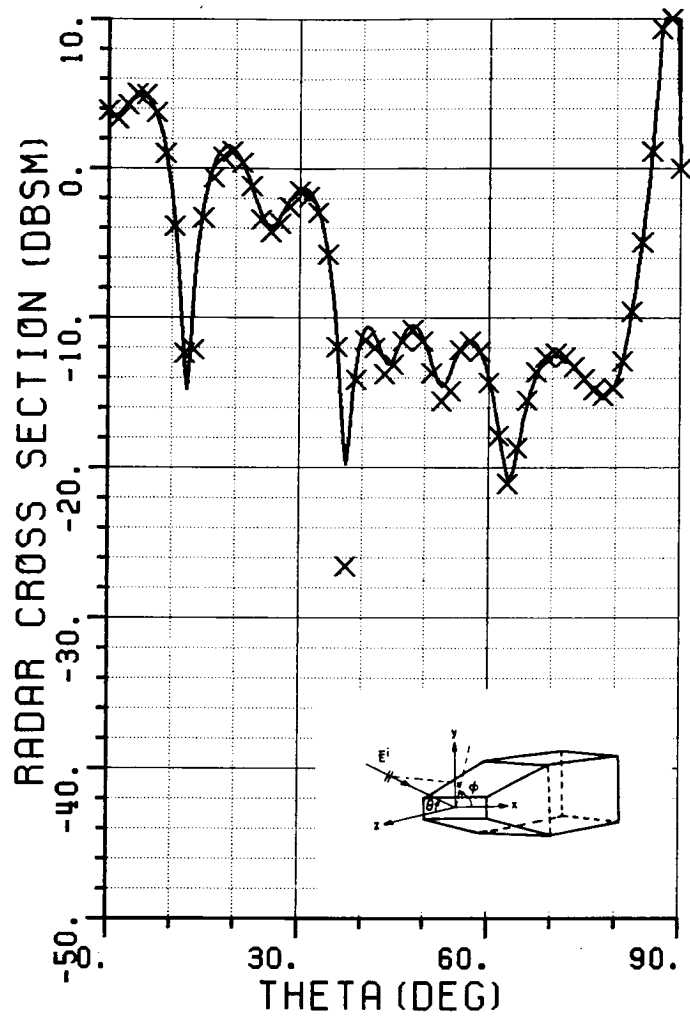


Figure 4.42. Calculated RCS pattern corresponding to Figure 4.41.

— All modes are included
 xxx Only 3 modes are included

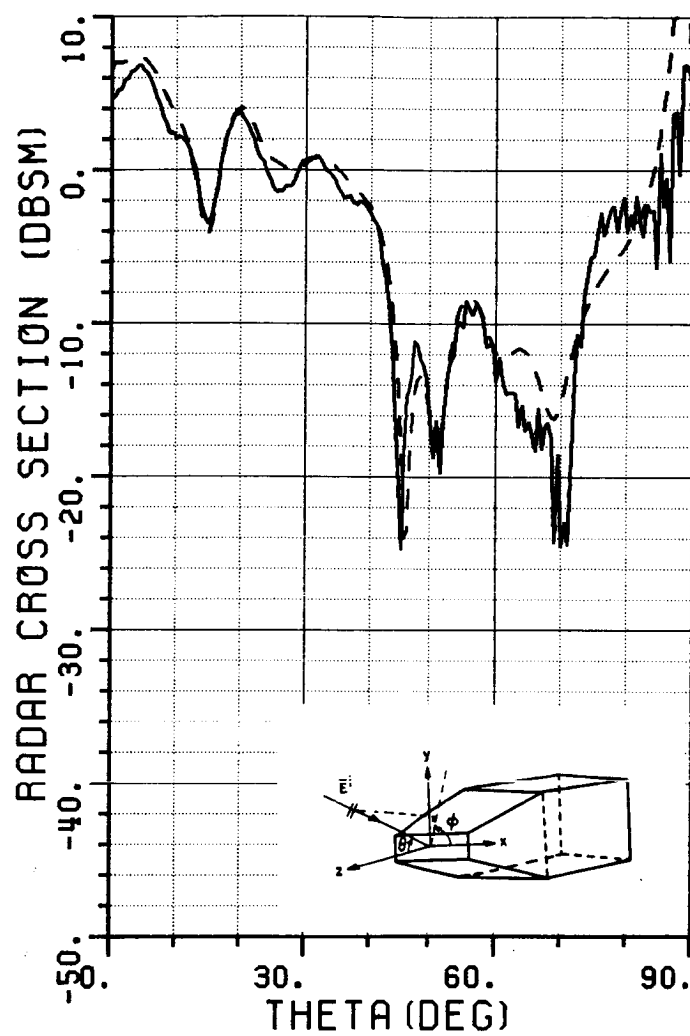


Figure 4.43. Radar cross section pattern at $f=10.00$ GHz,
 $\vec{E}^i = \hat{\phi}$, $\phi=0$ plane.
 — measured, --- calculated

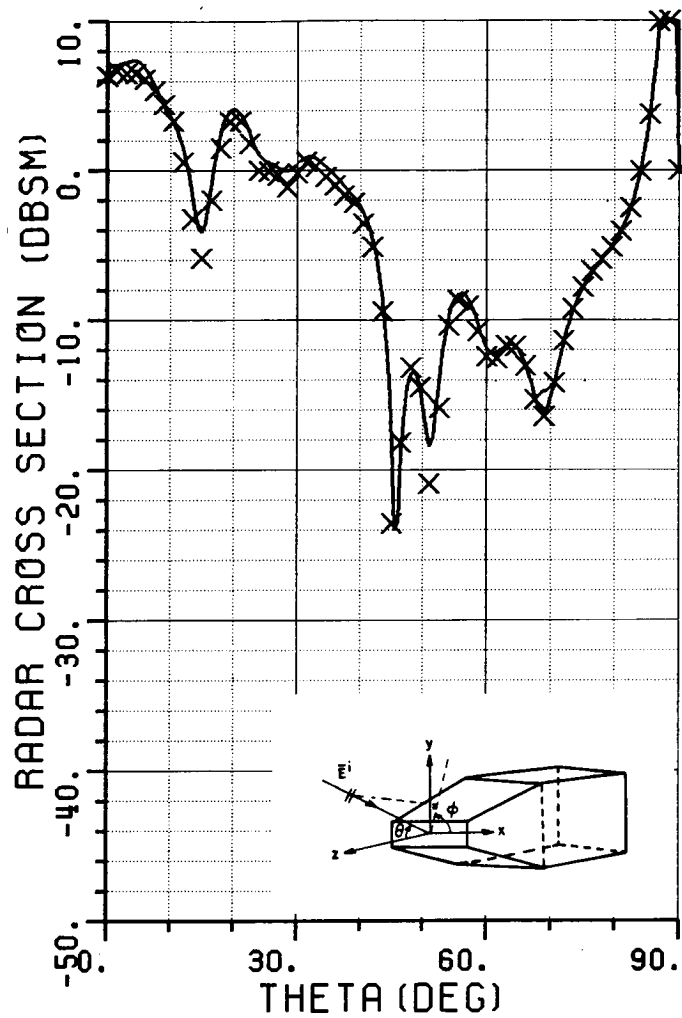


Figure 4.44. Calculated RCS pattern corresponding to Figure 4.43.

— All modes are included
 xxx Only 3 modes are included

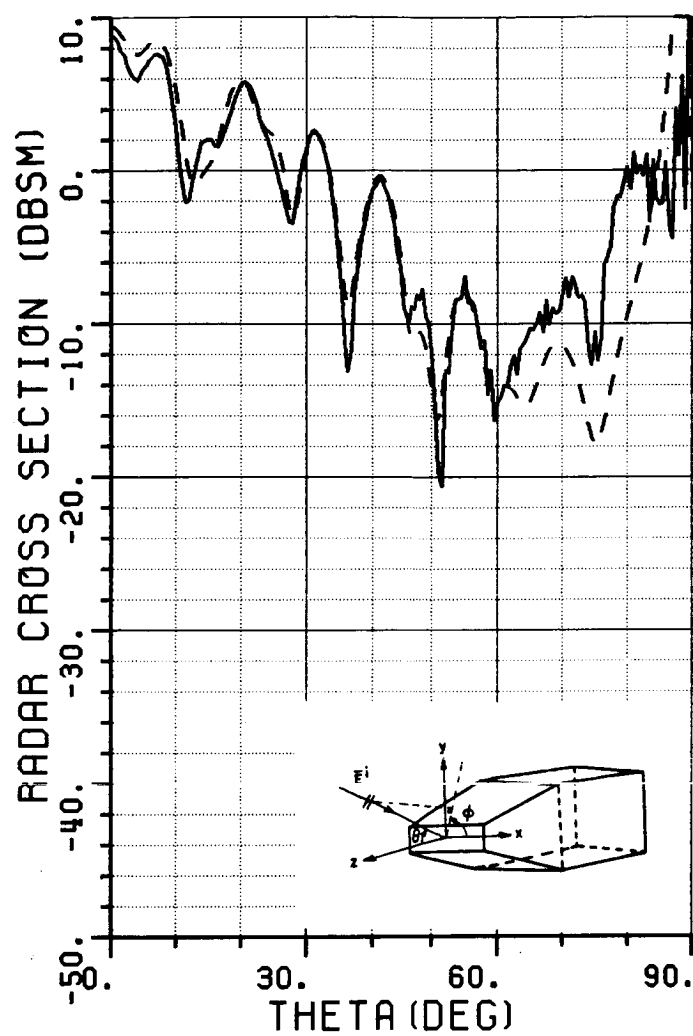


Figure 4.45. Radar cross section pattern at $f=12.00$ GHz,
 $E^i = \hat{\phi}$, $\phi=0$ plane.
 — measured, --- calculated

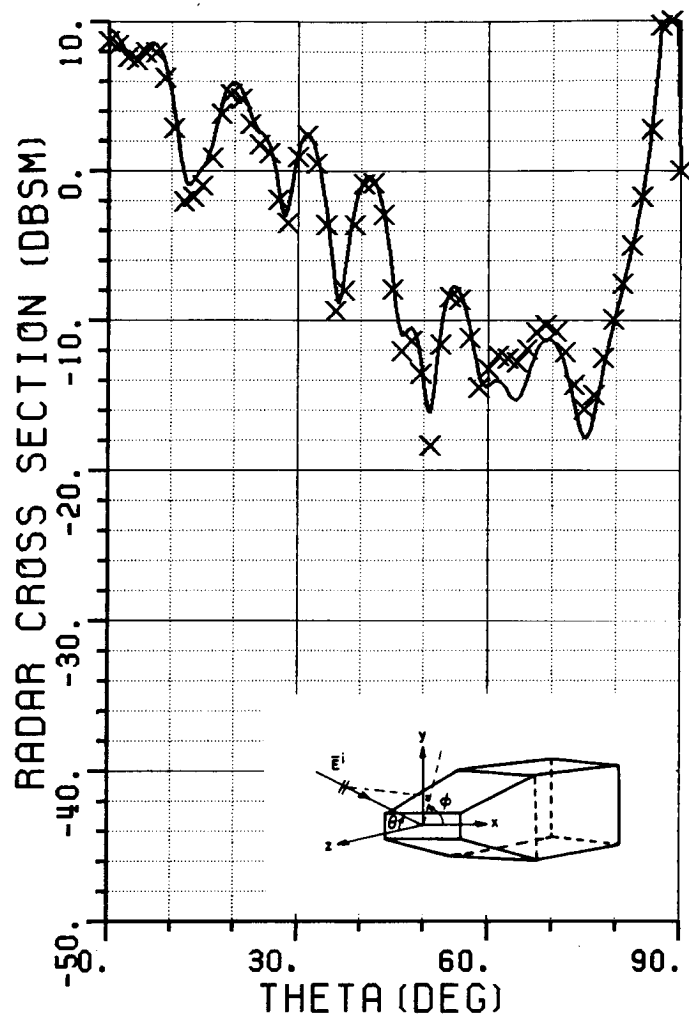


Figure 4.46. Calculated RCS pattern corresponding to Figure 4.45.

— All modes are included
xxx Only 3 modes are included

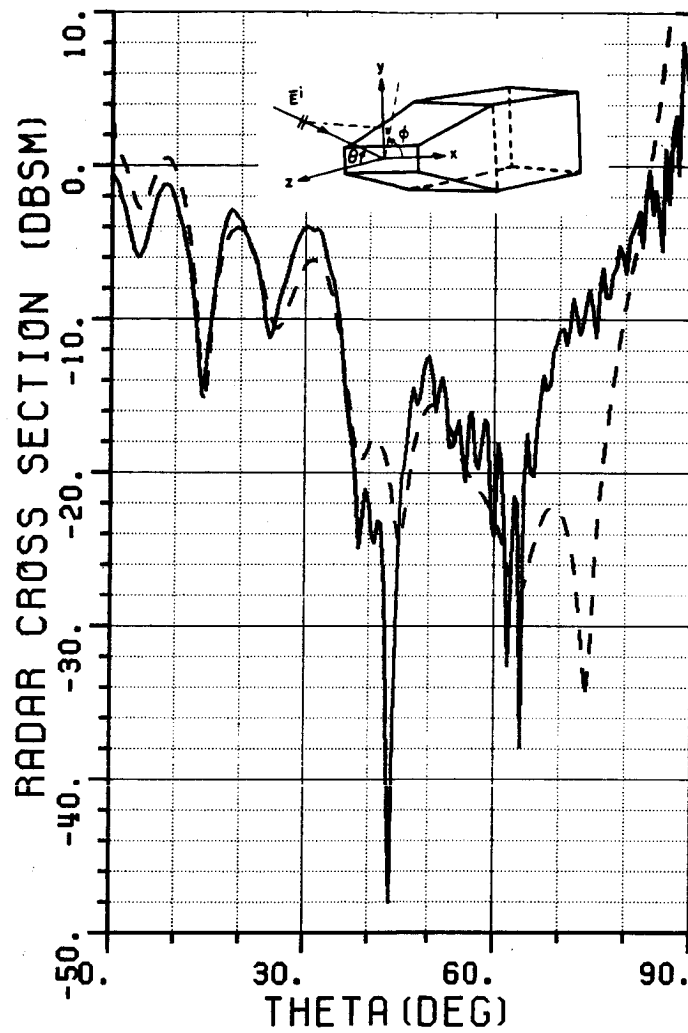


Figure 4.47. Radar cross section pattern at $f=8.02$ GHz,
 $\vec{E}^i = \hat{\theta}$, $\phi=0$ plane.
 — measured, --- calculated

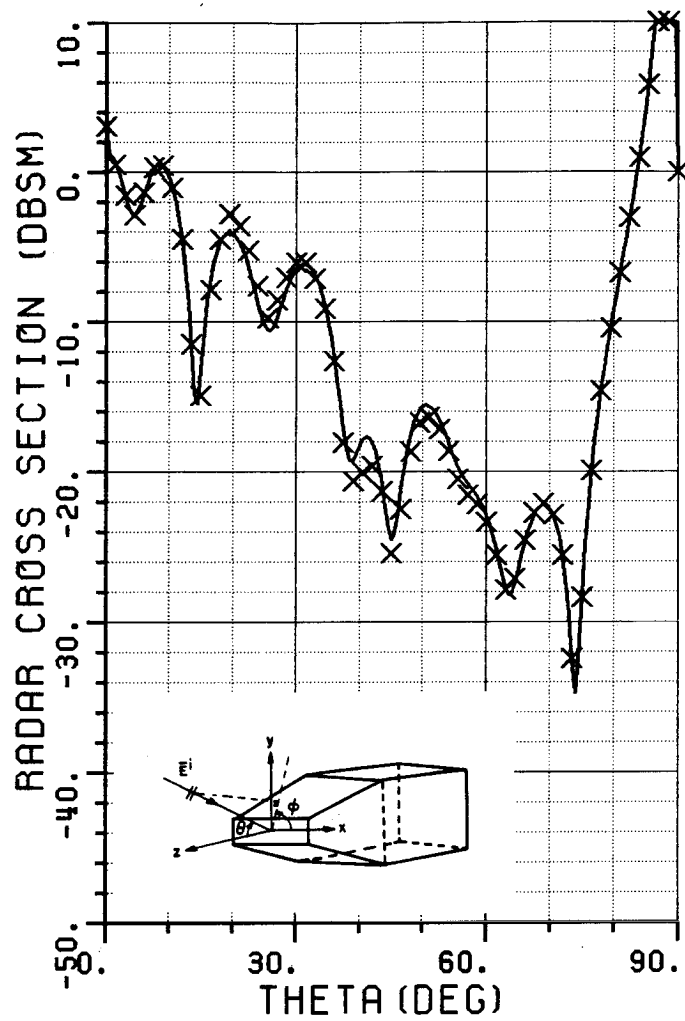


Figure 4.48. Calculated RCS pattern corresponding to Figure 4.47.

— All modes are included
 xxx Only 3 modes are included

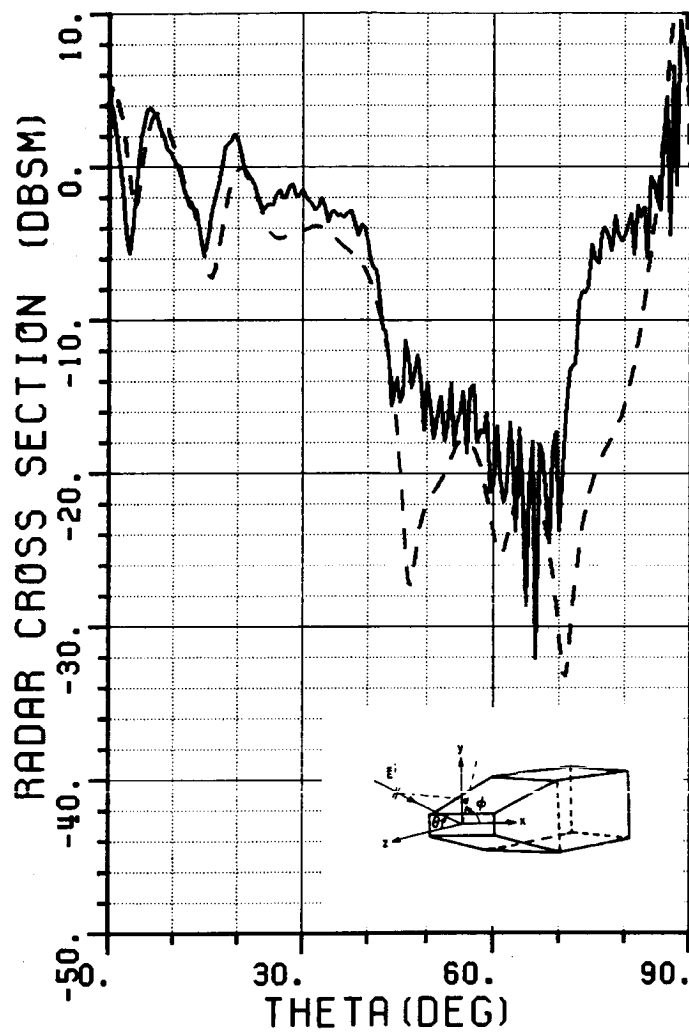


Figure 4.49. Radar cross section pattern at $f=9.98$ GHz,
 $\vec{E}_i = \hat{\theta}$, $\phi=0$ plane.
 — measured, --- calculated

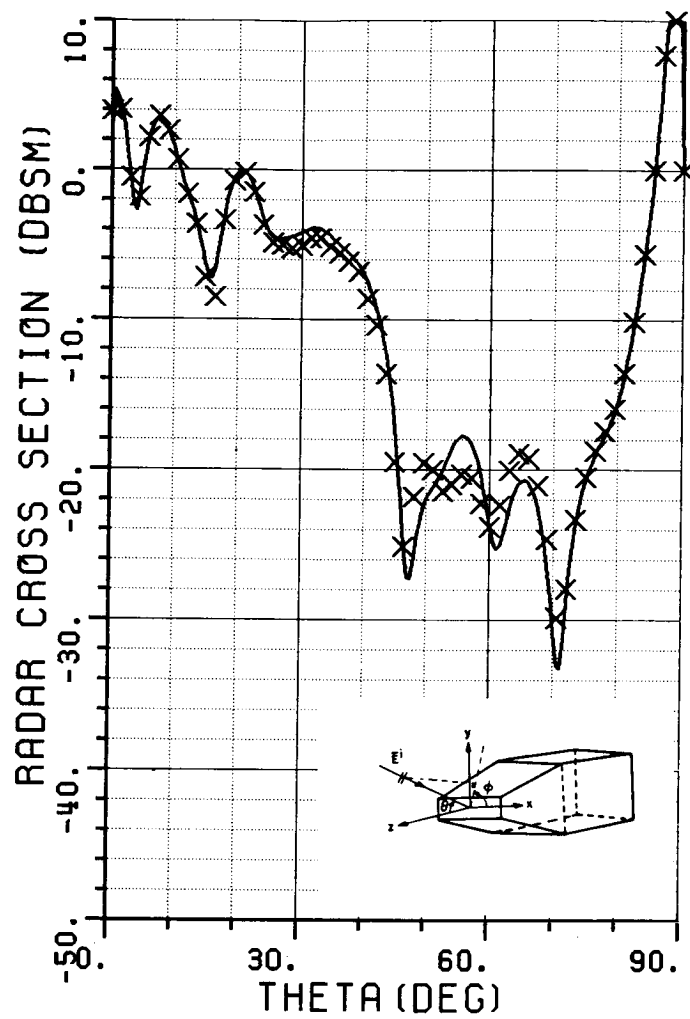


Figure 4.50. Calculated RCS pattern corresponding to Figure 4.49.

— All modes are included
 xxx Only 3 modes are included

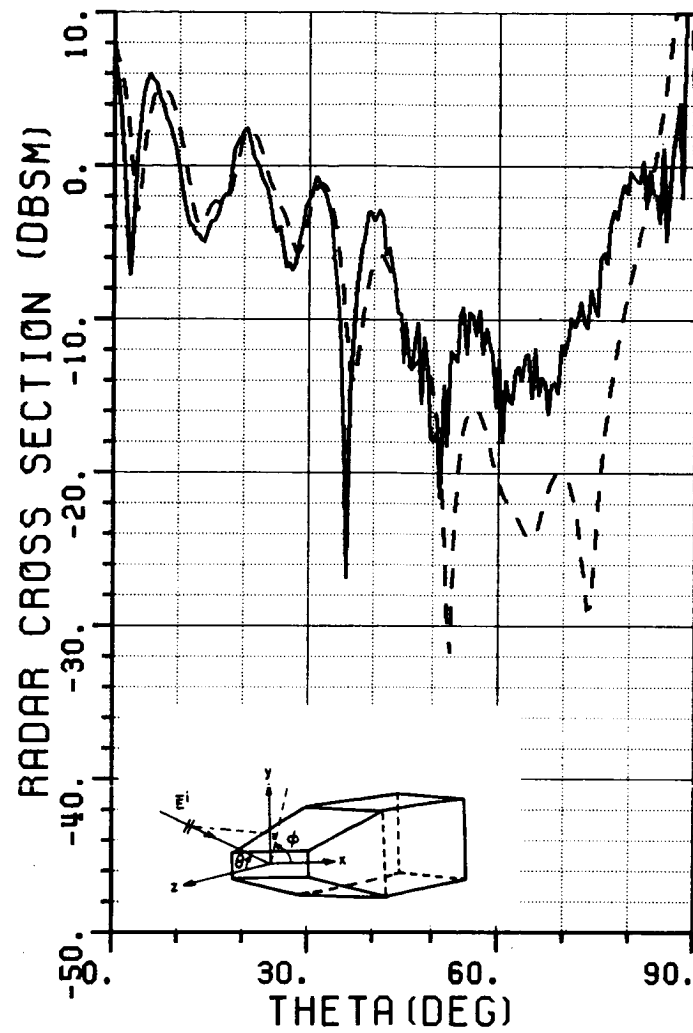


Figure 4.51. Radar cross section pattern at $f=11.95$ GHz,
 $\vec{E}^i = \hat{\theta}$, $\phi=0$ plane.
 — measured, --- calculated

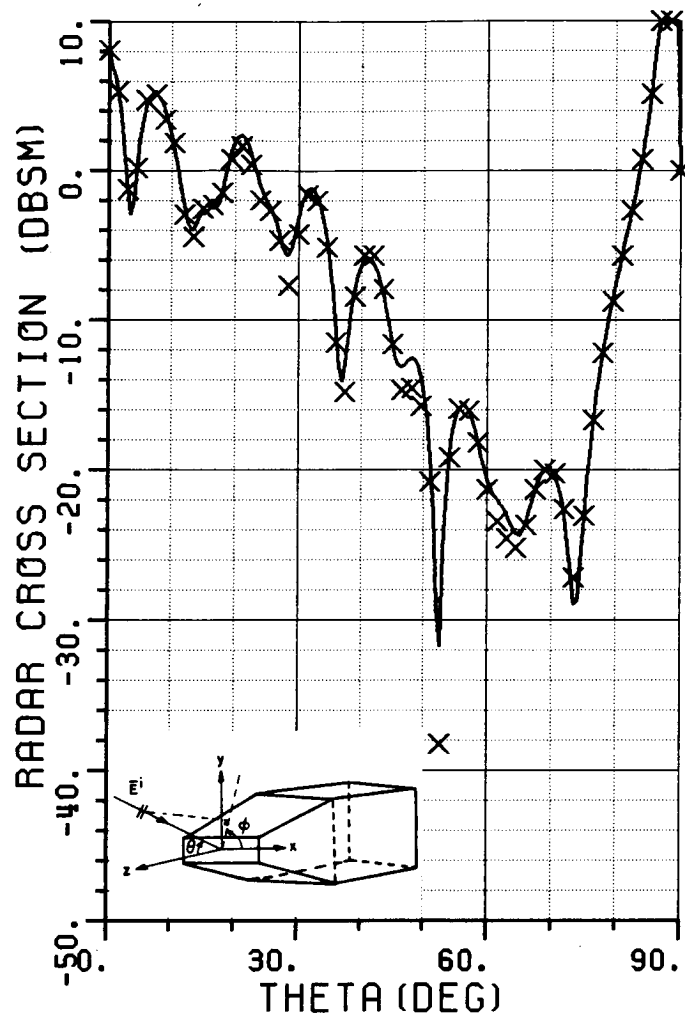


Figure 4.52. Calculated RCS pattern corresponding to Figure 4.51.

— All modes are included
 xxx Only 3 modes are included

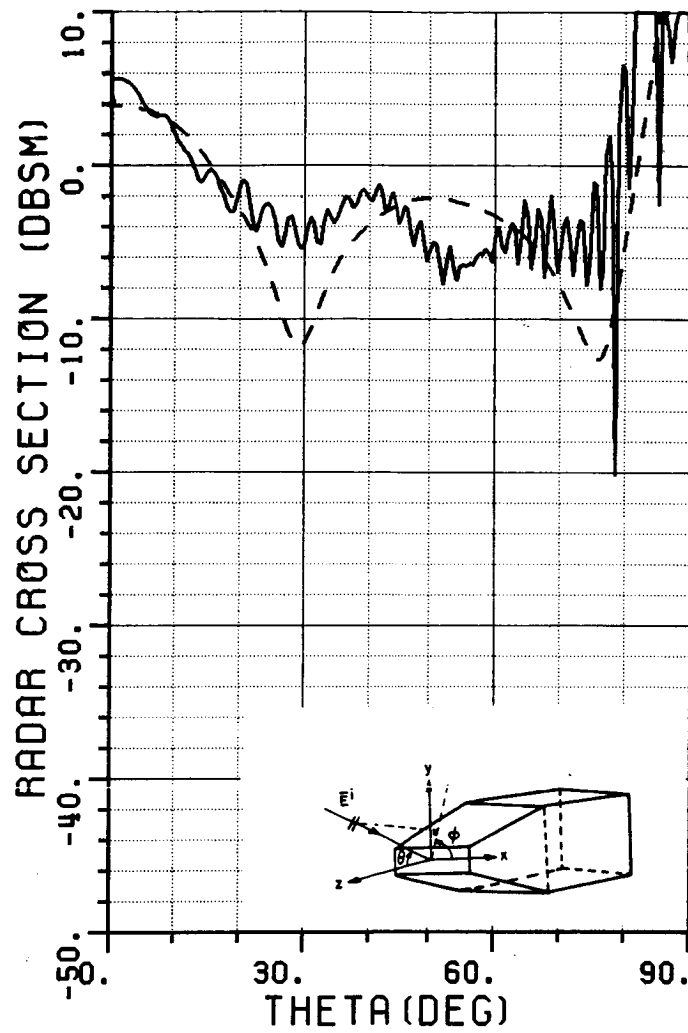


Figure 4.53. Radar cross section pattern at $f=8.02$ GHz,
 $\vec{E}^i = \hat{\theta}$, $\phi=90^\circ$ plane.
 — measured, --- calculated

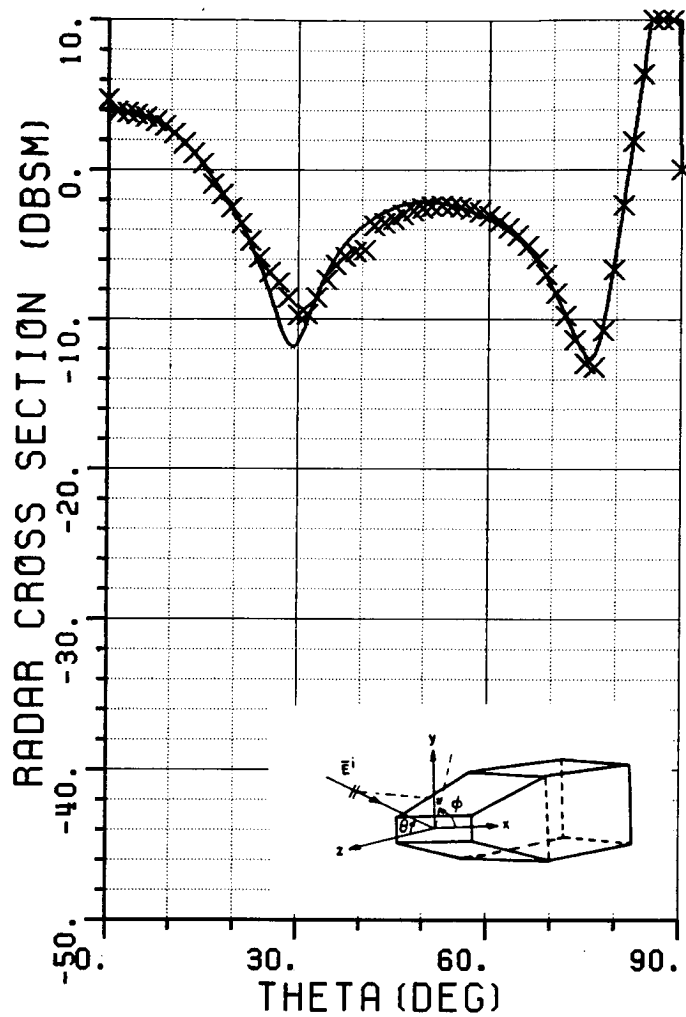


Figure 4.54. Calculated RCS pattern corresponding to Figure 4.53.

— All modes are included
 xxx Only 3 modes are included

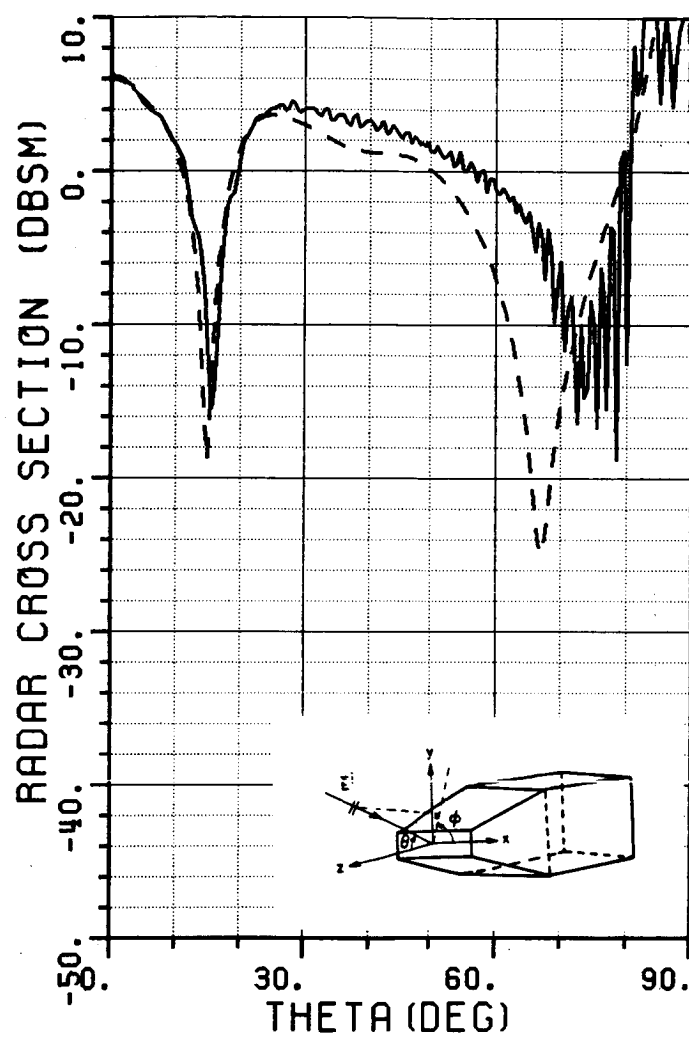


Figure 4.55. Radar cross section pattern at $f=10.01$ GHz,
 $\vec{E}^i = \hat{\theta}$, $\phi=90^\circ$ plane.
 — measured, --- calculated

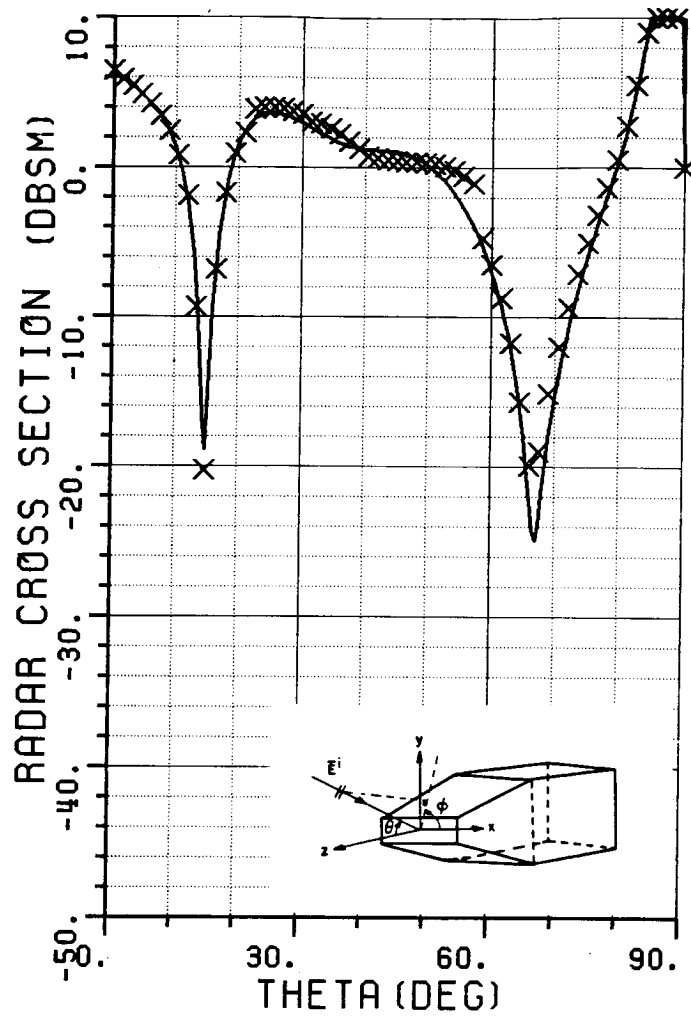


Figure 4.56. Calculated RCS pattern corresponding to Figure 4.55.

— All modes are included
 xxx Only 3 modes are included

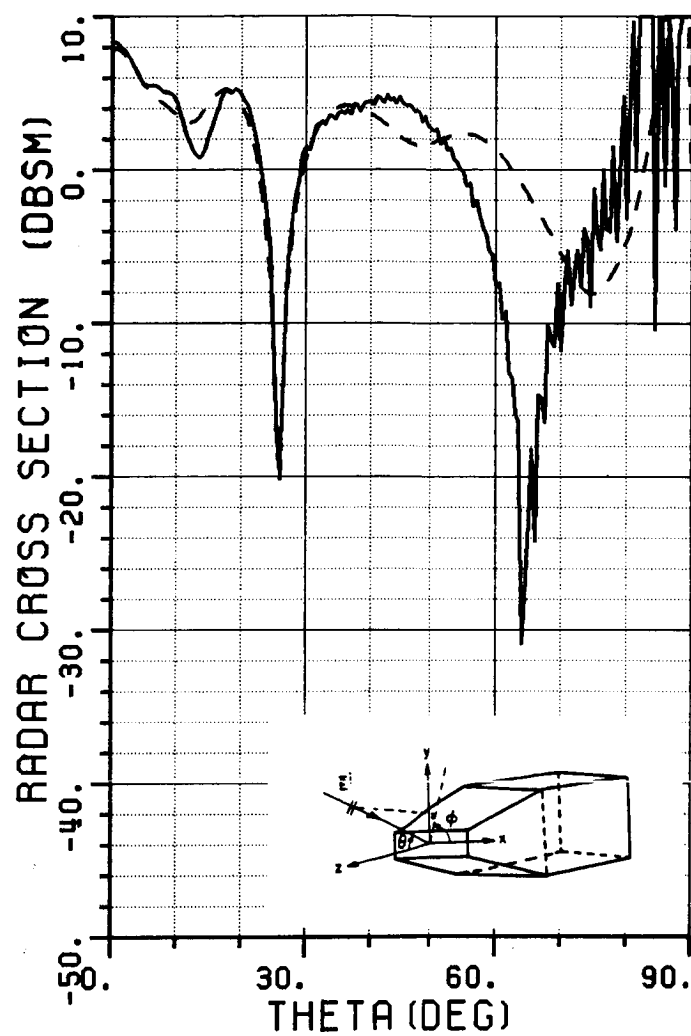


Figure 4.57. Radar cross section pattern at $f=11.96$ GHz,
 $\vec{E}^i = \hat{\theta}$, $\phi=90^\circ$ plane.
 — measured, --- calculated

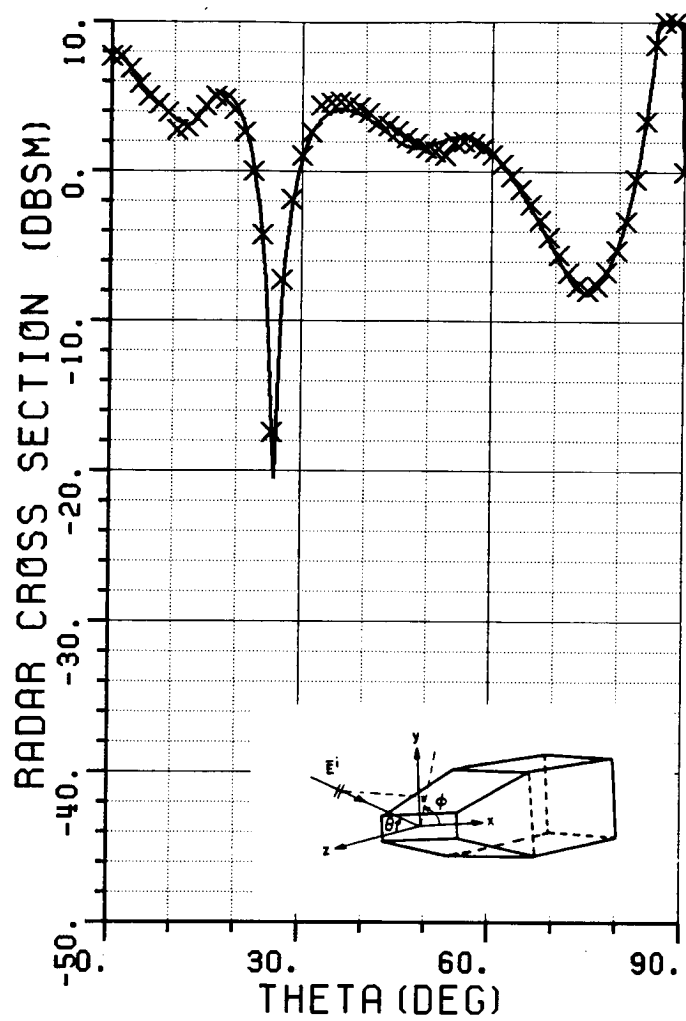


Figure 4.58. Calculated RCS pattern corresponding to Figure 4.57.

— All modes are included
 xxx Only 3 modes are included

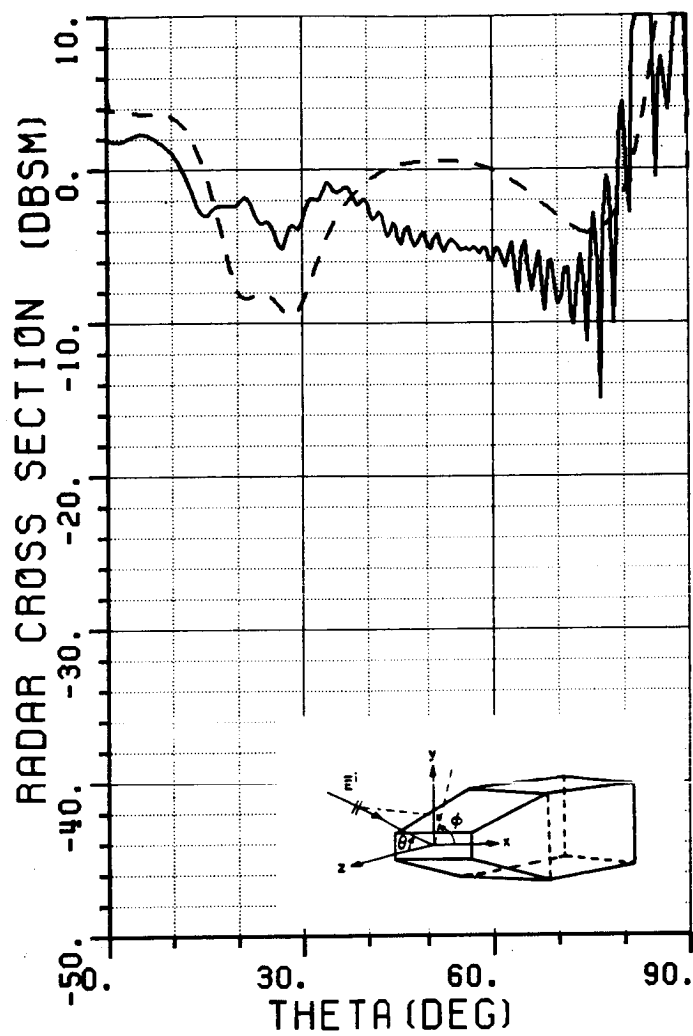


Figure 4.59. Radar cross section pattern at $f=8.02$ GHz,
 $\vec{E}^i = \hat{\phi}$, $\phi=90^\circ$ plane.
 — measured, --- calculated

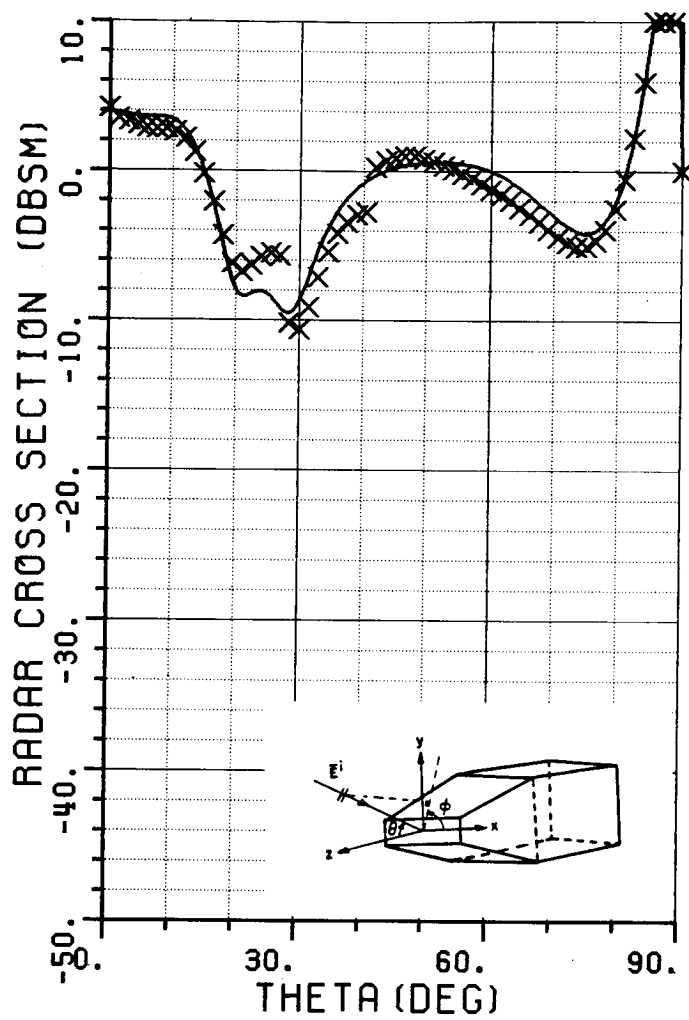


Figure 4.60. Calculated RCS pattern corresponding to Figure 4.59.

— All modes are included
 xxx Only 3 modes are included

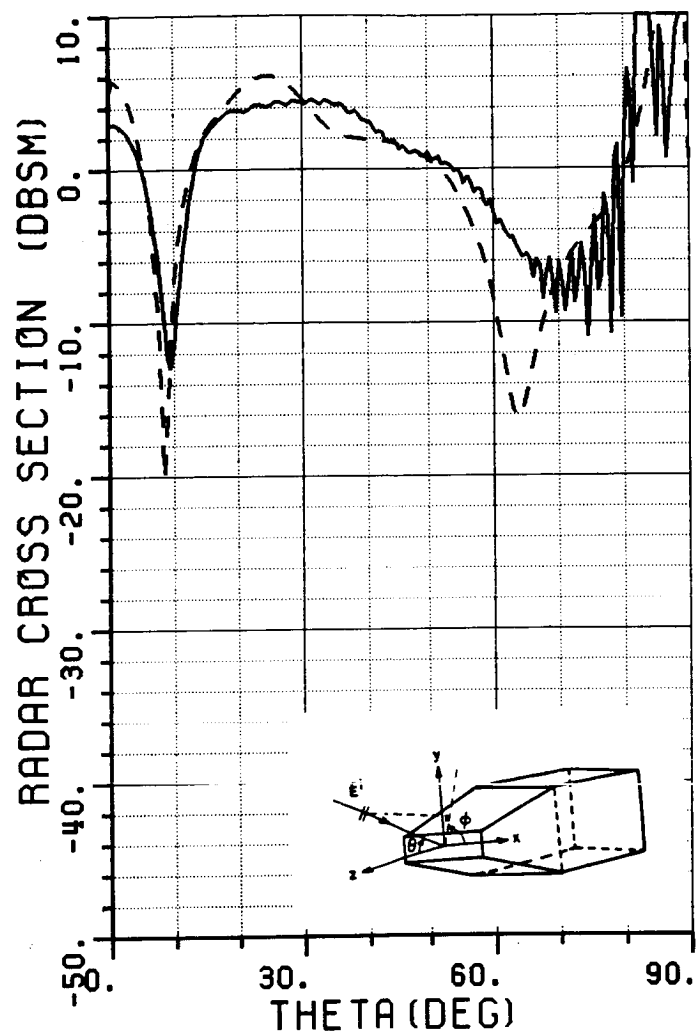


Figure 4.61. Radar cross section pattern at $f=10.01$ GHz,
 $\vec{E}^i = \hat{\phi}$, $\phi=90^\circ$ plane.
 — measured, --- calculated

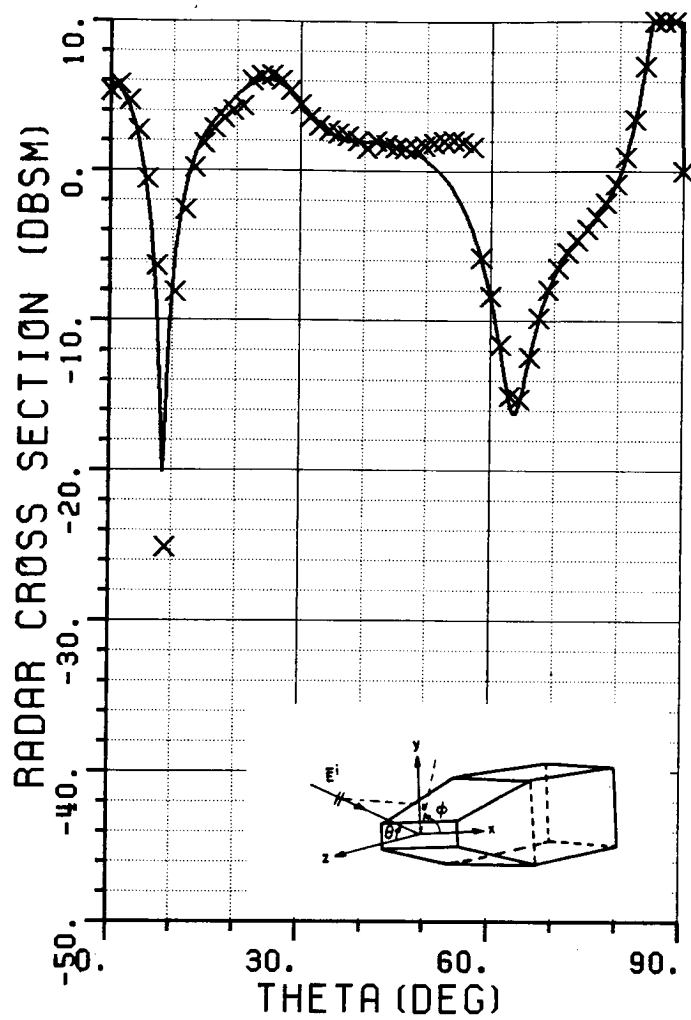


Figure 4.62. Calculated RCS pattern corresponding to Figure 4.61.
 — All modes are included
 xxx Only 3 modes are included

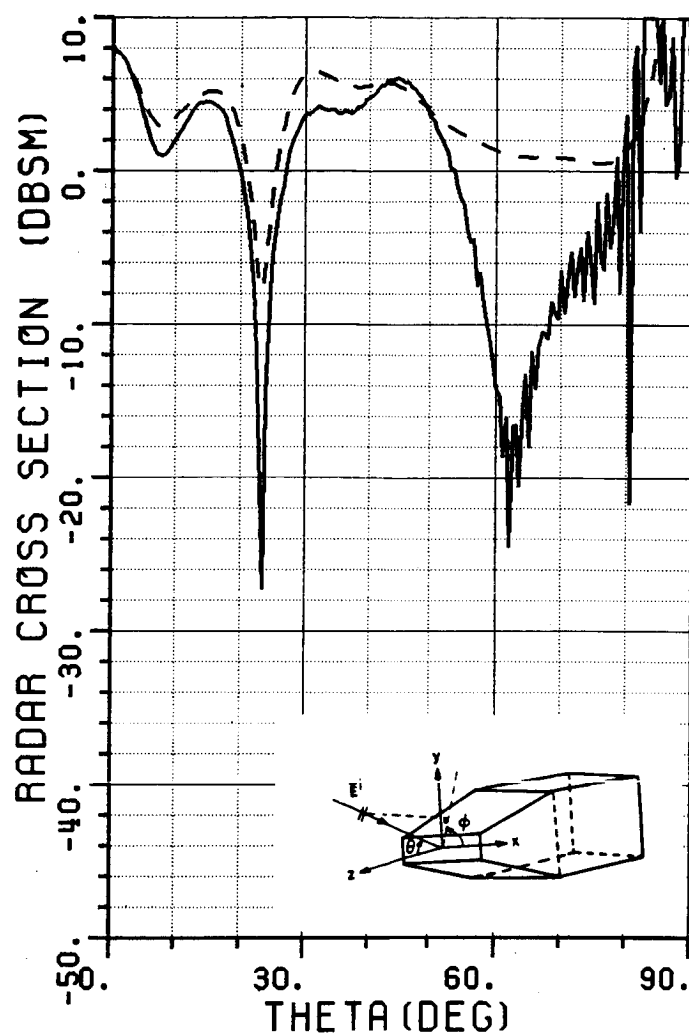


Figure 4.63. Radar cross section pattern at $f=11.96$ GHz,
 $E^i = \hat{\phi}$, $\phi=90^\circ$ plane.
 — measured, --- calculated

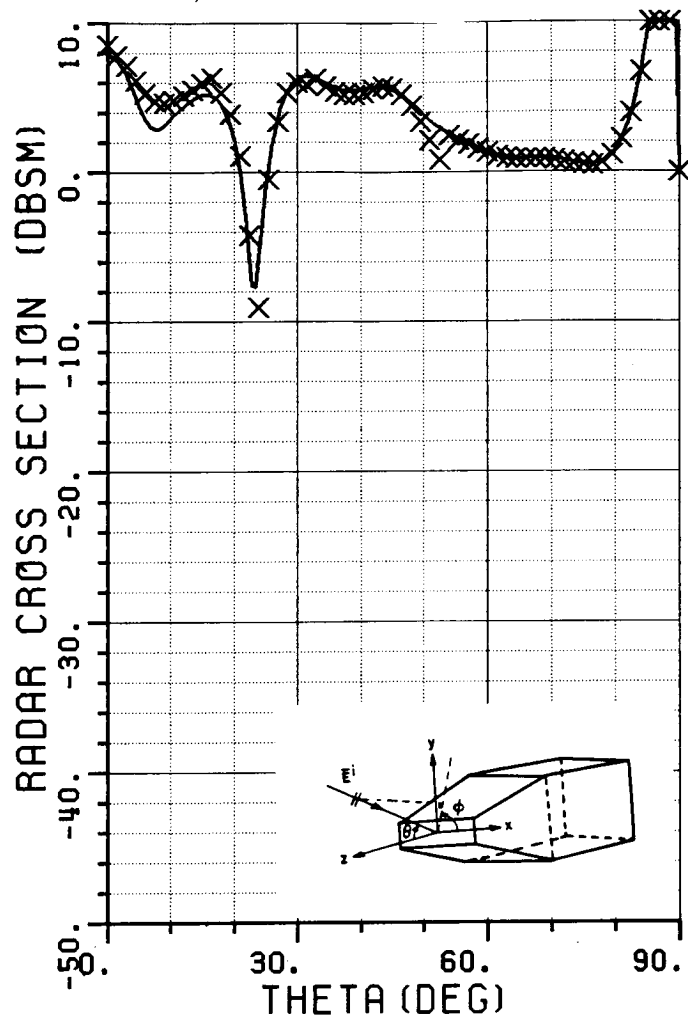


Figure 4.64. Calculated RCS pattern corresponding to Figure 4.63.
 — All modes are included
 xxx Only 3 modes are included

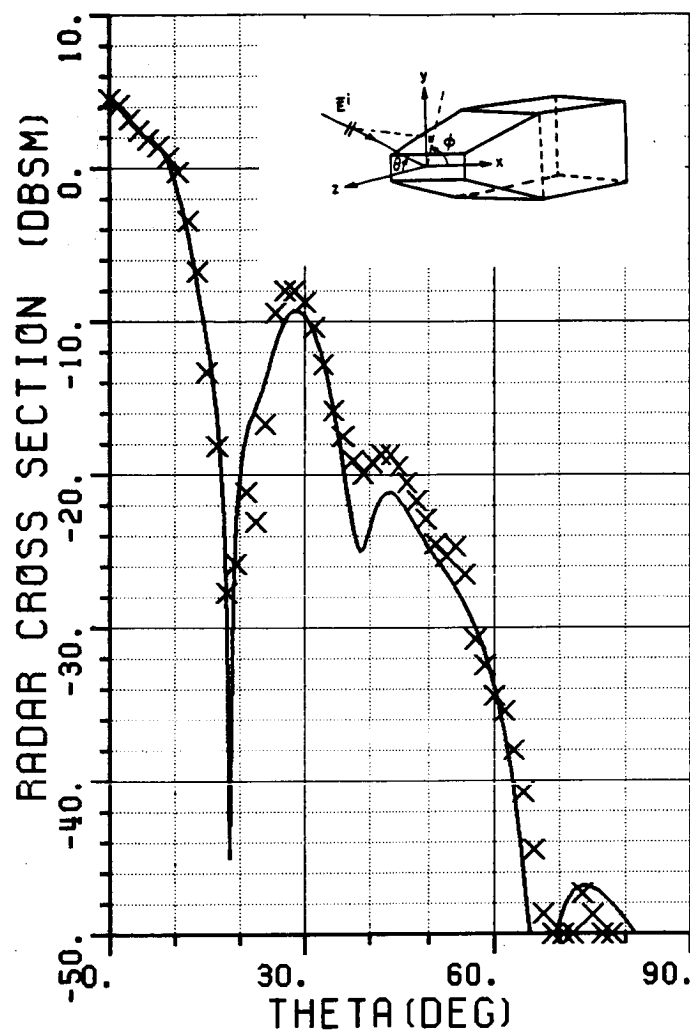


Figure 4.65. Radar cross section pattern at $f=10.00$ GHz,

$\vec{E}^i = \hat{\phi}$, $\phi=45^\circ$ plane.

— All 152 modes are included (86 TE, 66 TM modes)

xxx Only 18 modes are included (9 TE, 9 TM modes)

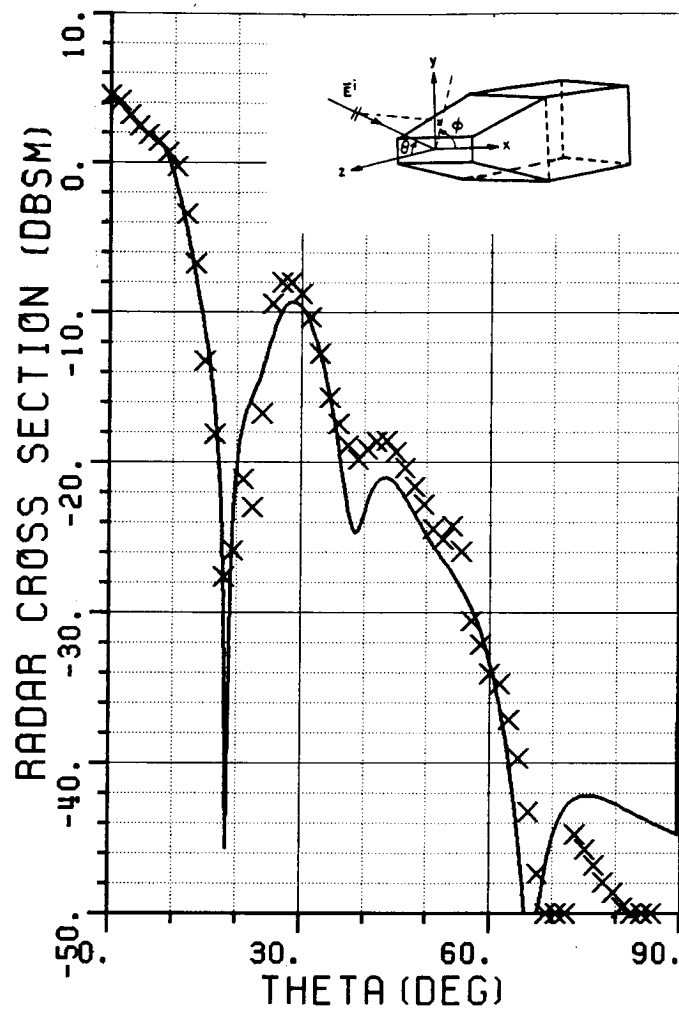


Figure 4.66. Radar cross section pattern at $f=10.00$ GHz,

$\vec{E}^i = \hat{\theta}$, $\phi=45^\circ$ plane.

— All 152 modes are included (86 TE, 66 TM modes)

xxx Only 18 modes are included (9 TE, 9 TM modes)

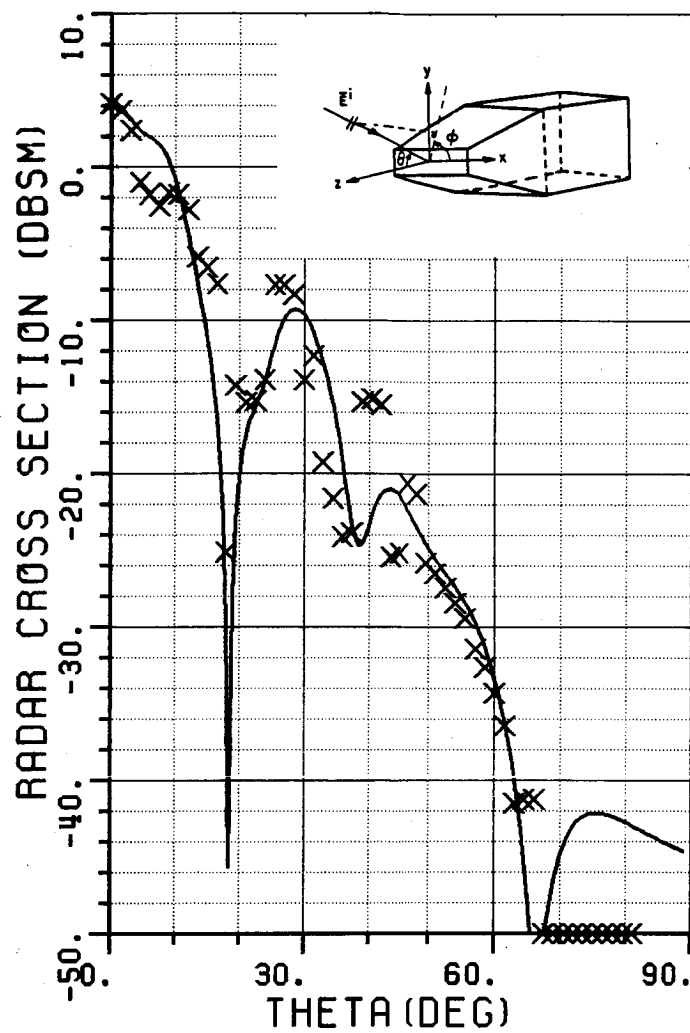


Figure 4.67. Radar cross section pattern at $f=10.00$ GHz,
 $E^i = \hat{\theta}$, $\phi=45^\circ$ plane.
 — All 152 modes are included (86 TE, 66 TM modes)
 xxx Only 6 modes are included (3 TE, 3 TM modes)

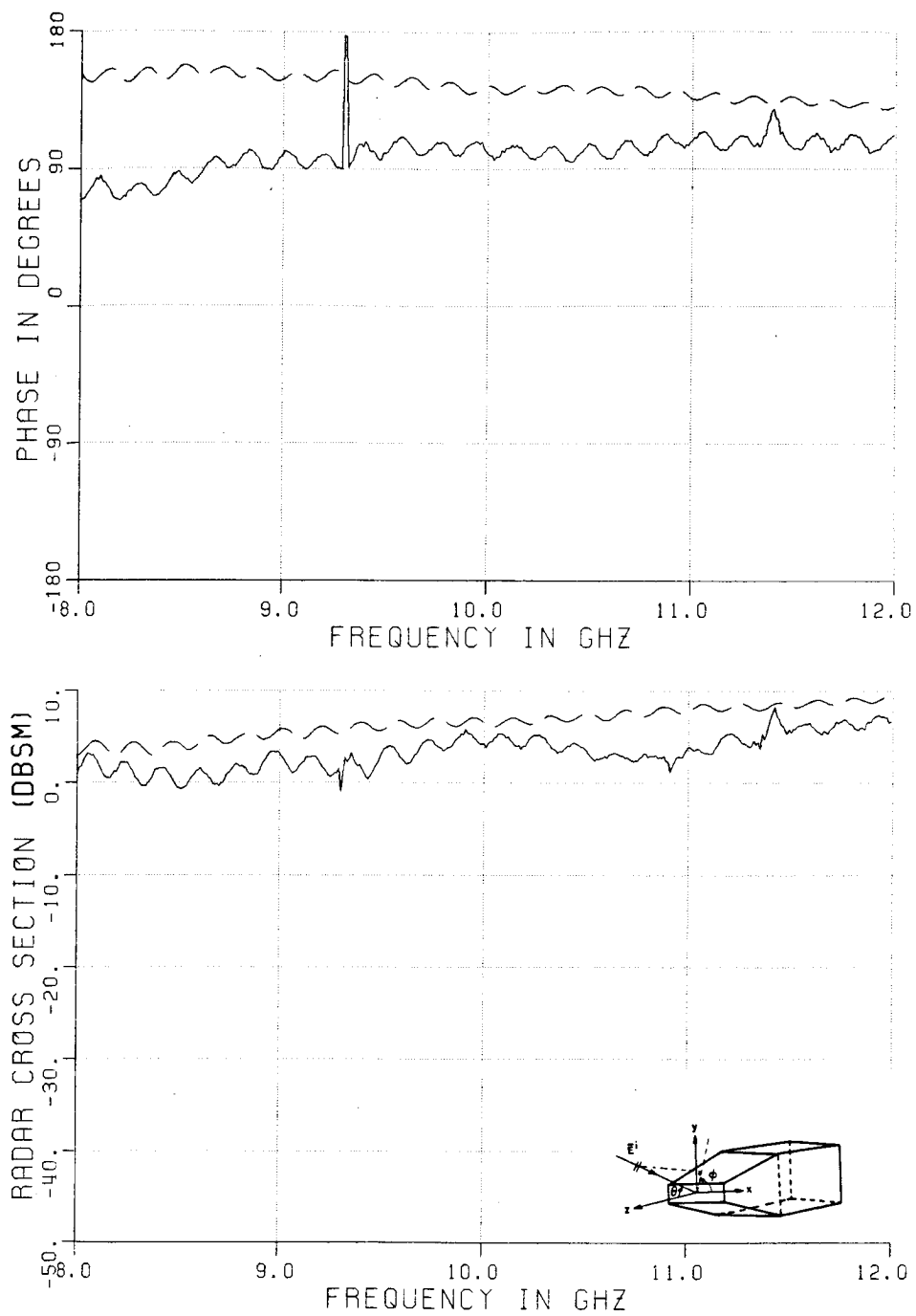


Figure 4.68. Variation of RCS with frequency $\bar{E}^i = \hat{\phi}$, $\phi=0$, $\theta=0$.

— measured --- calculated

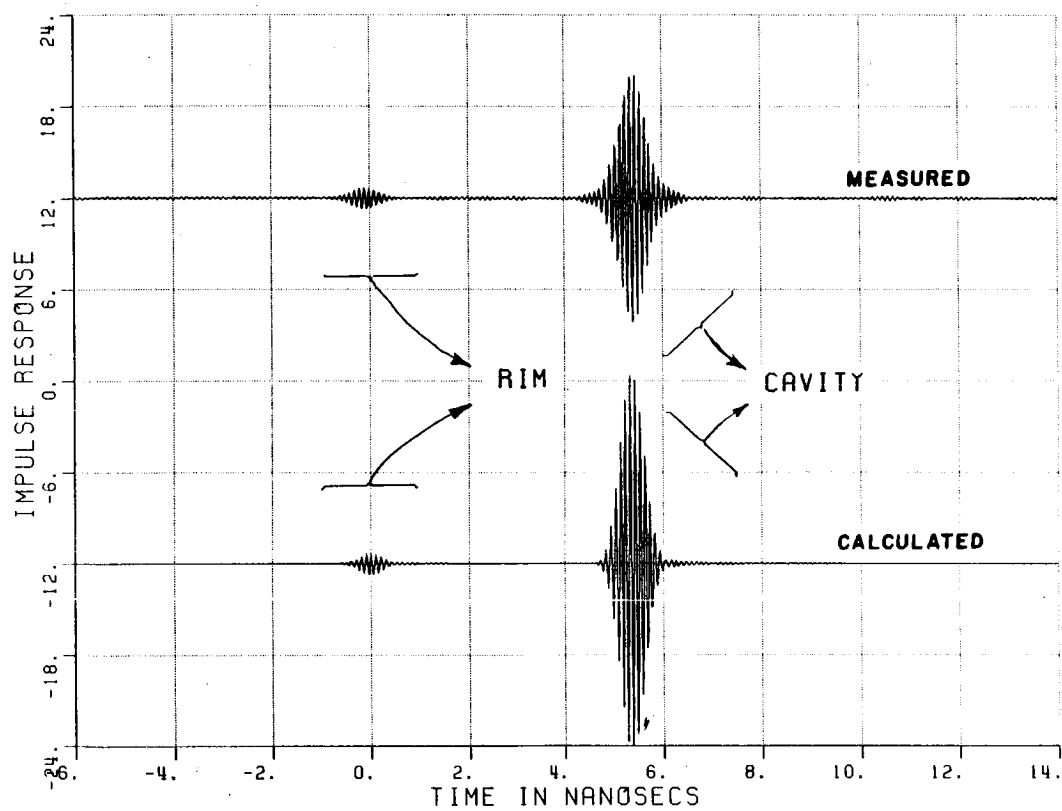


Figure 4.69. Inverse Fourier transforms (i.e., time domain plots) of the results in Figure 4.68.

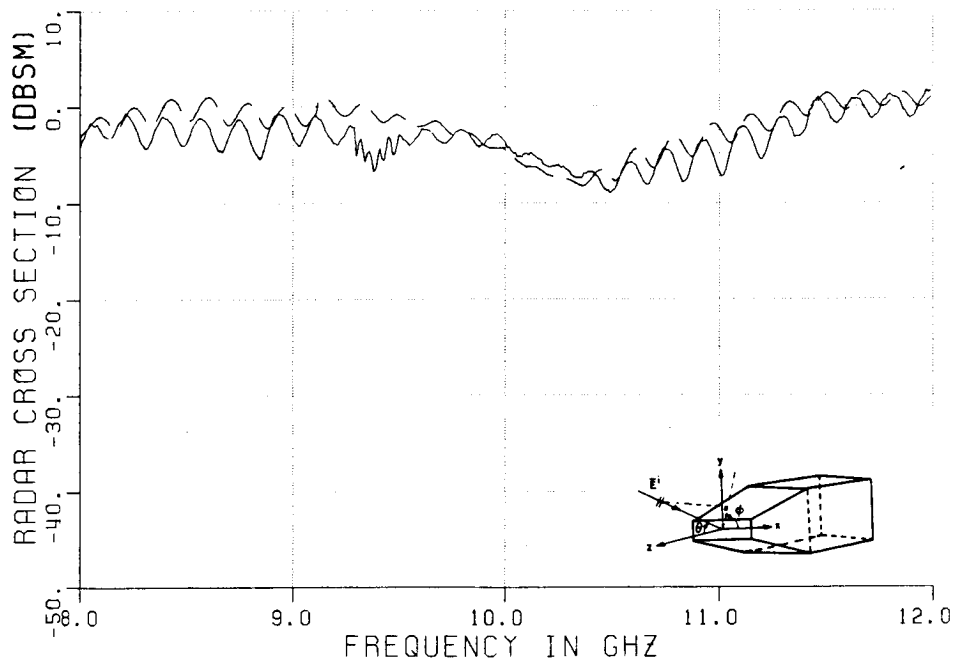
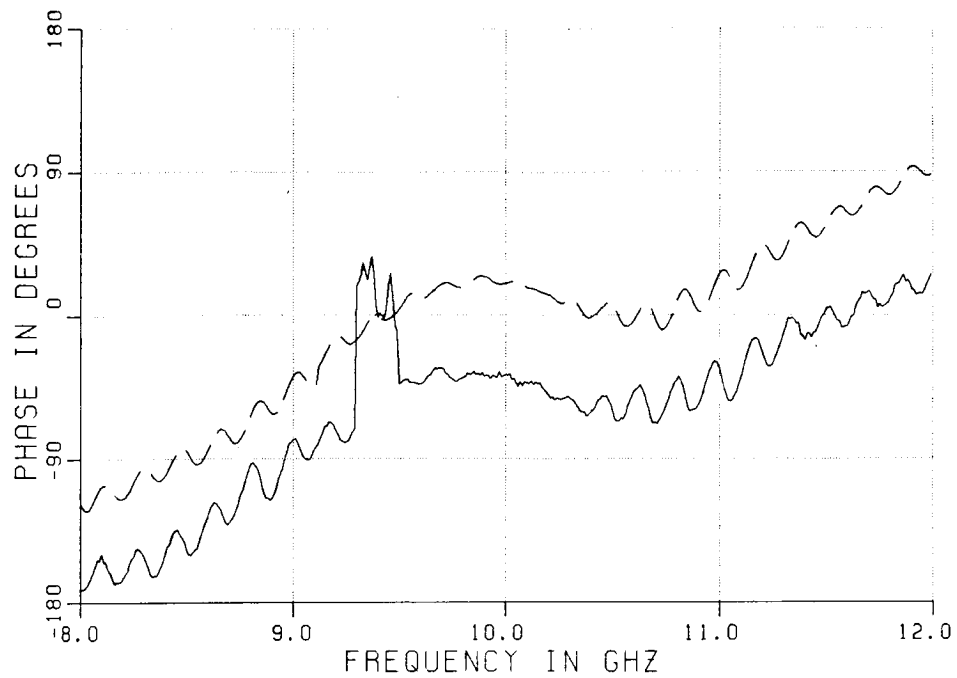


Figure 4.70. Variation of RCS with frequency $\vec{E}^i = \hat{\phi}$, $\phi=0$, $\theta=15^\circ$.
 — measured --- calculated

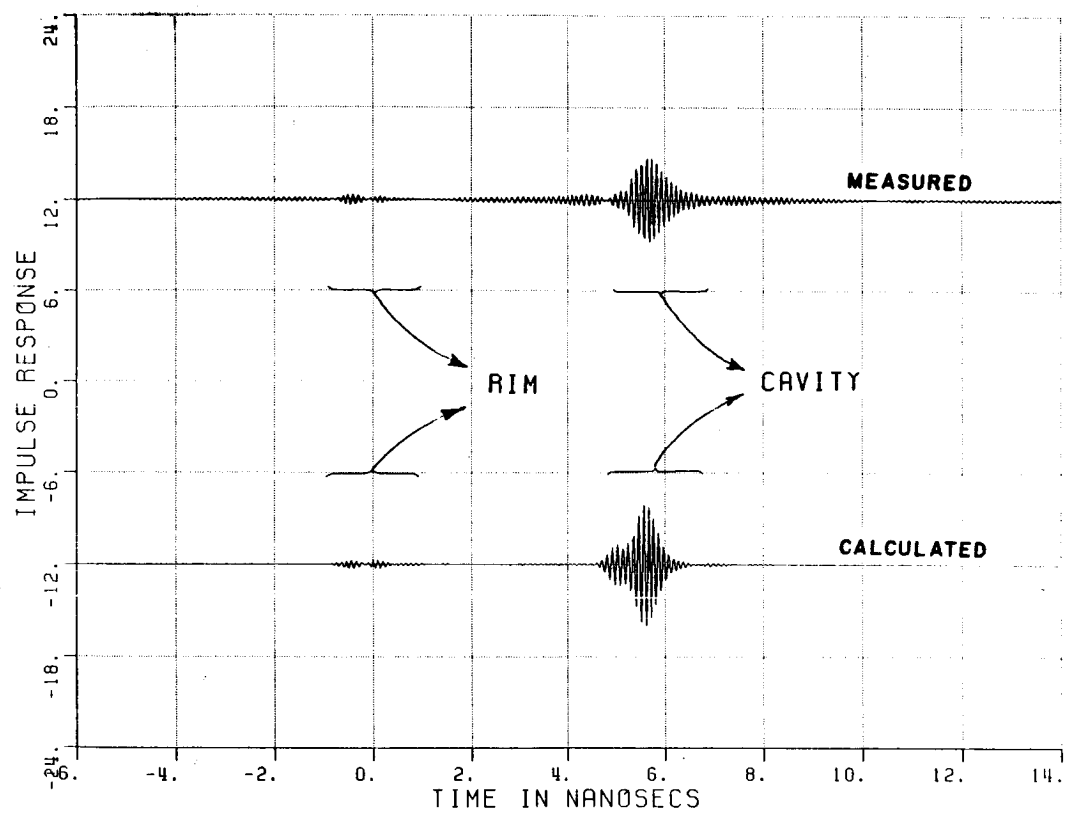


Figure 4.71. Inverse Fourier transforms (i.e., time domain plots) of the results in Figure 4.70.

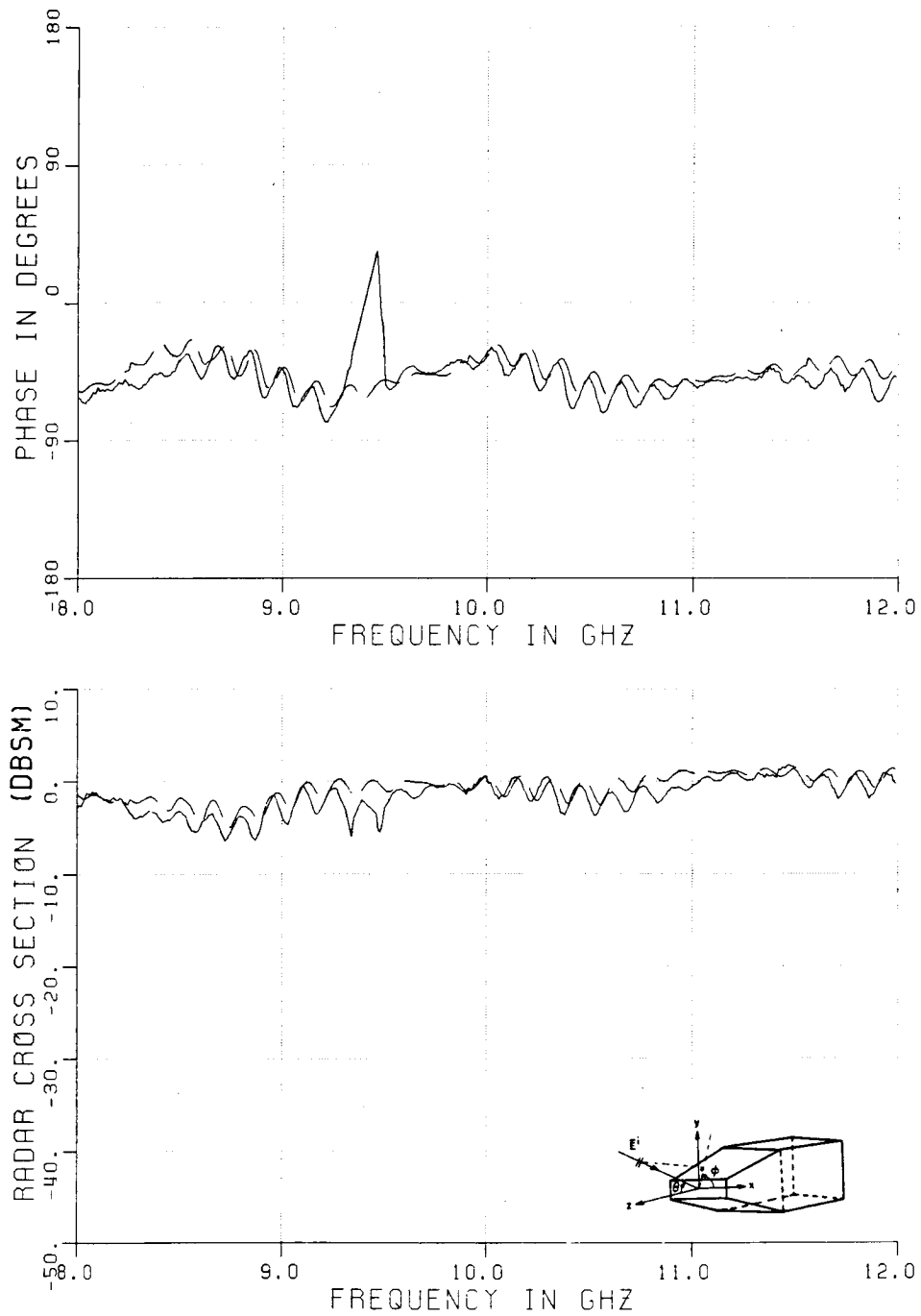


Figure 4.72. Variation of RCS with frequency $\vec{E}^i = \hat{\phi}$, $\phi=0$, $\theta=30^\circ$.
 — measured --- calculated

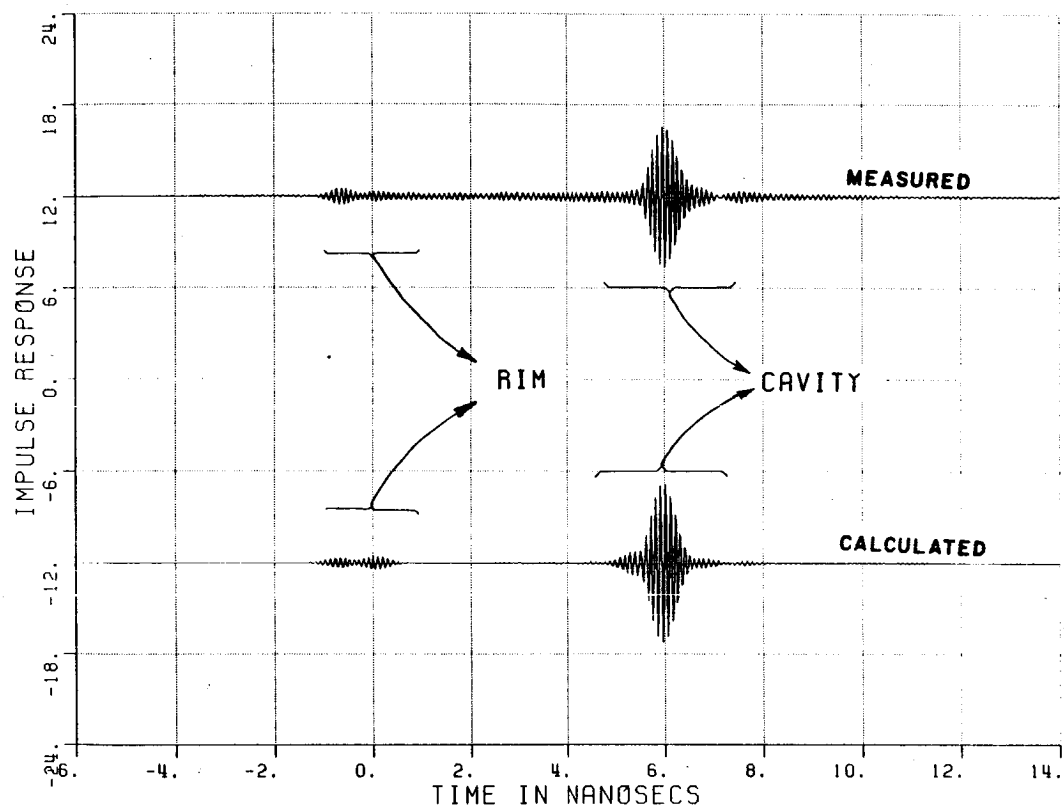


Figure 4.73. Inverse Fourier transforms (i.e., time domain plots) of the results in Figure 4.72.

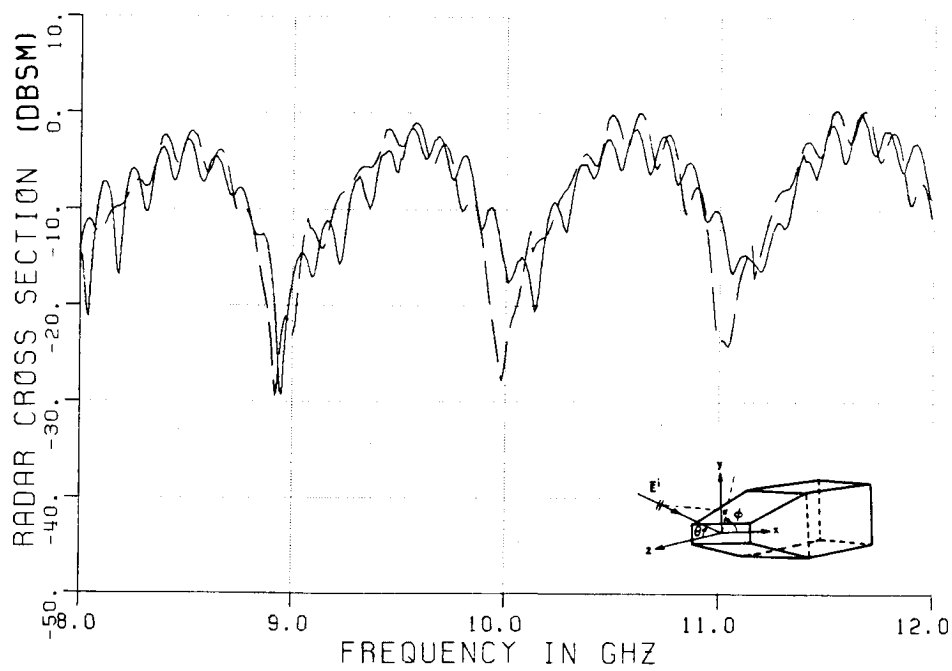
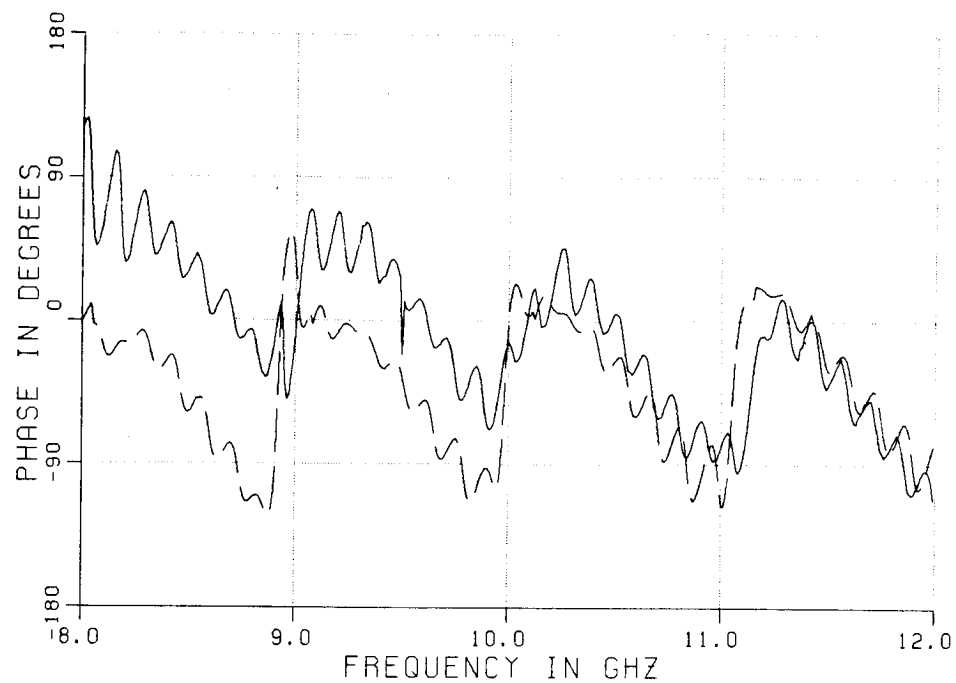


Figure 4.74. Variation of RCS with frequency $\bar{E}^i = \hat{\phi}$, $\phi=0$, $\theta=45^\circ$.
 — measured --- calculated

ORIGINAL PAGE IS
OF POOR QUALITY

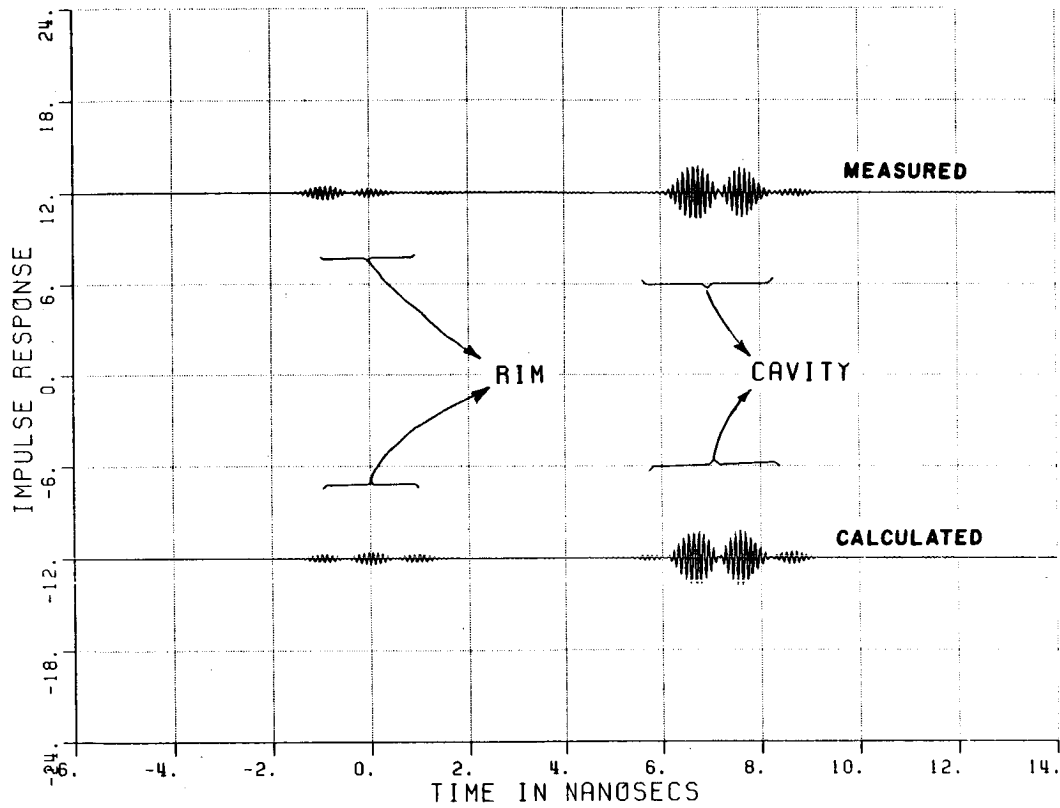


Figure 4.75. Inverse Fourier transforms (i.e., time domain plots) of the results in Figure 4.74.

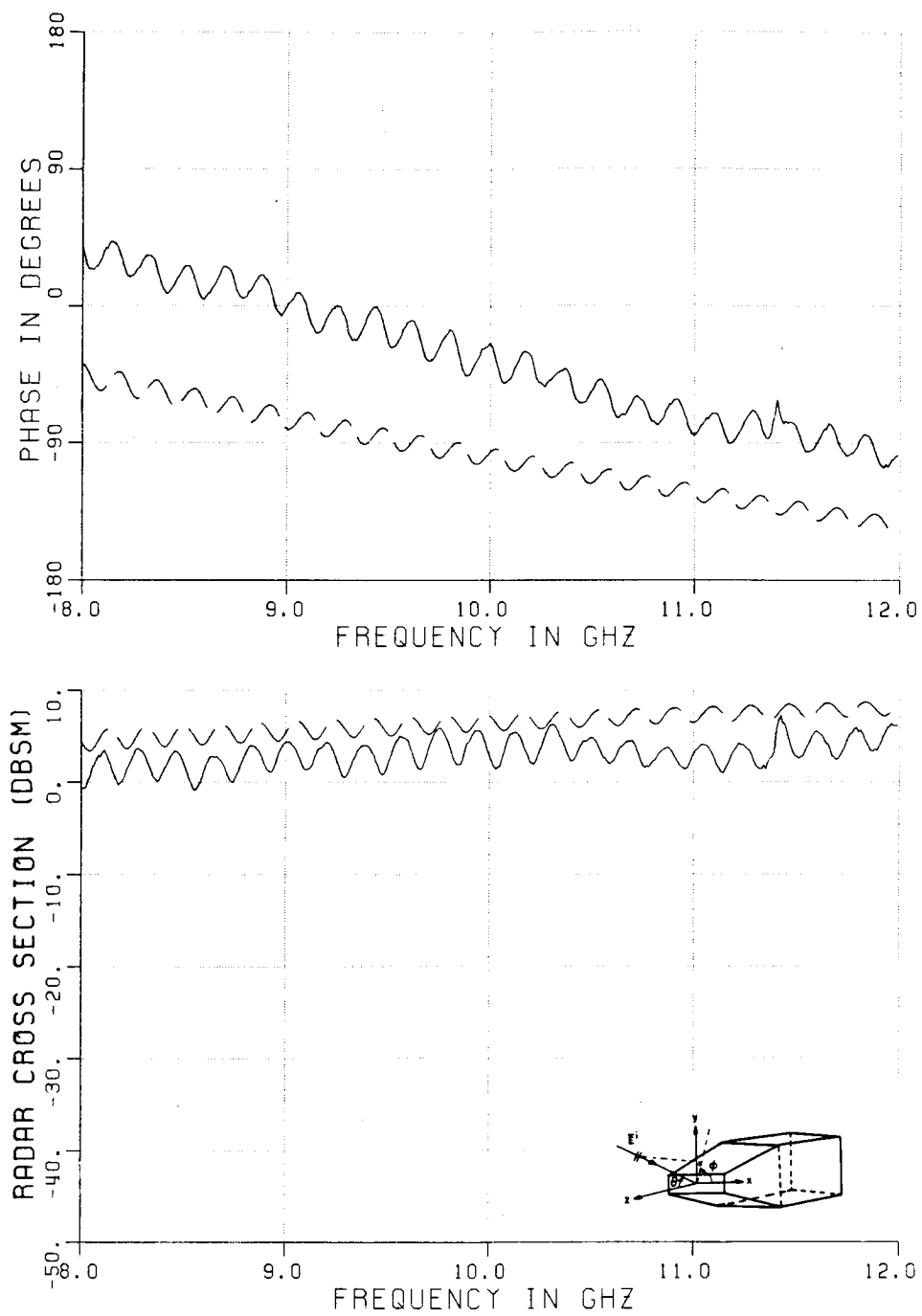


Figure 4.76. Variation of RCS with frequency $\vec{E}^i = \hat{\theta}$, $\phi=0$, $\theta=0$.
 — measured --- calculated

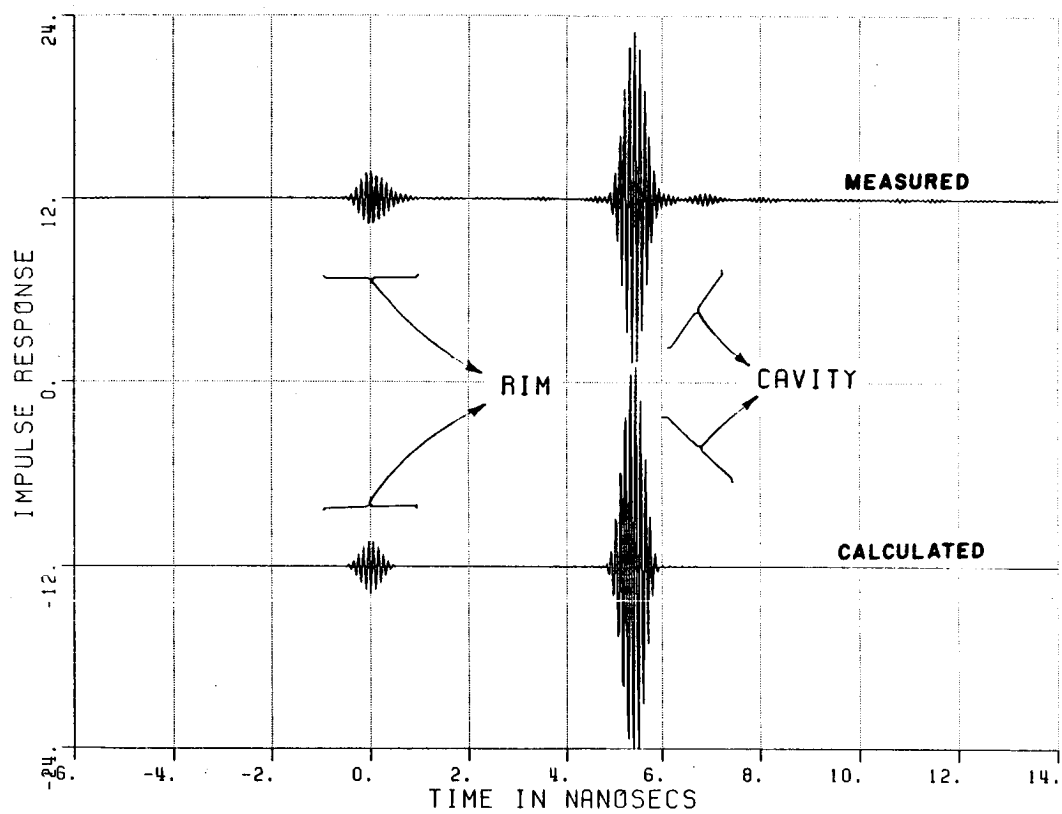


Figure 4.77. Inverse Fourier transforms (i.e., time domain plots) of the results in Figure 4.76.

ORIGINAL PAGE IS
OF POOR QUALITY

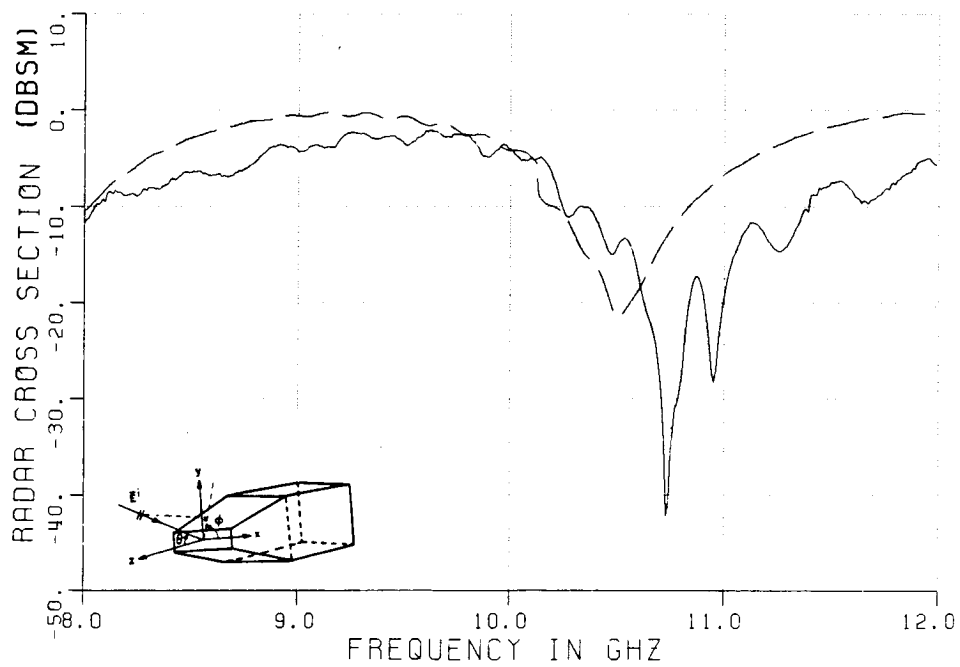
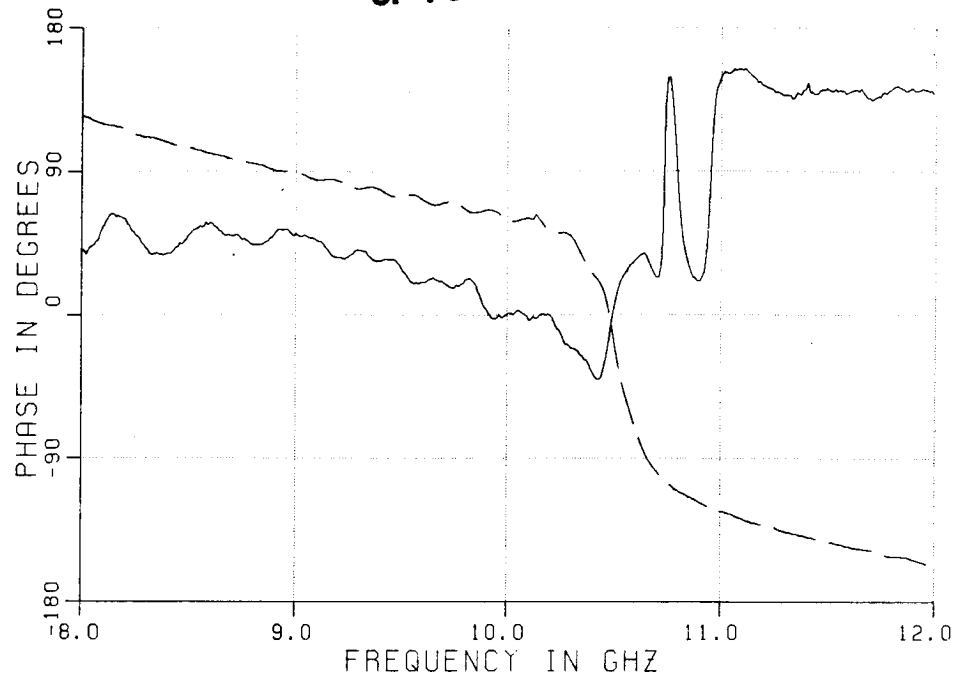


Figure 4.78. Variation of RCS with frequency $\vec{E}^i = \hat{\theta}$, $\phi=0$, $\theta=15^\circ$.

— measured --- calculated

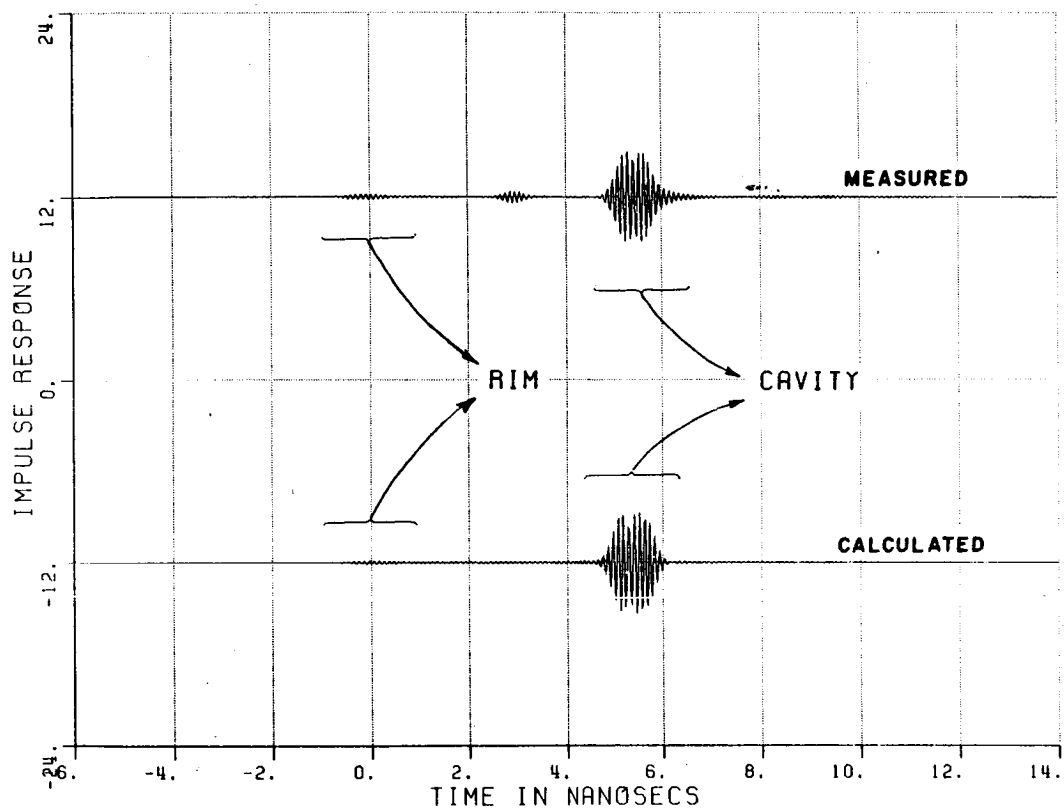


Figure 4.79. Inverse Fourier transforms (i.e., time domain plots) of the results in Figure 4.78.

ORIGINAL PAGE IS
OF POOR QUALITY

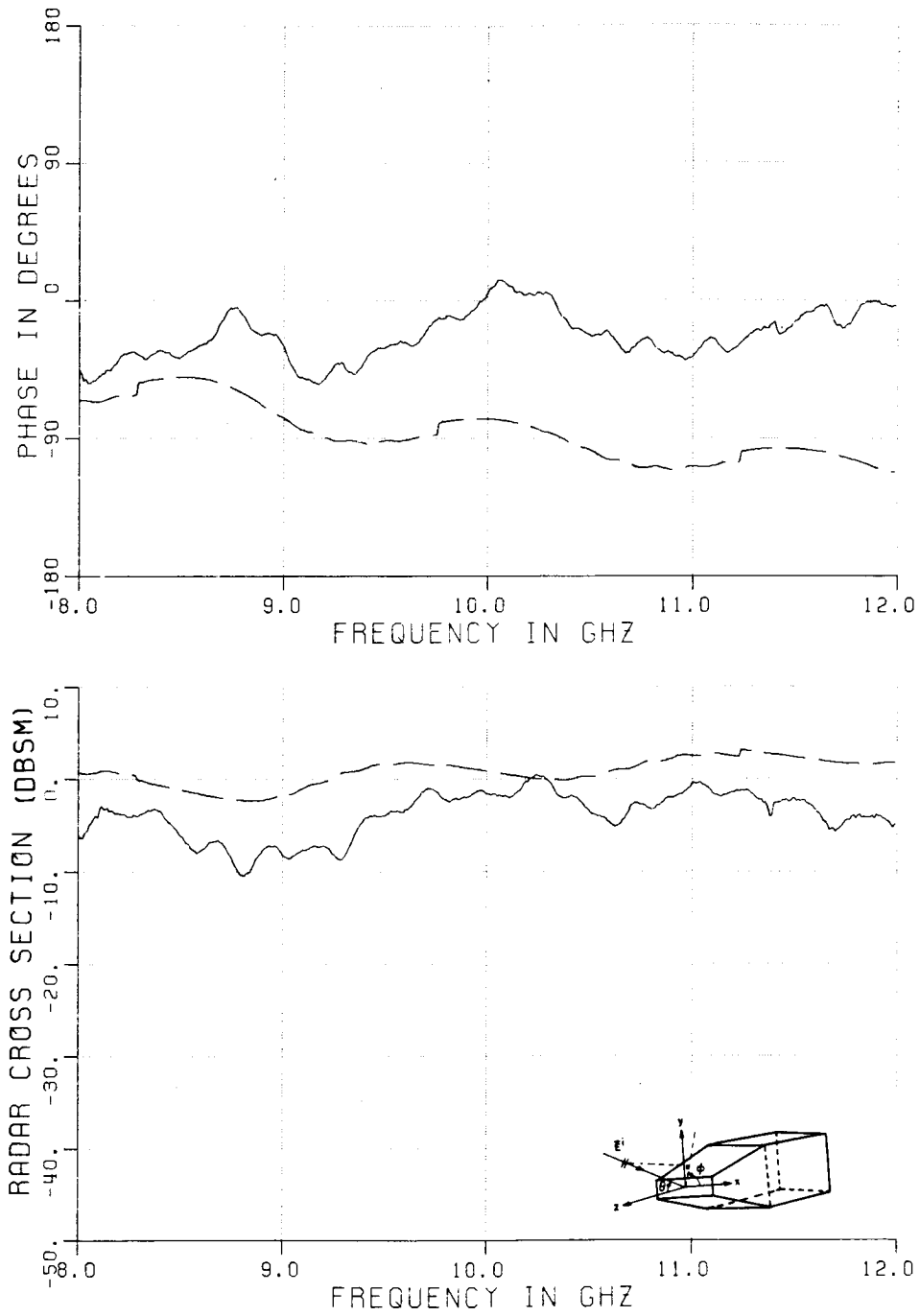


Figure 4.80. Variation of RCS with frequency $\vec{E}^i = \hat{\theta}$, $\phi = 0$, $\theta = 30^\circ$.
 — measured --- calculated

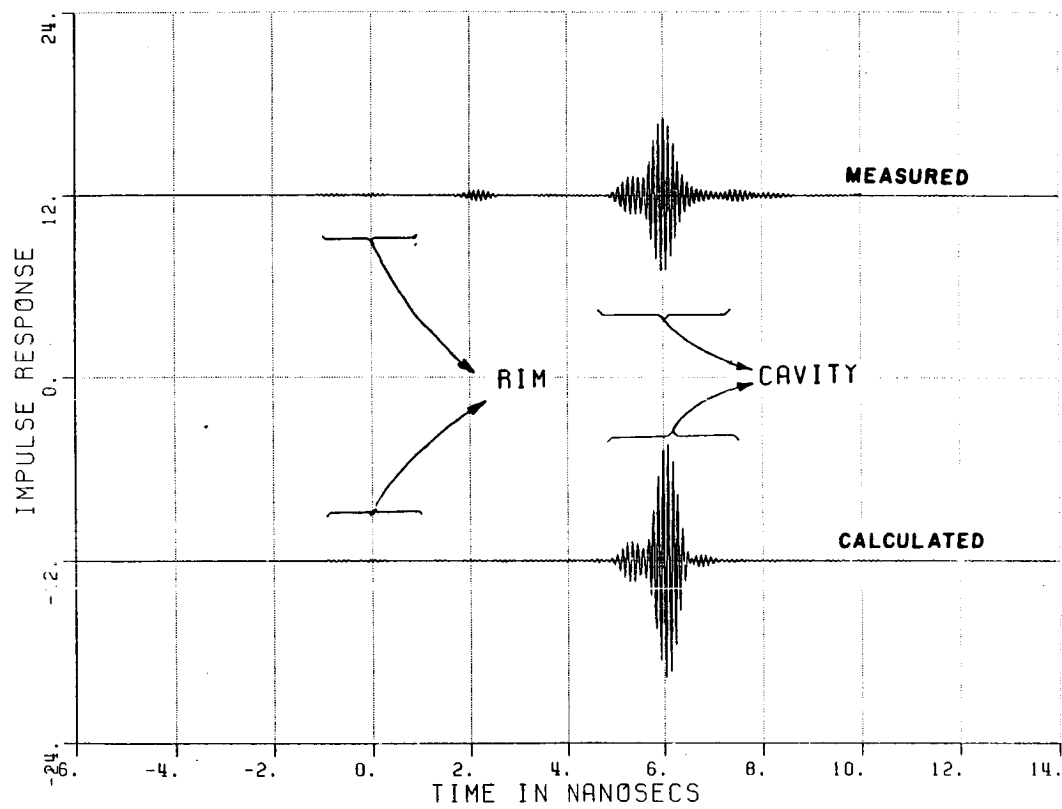


Figure 4.81. Inverse Fourier transforms (i.e., time domain plots) of the results in Figure 4.80.

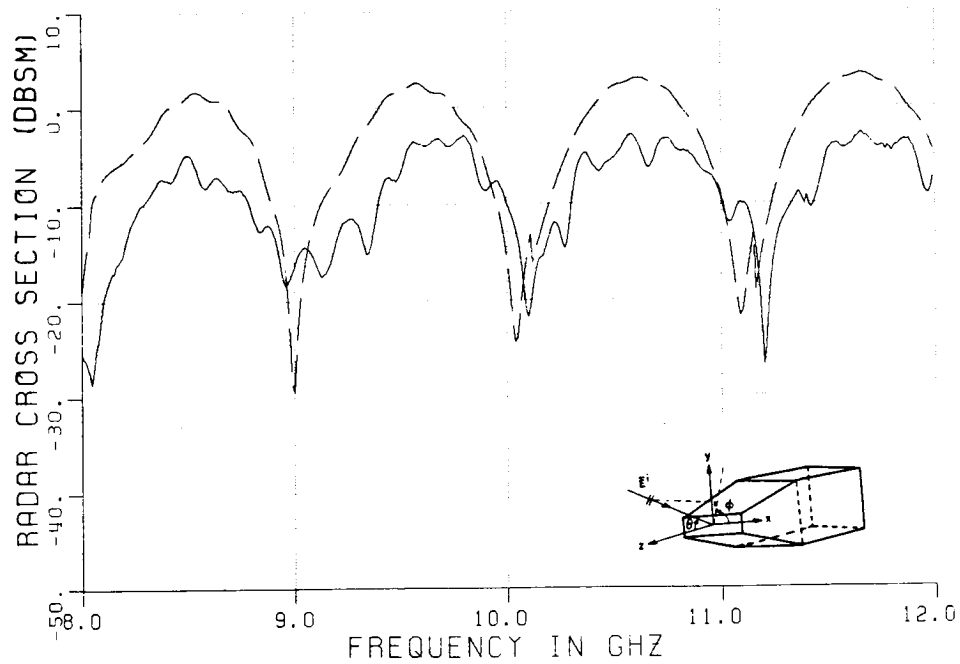
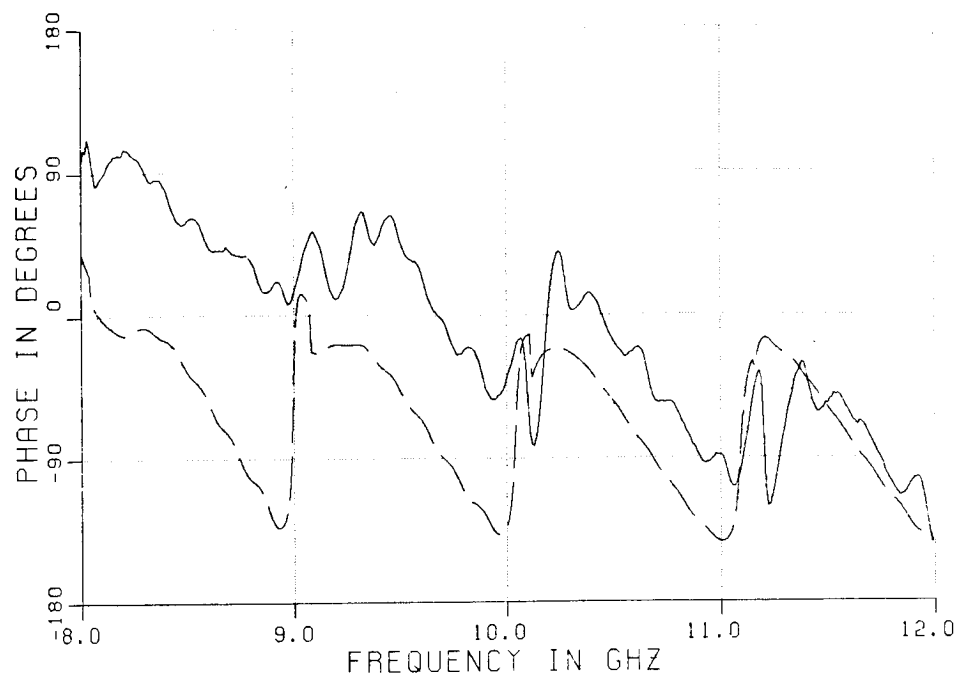


Figure 4.82. Variation of RCS with frequency $\vec{E}^i = \hat{\theta}$, $\phi=0$, $\theta=45^\circ$.
 — measured --- calculated

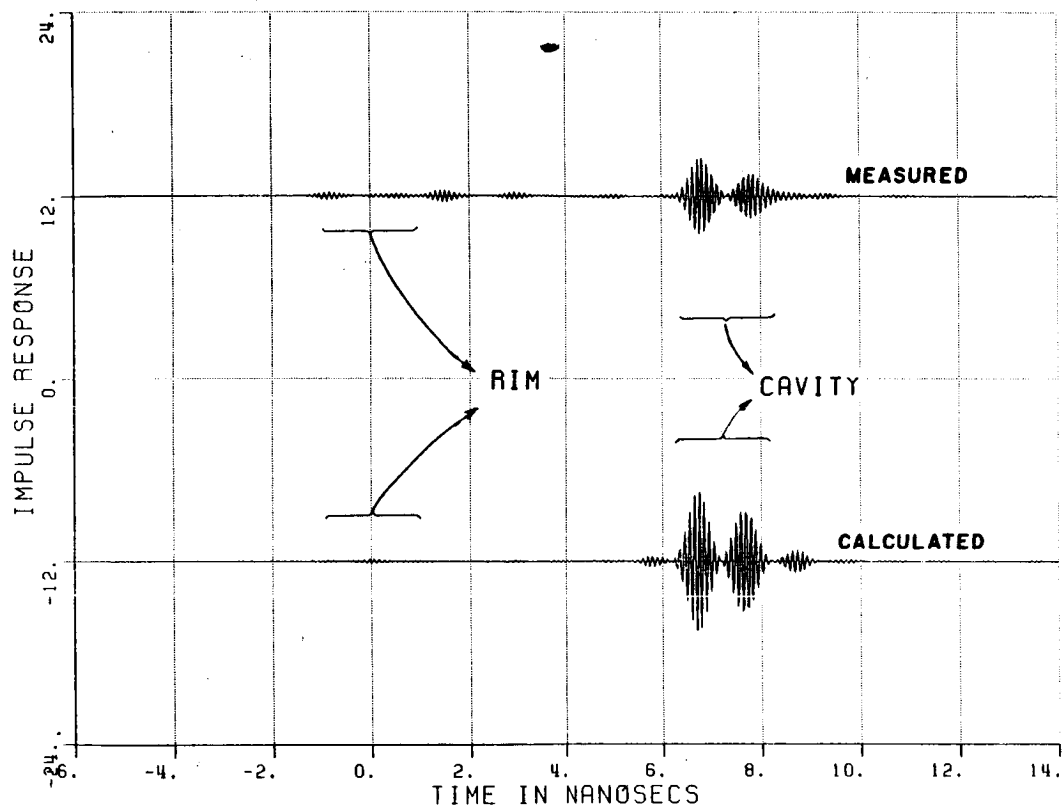


Figure 4.83. Inverse Fourier transforms (i.e., time domain plots) of the results in Figure 4.82.

ORIGINAL PAGE IS
OF POOR QUALITY

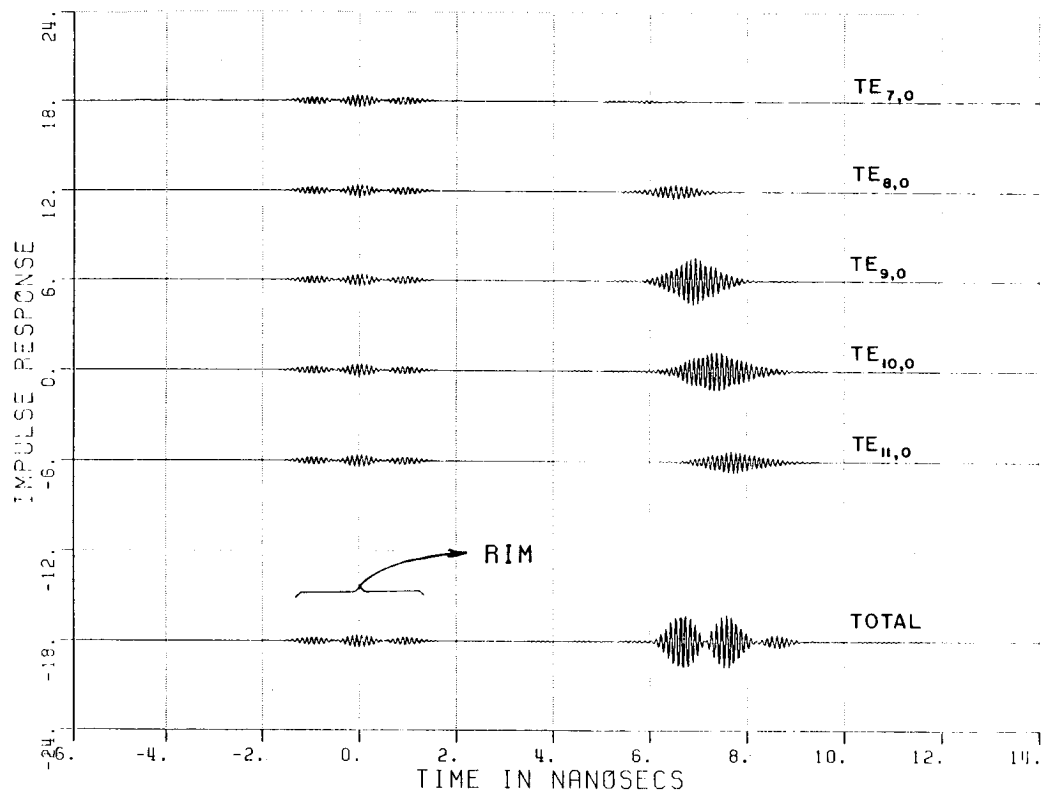


Figure 4.84. The separate returns of modes for the case in Figure 4.75.

Finally, the frequency scan results are calculated and compared with measurements in Figures 4.68 through 4.83. As in the previous section, the time domain results are deliberately shifted to better illustrate the comparisons. Note that in each case the comparisons are very good.

In Figure 4.84, the contribution of several modes is plotted separately for the geometry associated with the results of Figure 4.75. It is seen that as the mode number increases the given mode undergoes more bounces inside the waveguide, travels a longer distance, and therefore its return is received later in time; i.e., a stronger modal dispersion. Also note that the modal terms add up to form ripples in the total result from the cavity effect. If not understood correctly, one might think this is indicating different scattering centers, which would not be true. This shows that modal propagation should carefully be traced if one wishes to obtain the true response for the cavity effects.

e) Electromagnetic backscattering from a circular waveguide cavity:

The EM backscatter results based on (3.5), (3.6), (3.151) and (3.152) are calculated here. The rim and cavity effects are separately shown together with their superposition in Figures 4.86 through 4.89. The main contribution to the backscatter return is the cavity effect due to the perfectly-conducting termination; whereas, the rim scattering

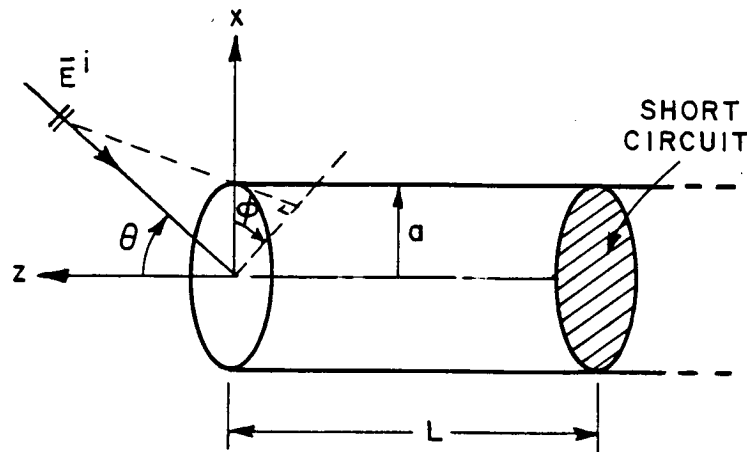


Figure 4.85. Circular waveguide cavity terminated by a short circuit.

contribution results in a perturbation to the cavity effects. The radius of the waveguide is taken as 3.34 wavelengths which allows 115 modes to propagate. The Figures 4.86 and 4.88 illustrate the contributions of all propagating modes; whereas in figures 4.87 and 4.89 only the modes are included with modal ray angles inside a 10° neighborhood of the observation direction. It is clear from these plots that by including only the few significant modes, one can substantially reduce the amount of calculations without seriously sacrificing accuracy. It is also noted that the length of the waveguide cavity is 10 wavelengths; therefore, all evanescent mode contributions are neglected.

ORIGINAL PAGE IS
OF POOR QUALITY

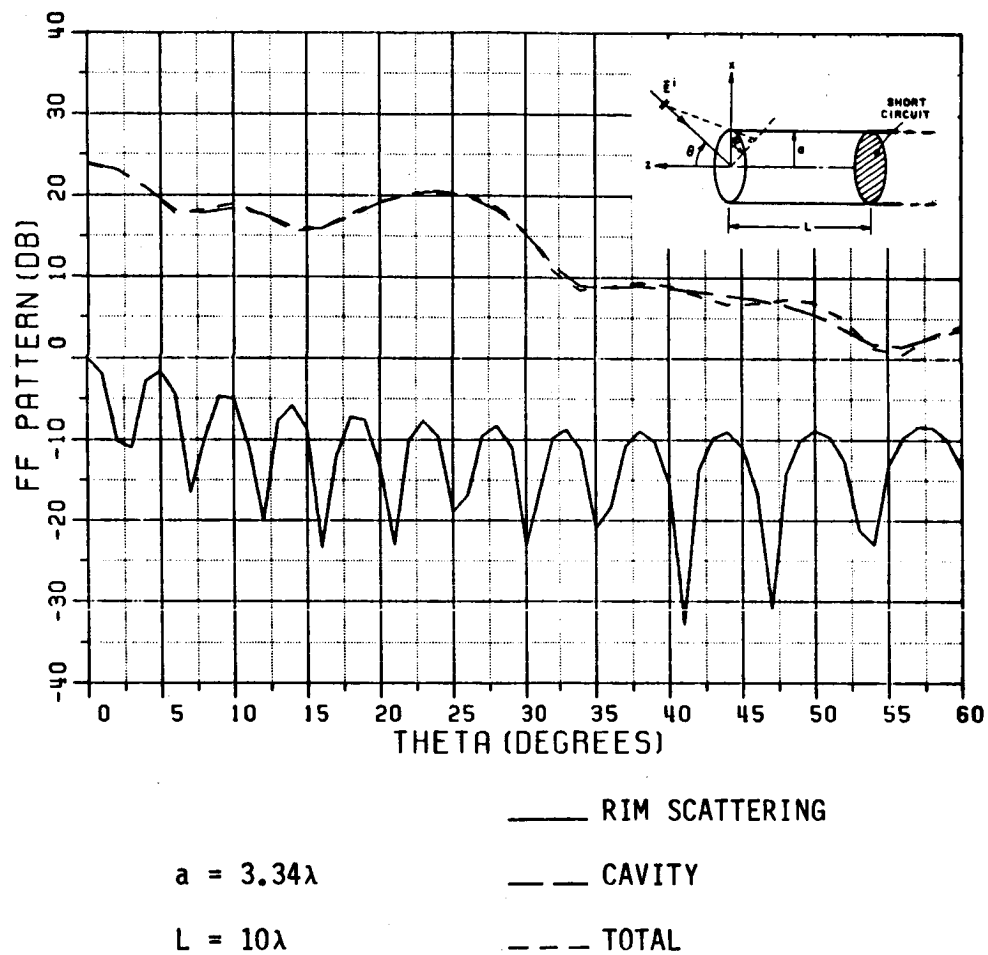


Figure 4.86. Backscattered field from a circular waveguide cavity, as a function of the angle from the axis. All propagating modes are included. $E^i = \hat{\phi}$.

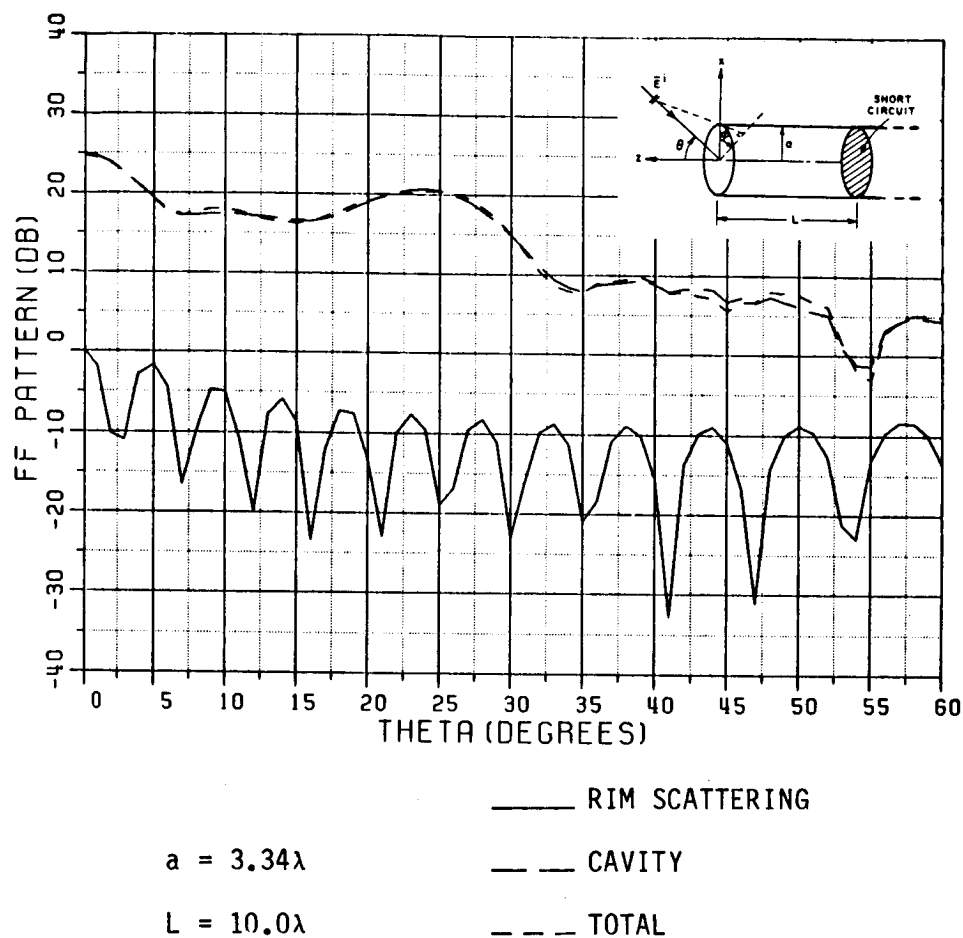


Figure 4.87. Backscattered field from a circular waveguide cavity, as a function of the angle from the axis. Only modes with modal ray angles closer than 10 degrees are included.

$$\hat{E}^i = \hat{\phi}.$$

ORIGINAL PAGE IS
OF POOR QUALITY

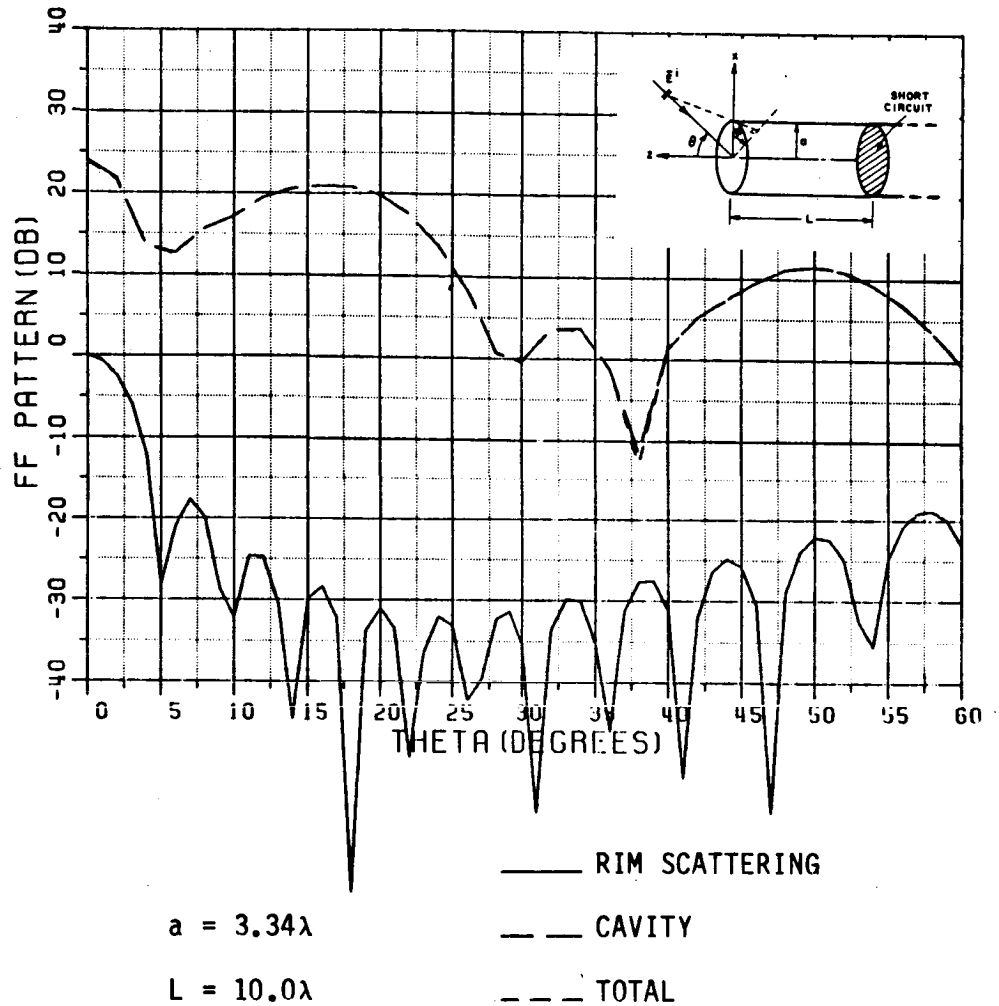


Figure 4.88. Backscattered field from a circular waveguide cavity, as a function of the angle from the axis. All propagating modes are included. $E^i = \hat{\theta}$.

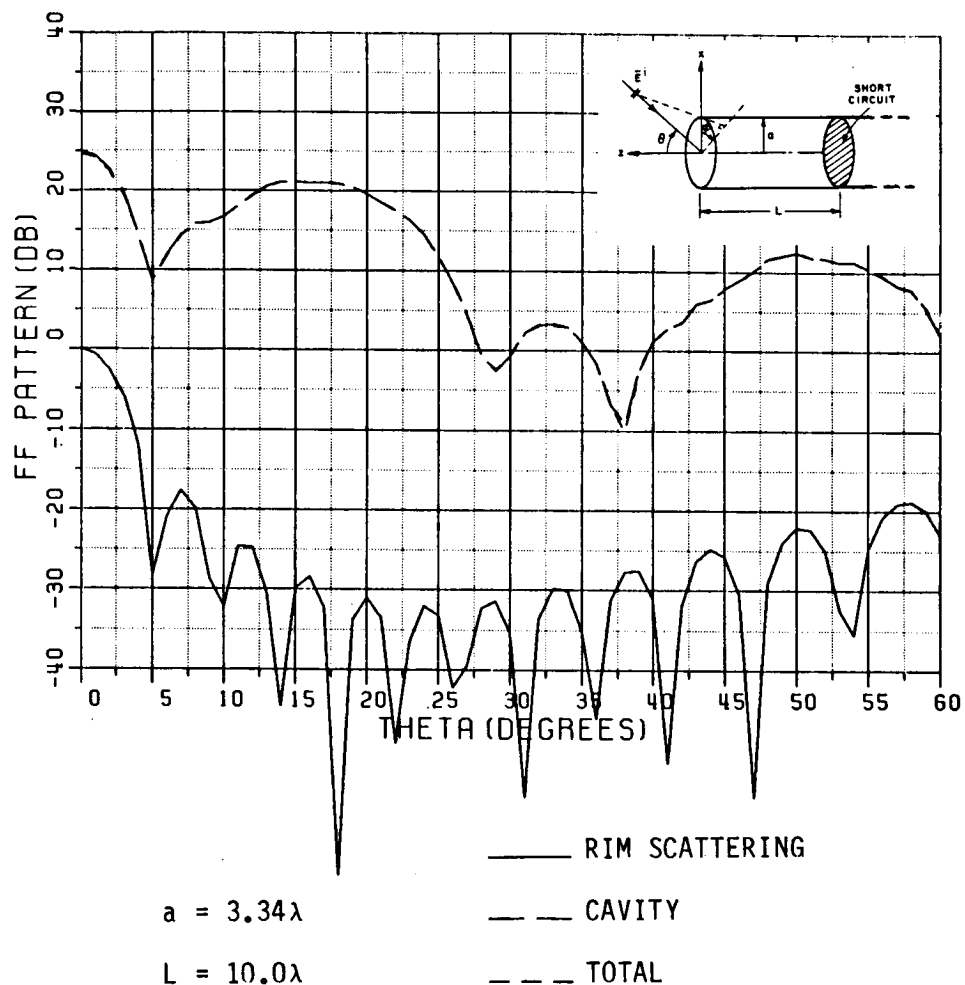


Figure 4.89. Backscattered field from a circular waveguide cavity, as a function of the angle from the axis. Only modes with modal ray angles closer than 10 degrees are included.

$\hat{E}^i = \hat{\theta}$.

CHAPTER V

CONCLUSIONS

A relatively simple, efficient and sufficiently accurate analysis of electromagnetic scattering by a class of electrically large, open-ended waveguide cavities was developed in this work using a hybrid combination of high frequency, modal and multiple scattering methods. The cavities are composed of waveguide sections in which the Helmholtz's equation is separable; therefore, the EM field inside each section can be written as a sum of waveguide modes. These modal waveguide field expressions are expressed in terms of "modal rays" through asymptotic approximations to the modal functions. The scattering properties of the discontinuities formed by the junctions between the sections are analyzed using high frequency techniques together with the modal rays. The latter techniques employ the GTD and the ECM which require a knowledge of the pertinent diffraction coefficients that are available from the asymptotic solutions to appropriate canonical problems. In some situations the analysis also employs high frequency approximations based on the PTD and its modifications. These high frequency techniques used in conjunction with the "modal rays" lead to a relatively simple description of the isolated junction scattering matrices. These individual junction scattering matrices are then combined in a

self-consistent multiple scattering approach to get the total scattering effect of the cavity.

Basically, the scattering matrices are analyzed in two categories. The reflection type scattering matrices include an integration of the GTD based equivalent currents over the edges of the junction apertures. It is important to note that the previous ray-optical techniques [10,14,20] to treat the reflection from the open-end of waveguides employed the GTD based equivalent electric and magnetic line sources in free-space. That procedure is applicable only to those geometries where one can sum up the radiation from equivalent sources and their images, such as parallel-plate and circular waveguide geometries. In the present work, the equivalent sources radiate in the presence of waveguide walls and therefore they are magnetic line sources and magnetic line dipoles. Hence, this proposed procedure can be generalized to many other geometries which lack the symmetry properties required by the previous methods. The transmission type equivalent currents are computed via a Kirchhoff-Huygens' approximation to the aperture field. It is shown in Appendix H that this aperture integration can be corrected in the same way as the PO is corrected via the PTD. However, the integration process does not give any physical insight to the problem, and as the number of propagating modes increases with frequency, it becomes cumbersome and inefficient.

In this research, new approaches to substantially improve the efficiency of the above mentioned aperture integrals were investigated. It was determined that for the open-ended rectangular and circular

waveguides the modal radiation from the open end is strongest along their modal ray directions. Therefore, for a given radiation direction one can include only the radiation of those modes whose modal ray directions are closest to the radiation direction. In Section 3.2, it was shown that for the cavities formed by parallel-plate waveguides, if one includes only the contributions of modes with modal ray angles which are less than a fixed angular distance from a given observation direction, then the error in the backscattered field stays bounded with increasing frequency, even though the number of propagating modes increases with frequency. In Chapter IV, numerical and experimental results were compared to assess the accuracy of the analysis, and to indicate that the contribution of only a few modes with modal ray directions closest to the observation direction accurately approximates the contribution of all the propagating modes. This is an important result, because it combines modal radiation with ray-optics, and therefore it can be applied to many different and complex waveguide geometries to effectively select only the few significant modes from the entire set of propagating modes.

The accuracy of the scattering from waveguide cavities is determined in turn by the accuracy of the scattering matrices involved. In this research, the accuracy of the analysis for scattering matrices has been verified by comparison with other analytical and experimental results on certain cavity geometries. It is noted that there were very few dependable numerical and experimental results available for the 3-D cavities formed by sections of linearly tapered and uniformly curved

waveguides even though they are very often encountered in practice. The experimental model with linearly tapered walls which was treated in Chapter IV had a small interior discontinuity, and, as expected, it did not seem to significantly influence the final results. As a part of future research, practical cavity models with more pronounced interior discontinuities will be built and analyzed.

APPENDIX A

MODAL FIELD EXPRESSIONS IN A RECTANGULAR WAVEGUIDE

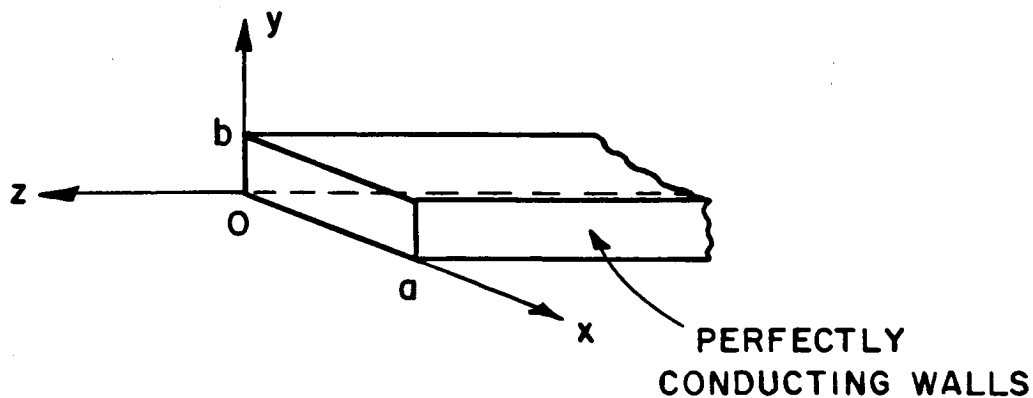


Figure A.1. Rectangular waveguide geometry.

As described in [44], the modes in a rectangular waveguide as shown in Figure A.1 can be classified into sets of fields transverse to a coordinate direction.

The mode sets transverse to the axial (\hat{z}) direction are important and widely used, because it applies to uniform nonrectangular cross-section guides. However, in many problems, mode sets transverse to \hat{x} or \hat{y} coordinate may be more suitable.

These sets can be calculated from an axial or transverse vector potential [44]. The TE_{nm} and TM_{nm} to \hat{z} type modal field expressions are given by:

$$\begin{array}{cc} \underline{TE_{nm}} & \underline{TM_{nm}} \\ h_z = N_{nm} Y_{nm} \frac{n_a^2 + m_b^2}{j\beta_{nm}} \cos n_a x \cos m_b y & 0 \end{array} \quad (A.1a;b)$$

$$e_z = 0 \quad -N_{nm} \frac{n_a^2 + m_b^2}{j\beta_{nm}} \sin n_a x \sin m_b y \quad (A.2a;b)$$

$$h_x = N_{nm} Y_{nm} n_a \sin n_a x \cos m_b y \quad -N_{nm} Y_{nm} m_b \sin n_a x \cos m_b y \quad (A.3a;b)$$

$$h_y = N_{nm} Y_{nm} m_b \cos n_a x \sin m_b y \quad N_{nm} Y_{nm} n_a \cos n_a x \sin m_b y \quad (A.4a;b)$$

$$e_x = N_{nm} m_b \cos n_a x \sin m_b y \quad N_{nm} n_a \cos n_a x \sin m_b y \quad (A.5a;b)$$

$$e_y = -N_{nm} n_a \sin n_a x \cos m_b y \quad N_{nm} m_b \sin n_a x \cos m_b y \quad (A.6a;b)$$

$$Y_{nm} = Y_o \beta_{nm} / k \quad Y_o k / \beta_{nm} \quad (A.7a;b)$$

$$0 < x < a, \quad 0 < y < b$$

Note that for both modes:

$$N_{nm} = 4 [2\epsilon_{on} \epsilon_{om} Y_{nm} ab (n_a^2 + m_b^2)]^{-1/2} \quad (A.8)$$

$$\beta_{nm} = [k^2 - n_a^2 - m_b^2]^{1/2} \quad (A.9)$$

$$n_a = n\pi/a \quad (A.10)$$

$$m_b = m\pi/b \quad (A.11)$$

$$\epsilon_{on} = \begin{cases} 2 & n=0 \\ 1 & n \neq 0 \end{cases} \quad (A.12)$$

where the normalization factor N_{nm} is defined such that

$$\frac{1}{2} \int_0^a \int_0^b \bar{e}_{nm} \times \bar{h}_{nm}^* \cdot \hat{z} \, dy \, dx = 1, \quad (A.13)$$

where \bar{e}_{nm} and \bar{h}_{nm} are the tangential components of the field as follows,

$$\bar{E}_{\text{modal}} = [e_x \hat{x} + e_y \hat{y} + e_z \hat{z}] e^{\mp j\beta_{nm}z} = [\bar{e}_{nm} \pm e_{z,nm} \hat{z}] e^{\mp j\beta_{nm}z} \quad (A.14)$$

$$\bar{H}_{\text{modal}} = [h_x \hat{x} + h_y \hat{y} + h_z \hat{z}] e^{\mp j\beta_{nm}z} = [\pm \bar{h}_{nm} + h_{z,nm} \hat{z}] e^{\mp j\beta_{nm}z} \quad (A.15)$$

and "*" denotes complex conjugation.

The upper or lower sign represents a mode propagating in $(+\hat{z})$ or $(-\hat{z})$ direction, respectively.

The modal field expressions in the rectangular waveguide can be decomposed into four plane waves. The transverse (to \hat{z}) components of the fields propagating in $+\hat{z}$ direction are written as follows:

$$\begin{aligned} \bar{e}_{nm} e^{-j\beta_{nm}z} = \frac{N_{nm}}{4j} & \left[(-\hat{x}u + \hat{y}v) e^{-jn_a x - jm_b y - j\beta_{nm}z} \right. \\ & + (-\hat{x}u - \hat{y}v) e^{jn_a x - jm_b y - j\beta_{nm}z} + (\hat{x}u - \hat{y}v) e^{jn_a x + jm_b y - j\beta_{nm}z} \\ & \left. + (\hat{x}u + \hat{y}v) e^{-jn_a x + jm_b y - j\beta_{nm}z} \right] \end{aligned} \quad (A.16)$$

$$\begin{aligned} \bar{h}_{nm} e^{-j\beta_{nm}z} = \frac{N_{nm} Y_{nm}}{4j} & \left[(-\hat{x}v - \hat{y}u) e^{-jn_a x - jm_b y - j\beta_{nm}z} \right. \\ & + (\hat{x}v - \hat{y}u) e^{jn_a x - jm_b y - j\beta_{nm}z} + (\hat{x}v + \hat{y}u) e^{jn_a x + jm_b y - j\beta_{nm}z} \\ & \left. + (-\hat{x}v + \hat{y}u) e^{-jn_a x + jm_b y - j\beta_{nm}z} \right] \end{aligned} \quad (A.17)$$

where

$$u = \begin{cases} m_b & \text{for TE modes} \\ n_a & \text{for TM modes} \end{cases} \quad (\text{A.18})$$

and

$$v = \begin{cases} n_a & \text{for TE modes} \\ -m_b & \text{for TM modes} \end{cases} \quad (\text{A.19})$$

The modal sets transverse to \hat{x} -axis can be written as follows:

	<u>TE_{x,nm} Modes</u>	<u>TM_{x,nm} Modes</u>	
e_x	0	$-N_{nm} T_{nm} \frac{(n_a^2 + m_b^2)}{j\beta_{nm}} \frac{k^2 - n_a^2}{j\beta_{nm}} \cos n_a x \sin m_b y$	(A.20a;b)

e_y	$-N_{nm} T_{nm} (n_a^2 + m_b^2) \sin n_a x \cos m_b y$	$N_{nm} T_{nm} \frac{(n_a^2 + m_b^2)}{j\beta_{nm}} \frac{n_a \cdot m_b}{j\beta_{nm}} \sin n_a x \cos m_b y$	(A.21a;b)
-------	--	---	-----------

e_z	$N_{nm} T_{nm} \frac{(n_a^2 + m_b^2)}{j\beta_{nm}} m_b \sin n_a x \sin m_b y$	$-N_{nm} T_{nm} \frac{(n_a^2 + m_b^2)}{j\beta_{nm}} n_a \sin n_a x \sin m_b y$	(A.22a;b)
-------	---	--	-----------

h_x	$N_{nm} T_{nm} \frac{Y_{nm}(n_a^2 + m_b^2)}{k\beta_{nm}^2} (k^2 - n_a^2) \sin n_a x \cos m_b y$	0	(A.23a;b)
-------	---	---	-----------

h_y	$-N_{nm} T_{nm} \frac{Y_{nm}}{\beta_{nm}^2} (n_a^2 + m_b^2) n_a \cdot m_b \cos n_a x \sin m_b y$	$N_{nm} T_{nm} (n_a^2 + m_b^2) Y_{nm} \cos n_a x \sin m_b y$	(A.24a;b)
-------	--	--	-----------

h_z	$N_{nm} T_{nm} \frac{Y_{nm}}{j\beta_{nm}} (n_a^2 + m_b^2) n_a \cos n_a x \cos m_b y$	$N_{nm} T_{nm} \frac{(n_a^2 + m_b^2)}{j\beta_{nm}} Y_{nm} m_b \cos n_a x \cos m_b y$	(A.25a;b)
-------	--	--	-----------

From (A.1) through (A.25), one can easily conclude that

$$TE_{x,nm} = T_{nm} \left(n_a TE_{nm} - m_b \frac{k}{\beta_{nm}} TM_{nm} \right) \quad (A.26)$$

$$TM_{x,nm} = T_{nm} \left(m_b \frac{k}{\beta_{nm}} TE_{nm} + n_a TM_{nm} \right) \quad (A.27)$$

where

$$T_{nm} = \frac{\beta_{nm}}{\sqrt{(n_a^2 + m_b^2) (k^2 - n_a^2)}} \quad (A.28)$$

or, alternatively,

$$TE_{nm} = T_{nm} \left[n_a TE_{x,nm} + m_b \frac{k}{\beta_{nm}} TM_{x,nm} \right] \quad (A.29)$$

$$TM_{nm} = T_{nm} \left[-m_b \frac{k}{\beta_{nm}} TE_{x,nm} + n_a TM_{x,nm} \right] \quad (A.30)$$

APPENDIX B

MODAL FIELD EXPRESSIONS IN A PARALLEL PLATE WAVEGUIDE

The modal field sets in a parallel plate waveguide of width a , shown in Figure B.1, can be obtained from (A.1) through (A.12), by discarding the field variation in \hat{y} -direction. They are expressed as follows:

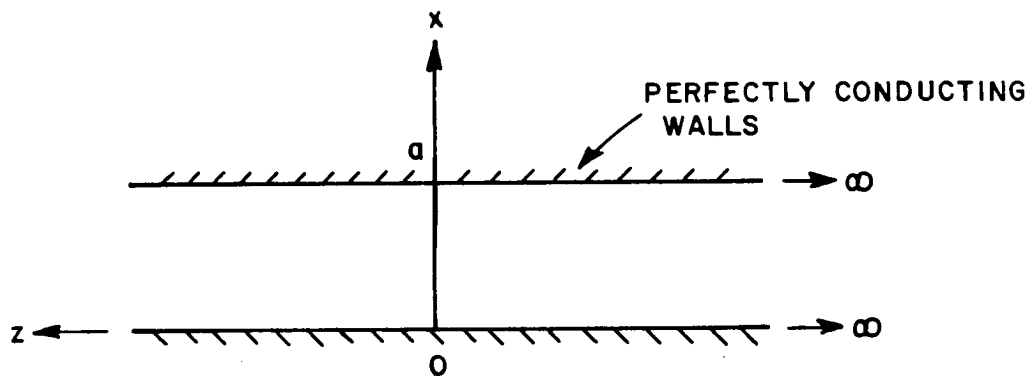


Figure B.1. Parallel-plate waveguide geometry.

$$\begin{array}{ccc} \underline{\text{TE}_n} & & \underline{\text{TM}_n} \\ h_z & N_n \frac{Y_n}{j\beta_n} \cos n_a x & 0 \end{array} \quad (\text{B.1a;b})$$

$$\begin{array}{ccc} e_z & 0 & \frac{-N_n}{j\beta_n} \sin n_a x \end{array} \quad (\text{B.2a;b})$$

$$\begin{array}{ccc} h_x & N_n Y_n \sin n_a x & 0 \end{array} \quad (\text{B.3a;b})$$

$$\begin{array}{ccc} h_y & 0 & N_n Y_n \cos n_a x \end{array} \quad (\text{B.4a;b})$$

$$\begin{array}{ccc} e_x & 0 & N_n \cos n_a x \end{array} \quad (\text{B.5a;b})$$

$$\begin{array}{ccc} e_y & -N_n \sin n_a x & 0 \end{array} \quad (\text{B.6a;b})$$

The normalization factor N_n now becomes

$$N_n = \frac{2}{\sqrt{\epsilon_{0n} \cdot a Y_n}} \quad (\text{B.7})$$

The rest of the parameters are obtained from (A.9) through (A.12), by letting $m=0$.

Each of these modes can be decomposed into two ray optical fields (plane waves) by writing

$$\vec{E} = -\hat{y} \frac{N_n}{2j} \begin{bmatrix} e^{jn_a x - j\beta_n z} & -e^{-jn_a x - j\beta_n z} \\ -e^{jn_a x - j\beta_n z} & e^{-jn_a x - j\beta_n z} \end{bmatrix} \quad (\text{B.8})$$

in the TE_z case, and

$$\bar{H} = \hat{y} \frac{N_n}{2} Y_n \left[e^{jn_a x - j\beta_n z} + e^{-jn_a x - j\beta_n z} \right] \quad (B.9)$$

in the TM_z case.

The propagation directions of these plane waves are called the modal ray directions and the angles between the modal ray directions and waveguide walls are the modal ray angles.

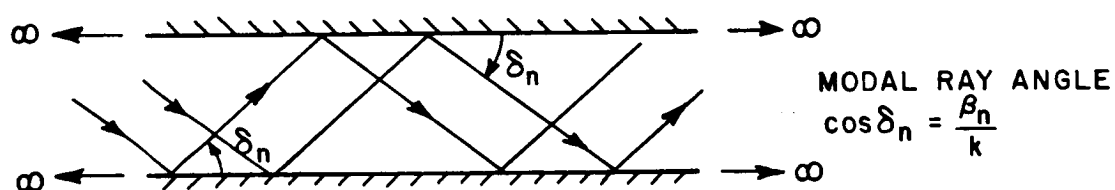


Figure B.2. Ray picture of n^{th} mode.

APPENDIX C
MODAL FIELD EXPRESSIONS IN A SECTORAL WAVEGUIDE

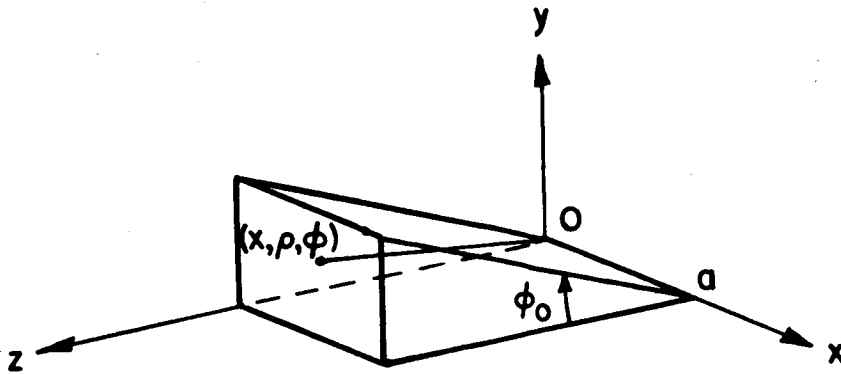


Figure C.1. Geometry of a sectoral waveguide.

In this problem, it is possible to find mode sets transverse to the \hat{x} -axis. The fields can be computed from the scalar function

$$\left[\frac{\partial^2}{\partial y^2} + \frac{\partial^2}{\partial z^2} + \left[k^2 - \left(\frac{n\pi}{a} \right)^2 \right] \right] \psi = 0 \quad (C.1)$$

with the appropriate boundary conditions. ψ is the x-component of the magnetic vector potential \bar{A} in the TM_x case and the x-component of the electric vector potential \bar{F} in the TE_x case [44].

Case 1 TE_x modes: These modes satisfy the relation $E_x=0$ and can be derived from $\vec{F}=\hat{x}\psi$.

The field components are given by;

$$E_\rho = \frac{-1}{\rho} \frac{\partial \psi}{\partial \phi} \quad H_\rho = \frac{1}{jkZ_0} \frac{\partial^2 \psi}{\partial \rho \partial x} \quad (C.2a;b)$$

$$E_\phi = \frac{\partial \psi}{\partial \rho} \quad H_\phi = \frac{1}{jkZ_0} \frac{1}{\rho} \frac{\partial^2 \psi}{\partial \phi \partial x} \quad (C.3a;b)$$

$$E_x = 0 \quad H_x = \frac{1}{jkZ_0} \left(\frac{\partial^2}{\partial x^2} + k^2 \right) \psi \quad (C.4a;b)$$

The appropriate scalar function ψ is given by

$$\psi_{nm} = \sin \left(\frac{n\pi}{a} x \right) \cos \left(\frac{m\pi}{\phi_0} \phi \right) \begin{bmatrix} H_{\frac{m\pi}{\phi_0}}^{(1)}(k_t \rho) \\ H_{\frac{m\pi}{\phi_0}}^{(2)}(k_t \rho) \end{bmatrix} \begin{matrix} \text{Ingoing Wave} \\ \text{Outgoing Wave} \end{matrix} \quad (C.5)$$

where

$$k_t^2 = k^2 - \left(\frac{n\pi}{a} \right)^2 \quad (C.6)$$

The explicit expressions for the outgoing field components are given by;

$$E_\rho = \frac{1}{\rho} \frac{m\pi}{\phi_0} \sin \left(\frac{n\pi}{a} x \right) \sin \left(\frac{m\pi}{\phi_0} \phi \right) \frac{H_{\frac{m\pi}{\phi_0}}^{(2)}(k_t \rho)}{\phi_0} \quad (C.7)$$

$$E_\phi = \sin \left(\frac{n\pi}{a} x \right) \cos \left(\frac{m\pi}{\phi_0} \phi \right) \frac{d}{d\rho} \frac{H_{\frac{m\pi}{\phi_0}}^{(2)}(k_t \rho)}{\phi_0} \quad (C.8)$$

$$E_x = 0 \quad (C.9)$$

$$H_\rho = \frac{1}{jkZ_0} \left(\frac{n\pi}{a}\right) \cos\left(\frac{n\pi}{a}x\right) \cos\left(\frac{m\pi}{\phi_0}\phi\right) \frac{d}{d\rho} \frac{H_{m\pi}^{(2)}(k_t \rho)}{\phi_0} \quad (C.10)$$

$$H_\phi = -\frac{1}{jkZ_0} \frac{1}{\rho} \left(\frac{m\pi}{\phi_0}\right) \left(\frac{n\pi}{a}\right) \cos\left(\frac{n\pi}{a}x\right) \sin\left(\frac{m\pi}{\phi_0}\phi\right) \frac{H_{m\pi}^{(2)}(k_t \rho)}{\phi_0} \quad (C.11)$$

$$H_x = \frac{1}{jkZ_0} k_t^2 \sin\left(\frac{n\pi}{a}x\right) \cos\left(\frac{m\pi}{\phi_0}\phi\right) \frac{H_{m\pi}^{(2)}(k_t \rho)}{\phi_0} \quad (C.12)$$

For small tapering angle ϕ_0 and large ρ , the Debye Asymptotic approximation for the Hankel function [45]

$$H_v^{(1)}(z) \sim \sqrt{\frac{2}{\pi v \sqrt{\left(\frac{z}{v}\right)^2 - 1}}} e^{\pm j \left[v \sqrt{\left(\frac{z}{v}\right)^2 - 1} - v \cos^{-1} \left(\frac{v}{z}\right) - \frac{\pi}{4} \right]} \quad (C.13)$$

can be used. For small $\frac{v}{z}$; $\cos^{-1} \frac{v}{z} \rightarrow \frac{\pi}{2}$, so the above relation becomes

$$H_v^{(1)}(z) \sim \sqrt{\frac{2}{\pi \sqrt{z^2 - v^2}}} (\mp j)^v e^{\pm j \sqrt{z^2 - v^2}} e^{\mp j \frac{\pi}{4}} \quad (C.14)$$

and

$$\frac{d}{dz} H_v^{(1)}(z) \sim \sqrt{\frac{2}{\pi \sqrt{z^2 - v^2}}} (\mp j)^v \left[\mp j \sqrt{1 - \left(\frac{v}{z}\right)^2} e^{\pm j \sqrt{z^2 - v^2}} \right] e^{\mp j \frac{\pi}{4}} \quad (C.15)$$

which goes to the large argument form [44] for $z \gg v$.

If one makes use of (C.14) and (C.15) in the field expressions of (C.7) through (C.12), one obtains the following expressions (up to a common factor) for an outgoing wave:

$$E_{\rho} = \frac{m\pi}{\rho\phi_0} \frac{L_{nm}}{\sqrt{\beta_{nm}\rho}} \sin\left(\frac{n\pi}{a}x\right) \sin\left(\frac{m\pi}{\phi_0}\phi\right) e^{-j\beta_{nm}\rho} \quad (C.16)$$

$$E_{\phi} = \frac{L_{nm}}{\sqrt{\beta_{nm}\rho}} \sin\left(\frac{n\pi}{a}x\right) \cos\left(\frac{m\pi}{\phi_0}\phi\right) (-j\beta_{nm}) e^{-j\beta_{nm}\rho} \quad (C.17)$$

$$E_x = 0 \quad (C.18)$$

$$H_{\rho} = \frac{L_{nm}}{jkZ_0} \left(\frac{n\pi}{a}\right) (-j\beta_{nm}) \frac{1}{\sqrt{\beta_{nm}\rho}} \cos\left(\frac{n\pi}{a}x\right) \cos\left(\frac{m\pi}{\phi_0}\phi\right) e^{-j\beta_{nm}\rho} \quad (C.19)$$

$$H_{\phi} = \frac{L_{nm}}{jkZ_0} \left(\frac{n\pi}{a}\right) \left(\frac{m\pi}{\rho\phi_0}\right) \frac{1}{\sqrt{\beta_{nm}\rho}} \cos\left(\frac{n\pi}{a}x\right) \sin\left(\frac{m\pi}{\phi_0}\phi\right) e^{-j\beta_{nm}\rho} \quad (C.20)$$

$$H_x = \frac{L_{nm}}{jkZ_0} (k^2 - (\frac{n\pi}{a})^2) \frac{1}{\sqrt{\beta_{nm}\rho}} \sin\left(\frac{n\pi}{a}x\right) \cos\left(\frac{m\pi}{\phi_0}\phi\right) e^{-j\beta_{nm}\rho} \quad (C.21)$$

where

$$\beta_{nm}^2 = k^2 - \left(\frac{n\pi}{a}\right)^2 - \left(\frac{m\pi}{\rho\phi_0}\right)^2 \quad (C.22)$$

is the function determining the phase advance in the ρ -direction. Note that β_{nm} is a function of ρ . Also, L_{nm} is the normalization factor given by

$$L_{nm} = \left[\frac{k \cdot 4 \cdot 2}{Y_0 \epsilon_{on} \epsilon_{om} a \phi_0 (k^2 - (\frac{n\pi}{a})^2)} \right]^{1/2} \quad (C.23)$$

in which

$$\epsilon_{on} = \begin{cases} 2; & n = 0 \\ 1; & n \neq 0 \end{cases} \quad (C.24)$$

so that

$$\frac{1}{2} \int_0^a \int_0^{\phi_0} \bar{\mathbf{E}} \times \bar{\mathbf{H}}^* \cdot \rho \, d\phi \, dx \quad . \quad (\text{C.25})$$

By comparing (C.16) through (C.22) with (B.20) through (B.25), one can see that the expressions of slightly tapered waveguide fields may be approximated by TE_x , TM_x -type rectangular waveguide mode sets. To do this, one has to make the following approximations:

$$\rho \rightarrow z \quad (\text{C.26})$$

$$\rho\phi \rightarrow y \quad (\text{C.27})$$

$$\rho\phi_0 \rightarrow b \quad (\text{C.28})$$

together with (C.25) where the ρ -dependence cannot be approximated by (C.28), since it is the function determining the phase advance which is more sensitive to the approximations.

Case 2 TM_x modes: These modes satisfy the relation $H_x=0$ and can be derived from $\bar{\mathbf{A}}=\hat{x}\psi$.

The field components are given by:

$$E_\rho = \frac{1}{jk} \frac{\partial^2 \psi}{\partial \rho \partial x} \quad H_\rho = \frac{1}{\rho} Y_0 \frac{\partial \psi}{\partial \phi} \quad (\text{C.29a;b})$$

$$E_\phi = \frac{1}{jk} \frac{1}{\rho} \frac{\partial^2 \psi}{\partial \phi \partial x} \quad H_\phi = -Y_0 \frac{\partial \psi}{\partial \rho} \quad (\text{C.30a;b})$$

$$E_x = \frac{1}{jk} \left(\frac{\partial^2}{\partial x^2} + k^2 \right) \psi \quad H_x = 0 \quad . \quad (\text{C.31a;b})$$

The appropriate scalar function ψ is given by:

$$\psi = \cos\left(\frac{n\pi}{a}x\right) \sin\left(\frac{m\pi}{\phi_0}\phi\right) \begin{bmatrix} H_{\frac{m\pi}{\phi_0}}^{(1)}(k_t \rho) \\ H_{\frac{m\pi}{\phi_0}}^{(2)}(k_t \rho) \end{bmatrix} \begin{matrix} \text{Ingoing wave} \\ \text{Outgoing wave} \end{matrix} \quad (\text{C.32})$$

The explicit expressions for the outgoing field components are given by:

$$E_{\rho} = \frac{-1}{jk} \left(\frac{n\pi}{a} \right) \sin \left(\frac{n\pi}{a} x \right) \sin \left(\frac{m\pi}{\phi_0} \phi \right) \frac{d}{d\rho} H_{\frac{m\pi}{\phi_0}}^{(2)}(k_t \rho) \quad (C.33)$$

$$E_{\phi} = \frac{-1}{jk} \frac{1}{\rho} \left(\frac{n\pi}{a} \right) \left(\frac{m\pi}{\phi_0} \right) \sin \left(\frac{n\pi}{a} x \right) \cos \left(\frac{m\pi}{\phi_0} \phi \right) H_{\frac{m\pi}{\phi_0}}^{(2)}(k_t \rho) \quad (C.34)$$

$$E_x = \frac{1}{jk} \left(k^2 - \left(\frac{n\pi}{a} \right)^2 \right) \cos \left(\frac{n\pi}{a} x \right) \sin \left(\frac{m\pi}{\phi_0} \phi \right) H_{\frac{m\pi}{\phi_0}}^{(2)}(k_t \rho) \quad (C.35)$$

$$H_{\rho} = \frac{Y_0}{\rho} \left(\frac{m\pi}{\phi_0} \right) \cos \left(\frac{n\pi}{a} x \right) \cos \left(\frac{m\pi}{\phi_0} \phi \right) H_{\frac{m\pi}{\phi_0}}^{(2)}(k_t \rho) \quad (C.36)$$

$$H_{\phi} = -Y_0 \cos \left(\frac{n\pi}{a} x \right) \sin \left(\frac{m\pi}{\phi_0} \phi \right) \frac{d}{d\rho} H_{\frac{m\pi}{\phi_0}}^{(2)}(k_t \rho) \quad (C.37)$$

$$H_x = 0 \quad (C.38)$$

Again using Debye's Asymptotic form for the Hankel function, one obtains the following field expressions:

$$E_{\rho} = -\frac{L_{nm}}{jk} \left(\frac{n\pi}{a} \right) \frac{1}{\sqrt{\beta_{nm}\rho}} \sin \left(\frac{n\pi}{a} x \right) \sin \left(\frac{m\pi}{\phi_0} \phi \right) (-j\beta_{nm}) e^{-j\beta_{nm}\rho} \quad (C.39)$$

$$E_{\phi} = -\frac{L_{nm}}{jk} \left(\frac{n\pi}{a} \right) \left(\frac{m\pi}{\phi_0} \right) \frac{1}{\sqrt{\beta_{nm}\rho}} \sin \left(\frac{n\pi}{a} x \right) \cos \left(\frac{m\pi}{\phi_0} \phi \right) e^{-j\beta_{nm}\rho} \quad (C.40)$$

$$E_x = \frac{L_{nm}}{jk} \left(k^2 - \left(\frac{n\pi}{a} \right)^2 \right) \frac{1}{\sqrt{\beta_{nm}\rho}} \cos \left(\frac{n\pi}{a} x \right) \sin \left(\frac{m\pi}{\phi_0} \phi \right) e^{-j\beta_{nm}\rho} \quad (C.41)$$

$$H_{\rho} = \left(\frac{m\pi}{\rho\phi_0} \right) \frac{Y_0 L_{nm}}{\sqrt{\beta_{nm}\rho}} \cos \left(\frac{n\pi}{a} x \right) \cos \left(\frac{m\pi}{\phi_0} \phi \right) e^{-j\beta_{nm}\rho} \quad (C.42)$$

$$H_{\phi} = -\frac{Y_0 L_{nm}}{\sqrt{\beta_{nm}\rho}} \cos \left(\frac{n\pi}{a} x \right) \sin \left(\frac{m\pi}{\phi_0} \phi \right) (-j\beta_{nm}) e^{-j\beta_{nm}\rho} \quad (C.43)$$

These modal expressions under the approximations defined by (C.26) through (C.28) become equivalent to the TM_x modes in a rectangular waveguide.

The ray picture of the modes can be obtained using a similar procedure performed for a rectangular waveguide. Each outgoing (or ingoing) mode corresponds to four rays which follow zig-zag paths inside the waveguide.

In the TE_x case, the ray optical fields are obtained from

$$E_{\rho} \hat{\rho} + E_{\phi} \hat{\phi} = \frac{L_{nm}}{4\sqrt{\beta_{nm}\rho}} \left[\begin{aligned} &+e^{j\left(\frac{n\pi}{a}x\right) + j\left(\frac{m\pi}{\phi_0}\phi\right) - j\beta_{nm}\rho} \left[\frac{m\pi}{-\rho\phi_0} - \beta_{nm} \right] \\ &+e^{j\left(\frac{n\pi}{a}x\right) - j\left(\frac{m\pi}{\phi_0}\phi\right) - j\beta_{nm}\rho} \left[\frac{m\pi}{\rho\phi_0} - \beta_{nm} \right] \\ &+e^{-j\left(\frac{n\pi}{a}x\right) + j\left(\frac{m\pi}{\phi_0}\phi\right) - j\beta_{nm}\rho} \left[\frac{m\pi}{\rho\phi_0} + \beta_{nm} \right] \\ &+e^{-j\left(\frac{n\pi}{a}x\right) - j\left(\frac{m\pi}{\phi_0}\phi\right) - j\beta_{nm}\rho} \left[-\frac{m\pi}{\rho\phi_0} + \beta_{nm} \right] \end{aligned} \right] . \quad (C.44)$$

In the TM_x case, the ray optical fields are obtained from

$$H_{\rho} \hat{\rho} + H_{\phi} \hat{\phi} = \frac{L_{nm}Y_0}{4\sqrt{\beta_{nm}\rho}} \left[\begin{aligned} &e^{j\left(\frac{n\pi}{a}x\right) + j\left(\frac{m\pi}{\phi_0}\phi\right) - j\beta_{nm}\rho} \left[\frac{m\pi}{\rho\phi_0} + \beta_{nm} \right] \\ &+e^{j\left(\frac{n\pi}{a}x\right) - j\left(\frac{m\pi}{\phi_0}\phi\right) - j\beta_{nm}\rho} \left[\frac{m\pi}{\rho\phi_0} - \beta_{nm} \right] \\ &+e^{-j\left(\frac{n\pi}{a}x\right) + j\left(\frac{m\pi}{\phi_0}\phi\right) - j\beta_{nm}\rho} \left[\frac{m\pi}{\rho\phi_0} + \beta_{nm} \right] \\ &+e^{-j\left(\frac{n\pi}{a}x\right) - j\left(\frac{m\pi}{\phi_0}\phi\right) - j\beta_{nm}\rho} \left[\frac{m\pi}{\rho\phi_0} - \beta_{nm} \right] \end{aligned} \right] . \quad (C.45)$$

If one looks at the projection of outgoing rays corresponding to n^{th} mode in the y - z plane, one obtains rays following zig zag paths along the guide bouncing from the tapered walls (via the approximation in (C.13)). The ray trajectories are tangent to the circular modal ray caustic whose radius is determined by the mode index as shown in Figure C.2. It is also noted that inside the circular modal ray caustic, the mode is cut-off and the ray representation is not valid.

The projection of the ray picture onto the x - z plane is shown in Figure C.3, where the rays are bouncing from the parallel walls.

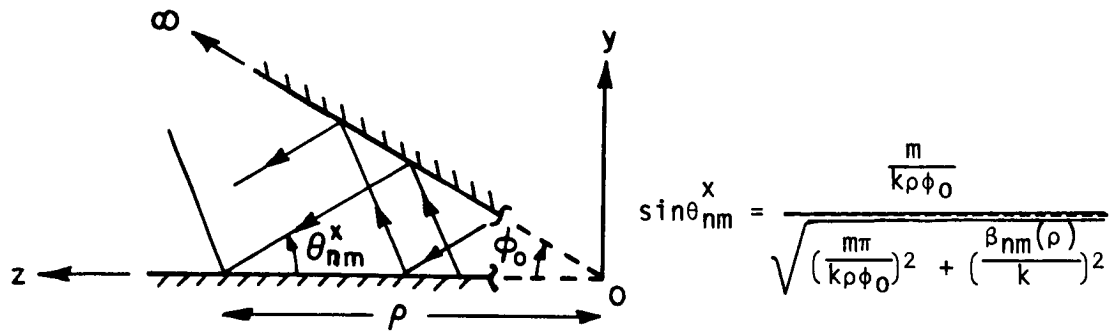


Figure C.2. Projection of ray picture into y - z plane.

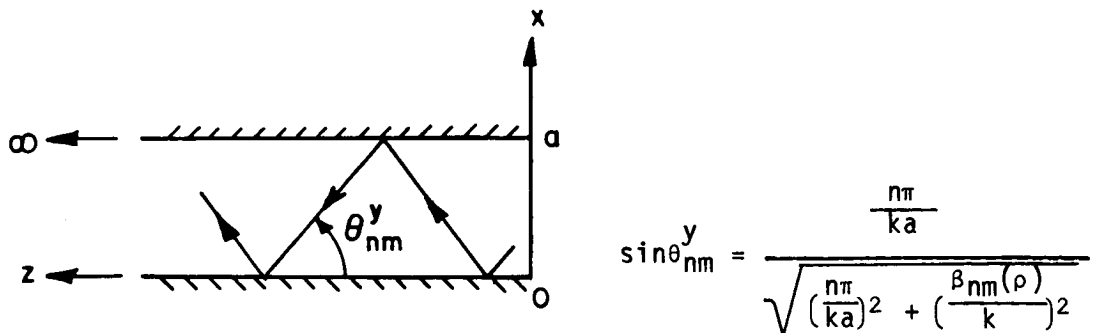


Figure C.3. Projection of ray picture into x - z plane.

APPENDIX D

MODAL FIELD EXPRESSIONS IN A 2-D LINEARLY TAPERED WAVEGUIDE

The geometry pertaining to the linearly tapered waveguide is shown in Figure D.1. The expressions for the modal fields can be deduced from the sectoral waveguide by taking the width "a" to infinity; they are given as follows:

	<u>TE_x</u>	<u>TM_x</u>	
E_ρ	$\frac{L_m}{\sqrt{\beta_{mp}}} \frac{j}{k\rho} \frac{m\pi}{\phi_0} \sin\left(\frac{m\pi}{\phi_0}\phi\right) e^{-j\beta_{mp}\rho}$	0	(D.1a;b)
E_ϕ	$\frac{L_m}{\sqrt{\beta_{mp}}} \frac{\beta_m}{k} \cos\left(\frac{m\pi}{\phi_0}\phi\right) e^{-j\beta_{mp}\rho}$	0	(D.2a;b)
E_x	0	$\frac{L_m}{\sqrt{\beta_{mp}}} \sin\frac{m\pi}{\phi_0}\phi e^{-j\beta_{mp}\rho}$	(D.3a;b)
H_ρ	0	$\frac{m\pi}{\rho\phi_0} \frac{L_m}{\sqrt{\beta_{mp}}} \frac{jY_0}{k} \cos\frac{m\pi}{\phi_0}\phi e^{-j\beta_{mp}\rho}$	(D.4a;b)
H_ϕ	0	$\frac{L_m}{-\sqrt{\beta_{mp}}} \sin\left(\frac{m\pi}{\phi_0}\phi\right)$	(D.5a;b)
H_x	$\frac{L_m Y_0}{\sqrt{\beta_{mp}}} \cos\left(\frac{m\pi}{\phi_0}\phi\right) e^{-j\beta_{mp}\rho}$	0	(D.6a;b)

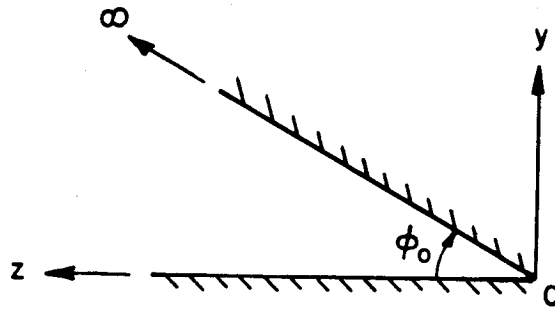


Figure D.1. Geometry of a linearly tapered waveguide.

where

$$L_m = 2 \sqrt{\frac{k}{\epsilon_{om} Y_0 \phi_0}} \quad (D.7)$$

is the normalization constant with

$$\epsilon_{om} = \begin{cases} 2; & n=0 \\ 1; & n \neq 0 \end{cases} \quad (D.8)$$

and

$$\beta_m = \sqrt{k^2 - \left(\frac{m\pi}{\rho\phi_0}\right)^2} \quad (D.9)$$

The next step is to write the modal field in ray-optical form. In the TE_x case one can write (D.6a) as follows:

$$H_x = \frac{Y_0 L_m}{2\sqrt{\beta_m \rho}} \left[e^{j \left[\frac{m\pi}{\phi_0} \phi - \beta_m \rho \right]} + e^{-j \left[\frac{m\pi}{\phi_0} \phi - \beta_m \rho \right]} \right] \quad (D.10)$$

Equation (D.10) shows that a modal field is composed of two ray optical fields. The ray picture of the modal fields is illustrated below [18].

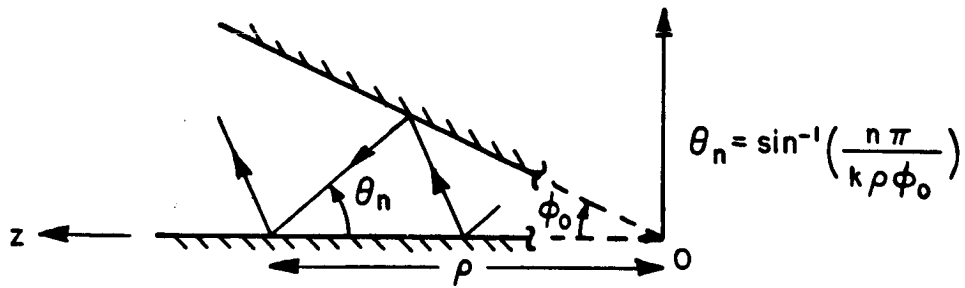


Figure D.2. Ray picture of n^{th} mode.

The ray field is obtained in the TM_y case by writing (D.3b) as follows:

$$E_x = \frac{Y_o L_m}{2j\sqrt{\beta_{mp}}} \left[e^{j \left(\frac{m\pi}{\phi_o} \phi - \beta_{mp} \rho \right)} - e^{-j \left(\frac{m\pi}{\phi_o} \phi + \beta_{mp} \rho \right)} \right] . \quad (D.11)$$

APPENDIX E
CIRCUMFERENTIALLY PROPAGATING MODES IN AN ANNULAR REGION

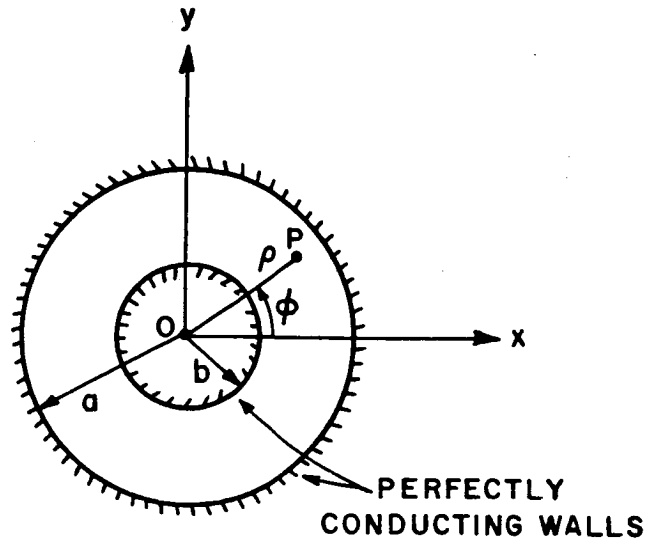


Figure E.1. Geometry of the annular region.

In this appendix, circumferentially propagating modes in an annular region will be obtained using Green's function techniques.

The direct determination of the Green's function for circumferentially propagating waves can be done in a way similar to that presented by Wasylkiwskyj [46] for the interior problem of a single circular shell. The Green's function is the solution of

$$\left(\frac{1}{\rho} \frac{\partial}{\partial \rho} \rho \frac{\partial}{\partial \rho} + \frac{1}{\rho^2} \frac{\partial^2}{\partial \phi^2} + k^2 \right) G(\bar{\rho}, \bar{\rho}') = -\frac{\delta(\rho - \rho') \delta(\phi - \phi')}{\rho'} \quad (\text{E.1})$$

with the boundary conditions

$$G = 0 \quad \text{at} \quad \rho = a, b \quad . \quad (E.2)$$

for the TM_z case. The TE_z case analysis can be performed similarly. In addition to (E.2), the radiation condition at $\phi \rightarrow \pm\infty$ has to be satisfied. The solution of (E.1) can be written as

$$G(\bar{\rho}, \bar{\rho}') = \sum_n g_\phi(\phi, \phi'; \nu_n) \psi_n(\rho) \psi_n(\rho') \quad (E.3)$$

where $g_\phi(\phi, \phi'; \nu_n)$ satisfies the differential equation:

$$\left[\frac{d^2}{d\phi^2} + \nu^2 \right] g_\phi = -\delta(\phi - \phi') \quad (E.4)$$

with

$$g_\phi \rightarrow e^{-j\nu|\phi - \phi'|} \quad \text{as} \quad \phi \rightarrow \pm\infty \quad (E.5)$$

and $\psi_n(\rho)$ are the normalized eigenfunctions in the radial direction which satisfy

$$\left[\rho \frac{d}{d\rho} \left(\rho \frac{d}{d\rho} \right) + k^2 \rho^2 \right] \psi(\rho) = \nu^2 \psi(\rho) \quad (E.6)$$

with

$$\psi = 0 \quad \text{at} \quad \rho = a, b \quad . \quad (E.7)$$

The solution of (E.4) and (E.5) is given by [46]

$$g_\phi(\phi, \phi'; \nu) = \frac{e^{-j\nu|\phi - \phi'|}}{2j\nu} \quad (E.8)$$

and $\psi_n(\rho)$ can be found from the radial Green's function $g_\rho(\rho, \rho'; \nu^2)$

$$\left[\frac{1}{\rho} \frac{d}{d\rho} \left(\rho \frac{d}{d\rho} \right) + k^2 \right] - \frac{\mu}{\rho^2} g_\rho = \frac{-\delta(\rho - \rho')}{\rho} \quad , \quad (E.9)$$

with

$$g_\rho = 0 \quad \text{at} \quad \rho = a, b \quad \text{and} \quad \mu = \nu^2 \quad . \quad (E.10)$$

$\psi_n(\rho)$ are obtained from g_ρ via the completeness relationship

$$\rho' \delta(\rho - \rho') = \sum_n \psi_n(\rho) \psi_n(\rho') = \frac{1}{2\pi j} \int_C g_\rho(\rho, \rho'; \mu) d\mu \quad , \quad (E.11)$$

where C is the contour encircling the singularities of g_ρ .

The solution to (E.9) and (E.10) is given by:

$$g_\rho(\rho, \rho'; \nu^2) = +j \frac{\pi}{4} \frac{[H_\nu^{(1)}(k\rho_<)H_\nu^{(2)}(kb) - H_\nu^{(1)}(kb)H_\nu^{(2)}(k\rho_<)] [H_\nu^{(1)}(k\rho_>)H_\nu^{(2)}(ka) - H_\nu^{(1)}(ka)H_\nu^{(2)}(k\rho_>)]}{[H_\nu^{(1)}(ka)H_\nu^{(2)}(kb) - H_\nu^{(1)}(kb)H_\nu^{(2)}(ka)]} \quad (E.12)$$

The expression in (E12) can be written in a more suitable form by letting

$$[H_\nu^{(1)}(k\rho_>)H_\nu^{(2)}(kb) - H_\nu^{(1)}(kb)H_\nu^{(2)}(k\rho_>)] \equiv f(\rho_>) \quad (E.13)$$

so that

$$g_\rho(\rho, \rho'; \nu^2) = \frac{j\pi}{4} \frac{H_\nu^{(2)}(ka)}{H_\nu^{(2)}(kb)} \frac{f(\rho_<)f(\rho_>)}{f(a)} \quad . \quad (E.14)$$

Using this expression in (E11),

$$\sum_n \psi_n(\rho) \psi_n(\rho') = + \sum_n \frac{\pi j}{2} v_n \frac{H_{v_n}^{(2)}(ka)}{H_{v_n}^{(2)}(kb)} \frac{f(\rho)f(\rho')}{\left. \frac{\partial f(a)}{\partial v} \right|_{v=v_n}} \quad (E.15)$$

Note that $d\mu=2v dv$ is used in obtaining the residue sum in (E.15), where residues are evaluated at the isolated, simple poles [47] given by

$$f(a) = 0 \quad (E.16)$$

The Green's function of (E.3) then is written as

$$G(\bar{\rho}, \bar{\rho}') = \sum_n \frac{\pi}{4} e^{-j v_n |\phi - \phi'|} \frac{H_{v_n}^{(2)}(ka)}{H_{v_n}^{(2)}(kb)} \frac{f(\rho)f(\rho')}{\left. \frac{\partial f(a)}{\partial v} \right|_{v=v_n}} \quad (E.17)$$

This result can also be obtained using an application of Watson's transformation [48,49] on 2π -periodic eigenfunctions. This will also be illustrated for the sake of completeness.

The Green's function of (E.3), can be written as follows:

$$G(\bar{\rho}, \bar{\rho}') = \sum_m \phi_m(\phi) \phi_m(\phi') g_\rho(\rho, \rho'; \lambda_m) \quad (E.18)$$

where eigenfunctions in the ϕ direction satisfy the boundary condition of being periodic in $0 < \phi < 2\pi$. These eigenfunctions are given by

$$\phi_m(\phi) \phi_m(\phi') = \frac{\epsilon_m}{2\pi} \cos m(\phi - \phi') \quad (E.19)$$

where

$$\epsilon_m = \begin{cases} 1; & m = 0 \\ 2; & m \neq 0 \end{cases} \quad (E.20)$$

g_ρ is given by Equation (E.12).

Substituting (E.14) and (E.19) in (E.18)

$$G(\bar{\rho}, \bar{\rho}') = \frac{1}{8j} \sum_{m=-\infty}^{\infty} e^{-jm(\phi-\phi')} \frac{H_m^{(2)}(ka)}{H_m^{(2)}(kb)} \left. \frac{f(\rho)f(\rho')}{f(a)} \right|_{\nu=m} \quad (E.21)$$

This summation can be written as the following integral

$$G(\bar{\rho}, \bar{\rho}') = \frac{1}{2j} \int_{C=C_++C_-} I(\nu) e^{j\nu(\phi-\phi')} \frac{e^{j\nu\pi}}{\sin \nu\pi} d\nu \quad (E.22)$$

where C encloses zeros of $\sin \nu\pi$ in the counterclockwise direction. In (E.22) $I(\nu)$ is given by:

$$I(\nu) = -\frac{1}{8j} \frac{H_\nu^{(2)}(ka)}{H_\nu^{(2)}(kb)} \frac{f(\rho)f(\rho')}{f(a)} \quad (E.23)$$

and has no singularities in C , as shown in Figure E.2.

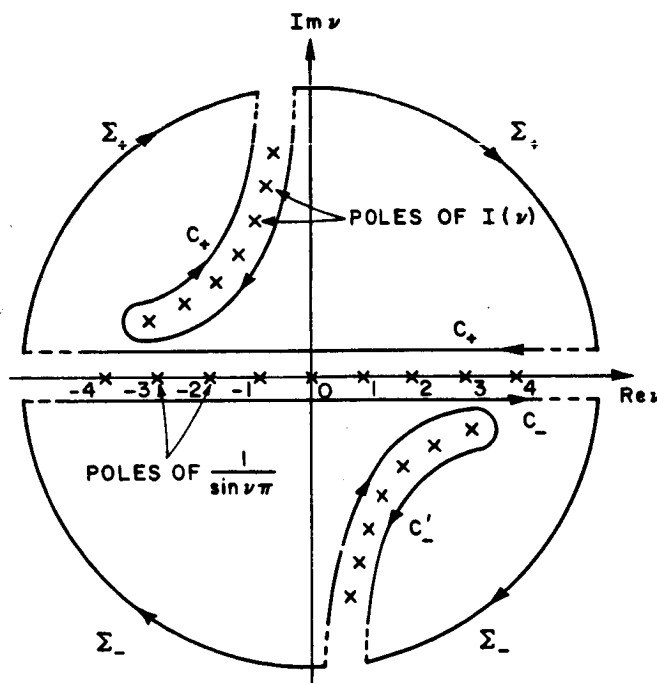


Figure E.2. Contours used in the Watson transformation.

In the figure, the singularities of $I(v)$ are assumed to be encircled by the contour C' ($C'=C'_++C'_-$) in the complex v -plane. Deforming the original contour C into C' and evaluating the integral as a residue sum, one obtains

$$\begin{aligned}
 G(\bar{\rho}, \bar{\rho}') = & \frac{\pi}{8j} \sum_{n=1}^{\infty} e^{-jv_n(\phi-\phi')} \frac{e^{jv_n\pi}}{\sin v_n\pi} \frac{H_{v_n}^{(2)}(ka)}{H_{v_n}^{(2)}(kb)} \frac{f(\rho)f(\rho')}{\left. \frac{\partial f(a)}{\partial v} \right|_{v=v_n}} \\
 & + \frac{\pi}{8j} \sum_{n=1}^{\infty} e^{-jv_n(\phi-\phi')} \frac{e^{jv_{-n}\pi}}{\sin v_{-n}\pi} \frac{H_{v_{-n}}^{(2)}(ka)}{H_{v_{-n}}^{(2)}(kb)} \frac{f(\rho)f(\rho')}{\left. \frac{\partial f(a)}{\partial v} \right|_{v=v_{-n}}} .
 \end{aligned} \quad (E.24)$$

The first sum corresponds to upper half plane poles which represent modes propagating in $+\hat{\phi}$ direction and the second summation is obtained from the residues of the poles in the lower half plane representing modes propagating in $-\hat{\phi}$ direction. By utilizing the symmetry properties of Hankel functions both kinds of modes can be included in one summation as follows:

$$G(\bar{\rho}, \bar{\rho}') = \frac{\pi}{8j} \sum_{n=1}^{\infty} e^{-jv_n|\phi-\phi'|} \frac{e^{jv_n\pi}}{\sin v_n\pi} \frac{f(\rho)f(\rho')}{\left. \frac{\partial f(a)}{\partial v} \right|_{v=v_n}} . \quad (E.25)$$

Also using

$$\frac{e^{jv_n\pi}}{\sin v_n\pi} = 2j \sum_{p=0}^{\infty} e^{-2jv_n\pi p} \quad (E.26)$$

one notices that each term in (E.25) corresponds to an infinite number of waves reaching the observation point after p complete encirclements. Therefore, this representation of Green's function contains multiply encircling waves, which are included in the 2π -periodic eigenfunctions.

The first encirclement ($p=0$) gives the following expression for the Green's functions;

$$G(\bar{\rho}, \bar{\rho}') = \frac{\pi}{4} \sum_{n=1}^{\infty} e^{-j\nu_n |\phi - \phi'|} \frac{H_{\nu_n}^{(2)}(ka)}{H_{\nu_n}^{(2)}(kb)} \frac{f(\rho)f(\rho')}{\left. \frac{\partial f(a)}{\partial \nu} \right|_{\nu=\nu_n}} \quad (\text{E.27})$$

which agrees with (E.17) above.

In deforming the contour C into C' , one has to show that the integrand of (E.22) is exponentially small on the semicircular contours Σ_{\pm} shown in Figure E.2 at infinity. This can be done using the Debye Approximations to Hankel functions [45,49] and the fact that

$$\lim_{R \rightarrow \infty} \left| \frac{e^{j\nu |\pi - \phi|}}{\sin \nu \phi} \right| \approx M e^{-R(\pi |\sin \theta| + (\pi - \theta) \sin \theta)} \quad (\text{E.28})$$

where M is bounded and $\nu = Re^{i\theta}$.

As is observed in (E.17) and (E.27), the eigenvalues of circumferentially propagating modes are determined through the zeros of $f(a)$, which is given by

$$f(a) = H_{\nu_n}^{(1)}(ka) H_{\nu_n}^{(2)}(kb) - H_{\nu_n}^{(1)}(kb) H_{\nu_n}^{(2)}(ka) \quad (\text{E.29})$$

Using asymptotic approximations to Hankel functions, the zeros of $f(a)$ can be located in the complex ν -plane. As shown in Figure E.3, the zeros are symmetrically located on the real and imaginary axes for real values of the wavenumber k . The purely imaginary eigenvalues correspond to evanescent modes which decay with the distance in the circumferential direction. The real eigenvalues correspond to propagating modes, which travel inside the annular region. The magnitudes of these real eigenvalues are less than the electrical radius of the outer shell (ka).

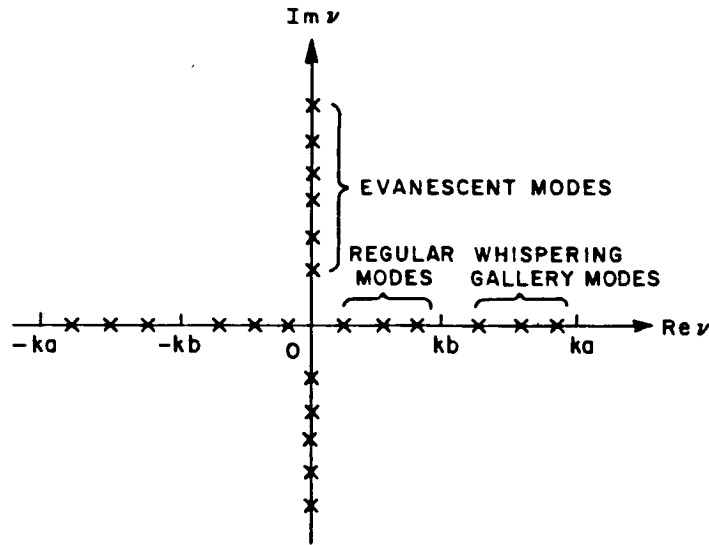


Figure E.3. Location of eigenvalues in the complex v -plane.

From (E.17) and (E.27), the expressions for the eigenfunctions corresponding to the eigenvalues v_n are given by;

$$Q_n = A_n^e (ka, kb) e^{-jv_n |\phi|} f(\rho) \quad (\text{E.30})$$

Where A_n^e is a normalization factor determined by the inner and outer radii. To get the ray picture of propagating modes, one needs to look at the eigenfunctions corresponding to real eigenvalues. If $|v_n| < kb < ka$, then the Hankel functions in $f(\rho)$ of (E.30) can be approximated by their Debye Asymptotic forms given in (C.13). This approximation gives incoming and outgoing rays, bouncing from the inner and outer shells and

staying tangent to a circle with electrical radius v_n as shown in Figure E.4. The modal ray angles δ_n^C are given by the following expressing:

$$\delta_n^C = \frac{\pi}{2} - \sin^{-1} \frac{v_n}{k \left(\frac{a}{b} \right)} \rightarrow \begin{cases} \text{upper shell} \\ \text{lower shell} \end{cases} \quad (\text{E.31})$$

This ray picture is similar to the ray picture in a parallel plate waveguide in the sense that the rays bounce from both walls. Therefore, these modes will be referred to as regular modes (RM).

For $kb < |v_n|ka$, one can use the following spatial filtering property of Bessel functions;

$$J_v(x) \approx 0 \quad \text{for } |v| > x \quad (\text{E.32})$$

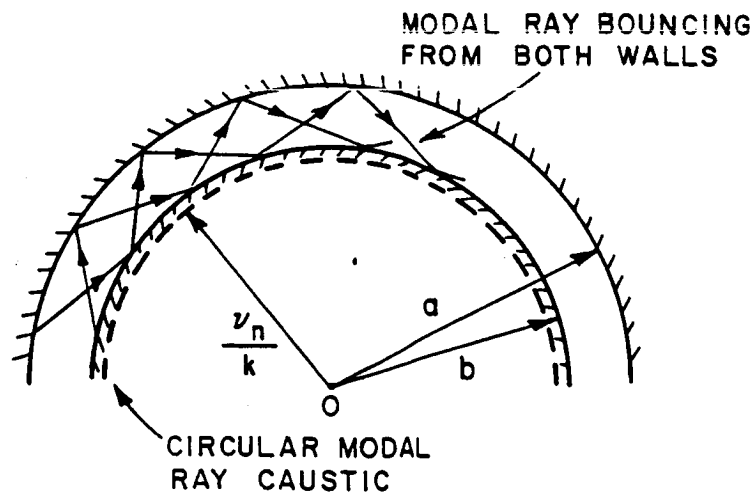


Figure E.4. Ray picture of regular modes.

in the expression for eigenfunctions. Then (E.30) can be written as;

$$Q_n \cong A_n(ka, kb) e^{-j\nu_n|\phi|} (-j2)N_{\nu_n}(kb)J_{\nu_n}(k\rho) \quad (E.33)$$

where $N_{\nu_n}(x)$ is the Neumann function of order ν_n . By use of (E.32), the mode expression in (E.33) reveals that most of the energy in this case is attached to a region close to the outer shell. The ray picture of these modes is shown in Figures E.5 and the caustic circle is in the annular region, resulting in the ray bounce occurring only on the outer shell. This ray interpretation is also discussed in [50] and similar to the ray interpretation of whispering gallery modes inside a circular cylindrical region [46,51]. Therefore, these modes will be referred as whispering gallery (WG) modes. The modal ray angles of these WG modes are given as follows:

$$\delta_n^w = \frac{\pi}{2} - \sin^{-1} \left(\frac{\nu_n}{ka} \right) \quad (E.34)$$

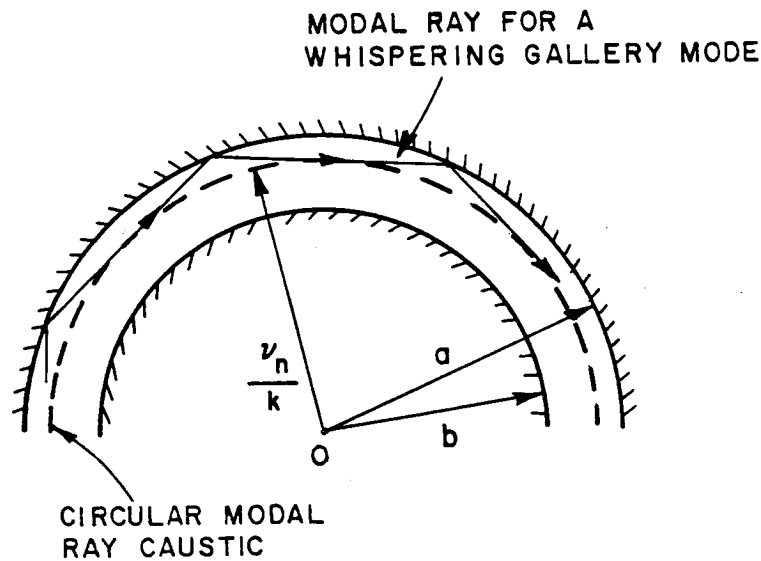


Figure E.5. Ray picture of whispering gallery modes.

APPENDIX F

MODAL FIELD EXPRESSIONS IN A CIRCULAR WAVEGUIDE

The circular waveguide has a radius a , as shown in Figure F.1. The field sets can be written as TE_z and TM_z types. The propagation constants of the TE_z and TM_z modes are given by

$$\beta'_{nm} = \sqrt{k^2 - \left(\frac{p'_{nm}}{a}\right)^2} \quad (F.1)$$

and

$$\beta_{nm} = \sqrt{k^2 - \left(\frac{p_{nm}}{a}\right)^2} \quad (F.2)$$

where p_{nm} is the m^{th} root of the n^{th} order Bessel function, namely

$$J_n(p_{nm}) = 0 \quad (F.3)$$

and p'_{nm} is the m^{th} root of the derivative of the Bessel function of order n ; as follows:

$$J'_n(p'_{nm}) = 0 \quad (F.4)$$

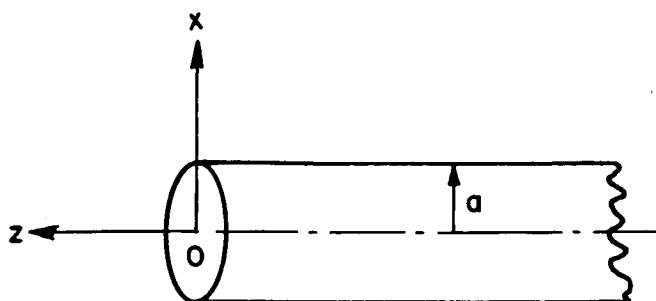


Figure F.1. The circular waveguide geometry.

The field expressions are given as follows apart from the phase factor along the \hat{z} direction:

TE modes

TM modes

$$h_z = jN_{nm}' \left(\frac{p_{nm}}{a} \right)^2 J_n' \left(\frac{p_{nm}\rho}{a} \right) \begin{cases} \cos n\phi \\ \sin n\phi \end{cases} \quad 0 \quad (F.5a;b)$$

$$e_z = 0 \quad jN_{nm} \left(\frac{p_{nm}}{a} \right)^2 J_n \left(\frac{p_{nm}\rho}{a} \right) \begin{cases} \cos n\phi \\ \sin n\phi \end{cases} \quad (F.6a;b)$$

$$h_\rho = N_{nm}' \frac{\beta_{nm} p_{nm}}{a} J_n' \left(\frac{p_{nm}\rho}{a} \right) \begin{cases} \cos n\phi \\ \sin n\phi \end{cases} \quad - \frac{e_\phi}{Z_{e,nm}} \quad (F.7a;b)$$

$$h_\phi = N_{nm}' \frac{n\beta_{nm}}{\rho} J_n \left(\frac{p_{nm}\rho}{a} \right) \begin{cases} -\sin n\phi \\ \cos n\phi \end{cases} \quad \frac{e_\rho}{Z_{e,nm}} \quad (F.8a;b)$$

$$e_\rho = Z_{h,nm} h_\phi \quad N_{nm} \frac{\beta_{nm} p_{nm}}{a} J_n' \left(\frac{p_{nm}\rho}{a} \right) \begin{cases} \cos n\phi \\ \sin n\phi \end{cases} \quad (F.9a;b)$$

$$e_\phi = -Z_{h,nm} h_\rho \quad N_{nm} \frac{n\beta_{nm}}{\rho} J_n \left(\frac{p_{nm}\rho}{a} \right) \begin{cases} -\sin n\phi \\ \cos n\phi \end{cases} \quad (F.10a;b)$$

$$Z_{h,nm} = \frac{k}{\beta_{nm}} Z_0 \quad (F.11a;b)$$

$$Z_{e,nm} = \frac{\beta_{nm}}{k} Z_0 \quad (F.12a;b)$$

$$N_{nm}' = \frac{2}{J_n(p_{nm}') \sqrt{\pi\omega\mu\beta_{nm}'\epsilon_{on}(p_{nm}'^2 - n^2)}} \quad (F.13)$$

$$N_{nm} = \frac{2}{p_{nm} J_n'(p_{nm}) \sqrt{\pi\omega\epsilon\beta_{nm}\epsilon_{on}}} \quad (F.14)$$

The normalization factors N_{nm} and N'_{nm} yield unit power in each mode. Here, $\epsilon_{0n} = 2$ for $n = 0$, and 1 for $n > 0$.

To obtain a ray picture for the typical modal field whose ρ and z variation is given by

$$J_n(\xi_{nm}\rho) e^{-j\gamma_{nm}|z|} \quad (F.15)$$

where

$$a \cdot \xi_{nm} = \begin{cases} p_{nm} & \text{for TE}_z \text{ modes} \\ p_{nm} & \text{for TM}_z \text{ modes} \end{cases} \quad (F.16)$$

and

$$\gamma_{nm} = \begin{cases} \beta_{nm} & \text{for TM}_z \text{ modes} \\ \beta_{nm} & \text{for TM}_z \text{ modes} \end{cases} \quad (F.17)$$

one may decompose $J_n(x)$ as

$$J_n(x) = \frac{H_n^{(2)}(x) + H_n^{(1)}(x)}{2} \quad (F.18)$$

Thus, the expression in (F.15) becomes

$$\frac{1}{2} H_n^{(2)}(\xi_{nm}\rho) e^{-j\gamma_{nm}|z|} + \frac{1}{2} H_n^{(1)}(\xi_{nm}\rho) e^{-j\gamma_{nm}|z|} \quad (F.19)$$

From the large argument asymptotic form of the Hankel functions, it can be determined that the first term represents conical rays propagating away from the axis of the waveguide and the second term represents

conical rays propagating toward the axis of the cylinder. The described ray picture has caustic along the guide center, therefore it is valid away from it. The modal ray picture is sketched in Figure F.2 below.

The modal ray angles δ'_{nm} and δ_{nm} are as follows:

$$\delta'_{nm} = \sin^{-1} \left(\frac{p'_{nm}}{a} \right) \quad (F.19)$$

and

$$\delta_{nm} = \sin^{-1} \left(\frac{p_{nm}}{a} \right) \quad (F.20)$$

It is also noted that the modal field is not completely transverse to the conical ray propagation direction, since the radial component of the field has contribution along the conical ray propagation direction. However, for the modes sufficiently away from cut-off this contribution is small and can be neglected to obtain a ray optical representation.

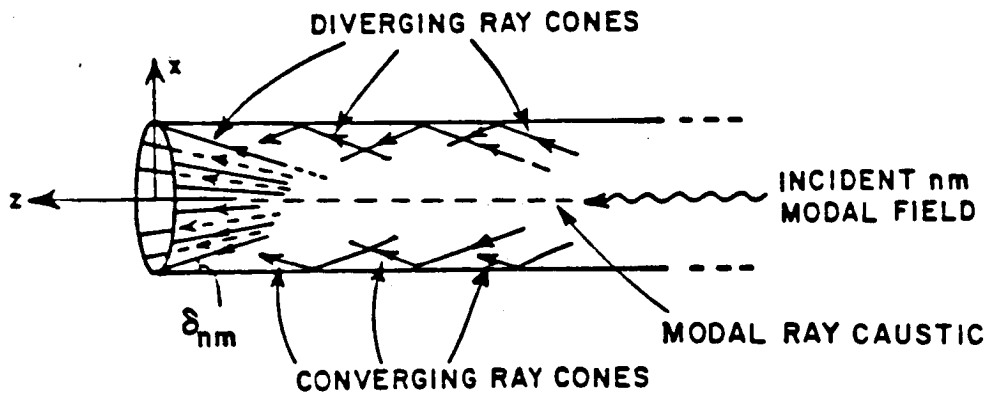


Figure F.2. Conversion of waveguide modal field into the conical ray field.

APPENDIX G
WAVEGUIDE EXCITATION PROBLEM

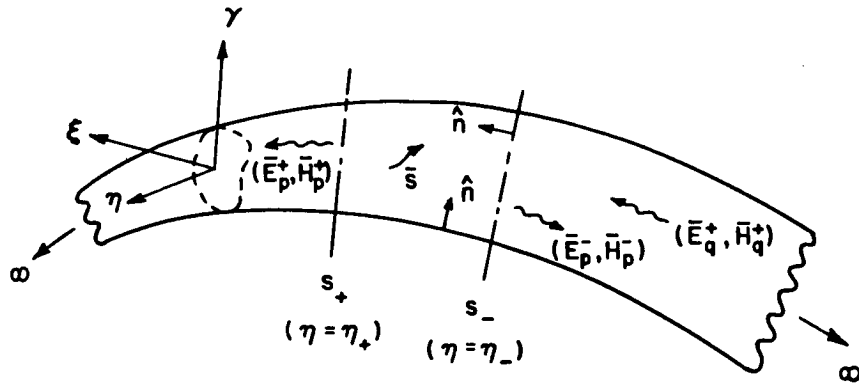


Figure G.1. Waveguide Geometry

Let a source \bar{S} be located inside a waveguide as shown in Figure G.1. \bar{S} can be an electric current source \bar{J} or a magnetic current source \bar{M} , which generates \bar{E}^\pm, \bar{H}^\pm . Thus,

$$\bar{E}^\pm, \bar{H}^\pm = \sum_p A_p^\pm (\bar{E}_p^\pm, \bar{H}_p^\pm) \quad (G.1)$$

are the fields generated by \bar{S} in the $\pm \hat{n}$ directions. In this summation p is the compact summation index representing the double summation over mode indices "n" and "m". It is of interest to find $(\bar{E}^\pm, \bar{H}^\pm)$. Here, \bar{E}^\pm will be determined via an application of the reciprocity theorem as in [1].

The modal fields can be decomposed into transverse and axial components as follows:

$$\bar{H}_p^\pm = (\pm \bar{H}_{pt} + \bar{H}_{pn}) e^{\mp j\beta_p n} \quad (G.2a)$$

$$\bar{E}_p^\pm = (\bar{E}_{pt} \pm \bar{E}_{pn}) e^{\mp j\beta_p n} \quad (G.2b)$$

Case (i): It is of interest to find the strength of the mode \bar{E}_q^- , \bar{H}_q^- generated by \bar{S} . (Here q is the compact index representing the mode indices "ij").

From the reciprocity theorem:

$$\iint_{S_+ + S_- + S_w} [\bar{E}x\bar{H}_q^+ - \bar{E}_q^+x\bar{H}] \cdot \hat{n} \, ds = \begin{cases} \iiint_V \bar{E}_q^+ \cdot \bar{J} \, dv & \text{for } \bar{S}=\bar{J} \\ -\iiint_V \bar{H}_q^+ \cdot \bar{M} \, dv & \text{for } \bar{S}=\bar{M} \end{cases} \quad (G.3)$$

where $\bar{E}, \bar{H} = \bar{E}^+, \bar{H}^+$ on S_+ and $\bar{E}, \bar{H} = \bar{E}^-, \bar{H}^-$ on S_- . Also, $\bar{E}_q^+ \times \hat{n} \Big|_{S_w} = 0$.

Thus, the above reciprocity relation simplifies to:

$$\begin{aligned} & \iint_{S_+} [\bar{E}^+x\bar{H}_q^+ - \bar{E}_q^+x\bar{H}^+] \cdot \hat{n} \, ds + \iint_{S_-} [\bar{E}^-x\bar{H}_q^+ - \bar{E}_q^+x\bar{H}^-] \cdot (-\hat{n}) \, ds \\ &= \begin{cases} \iiint_V \bar{E}_q^+ \cdot \bar{J} \, dv & \text{for } \bar{S}=\bar{J} \\ -\iiint_V \bar{H}_q^+ \cdot \bar{M} \, dv & \text{for } \bar{S}=\bar{M} \end{cases} \quad (G.4) \end{aligned}$$

Substituting \bar{E}^+ , \bar{H}^+ and \bar{E}^- , \bar{H}^- from (G.1) and using the orthogonality condition:

$$\iint_{S_+} [\bar{E}_p^+ \times \bar{H}_q^+] \cdot \hat{n} \, ds = 0 \quad \text{for } q \neq p \quad (G.5)$$

one obtains a relationship in terms of only the q^{th} mode (i.e., $p=q$ case)

$$\begin{aligned} & \iint_{S_+} A_q^+ [(\bar{E}_{qt} + \bar{E}_{qn}) \times (\bar{H}_{qt} \times \bar{H}_{qn}) e^{-j2\beta_q n_+} - (\bar{E}_{qt} + \bar{E}_{qn}) \times (\bar{H}_{qt} \times \bar{H}_{qn}) e^{-j2\beta_q n_+}] \cdot \hat{n} \, ds \\ & - \iint_{S_-} A_q^- [(\bar{E}_{qt} - \bar{E}_{qn}) \times (\bar{H}_{qt} + \bar{H}_{qn}) - (\bar{E}_{qt} + \bar{E}_{qn}) \times (-\bar{H}_{qt} + \bar{H}_{qn})] \cdot \hat{n} \, ds \\ & = \begin{cases} \iiint_V \bar{E}_q^+ \cdot \bar{J} \, dv & \text{for } \bar{S} = \bar{J} \\ -\iiint_V \bar{H}_q^+ \cdot \bar{M} \, dv & \text{for } \bar{S} = \bar{M} \end{cases} \quad (G.6) \end{aligned}$$

or

$$-2 A_q^- \iint_{S_-} \bar{E}_{qt} \times \bar{H}_{qt} \cdot \hat{n} \, ds = \begin{cases} \iiint_V (\bar{E}_{qt} + \bar{E}_{qn}) \cdot \bar{J} e^{-j\beta_q n} \, dv & \text{for } \bar{S} = \bar{J} \\ -\iiint_V (\bar{H}_{qt} + \bar{H}_{qn}) \cdot \bar{M} e^{-j\beta_q n} \, dv & \text{for } \bar{S} = \bar{M} \end{cases} \quad (G.7)$$

Thus

$$A_q^- = - \frac{1}{2 \iint_{S_-} \bar{E}_{qt} \times \bar{H}_{qt} \cdot \hat{n} \, ds} \begin{cases} \iiint_V (\bar{E}_{qt} + \bar{E}_{qn}) \cdot \bar{J} e^{-j\beta_q n} \, dv & \text{for } \bar{S} = \bar{J} \\ -\iiint_V (\bar{H}_{qt} + \bar{H}_{qn}) \cdot \bar{M} e^{-j\beta_q n} \, dv & \text{for } \bar{S} = \bar{M} \end{cases} \quad (G.8)$$

where A_q^- is the excitation coefficient of the mode \bar{E}_q^- traveling to the right of the source, i.e., in the region $n < n_-$ shown in Figure G.1.

Case (ii): If \bar{E}_q^-, \bar{H}_q^- is chosen as the waveguide mode of interest as in Figure G.2, then the coefficient A_q^+ of the mode \bar{E}_q^+ traveling to the left of the source ($n > n_+$) is given by:

$$A_q^+ = - \frac{1}{2 \iint_{S_+} \bar{E}_{qt} \times \bar{H}_{qt} \cdot \hat{n} \, ds} \left[\begin{array}{l} \iiint_V (\bar{E}_{qt} - \bar{E}_{qn}) \cdot \bar{J} e^{-j\beta_q n} \, dv \\ - \iiint_V (-\bar{H}_{qt} + \bar{H}_{qn}) \cdot \bar{M} e^{-j\beta_q n} \, dv \end{array} \right] \quad (G.9)$$

Note that $\iint_S \bar{E}_{qt} \times \bar{H}_{qt} \cdot \hat{n} \, ds = \iint_{S_+} \bar{E}_{qt} \times \bar{H}_{qt} \cdot \hat{n} \, ds = \iint_{S_c} \bar{E}_{qt} \times \bar{H}_{qt} \cdot \hat{n} \, ds$ where S_c is any cross-sectional area of the waveguide.

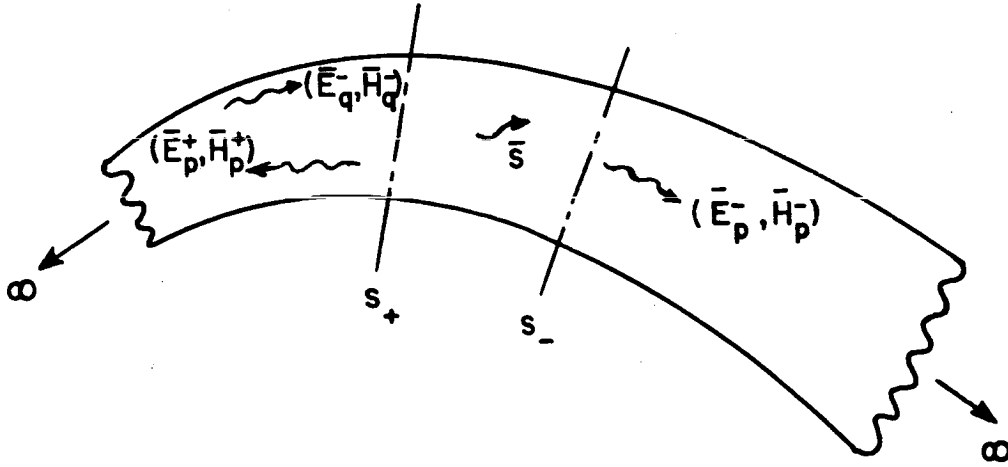


Figure G.2. Waveguide geometry with fields radiated to the left ($n > n_+$) of \bar{S} being of concern.

Although Equations (G.8) and (G.9) are given for a volume source distribution, it is very simple to modify them for a surface (or line) source distribution. For this purpose, the volume integral on the right hand side of Equations (G.8) or (G.9) should be replaced by a surface (or line) integral over the extent of the surface (or line) source distribution.

APPENDIX H
EDGE CORRECTION FOR APERTURE INTEGRATION

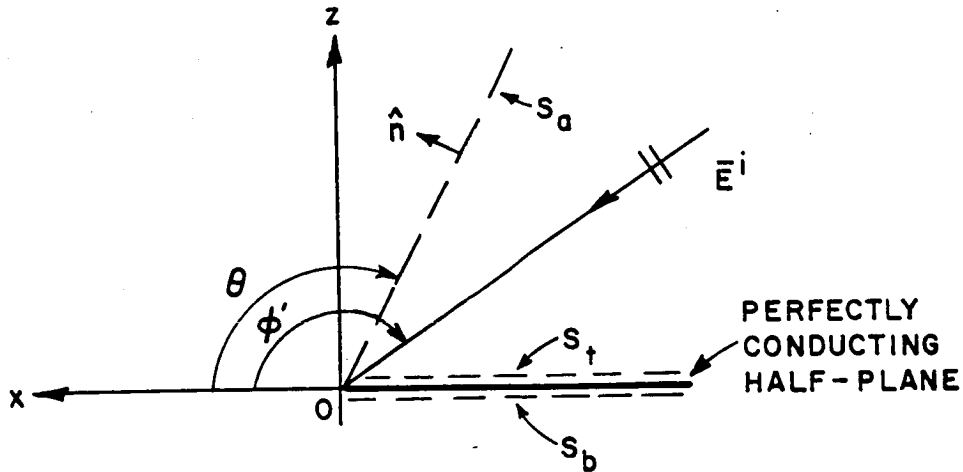


Figure H.1. Scattering from a perfectly-conducting half-plane.

As shown in the figure, a perfectly-conducting half-plane is located in the region $y=0, x<0$. The geometry is infinite in the \hat{z} -direction, therefore the problem can be reduced to a scalar problem in terms of the \hat{z} -component of the electric field (E_z) or the \hat{z} -component of the magnetic field (H_z). The former case is called the soft case and the latter is called the hard case. The analysis for both cases are very similar, therefore only the soft case will be considered here.

Let S_t , S_b , denote the top and bottom surfaces of the half-plane, respectively and S_a denote the aperture surface making an angle θ with the \hat{x} -axis as shown in the figure. The half-plane is illuminated by a plane-wave

$$E^i = e^{jk\rho\cos(\phi-\phi')} \quad (\theta < \phi' < \pi) \quad (\theta > \frac{\pi}{2}) \quad (H.1)$$

In (H.1) θ and ϕ' is restricted so that there exists reflected fields at the aperture surface S_a . The analysis can be similarly carried out to the cases where this restriction is not present. The total field E_z can be written as the combination of three contributions; namely, the incident, the reflected and the diffracted fields. The incident and reflected fields are also called the geometrical optics (GO) fields. The GO field is given by the following expression:

$$\begin{aligned} E_z^{go} &= e^{jk\rho\cos(\phi+\phi')} - e^{jk\rho\cos(\phi+\phi')} = e^{jk_x^i x} 2j\sin k_y^i y ; \text{ on } S_t, S_a \\ &= 0 ; \text{ on } S_b \end{aligned} \quad (H.2)$$

since S_b is in the shadow region of the half-plane. In (H.2),

$$k_x^i = k\cos\phi' \quad \text{and} \quad k_y^i = k\sin\phi' \quad (H.3a;b)$$

The transverse fields can be calculated using

$$-jkZ_0 \vec{H} = (-\hat{y} \frac{\partial}{\partial x} + \hat{x} \frac{\partial}{\partial y}) E_z \quad (H.4)$$

Therefore, the transverse geometrical optics fields can be obtained using Equations (H.2) and (H.3):

$$-jkZ_0 H_x^{go} = jk_y^i e^{jk_x^i x} 2\cos k_y^i y \quad (H.5)$$

$$-jkZ_0 H_y^{go} = -jk_x^i e^{jk_x^i x} 2\sin k_y^i y \quad (H.6)$$

In the physical optics (PO) approximation, one uses the radiation integral to get the scattered field using the G0 fields on the illuminated side of the half-plane (S_t).

Therefore the PO approximation to scattered field is given by:

$$E_z^{PO} = \int_{S_t} ds' [-jkZ_0 G_0 (\hat{n} \times \bar{H}^{go}) + (\hat{n} \times \bar{E}^{go}) \times \nabla G_0] \quad (H.7)$$

where $\nabla G_0 = (\hat{x} \frac{\partial}{\partial y} + \hat{y} \frac{\partial}{\partial x}) G_0$, and

$$G_0(x, y | x', y') = -\frac{j}{4} H_0^{(2)}(k|\bar{\rho} - \bar{\rho}'|) \quad (H.8)$$

is the free-space Green's function in two-dimensions, and \hat{n} is the unit normal to the surface. Using Equations (H.5) and (H.6) and the fact that $\bar{E}^{go} = 0$ on S_t , in (H.7), one obtains:

$$E_z^{PO} = - \int_0^\infty [-jkZ_0 H_x \cdot G_0] dx' \quad (H.9)$$

The Green's function G_0 can also be written as:

$$G_0 = -\frac{j}{4\pi} \int_{-\infty}^\infty dk_x \frac{e^{-jk_x x - jk_y |y-y'|}}{k_y} e^{jk_x x'} \quad (H.10)$$

where

$$k_x^2 + k_y^2 = k^2 \quad (H.11)$$

Substituting (H.5) and (H.10) into (H.9) and changing the order of integration, one obtains:

$$E_z^{PO} = \frac{-1}{2\pi} \int_{-\infty}^{\infty} dk_x \frac{e^{-jk_x x - jk_y y}}{k_y} k_y^i \int_0^{\infty} e^{jk_x^i x' + jk_x x'} dx' \quad (H.12)$$

$$E_z^{PO} = \frac{-j}{2\pi} \int_{-\infty}^{\infty} \frac{e^{-jk_x x - jk_y y}}{k_y} \frac{k_y^i}{k_x^i + k_x} dk_x \quad (H.13)$$

Using the transformation

$$k_x = k \cos \alpha \quad k_y = k \sin \alpha \quad , \quad (H.14a;b)$$

Equation (H.13) becomes

$$E_z^{PO} = \frac{-j}{2\pi} \int_{C_\alpha} e^{-jk \rho \cos(\alpha - \phi)} \frac{\sin \phi^i}{\cos \alpha + \cos \phi^i} d\alpha \quad (H.15)$$

where the integration path C_α is shown below:

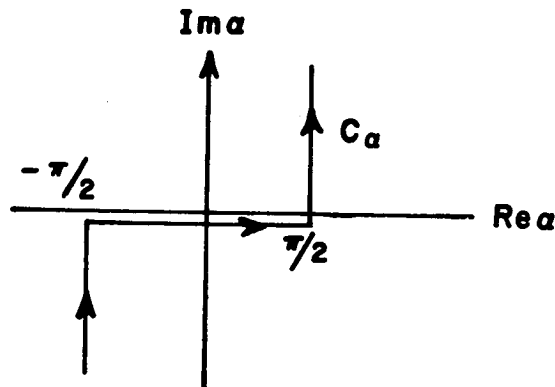


Figure H.2. The integration path C_α .

On the other hand, if one integrates the GO fields over S_a and S_b to get the scattered field, one obtains:

$$E_z^k = \int_{S_a} ds' [-jkZ_0 G_0 (\hat{n} \times \bar{H}^{g0}) + (\hat{n} \times \bar{E}^{g0}) \times \nabla G_0] \quad (H.16)$$

since GO field is zero on S_b .

Using (H.2), (H.5), (H.6) and (H.10) in (H.16), one obtains:

$$E_z^k = -\frac{j}{4\pi \sin \theta} \int_{-\infty}^{\infty} dk_y \frac{e^{-jk_y y - jk_x x}}{k_x} \left[[(-k_x^i + k_x) \sin \theta + k_y \cos \theta] \right. \\ \left[\frac{1}{k_y + (k_x^i + k_x) \cot \theta + k_x^i} - \frac{1}{k_y + (k_x^i + k_x) \cot \theta - k_y^i} \right] \\ \left. - k_y^i \cos \theta \left[\frac{1}{k_y + (k_x^i + k_x) \cot \theta + k_x^i} + \frac{1}{k_y + (k_x^i + k_x) \cot \theta - k_y^i} \right] \right] \cdot \quad (H.17)$$

Using the transformations in (H.14) and after some straightforward manipulations one finally obtains:

$$E_z^k = -\frac{j}{2\pi} \int_{\alpha} e^{-jk\rho \cos(\alpha - \phi)} \frac{\sin \phi'}{\cos \alpha + \cos \phi'} d\alpha \quad (H.18)$$

The Equations (H.15) and (H.18) are exactly the same, therefore the Ufimtsev edge correction [26] to (H.15) can be used without modification to correct for the aperture integration result of (H.18).

APPENDIX I

APPLICATION OF THE RECIPROCITY THEOREM TO FIND THE RELATION BETWEEN THE SCATTERING MATRICES $[S_{12}]$ AND $[S_{21}]$

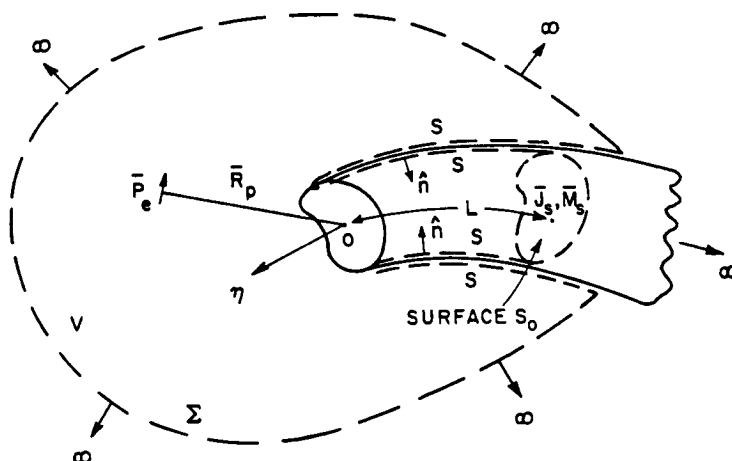


Figure I.1 The geometry of the problem.

Figure I.1 shows an open-ended waveguide cavity geometry with perfectly conducting walls. Let there be modal fields inside the waveguide propagating in $+\hat{n}$ direction represented by:

$$\bar{E}_n^+ = C_n^+ (\bar{e}_{nt} + \bar{e}_{nn}) e^{-j\beta_n n} \quad (I.1)$$

$$\bar{H}_n^+ = C_n^+ (\bar{h}_{nt} + \bar{h}_{nn}) e^{-j\beta_n n} \quad (I.2)$$

where \bar{e}_{nt} (or \bar{h}_{nt}) is the transverse electric (or magnetic) field, and \bar{e}_{nn} (or \bar{h}_{nn}) is the longitudinal electric (or magnetic) field. C_n^+ is the coefficient of the nth mode.

Some of the energy carried by this modal field will be radiated into the free space through the aperture. The far field radiation can be calculated approximately by the aperture integration of the modal field and the resulting radiated fields are shown by \bar{E}^r and \bar{H}^r .

The rest of the energy of the incident mode will reflect back to the guide in terms of an mth mode.

$$\bar{E}_m^- = \Gamma_{mn} C_n^+ (\bar{e}_{nt} - \bar{e}_{nn}) e^{j\beta_m n} \quad (I.3)$$

$$\bar{H}_m^- = \Gamma_{mn} C_n^+ (-\bar{h}_{nt} + \bar{h}_{nn}) e^{j\beta_m n} \quad (I.4)$$

where Γ_{nm} is the modal reflection coefficient from the open end.

First consider the geometric plane defined by $n=-L$ inside the semi-infinite waveguide and let S_0 denote the area of this waveguide cross section at $n=-L$ as shown in Figure I.1. Then let S denote the surface area which tightly encapsulates the complete outer (exterior) surface of the semi-infinite waveguide, and also a portion of the inner walls of this waveguide up to the distance $n=-L$ within the guide. The surface S does not include the plane at $n=-L$ within the guide. Let Σ denote the sphere at infinity which surrounds the semi-infinite guide such that S on the exterior or outer wall of the semi-infinite guide is

connected to the surface Σ at $\eta \rightarrow -\infty$ as in Figure A.1. Next, consider the following two cases. In the first case, the semi-infinite rectangular waveguide is excited from within by the modal fields with amplitude C_n^+ which propagate in the $+\hat{n}$ direction. However, in the second case, the geometry is excited by external fields, \bar{E}^e and \bar{H}^e , which for convenience is assumed to be produced by an electric test source \bar{J}_e at \bar{R}_p exterior to and in the far zone of the semi-infinite guide.

Let the equivalent sources \bar{J}_s and \bar{M}_s be located at $\eta = -L$ in the guide,

$$\bar{J}_s = \hat{n} \times \left[C_n^+ (\bar{h}_{nt} + \bar{h}_{n\eta}) e^{j\beta_n L} + \sum_m r_{mn} C_n^+ (-\bar{h}_{mt} + \bar{h}_{m\eta}) e^{-j\beta_m L} \right] \quad (I.5)$$

$$\bar{M}_s = -\hat{n} \times \left[C_n^+ (\bar{e}_{nt} + \bar{e}_{n\eta}) e^{j\beta_n L} + \sum_m r_{mn} C_n^+ (\bar{e}_{mt} - \bar{e}_{m\eta}) e^{-j\beta_m L} \right] \quad (I.6)$$

where \hat{n} is the unit vector pointing into the volume V , enclosed by surfaces $S+S_0+\Sigma$. From reciprocity one obtains:

$$\iiint_{\Sigma+S+S_0} \left[\bar{E}^r \times \bar{H}^e - \bar{E}^e \times \bar{H}^r \right] \cdot \hat{n} ds = \iiint_V \bar{J}_e \cdot \bar{E}^r dv \quad (I.7)$$

However, by the boundary conditions

$$\hat{n} \times \bar{E}^r \Big|_{\text{on } S} = 0, \quad (I.8)$$

and

$$\hat{n} \times \bar{E}^e \Big|_{\text{on } S} = 0. \quad (I.9)$$

Also, (\bar{E}^r, \bar{H}^r) and (\bar{E}^e, \bar{H}^e) satisfy the radiation condition on Σ .

Therefore (I.7) reduces to:

$$-\iint_{S_0} \bar{H}^e \cdot \bar{M}_s ds + \iint_{S_0} \bar{E}^e \cdot \bar{J}_s ds = \bar{p}_e \cdot \bar{E}^r(\bar{R}_p) \quad , \quad (I.10)$$

since

$$\bar{J}_e = \bar{p}_e \delta(|\bar{R} - \bar{R}_p|) \quad , \quad (I.11)$$

a point source in the far field.

In (I.11) \bar{R}_p is the position vector from the reference point to point P.

Inside the waveguide the fields \bar{E}^e and \bar{H}^e will have the following representation

$$\bar{E}^e = \sum_p A_p^- (\bar{e}_{pt} - \bar{e}_{pn}) e^{j\beta_p n} \quad (I.12)$$

$$\bar{H}^e = \sum_p A_p^- (-\bar{h}_{pt} + \bar{h}_{pn}) e^{j\beta_p n} \quad (I.13)$$

Substituting (I.12) and (I.13) into (I.10) one obtains:

$$\begin{aligned} & - \iint_{S_0} \sum_p A_p^- (-\bar{h}_{pt} + \bar{h}_{pn}) e^{-j\beta_p L} C_n^+ \left[\bar{e}_{nt} \hat{x} \hat{n} e^{j\beta_n L} + \sum_m \Gamma_{mn} (\bar{e}_{mt} \hat{x} \hat{n}) e^{-j\beta_m L} \right] ds \\ & - \iint_{S_0} \sum_p A_p^- (\bar{e}_{pt} - \bar{e}_{pn}) e^{-j\beta_p L} C_n^+ \left[(\hat{n} \times \bar{h}_{nt}) e^{j\beta_n L} - \sum_m \Gamma_{mn} (\hat{n} \times \bar{h}_{mt}) e^{-j\beta_m L} \right] ds \\ & = \bar{p}_e \cdot \bar{E}^r(\bar{R}_p) \quad . \quad (I.14) \end{aligned}$$

Using the orthogonality property of waveguide modes one obtains:

$$\left[\iint_{S_0} \bar{\mathbf{e}}_{nt} \times \bar{\mathbf{h}}_{nt} \cdot \hat{\mathbf{n}} \, ds \right] (-C_n^+ A_n^-)^2 = \bar{\mathbf{p}}_e \cdot \bar{\mathbf{E}}^r(\bar{\mathbf{R}}_p) \quad (\text{I.15})$$

$$-2 C_n^+ A_n^- = \frac{\bar{\mathbf{p}}_e \cdot \bar{\mathbf{E}}^r(\bar{\mathbf{R}}_p)}{\iint_{S_0} \bar{\mathbf{e}}_n \times \bar{\mathbf{h}}_n \cdot \hat{\mathbf{n}} \, ds} \quad (\text{I.16})$$

In order to produce an incident field $\bar{\mathbf{E}}^i = \hat{\theta} E_\theta^i + \hat{\phi} E_\phi^i$ at the opening of the waveguide, one can let

$$\bar{\mathbf{p}}_e = -(\hat{\theta} E_\theta^i + \hat{\phi} E_\phi^i) \frac{4\pi}{j\omega\mu} R_p e^{jkR_p} \quad (\text{I.17})$$

where θ and ϕ are defined as the elevation and azimuth angles in a spherical coordinate system located at 0, in Figure I.1. Thus,

$$A_n^- = \frac{(\hat{\theta} E_\theta^i + \hat{\phi} E_\phi^i) \cdot \bar{\mathbf{E}}^r(\bar{\mathbf{R}}_p) R_p e^{jkR_p}}{-2 C_n^+ \iint_{S_0} \bar{\mathbf{e}}_{nt} \times \bar{\mathbf{h}}_{nt} \cdot \hat{\mathbf{n}} \, ds} \frac{4\pi}{j\omega\mu} \quad (\text{I.18})$$

In matrix notation, it is clear that (I.15) can be expressed as:

$$[E_x^r(P) \ E_y^r(P) \ E_z^r(P)] \begin{bmatrix} p_{ex} \\ p_{ey} \\ p_{ez} \end{bmatrix} = ([C_n^+]^T) (-2 [\iint_{S_0} \bar{\mathbf{e}}_{nt} \times \bar{\mathbf{h}}_{nt} \cdot \hat{\mathbf{n}} \, ds]) ([A_n^-]) \quad (\text{I.19})$$

where $(-2[\int_{S_0} \bar{e}_{nt} x \bar{h}_{nt} \cdot \hat{n} ds])$ is a diagonal matrix. It is noted that

\bar{E}^r contains C_n^+ since $\bar{E}^r(P)$ is produced by the radiation of \bar{E}_n^+ .

Furthermore, it is obvious from (2.13) and (2.21) that

$$\begin{bmatrix} E_x^r(P) \\ E_y^r(P) \\ E_z^r(P) \end{bmatrix} = [S_{12}] [C_n^+] \quad (I.20)$$

and

$$[A_n^-] = [S_{21}^p] \begin{bmatrix} p_{ex} \\ p_{ey} \\ p_{ez} \end{bmatrix} \quad (I.21)$$

Incorporating (I.20) and (I.21) into (I.19) yields:

$$([C_n^+]^T) ([S_{12}])^T \begin{bmatrix} p_{ex} \\ p_{ey} \\ p_{ez} \end{bmatrix} = ([C_n^+])^T (-2[\int_{S_0} \bar{e}_{nt} x \bar{h}_{nt} \cdot \hat{n} ds]) ([S_{21}^p]) \begin{bmatrix} p_{ex} \\ p_{ey} \\ p_{ez} \end{bmatrix} \quad (I.22)$$

The relationship between $[S_{12}]$ and $[S_{21}^p]$ becomes evident from (I.22); namely

$$[S_{12}]^T = (-2[\int_{S_0} \bar{e}_{nt} x \bar{h}_{nt} \cdot \hat{n} ds]) [S_{21}^p] \quad (I.23)$$

APPENDIX J
EQUIVALENT MAGNETIC LINE DIPOLE

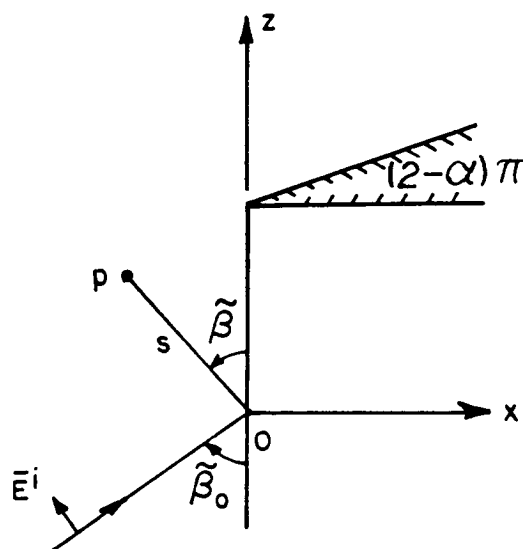


Figure J.1. A wedge illuminated by a $\hat{\beta}_0$ -polarized plane wave.

In this appendix, the edge diffracted field from a wedge illuminated by a $\hat{\beta}_0$ -polarized plane wave (shown in Figure J.1) will be represented by the free-space radiation from magnetic line dipoles located at the edge position. The incident plane wave is in the following form:

$$\bar{E}^i(s) = \hat{\beta}_0 e^{-jk^i \cdot \bar{s}} E^i \quad (J.1)$$

where

$$\bar{k}^i = -k(\sin\theta^i \cos\phi^i \hat{x} + \sin\theta^i \sin\phi^i \hat{y} + \cos\theta^i \hat{z}) \quad (J.2)$$

and \bar{s} is the vector defining an observation point. The angles θ^i and ϕ^i are the elevation and the azimuth angles, respectively of the direction of the incident plane wave with respect to the wave with respect to the spherical coordinates. It is clear from Figure J.1 that $\theta^i = \pi - \tilde{\beta}_0$.

The electric field diffracted from the wedge and observed at the observation point P shown in Figure J.1 is given by [26]

$$E^d = -\tilde{\beta} D_s(\phi, \phi^i; \tilde{\beta}_0, \tilde{\beta}, \alpha) \sqrt{\frac{\rho}{s(\rho+s)}} e^{-jks} E^i \quad (J.3)$$

where D_s is the soft diffraction coefficient (non-uniform soft diffraction coefficient is given in (3.3)), and ρ is the caustic distance for the diffracted rays. If $\rho \gg s$, then the diffracted field expression becomes

$$\bar{E}^d = -\tilde{\beta} D_s(\phi, \phi^i; \tilde{\beta}_0, \tilde{\beta}, \alpha) \frac{e^{-jks}}{\sqrt{s}} E^i \quad (J.4)$$

Now, consider the free-space radiation from magnetic line dipoles located along the \hat{z} -axis as shown in Figure J.2. For an observation point with an elevation angle θ , the dipoles are given by

$$\bar{M}_d = (\hat{x} \sin\theta + \hat{z} \cos\theta \cos\phi) M_d e^{-jkz \cos\theta} \delta(x) \delta(y) \quad (J.5)$$

where θ is elevation angle and ϕ_0 is a constant angle and $\delta(x)$ is the Dirac delta function.

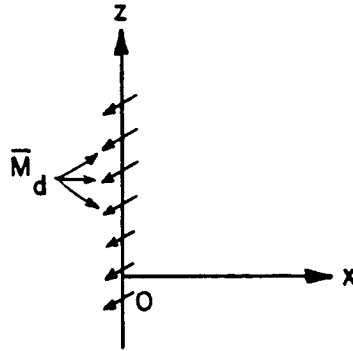


Figure J.2. Magnetic line dipoles along \hat{z} -axis.

The electric vector potential \bar{F} is given by

$$\bar{F} = (\hat{k} \sin \theta + \hat{z} \cos \theta \cos \phi_0) \frac{M_d}{4j} H_0^{(2)}(k \sqrt{x^2 + y^2} \sin \theta) e^{-jkz \cos \theta} \quad (J.6)$$

The radiated electric field is given by

$$\begin{aligned} \bar{E} = -\nabla \times \bar{F} = & \hat{\phi} \frac{M_d}{4j} \{-k \cos \theta \cos \phi_0 \sin \theta H_1^{(2)} + jk \cos \theta \sin \theta \cos \phi_0 H_0^{(2)}\} e^{-jkz \cos \theta} \\ & + \hat{\rho} \frac{M_d}{4j} \{jk \cos \theta \sin \theta \sin \phi_0 H_0^{(2)}\} e^{-jkz \cos \theta} \\ & - \hat{z} \frac{M_d}{4j} \{k \sin^2 \theta \sin \phi_0 H_1^{(2)}\} e^{-jkz \cos \theta} \end{aligned} \quad (J.7)$$

where the arguments of the Hankel functions are as in (J.6). If one employs the large argument approximations to Hankel functions [44],

one obtains

$$\bar{E} = \hat{\beta} M_d \cdot \sin\phi \sqrt{\frac{jk}{8\pi}} \frac{e^{-jks}}{\sqrt{s}} \quad (J.8)$$

where

$$s = \sqrt{x^2 + y^2 + z^2} \quad (J.9)$$

In (J.8) the angles θ and ϕ_0 are replaced by $\tilde{\beta}$ and ϕ , respectively.

Therefore, (J.8) applies for the observation point P of Figure J.1. By comparing (J.4) and (J.8), one deduces the strength of magnetic dipoles as follows:

$$M_d = -\sqrt{\frac{8\pi}{jk}} \frac{D_s(\phi, \phi^i; \tilde{\beta}_0, \tilde{\beta}, \alpha)}{\sin\phi} E^i(0) \quad (J.10)$$

APPENDIX K

DESCRIPTION OF THE EQUIVALENCE PRINCIPLE EMPLOYED IN THE CALCULATION OF SCATTERING MATRICES

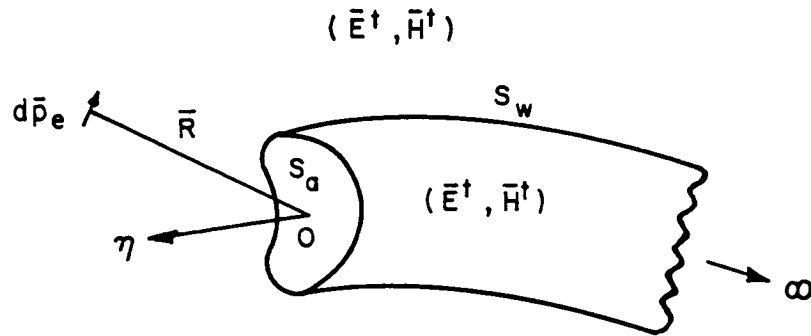


Figure K.1. Radiation of a dipole $d\vec{p}_e$ in the presence of the semi-infinite waveguide.

Let a dipole $d\vec{p}_e$ radiate in the presence of the semi-infinite waveguide structure. The aperture of the waveguide is shown by S_a and S_w denotes the surface of the waveguide wall. Let the total field be represented by \vec{E}^t, \vec{H}^t . By the equivalence principle one can use the equivalent sources \vec{J}_{eq} and \vec{M}_{eq} on S_a and S_w which radiate the total field inside the waveguide region and null field in the outside region, as shown in Figure K.2.

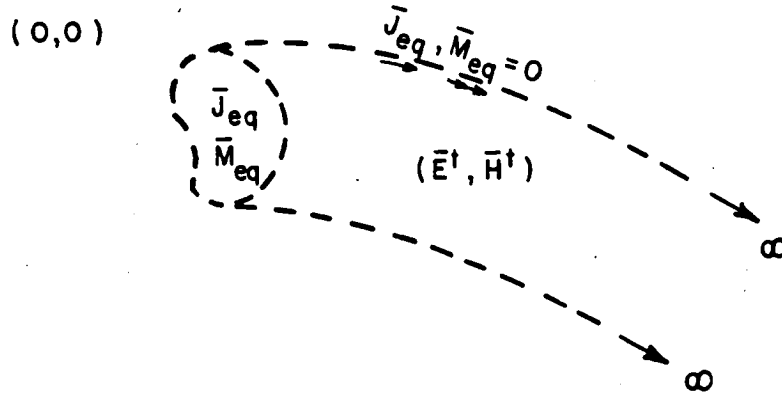


Figure K.2. The equivalent problem of Figure K.1.

The equivalent sources are given by

$$\bar{J}_{eq} = \hat{n} \times \bar{H}^t \quad (K.1)$$

$$\bar{M}_{eq} = \bar{E}^t \times \hat{n} \quad (K.2)$$

where \hat{n} is the unit vector pointing into the waveguide region. By the boundary conditions, the equivalent magnetic sources on S_w is zero. If these sources are known, then the fields \bar{E}^t, \bar{H}^t coupled through the waveguide can be obtained. In order to calculate the fields one can react the sources and fields of Figure K.2 with the sources and the fields of Figure K.3, where a dipole $d\bar{p}_e$ is radiating inside the infinite waveguide. That infinite waveguide is obtained by extending the semi-infinite waveguide of Figure K.1.

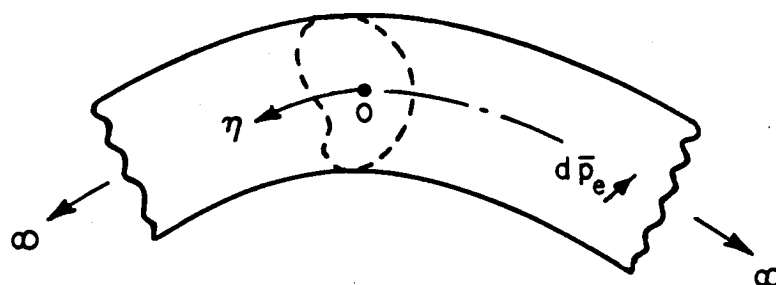


Figure K.3. The dipole $d\bar{p}_e$ radiating in the infinite waveguide.

Clearly, the equivalent electric source \bar{J}_{eq} on S_w , will not react with the modal fields of the dipole $d\bar{p}_e$, since the tangential electric field in the modal expressions vanishes on S_w . Therefore, coupling through the waveguide modes will be determined by only the equivalent sources at the aperture S_a . Also, it is noted that since the equivalent sources radiate null field external to the semi-infinite waveguide, the reaction of these fields with the dipole source of Figure K.3 will be zero.

APPENDIX L

ILLUSTRATION OF RECIPROCITY IN THE APERTURE INTEGRATION

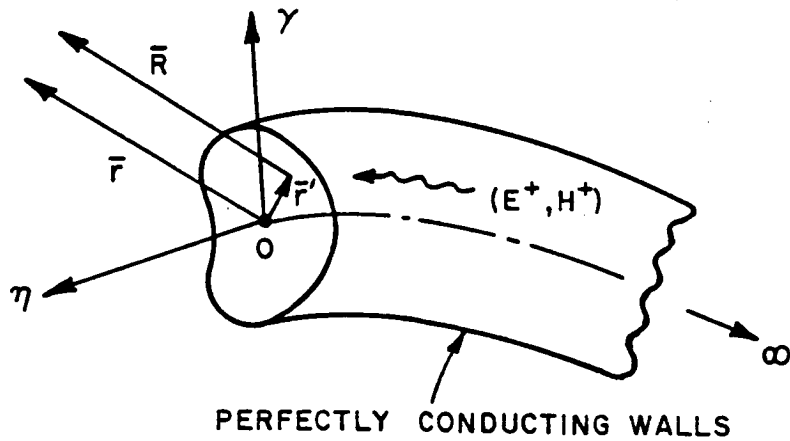


Figure L.1. Modal radiation from the open end.

In this appendix, the aperture integration technique will be used to obtain the modal radiation from and coupling through the open end of a semi-infinite waveguide in the front half-space. It will be shown that these two results satisfy the reciprocity relationship stated in Appendix I.

The radiation problem is sketched in Figure L.1. The interior fields (\bar{E}^+, \bar{H}^+) propagate through the aperture at the open end and radiate into the exterior region. In order to simplify the analysis the

observation point is assumed to be in the far field of the aperture and separated by the distance \bar{r} from the origin. The interior fields \bar{E}^+ and \bar{H}^+ are given in terms of a summation of waveguide modes, so

$$\bar{E}^+ = \sum_n C_n^+ \bar{E}_n^+ \quad (L.1)$$

and

$$\bar{H}^+ = \sum_n C_n^+ \bar{H}_n^+ \quad (L.2)$$

where C_n^+ is the amplitude of the n^{th} modal field. The aperture integration procedure assumes that the radiated field is due to the approximate equivalent electric and magnetic currents \bar{J}_s and \bar{M}_s located at the aperture. The currents \bar{J}_s and \bar{M}_s are given by

$$\bar{J}_s = \hat{n} \times \bar{H}^+ \quad (L.3)$$

$$\bar{M}_s = \bar{E}^+ \times \hat{n} \quad (L.4)$$

where \hat{n} is the unit normal vector at the surface of the aperture pointing into the exterior region. The approximate currents are then assumed to radiate in free-space. Therefore, the far-zone field radiated by the equivalent sources is written as

$$\bar{E}^{\text{rad}} = \frac{jk}{4\pi} \frac{e^{-jk\bar{r}}}{\bar{r}} \iint_{S_a} e^{jk\hat{r} \cdot \bar{r}'} [Z_0 \hat{R} \times \hat{R} \times \bar{J}_s + \hat{R} \times \bar{M}_s] ds' \quad (L.5)$$

where the unit vectors \hat{r} and \hat{R} are in \bar{r} and \bar{R} directions, respectively as shown in Figure L.1, and \bar{r}' is the vector from the origin to the source point. The substitution of (L.1) through (L.4) into (L.5) yields

$$\bar{E}^{\text{rad}} = \frac{jk}{4\pi} \frac{e^{-jkr}}{r} \sum_n C_n^+ \iint_{S_a} e^{jk\bar{r}' \cdot \hat{r}} [Z_0 \hat{R} \times \hat{R} \times (\hat{n} \times \bar{H}_n^+) + \hat{R} \times (\bar{E}_n^+ \times \hat{n})] d\bar{s}' \quad (\text{L.6})$$

The next step is to calculate the coupling of incident energy due to a small electric dipole $d\bar{p}_e$ into the waveguide modes using the aperture integration. The dipole $d\bar{p}_e$ is located at \bar{s}^i from the origin and the amplitudes of the modes excited by the dipole is shown by (C_n^{GO}) . The mode amplitudes are given by (3.97)

$$C_n^{\text{GO}} = \frac{\iint_{S_a} (\bar{E}_n^+ \cdot \bar{J}_s^{\text{GO}} - \bar{H}_n^+ \cdot \bar{M}_s^{\text{GO}}) d\bar{s}'}{2 \iint_{S_a} \bar{E}_n^+ \times \bar{H}_n^+ \cdot d\bar{s}'} \quad (\text{L.7})$$

where \bar{J}_s^{GO} and \bar{M}_s^{GO} are given by (3.92) and (3.93),

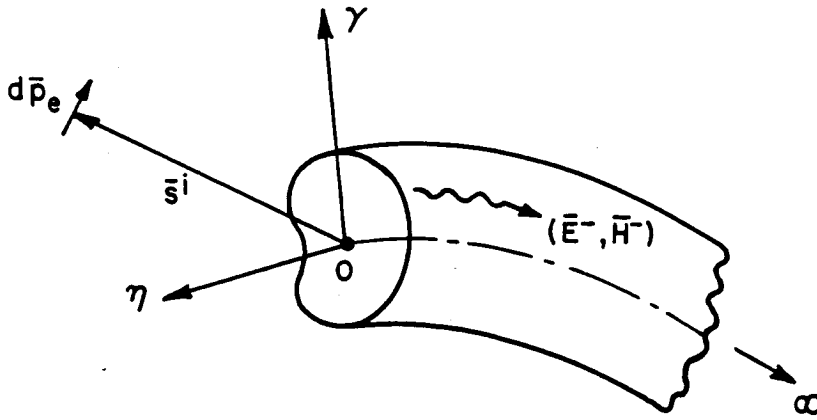


Figure L.2. Coupling of incident dipole field.

If (3.92) through (3.95) is employed in (L.7) the following is obtained

$$P_n \cdot C_n^{G0} = -\frac{jk}{4\pi} \frac{e^{-jks^i}}{s^i} \iint_{S_a} [\bar{E}_n^+ \cdot (\hat{s}^i \times d\bar{p}_e) \times \hat{n} - Z_0 \bar{H}_n^+ \cdot \hat{n} \times (\hat{s}^i \times \hat{s}^i \times d\bar{p}_e)] e^{jk\bar{r}' \cdot \hat{s}^i} ds' \quad (L.8)$$

where

$$P_n = 2 \iint_{S_a} \bar{E}_n^+ \times \bar{H}_n^+ \cdot d\bar{S}' \quad (L.9)$$

By rearranging (L.8) one obtains

$$P_n \cdot C_n^{G0} = -\frac{jk}{4\pi} \frac{e^{-jks^i}}{s^i} \iint_{S_a} [d\bar{p}_e \cdot \hat{s}^i \times (\bar{E}_n^+ \times \hat{n}) + Z_0 d\bar{p}_e \cdot \hat{s}^i \times \hat{s}^i \times (\hat{n} \times \bar{H}_n^+)] ds' \quad (L.10)$$

If the dipole is located at \bar{r} , then from (L.6) and (L.10) one obtains

$$d\bar{p}_e \cdot \bar{E}^{rad} = -P_n \cdot C_n^{G0} \quad (L.11)$$

which is the reciprocity relationship between the problems of the modal radiation and the coupling into the waveguide due to a dipole source.

REFERENCES

- [1] R.E. Collin, Field Theory of Guided Waves, McGraw Hill, New York, 1960.
- [2] R. Mittra and S.W. Lee, Analytical Techniques in the Theory of Guided Waves, The Macmillan Company, New York, 1971.
- [3] L. Lewin, Theory of Waveguides, John Wiley and Sons, New York, 1975.
- [4] V.V. Schevchenko, Continuous Transitions in Open Waveguides, The Golem Press, Boulder, Colorado, 1971.
- [5] S.A. Schelkunoff, "Conversion of Maxwell's Equations into Generalized Telegraphist's Equations", Bell Syst. Tech. J., 34, pp. 995-1043, 1955.
- [6] F. Sporleder and H.G. Unger, Waveguide Tapers, Transitions and Couplers, Peter Peregrinus Ltd., Institution of Electrical Engineers, London, 1977.
- [7] W.H. Louisell, "Analysis of the Single Tapered Mode Coupler", Bell Syst. Tech. J., 34, pp. 853-870, 1955.
- [8] L. Lewin, D.C. Chang and E.F. Kuester, Electromagnetic Waves and Curved Structures, Peter Peregrinus Ltd., Institution of Electrical Engineers, London, 1977.
- [9] R.C. Rudduck and L.L. Tsai, "Aperture Reflection Coefficients of TEM and TE₁₀ Mode Parallel-Plate Waveguides", IEEE AP, Vol. AP-16, No. 1, pp. 83-89, January 1968.
- [10] H.Y. Yee, L.B. Felsen and J.B. Keller, "Ray Theory of Reflection from the Open End of a Waveguide", SIAM J. App. Math., Vol. 16, No. 2, pp. 268-300, 1968.
- [11] J.B. Keller, "Geometrical Theory of Diffraction", J. Opt. Soc. Amer., Vol. 52, pp. 116-130, 1962.
- [12] S.W. Lee, "Ray Theory of Diffraction by Open Ended Waveguides I. Fields in Waveguides" J. Math. Phys., Vol. 11, No. 9, pp. 2830-2850, Sept. 1970.

- [13] S.W. Lee, "Ray Theory of Diffraction by Open-Ended Waveguides, II. Applications", J. Math. Phys., Vol. 13, No. 5, pp. 656-664, May 1972.
- [14] J. Boersma, "Ray Optical Analysis of Reflections in an Open-Ended Parallel Plane Waveguide, I: TM Case", SIAM J. Appl. Math., Vol. 29, No. 1, pp. 164-195, July 1975.
- [15] S.W. Lee and J. Boersma, "Ray-Optical Analysis of Fields on Shadow Boundaries of two Parallel Plates", J. Math., Phys, Vol. 16, No. 9, pp. 1746-1764, Sept. 1975.
- [16] J. Boersma, "Ray-Optical Analysis of Reflection in an Open-Ended Parallel-Plate Waveguide, II: TE Case", Proc., IEEE, Vol. 62, pp. 1475-1481, 1974.
- [17] E.V. Jull, "Reflection from the Aperture of a Long E-Plane Sectoral Horn", IEEE AP, Vol. AP-20, No. 1, pp. 62-68, Jan. 1972.
- [18] S.J. Maurer, L.B. Felsen, "Ray-Optical Techniques for Guided Waves", Proc. IEEE, Vol. 55, No. 10, pp. 1718-1729, Oct. 1967.
- [19] L.B. Felsen, S.J. Maurer, "Ray Interpretation of Modes in Curved Nonuniform Waveguides", Elec. Lett., Vol. 4, No. 4, pp. 70-72, Feb. 1968.
- [20] L.B. Felsen, H.Y. Yee, "Ray Method for Sound-Wave Reflection in an Open-Ended Circular Pipe", J. Acoust. Soc. of Amer., Vol. 44, No. 4, pp. 1028-1039, 1968.
- [21] M.I. Ivanyan, "Radiation from the Open End of a Circular Waveguide with a Conical Flange in the Approximation of Geometric Theory of Diffraction, The Scalar Problems", Rad. Eng. and Elec. Phys., Vol. 27, pp. 31-41, April 1982.
- [22] C.C. Huang, P.H. Pathak, C.Y. Lai, D.L. Moffatt, "Analysis of Electromagnetic Backscatter from an Inlet Cavity Configuration", The Ohio State University ElectroScience Laboratory, Dept. of Electrical Engineering; prepared under Contract No. N00014-79-H-0039 for the Department of the Air Force, Electronic Systems Division, Hanscom AFB, Massachusetts, Report No. 712661, Oct. 1982.
- [23] J. Pace and R. Mittra, "Generalized Scattering Matrix Analysis of Waveguide Discontinuity Problems", Quasi-Optics, Vol. XIV, pp. 177-197, Polytechnic Institute of Brooklyn Press, New York, 1964.

- [24] C.E. Ryan and L. Peters, Jr., "Evaluation of Edge-Diffracted Fields Including Equivalent Currents for the Caustic Regions", IEEE AP, Vol. AP-17, No. 3, pp. 292-299, May 1969.
- [25] W.D. Burnside and L. Peters, Jr., "Axial-radar Cross Section of Finite Cones by the Equivalent-current Concept with Higher-order Diffraction", Radio Science, Vol. 7, No. 10, pp. 943-948, Oct. 1972.
- [26] P.H. Pathak, "Techniques for High Frequency Problems", Chapter A7 in Handbook of Antenna Theory and Design, Eds., Y.T. Lo and S.W. Lee, to be published by ITT-Howard W. Sams and Co., Inc.
- [27] P. Ya Ufimtsev, "Method of Edge Waves in the Physical Theory of Diffraction", (from the Russian "Method Krayevykh voln v frizicheskoy teorii diffraksii", Izd-Vo Sov. Radio, pp. 1-243, 1962), translation prepared by the U.S. Air Force Foreign Technology Division, Wright-Patterson AFB, Ohio; released for public distribution, Sept. 7, 1971.
- [28] L.A. Weinstein, The Theory and Diffraction and the Factorization Method, The Golem Press, Boulder, Colorado, 1969.
- [29] J.J. Bowman, "Comparison of ray theory with exact theory for scattering by open waveguides", SIAM, J. Appl. Math., Vol. 18, pp. 818-829, 1970.
- [30] D.S. Ahluwalia, R.M. Lewis and J. Boersma, "Uniform Asymptotic Theory of Diffraction by a Plane Screen", SIAM, J. Appl. Math., Vol. 16, pp. 783-807, 1968.
- [31] E.F. Knott and T.B.A. Senior, "Comparison of Three High-frequency Diffraction Techniques", Proc. IEEE, Vol. 62, pp. 1468-1474, 1974.
- [32] E.D. Greer and W.D. Burnside, "High Frequency Near Field Scattering by an Elliptic Disk," Technical Report 4583-1, The Ohio State University, ElectroScience Laboratory, prepared under Contract No. N62269-76-C-0554, for Naval Air Development Center, Warminster, PA, December 1976.
- [33] P.H. Pathak, A. Altintas, C.D. Chuang and S. Barkeshli, "Near Field Scattering by Rectangular and Circular Inlet Configurations with an Impedance Surface Termination", Final Report 715267-1, The Ohio State University, ElectroScience Laboratory, prepared under contract No. N60530-83-M-40RD for Naval Weapons Center, China Lake, CA, July 1984.

- [34] P.H. Pathak, C.D. Chuang, "Continuation of work on near and far field scattering by rectangular and circular inlet configurations with an impedance surface termination", Final Report 715979-1, The Ohio State University, ElectroScience Laboratory, prepared under contract no. N60530-84-C-0143 for Naval Weapons Center, China Lake, CA, June 1985.
- [35] P.H. Pathak, C.W. Chuang, M.C. Liang, N. Wang, H.T. Kim, "Rim and Inlet Modeling Studies", Final Report 716495-2, The Ohio State University, ElectroScience Laboratory prepared under contract no. N60530-84-C-0143 for Naval Weapons Center, China Lake, CA, October 1985.
- [36] A.D. Yaghjian, "Approximate Formulas for the Far Fields and Grain of Open-Ended Rectangular Waveguide", Report NBSIR83-1689, National Bureau of Standards, 1983.
- [37] T.B.A. Senior, "The diffraction Matrix for a Discontinuity in Curvature", IEEE AP, Vol. AP-20, No. 3, pp. 326-333, May 1972.
- [38] N. Marcuvitz, Waveguide Handbook, McGraw-Hill Book Co. Inc., New York, 1951.
- [39] E. Bahar, "Fields in Waveguide Bends Expressed in Terms of Coupled Local Annular Waveguide Modes," IEEE MTT, Vol. MTT-17, No. 4, pp. 210-217, April 1969.
- [40] E.V. Jull, "Aperture Fields and Gain of Open-Ended Parallel-Plate Waveguide", IEEE Trans. Antennas Propagation, Vol. AP-21, No. 1, pp. 14-18, Jan. 1973.
- [41] A.O. Howard, Jr., "A Comparison of Mode Match, Geometrical Theory of Diffraction, and Kirchhoff Radiation", IEEE Trans. Antennas on Propagation, Vol. AP-21, No.1, pp. 100-102, Jan. 1973.
- [42] L. Grun and S.W. Lee, "Transmission into Staggered Parallel-Plate Waveguides," IEEE Trans. Antennas and Propagation, Vol. AP-30, No. 1, pp. 35-43, Jan. 1982.
- [43] A.J. Terzuoli, Jr., C.W. Chuang, and L. Peters, Jr., "An Integral Equation Approach to Obtain the Significant Parameters of Dihedral Corrugated Horns", The Ohio State University, Report 3821-2, July 1976.
- [44] R.F. Harrington, Time Harmonic Electromagnetic Fields, McGraw Hill, New York, 1961.
- [45] M. Abramowitz and I.A. Stegun, Handbook of Mathematical Functions, Dover Publications, Inc., New York, 1965.

- [46] W. Wasylkiwskyj, "Diffraction by a Concave Perfectly Conducting Circular Cylinder," IEEE Trans. Antennas Propagation, Vol. AP-23, No. 4, pp. 480-492, July 1975.
- [47] N. Marcuvitz, "Field Representations in Spherically Stratified Regions", section in The Theory of Electromagnetic Waves, Ed. M. Kline, Dover Publications, Inc., New York, 1965.
- [48] L.B. Felsen and N. Marcuvitz, Radiation and Scattering of Waves, Prentice Hall, 1973.
- [49] J.R. Wait, Electromagnetic Waves in Stratified Media, Second Edition, Pergamon Press, New York, 1970.
- [50] J.R. Wait, "The Whispering Gallery Nature of the Earth-Ionosphere Waveguide at VLF", IEEE Trans. on Antennas and Propagation, Vol. AP-15, No. 4, pp. 580-581, July 1967.
- [51] T. Ishihara, L.B. Felsen, A. Green, "High-Frequency Fields Excited by a Line Source Located on a Perfectly Conducting Concave Cylindrical Surface", IEEE Trans. on Antennas and Propagation, Vol. AP-26, No. 6, pp. 757-767, Nov. 1978.